



Norwegian University of
Science and Technology

Wave-in-Deck Forces and Response of Semi-Submersibles

Erik Skjeggedal

Marine Technology

Submission date: June 2017

Supervisor: Jørgen Amdahl, IMT

Norwegian University of Science and Technology
Department of Marine Technology

MASTER THESIS 2017
for
Stud. Techn. Erik Skjeggedal



Wave-in-deck forces and response for semi-submersibles

Krefter fra bølgeslag i dekk og responsberegninger for halvt nedsenkbare plattformer

Following the COSL Innovator accident on the 30th of December 2015, the current industry practises for calculating air gaps and slamming loads on deck box in the case of negative air gap have been put under review. Platforms with negative air gap, i.e. the distance between wave crest and bottom of steel, may experience large loads due to wave impacts. Common practise is to use linear diffraction analysis combined with model tests in order to determine the loads.

Recent model tests have revealed that also the impact loads on the columns from breaking, or near breaking, waves are significant and possible considerably higher than what is indicated in the relevant rules and regulations. The loads are characterized by short durations, large spatial variations and high values, which put the measurement system at a considerable stress.

Further, the interpretation of the test results is challenging for several reasons:

1. Froude scaling may not be appropriate
2. Large fluctuations in the measurements may indicate a dynamic load (possibly entrapped air), or unforeseen dynamic responses in the measurement system
3. The statistical distributions of the extreme loads are not well behaved or do possibly not follow a Gumbel distribution

In spite of the challenges above, the model test results are at this stage the best there is. Currently there is a push from both the industry and the academia to resolve the uncertainties, but it is likely that any results will not be available in the short term.

Traditional design, accompanied with traditional analyses, will not be sufficient to prove that the semi columns will be able to withstand the measured wave impact loads. As such, the work should focus on local structural integrity/capacity of the column designs for a semi-submersible subject to slamming loads from breaking waves. Non-linear structural analyses shall be performed in order to investigate the structural capacity for different slamming loads with different horizontal and vertical extent, duration and slamming pressure. Variations to

the global design (column width, square vs. round), as well as local design (girder spacing, plate thickness etc) may be studied. Load time series will be made available for interpretation and implementation.

Statoil has performed extensive model testing including slamming load measurements on a North Sea platform column. If Statoil approves the use of these data, it will be a good case study for the project/master thesis.

The purpose of the project thesis is to investigate the theory and established engineering practise for how to conduct dynamic response of a stiffened plated vertical surface on a floating platform and to familiarize with nonlinear finite element analysis the response to slamming loads.

The project work is proposed carried out in the following steps:

1. Investigate the effect of nonlinear floater pitch motion on air gap calculations by using frequency domain calculations (WADAM) and time domain calculations (WASIM) (Optional: CFD calculations).
2. Discuss the possibility to conduct hydro-*elastoplastic* structure interaction analysis of slamming events with explicit software (LS-DYNA or ABAQUS) using ALE or CFD approach.
3. Simulate drop tests with rigid panels and compare the simulated response with measurements from the tests. Focus shall especially be placed on pressure-time histories and impulses for the slamming load.
4. Provided that reasonable agreement with test results is obtained in pt. 4, simulate identical drop tests with elastic and elasto-plastic panels where the panels may be subjected to large, finite deformations. The failure mode of the panels shall be thoroughly documented and discussed. Key results will be pressure-time histories, area distributions and impulses. How does the structural deformations influence the slamming forces. Compare the results with those from simulations based on pressure-time histories for rigid panels (obtained in pt.4).
5. Compare simulated loads with predictions based on DNVGL-OTG –14
6. Investigate whether the panel response may be estimated by means of simplified methods, e.g. the SDOF approach for blast loading, refer DNV-GL RPC204. Resistance model for stiffened plate developed by Yu & Amdahl may be applied. The response for arbitrary or standardized pressure histories for SDOF models should be solved by numerical integration. Present results in the form of Bigg's charts or pressure-impulse diagrams. On the basis of the investigation propose a simple, design-oriented shape of the pressure-pulse.
7. Use recorded pressure histories from laboratory slamming tests on platform column models to estimate the structural for accidental slamming events on full-scale steel platform columns. Use the experience from simulation of the panel drop tests to estimate the influence of structural deformation of the pressure histories.
8. Conclusions and recommendations for further work in the master thesis project

Literature studies of specific topics relevant to the thesis work may be included.

The work scope may prove to be larger than initially anticipated. Subject to approval from the supervisor, topics may be deleted from the list above or reduced in extent.

In the thesis the candidate shall present his personal contribution to the resolution of problems within the scope of the thesis work.

Theories and conclusions should be based on mathematical derivations and/or logic reasoning identifying the various steps in the deduction.

The candidate should utilise the existing possibilities for obtaining relevant literature.

The thesis should be organised in a rational manner to give a clear exposition of results, assessments, and conclusions. The text should be brief and to the point, with a clear language. Telegraphic language should be avoided.

The thesis shall contain the following elements: A text defining the scope, preface, list of contents, summary, main body of thesis, conclusions with recommendations for further work, list of symbols and acronyms, references and (optional) appendices. All figures, tables and equations shall be numerated.

The supervisor may require that the candidate, in an early stage of the work, presents a written plan for the completion of the work. The plan should include a budget for the use of computer and laboratory resources, which will be charged to the department. Overruns shall be reported to the supervisor.

The original contribution of the candidate and material taken from other sources shall be clearly defined. Work from other sources shall be properly referenced using an acknowledged referencing system.

The report shall be submitted in two copies:

- Signed by the candidate
- The text defining the scope included
- In bound volume(s)
- Drawings and/or computer prints which cannot be bound should be organised in a separate folder.

Supervisor:

Prof. Jørgen Amdahl

Co-supervisors

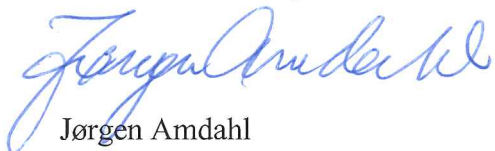
DNV GL: Arne Nestegård

SINTEF OCEANS: Hagbart S. Alsos

Phd stud. Zhaolong Yu

Deadline:, June 10, 2017

Trondheim, January 11 2017


Jørgen Amdahl

Preface

The thesis is a master thesis written for the study program marine technology, at the department of structural engineering during the spring semester of 2017. The thesis is a continuation of the project thesis written in the autumn of 2016 where the outline for the thesis was developed during my summer job at DNV GL. The topic was developed in cooperation with both my supervisors where my main supervisor was professor Jørgen Amdahl at the department of marine technology who is a specialist in marine structural engineering. The thesis was written in cooperation with DNV GL where DNV GL contributed with data relevant for the thesis work as well as an additional supervisor, Arne Nestegård who is a specialist in marine hydrodynamics. In the project thesis, it was found that wave impacts might be described by drop tests, so drop tests are simulated in this master thesis as a continuation of this work. In addition, I have a third supervisor for the master thesis, Hagbart S. Alsos. He works in Sintef Ocean and has knowledge within drop tests and the use of the LS-Dyna FEM software.

The thesis studies the loads and responses of wave slamming on semi-submersibles with an emphasis on methods for simulating large wave loads and different methods for response calculations are presented. The estimated loads are compared to results from model tests and loads given in DNV GL's OTG-14. The data from the model tests are classified, thus, the results are slightly modified to not reveal any sensitive information. The responses are calculated for vertical stiffened panels on a general semi-submersible.

Most of the analysis were carried out on a personal computer running Windows 10. The computer has 8GB of ram and an i7-4500 CPU with a clock speed of 2.40GHz. More advanced simulations were carried out on NTNU's super computer, "Vilje".

Trondheim, 2017-06-08



Erik Skjeggedal

Acknowledgment

Firstly, I would like to thank my supervisors for their contribution and interest in the topic. I would like to thank Professor Jørgen Amdahl for great help and guidance, not only during the development of the thesis, but also when creating the outline for the thesis during the summer. I would also like to thank Arne Nestegård for the interesting discussions when outlining the thesis and general guidance when writing the thesis. He has also been of great help with the formalities in allowing me access to the confidential test data to compare my results with. Moreover, I would like to thank Hagbart S. Alsos who has not only helped out with useful information and suggestions, but who has also been of great help in learning the LS-Dyna software.

In addition, I want to thank Bjørn Christian Abrahamsen for good input and feedback during guidance meetings as well as Odd Faltinsen for taking the time to explain certain aspects related to his literature on slamming and hydroelasticity. In addition, I would like to thank both Yanyan Sha and John Floan who has helped me in getting LS-Dyna to run on NTNU's super computer, "Vilje". Finally, I would like to thank my fellow students with whom I share an office at Tyholt for providing a fun and professional environment to write my thesis in.

E.S.

Summary

In critical sea states, semi-submersibles may experience large negative air gaps in which incoming waves cause large slamming loads that may lead to severe structural deformations. Wave loads due to slamming are difficult to predict using analytical approaches as there are many uncertainties involved. Older rules and guidelines base the loading estimates on the particle velocities in the waves whereas newer guidelines have based the loading on the relative upwelling on the platform.

Model tests are among the most accurate ways of estimating wave loads on offshore platforms and are recommended by classification societies. However, model tests are expensive and difficult to execute as it is complicated to recreate the critical sea states that offshore platforms may experience. In this thesis, it is therefore proposed to investigate if drop tests at equivalent velocities as the particle velocities in incoming waves may be used to recreate the same loading conditions. Drop tests were simulated using the arbitrary Lagrangian Eulerian, denoted ALE, approach. To verify both the parameters and the ALE-approach, a drop test described in (Faltinsen, 2005) was recreated in the finite element software, LS-Dyna. The results showed good agreement with the measured strains, pressures and natural periods adding credibility to the subsequent results obtained in the thesis.

The structural components may undergo large deformations which in turn affects the pressure distribution on the structure. The interaction between the fluid pressure and structural deformation is known as hydroelasticity. In general, not accounting for hydroelastic structure response is conservative. Pressure distributions for rigid and deformable panels, where hydroelastic effects become increasingly prominent, were compared for the same parameters as in (Faltinsen, 2005). The initial pressure impulses observed at impact were smaller for the deformable plate than the rigid plate at the same impact velocity, but the initial pressure peak was equal. For the deformable plate, a pressure approximately proportional to the acceleration of the plate is observed after the initial pressure pulse during the deformation phase and may be viewed as an added mass pressure. A larger deformation was seen when solving for an equivalent beam with the rigid pressure pulse.

Drop tests were simulated for different impact velocities. At an angle of impact of 0° , the initial pressure peak appears to be linearly dependent upon the impact velocity. It was also

observed that the larger loads associated with higher impact velocities led to larger deformations where membrane forces became prominent, hence decreasing both the wet and dry natural period of the structure. For the two-dimensional drop tests, the wet natural period was found to be approximately the same for both the elastic and elasto-plastic drop tests. For the three dimensional drop tests, the elasto-plastic plate had a longer period than the elastic plate. The peak of the second pressure surge was larger for the elastic plate compared to the elasto-plastic plate. By increasing the velocity, the difference increased.

The pressure-time curves for the simulated drop tests of deformable plates display some different properties compared to the pressure time curves for wave impact. The peak pressures are seen to be larger for the drop tests where the duration of the load is shorter. It is however seen that the structural deformations obtained in the deformable drop tests are in the same order of magnitude as those obtained using the loading model from (GL, 2016b). About the same levels of structural response was observed for a 3[m] by 3[m] deformable panel dropped at a velocity of 11.19[m/s] as when loaded by an OTG-pressure-time curve with a pressure peak of 1200[kPa]. Moreover, the same structural response was observed for a column dropped at a velocity of 20[m/s] into water as when loaded with an OTG-pressure-time curve with a pressure peak of 2300[kPa].

Relative velocity seems to be the driving factor in structural deformations in the drop tests of deformable plates with the narrow pressure peaks of limited importance. Two main benefits are seen with response calculations where drop tests of deformable panels are simulated. The first is that the spatial pressure distribution is captured. The second is that added mass is included in the analysis, reducing the uncertainty in establishing added mass.

The simulated drop tests of rigid plates yield pressure curves that are unrealistic in terms of both magnitude and duration compared to the loading seen from deformable panels and in the technical guidelines.

Overall, the results for simulating wave impact loading by drop tests were promising. However, there are much that should be explained before the method can be applied in practice. For instance, the differences in pressure-time-curves should be explained. In addition, more precise methods for establishing the impact velocity and angle of impact should be developed.

Sammendrag

I ekstreme sjøtilstander kan bølger slå over hoveddekket til halvt nedsenkbare plattformer hvilket kan lede til store bølgelaster og store deformasjoner i komponenter. Laster grunnet bølgeslag er vanskelige å predikere analytisk da det er mange usikkerheter involvert. I eldre regelverk og retningslinjer er lastene ofte basert på bølgens partikkelhastighet mens i de nye retningslinjene er lastene i stor grad basert på den relative oppvellingen på plattformen. Modellforsøk er blant de mest presise metodene for å beregne laster på offshore plattformer og er anbefalt brukt av klassifikasjonsselskapene. Likevel, det er både dyrt og vanskelig å gjennomføre modellforsøk, da det er komplisert å gjenskape de kritiske sjøtilstandene plattformen kan oppleve. I denne oppgaven er det derfor foreslått å undersøke hvorvidt man kan gjenskape de samme lastene ved å slippe en plate ned i vann med samme hastighet som partikkelhastigheten i den innkommende bølgen. Slike dropptester er simulert ved en "Arbitrary Lagrangian Eulerian" eller "ALE"-metode. For å verifisere modellparameterne så vel som metoden, ble en dropptest beskrevet i (Faltinsen, 2005) gjenskapt i elementmetode programvaren LS-Dyna. Resultatene viste samsvar mellom målte tøyninger, trykk og egenperioder hvilket gir kredibilitet til de videre resultatene i oppgaven fremstilt ved samme metode.

Komponentene kan gjennomgå store deformasjoner som vil påvirke trykkbildet på komponenten. Samhandlingen mellom trykk i fluider og deformasjoner er kjent som hydroelastisitet. Generelt er det konservativt å ikke vurdere hydroelastisitet. Trykkbilder for rigide og deformerbare paneler sluppet med samme betingelser som beskrevet i (Faltinsen, 2005) ble sammenlignet. Den initiale trykkimpulsen ved sammenstøt var større for de rigide panelene enn for de deformerbare panelene, selv om trykktoppen ble målt til å være lik. For de deformerbare panelene kan man observere et trykk som er tilnærmet proporsjonalt med platens akselerasjon og kan sees på som trykk fra tilleggsmasse. Det ble observert større deformasjoner for en elastisk plate utsatt for det rigide trykket enn hva som ble observert for den elastiske platen sluppet i vann.

Dropptester ble simulert for ulike hastigheter ved sammenstøt. Ved en vinkel på 0° ved sammenstøt synes det maksimale trykket å øke lineært med hastigheten. Det var også sett at de høyere lastene forbundet med økt hastighet ledet til store deformasjoner der membrankrefter opptrer i større grad, noe som senket både den våte og tørre egenperioden til strukturen. Det ble ikke observert noen konkrete trender for den naturlige perioden ved

elasto-plastisk respons kontra elastisk respons. Det ble likevel observert at ved store deformasjoner var den andre trykktoppen lavere ved elasto-plastisk respons enn ved elastisk respons. Forskjellen mellom trykkkurvene økte for større deformasjoner.

Trykk-tid-kurvene fra de simulerte droppstestene viste andre egenskaper enn trykk-tid-kurvene for bølgeslag på offshore plattformer. De målte maksimaltrykkene er høyere for droppstestene enn ved bølgeslag på plattformer samtidig som varigheten var kortere. Likevel ble det observert strukturell respons i samme størrelsesorden ved simulerte droppstester av deformerbare paneler som ved trykk fra lastmodellen gitt i (GL, 2016b). Om lag samme strukturelle respons ble målt ved en droppstest av et 3[m] ganger 3[m] panel ved en hastighet på 11.19[m/s] som ved lasting med en OTG-trykk-tid-kurve med maksimaltrykk på 1200[kPa]. Videre ble samme strukturelle respons ble oppnådd ved en simulert droppstest av en søyle på 20[m/s] som ved lasting av OTG-trykk-tid-kurve med maksimaltrykk på 2300[kPa].

Mye tyder på at det er de relative hastighetene i det deformerbare panelet som er dominerende for platerespons der det smale initiale trykkmaksima er av begrenset betydning. To fordeler er observert ved å beregne respons ved simulering droppstester av deformerbare paneler. Den første er at trykkbildet over platen er korrekt. Den andre er at tilleggsmassen blir inkludert i analysen hvilket reduserer usikkerheten tilknyttet beregning av tilleggsmasse.

De simulerte droppstestene av rigide paneler ga trykk-tid-kurver som var urealistiske i forhold til målte trykk-tid-historier ved bølgeslag der varigheten er kortere samtidig som trykkamplituden er høyere. Ved å laste deformerbare plater med trykk oppnådd ved rigide droppstester ble responsen typisk større enn ved deformerbare droppstester.

Resultatene oppnådd ved å simulere bølgeslag ved droppstester er lovende. Likevel er det mye som bør utredes før metoden kan brukes i praktiske anvendelser. Trykk-tid-kurvenes forskjeller fra det som er målt ved bølgeslag bør utredes. I tillegg bør mer presise metoder knyttet til etablering av dropphastighet og støtvinkel etableres.

Contents

- Preface i
- Acknowledgment ii
- Summary iii
- Sammendrag v
- Nomenclature xxii
- Symbols xxiv

- 1 Introduction 1**
- 1.1 Background 2
- 1.2 Objectives 2
- 1.3 Literature Review 3
 - 1.3.1 Rules and Guidelines for Load Pulses 3
 - 1.3.2 Water Entry 4
 - 1.3.3 Hydroelastic Structure Response 5
 - 1.3.4 Wave in Deck Forces 5
- 1.4 Limitations 6
- 1.5 Approach 7
- 1.6 Structure of the Report 7

- 2 Theory 11**
- 2.1 Wave Theory 11
 - 2.1.1 Linear Wave Theory 11
 - 2.1.2 Velocity Estimates by Wheeler Stretching 12
 - 2.1.3 Velocity Estimates by the Second Order Kinematics Model 13
 - 2.1.4 Energy Content in Waves 13
 - 2.1.5 Wave Breakage and Shoaling 14

2.2	Estimates of Load Pulses on Offshore Structures	15
2.2.1	Sea States Given by Steepness Criterion and Probability Contours	16
2.2.2	Equations of Motion	17
2.2.3	Calculating Air Gap by the Simplified Approach	18
2.2.4	Applying Asymmetry Factors	20
2.2.5	Air Gap Calculations in Wadam	20
2.2.6	Loads Based on Offshore Technical Guidelines	21
2.2.7	Loads Based on Recommended Practices	24
2.3	Slamming	25
2.3.1	General Slamming Theory	25
2.3.2	Experimental Drop Test	26
2.4	Hydroelastic Structure Interaction	28
2.4.1	Criteria for Hydroelastic Calculations	28
2.4.2	Analytical Hydroelastic Calculations	29
2.4.3	Hydroelastic Calculations in LS-Dyna	30
2.4.4	ALE	31
2.4.5	ALE in LS-Dyna	32
2.4.6	Penalty Algorithm	33
2.5	Structural Analysis	34
2.5.1	Failure Modes of Plates	34
2.5.2	Resistance Model for Stiffened Plate	35
2.5.3	SDOF Analysis	37
2.5.4	Methods for Calculating Dynamic Response	38
2.5.5	Added Mass	40
2.5.6	Nonlinear Strain	41
2.5.7	Strain Rate Hardening	42
2.5.8	Eigen Period for a Beam in Tension	43
3	Global Air Gap Analysis of Semi-Submersible	45
3.1	Semi-Submersible Parameters	45
3.1.1	Modelling	45
3.1.2	Post Processing RAOs	48
3.2	Air Gap Results	49

3.3	Particle Velocities	51
3.3.1	Velocity Estimates by Wheeler Stretching	52
3.3.2	Velocity Estimates by the Second Order Kinematics Model	53
3.3.3	Sea State Properties	53
4	Verification of FSI-Model by 2D-Experiments	55
4.1	Experimental Layout	55
4.1.1	Experimental Results	56
4.2	Finite Element Modelling of Drop Tests	58
4.2.1	Water and Air Modelling in LS-Dyna	58
4.2.2	2D Panel Model	59
4.2.3	Analytical Plate Properties for Verification Study	62
4.3	Results from Drop Test Simulations	63
5	FEM Studies of 2D and 3D Panels	67
5.1	2D Panels	67
5.1.1	Pressures and Deformations for Drop Velocity of 3[m/s]	67
5.1.2	Velocity Dependency	69
5.1.3	Elasto-Plastic Plate Response	69
5.1.4	2D Drop Test Summary	72
5.2	3D Panels Exposed to Slamming Loads	73
5.2.1	Modelling of 3D Panels	73
5.2.2	Calculating Added Mass	75
5.2.3	Elemental and Material Properties of Model	76
5.2.4	Loads Based on RP-C205	77
5.2.5	Response Based on RP-C205	79
5.2.6	Loads Based on OTG-14	81
5.2.7	Response Based on OTG-14	82
5.3	3D Panel Drop Tests	84
5.3.1	Water and Air Modelling	84
5.3.2	FEM Model of 3D Panel	85
5.3.3	Pressure Development and Relative Volume for 3D Drop Tests	86
5.4	Drop Test Responses	89

5.4.1	Response Based on Hydro-Elasto-Plastic Behaviour	89
5.4.2	Response Based on "Rigid Drop Pulse"	91
5.4.3	Pressure Peak from Experimental Drop Test	92
5.4.4	Comparing the Loading Models and Experimental Data	92
5.4.5	Summary FEA Response Estimates	93
6	Steel Columns	95
6.1	Finite Element Modelling	95
6.1.1	Water and Air modelling	95
6.1.2	Stiffened Column Model	96
6.2	Results from Drop Test Simulations	99
6.2.1	Pressure Pulse Histories	99
6.2.2	Structural Deformations	99
6.2.3	Response Based on Hydro-Elasto-Plastic Behaviour	101
6.2.4	Response Based on "Mean Rigid Drop Pulse"	102
6.2.5	Response Based on "Adjusted Rigid Drop Pulse"	103
6.3	Results from OTG Loading	103
6.3.1	Pressure Pulse from OTG	103
6.3.2	Response based Pressure Pulse from OTG	104
7	SDOF Analysis	107
7.1	SDOF Analysis of Test Rig	107
7.2	3D Simplified Response	108
7.2.1	Beam Analogy for Stiffened Panel	108
7.2.2	Added Mass Calculation	109
7.2.3	Parameters for SDOF Analysis by RP Stiffness Model	110
7.2.4	Linear Stiffness from FEA	111
7.2.5	Numerical Integration of Response	112
7.2.6	RP Stiffness Model with "Rigid Drop Pulse"	113
7.2.7	FEM Stiffness Model with "Rigid Drop Pulse"	114
7.2.8	RP Stiffness Model with OTG Load	115
7.2.9	FEM Stiffness Model with OTG Load	116
7.2.10	Summary SDOF Response	116

7.2.11 Energy Contents in Waves Relative to Response	118
8 Discussion	121
8.1 Establishing the Most Critical Sea State	121
8.2 Different Loading Models	121
8.3 Hydroelasticity	122
8.4 Applying Mean Pressure	122
8.5 Simulating Wave Impacts in Drop Tests	123
9 Conclusion and Recommendations for Further Work	125
9.1 Conclusion	125
9.1.1 Influence of Negative Air Gap	125
9.1.2 Drop Tests	125
9.1.3 Hydroelasticity	126
9.1.4 Simulating Wave Impact by Water Entry	127
9.1.5 Sources of Error	127
9.2 Recommendations for Further Work	127
References	I
A RAOs	V
B Spectra	IX
C Air Gap Results	XI
D OTG Pressure Curves	XIII
E Air Gap Calculation Script	XV
F LS-Dyna Results	XXIII
G Transformation Factors for Beams	XXVII
H SDOF Analysis	XXIX
H.1 Timeintegration Function from MatLab	XXIX
H.2 SDOF Plots	XXX
H.2.1 Rigid Load Pressure	XXXI

H.2.2 Load From OTG XXXIII

List of Figures

- 2.1 Principles of an effective height used in wheeler stretching (DNV, 2014b) 12
- 2.2 Principles of a horizontal velocity calculation according to the second order kinematics model (DNV, 2014b) 13
- 2.3 Geometry of a breaking wave as seen in (Kjeldsen et al., 1979) 15
- 2.4 Example of a design contour on the Norwegian Continental Shelf (GL, 2016a) . 16
- 2.5 Principle of an Air Gap Analysis 18
- 2.6 Wave asymmetry factors w.r.t. to position and wave direction (GL, 2016a) 20
- 2.7 21
- 2.8 ULS peak pressures for vertical positions in terms of relative upwelling as given in (GL, 2016b) 22
- 2.9 Temporal Pressure w.r.t. peak pressure. (GL, 2016b) 23
- 2.10 Description of the idealised slamming pulse (GL, 2016b) 24
- 2.11 C_S plotted as a function of δt^* and α (Huera-Huarte et al., 2011) 27
- 2.12 Measured force development w.r.t time (Huera-Huarte et al., 2011) 28
- 2.13 Hydroelastic versus rigid quasi static deflection (Stenius et al., 2011) 30
- 2.14 Principles of the penalty algorithm (Aquelet et al., 2006) 34
- 2.15 Different failure modes for a stiffened plate. (DNV, 2014a) 35
- 2.16 Plastic resistance according to (Standard, 2004) 36
- 2.17 A typical Biggs chart as given in (DNV, 2014a) 38
- 2.18 Added mass for a 2D plate as given by (DNV, 2014b) 40

- 3.1 The typical semi-submersible model used in the air gap analysis 46
- 3.2 The 19 air gap points used in the air gap analysis 46
- 3.3 Maximum negative air gap measured by sampling point and sea state 50

3.4	Negative air gap at the front of the semi-submersible at head sea with 0 wave spreading	51
3.5	Estimated are of non-breaking wave	53
4.1	Experimental setup of the drop test described in (Faltinsen, 2005)	56
4.2	Pressures measured in the middle and at $\frac{z_a}{L} = \frac{1}{10}$ (Faltinsen, 2005)	57
4.3	Structural strain measured in the middle and at $\frac{z_a}{L} = \frac{1}{10}$ (Faltinsen, 2005)	58
4.4	Set up of 2D plate structure in LS-Dyna with elastic spring	60
4.5	Setup of 2D plate structure in LS-Dyna with rotational spring	60
4.6	Water rise due to water entry of elastic plate at a velocity of 2.94 [m/s]	63
4.7	Upper x-strains measured at $x/L = 0.1$ and 0.5	64
4.8	Pressure distribution at $L = 50\%$ and $L = 10\%$ for the deformable plate based on the experimental drop test described in (Faltinsen, 2005) with an impact velocity of 2.94m/s	65
5.1	Mean pressure development for two-dimensional drop test with an impact velocity of 2.94[m/s]	68
5.2	Pressure distribution upon water impact for deformable and non-deformable plate	69
5.3	Mean pressure time series for a drop velocity of 9[m/s]	70
5.4	Mean pressure time series for a drop velocity of 12[m/s]	70
5.5	Elastic and elasto plastic deflection at a drop velocity of 9[m/s]	71
5.6	Elastic and elasto-plastic deflection at a drop velocity of 12[m/s]	72
5.7	Cross section of the beam model of the stiffened plate	74
5.8	Finite element model of the stiffened plate	75
5.9	Stokes wave approximation used for estimated wetted length	77
5.10	Deflection of the stiffened clamped plate subjected to the rigid design load pulse from FEA	79
5.11	Maximum Von Mises stress from maximum static design wave load	80
5.12	Maximum deflection measured for the dynamic loading condition based on the RPC	81
5.13	Pressure development based on OTG for sea state 15	82

5.14 Maximum deflection measured for the dynamic loading condition based on the OTG 83

5.15 Von Mises stress at maximum deflection with OTG loading 84

5.16 Finite element model of the stiffened plate drop rig 85

5.17 Pressure time history for 3D drop test into sea water at the design wave condition 87

5.18 Mean spatial pressure distribution seen at the middle of 3D rigid panel 88

5.19 Relative volume fraction of the fluid upon impact 89

5.20 Maximum deflection at an impact velocity of 11.19[m/s] for deformable plate . 90

5.21 Von Mises stress at maximum deflection for elasto-plastic drop test with strain rate hardening 90

5.22 Maximum deflection at an impact velocity of 11.19[m/s] for rigid drop pulse . . 91

5.23 Von Mises stress at maximum deflection for elasto-plastic plate test with strain rate hardening subjected to the rigid drop pressure 92

6.1 Finite element model of the column 96

6.2 Loaded area of column 97

6.3 Pressure time series for the 6[m] by 6[m] plate on the column 99

6.4 Maximum deformation found for the column subjected to loading at an impact velocity of 20[m/s] 100

6.5 Relative displacement for deformable stiffened plate on column dropped into sea water at a velocity of 20[m/s] 101

6.6 Von Mises stress in column at maximum deflection the coupled analysis 102

6.7 Von Mises stress in column at maximum deflection for "mean rigid load pulse" 102

6.8 Von Mises stress in column at maximum deflection for "adjusted rigid load pulse" 103

6.9 Pressure pulse curve for OTG loading of steel column based on maximum girder loading of a 6[m] by 6[m] area 104

6.10 Maximum deflection of steel column with loading condition from OTG-14 . . . 105

6.11 Maximum Von Mises stress distribution for OTG loading on the steel column . 105

7.1 Comparison of maximum deflection estimated from numerical integration and LS-Dyna 108

7.2 Coefficient for establishing effective flange width (Veritas, 2011a) 109

7.3 Plastic resistance for beam model of the stiffened clamped plate 110

7.4	Pressure deflection curve obtained from LS-Dyna	111
7.5	Linearisation of response as recommended in (DNV, 2014a)	113
7.6	Deflection of the stiffened clamped plate subjected to the rigid design load pulse	113
7.7	Deflection of the plate subjected to the "rigid design load pulse" with stiffness obtained from LS-Dyna	114
7.8	Deflection of the stiffened clamped plate subjected to the load pulse from the OTG	115
7.9	Deflection of the plate subjected to the load pulse from the OTG with stiffness extracted from LS-Dyna	116
7.10	Deflection calculated for the stiffened plate subjected to the rigid design load pulse	117
7.11	Deflection calculated for the stiffened plate subjected to the load given by the OTG	118
A.1	Surge RAO from Wadam air gap analysis	V
A.2	Sway RAO from Wadam air gap analysis	VI
A.3	Heave RAO from Wadam air gap analysis	VI
A.4	Roll RAO from Wadam air gap analysis. The amplitude is in degrees	VII
A.5	Pitch RAO from Wadam air gap analysis. The amplitude is in degrees	VII
A.6	Yaw RAO from Wadam air gap analysis. The amplitude is in degrees	VIII
B.1	Jonswap spectrum for run ID 6	IX
B.2	Jonswap spectrum for run ID 15	X
D.1	Pressure development based on OTG for sea state 6	XIII
E.1	The 2D defection shape in LS-Dyna compared to the chosen cosine deflection shape	XXIII
E.2	Mean pressure development for a drop velocity of 0.75m/s for 2D plate	XXIV
E.3	Mean pressure development for a drop velocity of 1.5m/s for 2D plate	XXIV
E.4	Mean pressure development for a drop velocity of 6m/s for 2D plate	XXV
E.5	Mean pressure development for a drop velocity of 11.19m/s into sea water for 2D plate	XXV
E.6	Mean pressure development for a drop velocity of 18m/s for 2D plate	XXVI

E.7 Elastic and elasto plastic deflection at a drop velocity of 18[m/s] for 2D plate . XXVI

G.1 Transformation factor for simply supported beam in SDOF XXVII

G.2 Transformation factor for clamped beam in SDOF XXVII

H.1 Beam stiffness k found from LS-Dyna w.r.t. maximum deflection XXX

H.2 Velocity of the stiffened clamped plate subjected to the rigid design load pulse XXXI

H.3 Acceleration of the stiffened clamped plate subjected to the rigid design load pulse XXXI

H.4 Velocity of the stiffened plate with the stiffness function obtained from LS-Dyna subjected to the rigid design load pressure XXXII

H.5 Acceleration of the stiffened plate with the stiffness function obtained from LS-Dyna subjected to the rigid design load pressure XXXII

H.6 Velocity of the stiffened clamped plate subjected to pressure from the OTG . . . XXXIII

H.7 Acceleration of the stiffened clamped plate subjected to pressure from the OTG XXXIII

H.8 Velocity of the stiffened plate with the stiffness function obtained from LS-Dyna subjected to the pressure from the OTG XXXIV

H.9 Acceleration of the stiffened plate with the stiffness function obtained from LS-Dyna subjected to the pressure from the OTG XXXIV

List of Tables

- 2.1 Gruneisen EOS from literature 33
- 2.2 Non dimensional added mass by dipole singularities as described in
(Meyerhoff, 1970) 40
- 2.3 Nonlinear material parameters for S235 steel 42
- 2.4 Nonlinear material parameters for S355 steel 42
- 2.5 Nonlinear material parameters for S420 steel 42

- 3.1 Locations for air gap sampling points 47
- 3.2 General parameters for test semi-submersible 47
- 3.3 Parameters for Morison model 48
- 3.4 Jonswap spectra defined by the DNV steepness criteria for use in air gap
analysis 48
- 3.5 Approximate wave parameters for sea state 6 and 15 51
- 3.6 Relative location, particle velocity and acceleration given by Wheeler stretching 52
- 3.7 Relative location, particle velocity and particle acceleration given by the
second order kinematics model 53
- 3.8 Wave properties of a non-breaking wave 53
- 3.9 Wave energy content for the most critical sea state 54

- 4.1 Parameters for deformable plates used in drop tests (Faltinsen, 2005) 56
- 4.2 Material properties applied in LS-Dyna 58
- 4.3 EOS applied for water, air and steel 59
- 4.4 Properties for the finite element model used in the 2D drop test verification study 61
- 4.5 Linear material properties used in 2D drop tests 61
- 4.6 Nonlinear material properties used in 2D drop tests 62
- 4.7 Analytical properties of the flat plate subjected to drop tests 63

5.1	Key results from drop tests based on the test rig in (Faltinsen, 2005)	73
5.2	Properties of the chosen bulb flat	74
5.3	Approximate bulb flat stiffener parameters	75
5.4	Added mass calculation for 3D stiffened panel	76
5.5	Elemental properties of stiffened panel subjected to load pulse	76
5.6	Linear material properties used for stiffened 3[m] by 3[m] panel	76
5.7	Nonlinear material properties used for stiffened 3[m] by 3[m] panel	77
5.8	Design loads based on recommended practices	78
5.9	Pressure time series for sea state 6	78
5.10	Pressure time series for sea state 15	79
5.11	Values for thickness calculations by equation 5.2 with design stresses given by (DNV, 2014b)	80
5.12	Values for section modulus calculations by equation 5.3 with design stresses given by (DNV, 2014b)	81
5.13	Peak pressure based on OTG 14	82
5.14	Fluid properties applied in LS-Dyna	84
5.15	EOS applied for water, air and steel	85
5.16	Elemental properties for the 3D dropped panel rig	86
5.17	Linear material properties applied in the 3D panel drop rig	86
5.18	Nonlinear material properties applied in the 3D panel drop rig	86
5.19	Peak pressures given by the loading model from (Huera-Huarte et al., 2011), . .	92
6.1	Fluid properties applied in LS-Dyna	95
6.2	EOS applied for water, air and steel	95
6.3	Calculation of added mass on the 6[m] by 6[m] panel using Meyerhoff's formula	97
6.4	Elemental properties for steel columns,	98
6.5	Linear material properties for steel columns	98
6.6	Nonlinear material properties for steel columns	98
7.1	Generalised parameters used in SDOF of 2D test rig	107
7.2	Structural parameters for stiffened plate response for clamped beam	110
7.3	Parameters for elastic and plastic part of the SDOF analysis for clamped beam .	111
7.4	Mass and stiffness parameters used in SDOF with stiffness model from FEA . .	112

- 7.5 Summary of the response for the plate with the RP stiffness model subjected to a rigid load pulse 114
- 7.6 Summary of the response for the plate with the LS-Dyna stiffness model subjected to a rigid load pulse 115
- 7.7 Summary of the response for the plate with the RP stiffness model subjected to the OTG load 115
- 7.8 Summarised response for plate subjected to the load pulse from the OTG with stiffness extracted from LS-Dyna 116
- 7.9 Energy in plate relative to wave energy calculated at maximum deflection for pinned and clamped plate 119

- C.1 Sea states leading to the largest negative air gaps for each sampling point XI

Nomenclature

DOF Degree of freedom

SDOF Single degree of freedom

MDOF Multiple degree of freedom

ULS Ultimate limit state

ALS Accidental limit state

FEM Finite element method

FEA Finite element analysis

CAE Computer aided engineering

NCS Norwegian continental shelf

CFD Computational fluid dynamics

SWL Still water line

RAO Response amplitude operator

DLF Dynamic load factor

EOS Equation of state

FSI Fluid structure interaction

SOKM Second order kinematics model

RP Recommended practice

OTG Offshore technical guidelines

Symbols

η_i Global response in DOF i

ζ Free surface elevation

ζ_A Wave amplitude

u Water particle velocity in the x-direction

w Water particle velocity in the z-direction

M Mass

M_a Added mass

w Beam deflection

ρ Density

H_S Significant wave height

T_Z Zero mean crossing period

T_P Peak period

s Wave steepness $\frac{H}{\lambda}$

s Stiffener spacing

L Length of stiffener

λ Wave length

a_o Static air gap

a Instantaneous air gap

α Wave asymmetry factor

p Pressure

ω Radial frequency

h Water depth

C Wave celerity

c Wetted length

β Angle of impact

t Time

k Wave number

χ Upwelling

Chapter 1

Introduction

Following the COSL Innovator accident on the 30th of December 2015, the current industry practices concerning wave loads have been put under review. Rules and guidelines concerning wave loads are based on establishing the water particle velocity in the incoming waves as well as the extent of negative air gap. Air gap is understood as the distance between the wave crest and the bottom of steel, i.e. for a platform with negative air gap, the crest of the wave reaches above the bottom of steel. For large and steep waves, this may lead to severe and damaging loads on structural components on the platform.

For extreme sea states, platforms are raised to a survival condition, increasing the static air gap. In such extreme sea states, waves are generally steep and higher order effects are of high importance. Thus, general linear theory must be used with caution as it in general is no longer valid in calculating the wave impact loads acting on the platform. Theories on how to account for these effects must be looked into in order to get loads of the correct magnitude and duration.

After establishing the load, the response of the semi-submersible's structural component may be calculated. The large loads associated with vessels with negative air gaps may cause large deformations to both unstiffened and stiffened plates. Commonly, these responses will be plastic and must be handled using nonlinear theory. Moreover, large plate deformations will have an effect on the fluid pressure acting on the plate and the thesis will investigate if it should, and if so, how these hydroelastic effects should be taken into account in terms of representing the load and analyzing the plate response. Estimates will consist of simulating slamming problems where deformable and non-deformable plates are dropped into water with velocities equivalent to the particle velocities in waves and study if

the loads are comparable to wave in-deck-loads on offshore platforms.

1.1 Background

Performing model tests of semi-submersibles to establish negative air gaps and pressure-time histories is expensive and time consuming. In addition, the methods based on linear theory and software to establish pressures and negative air gap is not yet accurate enough to be applied without conservative safety factors. Therefore, new methods for establishing wave-in deck loads on offshore platforms should be investigated. Water entry problems consist of many of the same load components and measured pressure development w.r.t. time shows many of the same properties as seen in for wave in deck forces.

Experimental drop tests are less complex and cheaper to execute than model tests of semi-submersibles and might be a viable option to test structural integrity and loads in critical sea states. LS-Dyna is a finite element software that has proven to be useful in simulating fluid structure interaction problems, among other impact problems. The software is able to account for the interaction between the fluid pressures and the deformation of the plate, allowing for hydroelastic effects to be investigated as well. By simulating drop tests in LS-Dyna, and comparing the pressure-time series with pressure time-series obtained by model tests and guidelines, the procedure may be evaluated in terms of how accurately a wave impact may be simulated by water entry.

1.2 Objectives

1. Discuss the possibility to conduct hydro-elastoplastic structure interaction analysis of slamming events with explicit software (LS-DYNA or ABAQUS) using ALE or CFD approach.
2. Simulate drop tests with rigid panels and compare the simulated response with measurements from the tests. Focus shall especially be placed on pressure-time histories and impulses for the slamming load.
3. Provided that reasonable agreement with test results is obtained in pt. 4, simulate identical drop tests with elastic and elasto-plastic panels where the panels may be

subjected to large, finite deformations. The failure mode of the panels shall be thoroughly documented and discussed. Key results will be pressure-time histories, area distributions and impulses. How does the structural deformations influence the slamming forces. Compare the results with those from simulations based on pressure-time histories for rigid panels (obtained in pt.4).

4. Compare simulated loads with predictions based on DNVGL-OTG –14
5. Investigate whether the panel response may be estimated by means of simplified methods, e.g. the SDOF approach for blast loading, refer DNV-GL RPC204. Resistance model for stiffened plate developed by Yu & Amdahl may be applied. The response for arbitrary or standardized pressure histories for SDOF models should be solved by numerical integration. Present results in the form of Bigg's charts or pressure-impulse diagrams. On the basis of the investigation propose a simple, design-oriented shape of the pressure-pulse.
6. Use recorded pressure histories from laboratory slamming tests on platform column models to estimate the structural for accidental slamming events on full-scale steel platform columns. Use the experience from simulation of the panel drop tests to estimate the influence of structural deformation of the pressure histories.
7. Conclusions and recommendations for further work in the master thesis project

1.3 Literature Review

1.3.1 Rules and Guidelines for Load Pulses

Loading in the form of pressure pulses are common for accidental loads. Classification societies like DNV GL have collected the most relevant literature in terms of dynamic loading for offshore applications. For accidental loads on offshore structures, DNV GL's recommended practice (DNV, 2014a) deals with accidental load pulses in the form of explosion. There are many similarities between the loading due to wave impact and the loading due to explosion loads. Both loads may be described in the temporal and spatial domain and techniques for estimating the response are given as well. With the pressure-time series known, responses may be calculated with Biggs curves corresponding

to the pressure-time series, numerical integration, simplified response or other techniques. The methods presented for calculating the response is largely the same as in (Standard, 2004) and can thus be viewed as an accepted standard in terms of calculating dynamic response.

Load pulses due to wave impact are presented in (GL, 2016b). The OTG describes both theoretical methods for establishing the loading conditions as well as how to process data from model tests in order to establish loads. For the theoretical model based on the relative upwelling, the maximum peak pressures are seen to approach 3[MPa] with loading durations typically in the range of 0.2[s] which is in the same order of magnitude for ULS loads observed on offshore platforms.

1.3.2 Water Entry

Water entry problems have been of interest for many years and there has been a lot of research on the topic. The topic has been explored in a variety of manners, both in terms of actual tests, numerical simulations as well as analytical solutions. In (Faltinsen, 1993), analytical solutions are given both for the water entry of a wedge as well as the water entry for a cylinder. In part, the solution consists of a slamming component denoting the differentiated wet surface area. For a perfectly straight, rigid plate entering the water at an angle normal to the water surface, the angle of impact is 0° and the pressure component would be infinitely large by this approach.

Analytical solutions are useful benchmarks, but they might not capture nonlinearities and other effect which are of interest when solving large and complicated problems in fluid mechanics. Computational fluid dynamics or CFD is a common numerical approach procedure in order to calculate pressure distribution and flow surrounding moving objects. However, as stated in (Tutt et al., 2010), CFD can only solve fluid structure interaction one way, i.e. how the structure interacts with the fluid. For two way FSI-problems, coupled finite element analysis, FEM, and CFD analyses have been used. For instance, in (Aksenov et al., 2008) a two way coupling approach is described for FSI using the FEM software Abaqus and the CFD software FlowVision. However, for deformable drop tests, the most common procedure for simulating drop tests numerically have been using the arbitrary Lagrangian Eulerian Approach, ALE, by applying the FEM software LS-Dyna developed by the Livermore Software Technology Corporation.

Many experiments have been carried out where plates have been dropped into water where the corresponding pressures have been measured. One test with pressure-time series related to drop velocities and angles of impacts are given in (Huera-Huarte et al., 2011). Experimental drop tests at an angle of impact equal to 0° are described in (Faltinsen, 2000). Both of the experiments have yielded good results which could be of use to verify loads obtained by simulating water entry problems.

1.3.3 Hydroelastic Structure Response

Both Faltinsen and Stenius has done a great deal of research in hydroelastic response on high speed marine vessels. The experimental drop test described in (Faltinsen, 2000) does not only describe the resulting pressures at an angle of impact equal to 0° , it also describes the effect of hydroelasticity, i.e, the interaction between structural responses and fluid behavior. Furthermore, a lot of research in terms of modeling and analyzing hydroelastic problems has been carried out by Stenius. In his work, he has been using commercial finite element software in order to model the effects. In (Stenius et al., 2011) he has by using the ALE approach, achieved results with good agreement with experiments and linear theory on water entry of a wedge.

For offshore structures, responses for structural components such as plates will typically not be as large as is common for catamarans. Still, particle velocities of incoming waves and structural responses could still be so large that hydroelasticity should be considered. Criteria in terms of when hydroelastic effects are to be considered are given in DNV GL's recommended practice (DNV, 2014b) and it is indicated that hydroelastic effects become increasingly important for small impact angles.

1.3.4 Wave in Deck Forces

(Bea et al., 2001) deals with horizontal slamming loads on offshore jackets. Here, total force is expressed as a sum of five force components: the buoyancy term, F_b , the slamming term, F_s , the drag term, F_d , the lift term, F_l and the inertia term, F_i . For horizontal impact loads, the lift term and buoyancy term can generally be neglected.

In (Bea et al., 2001), the most conservative estimates of wave in deck forces was given by the Kaplan model. The Kaplan model is described in (BOM) and the loads are described as in equation 1.1. The first term relates to the change in added mass, the second term relates to

the change in velocity while the third term accounts for changes in the flow on a closed body. The plate in question is not a closed body, so the third term may be neglected and so may the buoyancy term since we are looking at horizontal forces.

$$F_i = \frac{dM_i}{dt} V_i + M_i \frac{dV_i}{dt} + \rho S_i \frac{dV_i}{dt} + drag + buoyancy \quad (1.1)$$

The Kaplan model is a so called quasi-linear approach where velocities and accelerations are obtained using linear theory and Wheeler stretching in the vertical direction. The wave heights are obtained either by tests or empirical models. The theory has also been applied using second order Stoke's wave theory. Some of the downsides of the approach is that some of the terms are complicated to obtain, making the equation difficult to apply for practical purposes.

Analytical solutions are inaccurate when solving large and complicated problems in fluid mechanics. Therefore, large problems are commonly solved numerically using CFD. In (Brodtkorb, 2008), CFD is shown to give a good agreement with the API-method described in recommended practices for establishing wave load on offshore structures.

1.4 Limitations

During the development of the thesis, the thesis gradually focused more heavily on the interaction between a pressure pulse from a wave impact, simulated in drop tests and the response of plates. The work load proved to be larger than anticipated. After discussions with my supervisor Jørgen Amdahl, it was therefore chosen to remove the study of nonlinear floater pitch motion from the thesis. Nonlinear floater pitch motions are mainly related to air gap and removing the topic will have a small effect on the main objectives of the thesis related to loading curves, responses and FSI.

Nonlinear effects in steep waves are discussed, but are treated using simplified method. The incoming waves may hit at many different angles of impact, but in this thesis, the tests are limited to an angle of impact equal to 0°.

In addition, the effect of damping is neglected in the local analysis as damping will have an overall small effect on the maximum response, as stated in (Faltinsen, 2000).

1.5 Approach

The approach of the report will center around finding the most critical sea state, i.e. the sea state with the most critical air gap. The method described in DNV GL's offshore technical guidelines, (GL, 2016b) uses the size of the relative upwelling to predict the design pressures. This loading pulse and response will be used as a reference for the load prediction based on the simulated drop tests. The sea state with the largest negative air gap will be taken to be the most critical sea state. Furthermore, by applying the most critical wave height and the dominating frequency in the sea state, an estimate of the particle velocity will be made in accordance with the recommended practice in (DNV, 2014b).

With an estimated velocity, drop tests will be simulated using LS-Dyna in order to estimate loads and responses on a vertical platform deck. Initially, the software and input parameters will be configured so that the results agree reasonably well with model tests conducted in (Faltinsen, 2000). Drop tests with the velocity obtained from the air gap analysis will then be simulated, both for rigid and deformable plates. Thus, the pressure impulses as well as the response of an coupled, hydroelastic analysis and a standard analysis could be compared. Finally, the loads and responses will be compared with the ones estimated from DNV GL's technical guidelines.

In the final stage of the thesis, the same fluid parameters as was used for the small scale drop tests will be used for a full scale column. Only a 6[m] by 6[m] area of the column will be loaded, but a large part of the column is modeled in order to obtain correct boundary conditions. For the column, the focus will lie on comparing coupled analysis where hydroelastic effects are taken into account with pressures obtained from rigid drop tests.

1.6 Structure of the Report

The report is structured into nine main parts: introduction, theory, global analysis, a verification study, panel studies, column studies, calculations by the SDOF method, discussion and conclusions. Chapter 2 goes into detail on the theory behind the calculations which are conducted in the software as well as describing the theory behind the procedures in recommended practices and guidelines. In addition, general wave and response theory is described as well as how the theory may be used to establish the loads and responses on panels on offshore platforms.

Chapter 3 described how the semi-submersible and operating environments were modeled and how the results were obtained. In the chapter, it is described how air gap analysis were carried out using the Sesam software package. The chapter also describes the how the loading loading models are developed from the air gap analysis with an emphasis on water particle velocity and wave energy content.

In chapter 4, a verification study of the parameters applied in LS-Dyna is conducted. The experimental setup from (Faltinsen, 2000) is described as well as the model used the numerically recreate the experiment in LS-Dyna. The results from the experiments and theory are presented as well as the results from the simulations. The theory behind the numerical SDOF analysis is also described.

The modeling of 3D stiffened panels is presented as well as the structural responses of 2D and 3D panels are presented in chapter 5. This includes results with different drop velocities and material behavior for 2D panels with the resulting pressure-time curves. The responses for the $3[m]$ by $3[m]$ are calculated using FEM for the loading models from the RP, OTG and pressures obtained from drop tests of rigid panels. Resulting deformations from deformable drop tests are also presented.

In chapter 6, the modeling of section of a column of a semi-submersible is presented. To generate the load, a section of the column is dropped into water at high velocity where both the pressure pulse for a deformable and non-deformable panel are obtained. Subsequently, the responses given these loading conditions are presented. The chapter also includes loads from (GL, 2016b) and the resulting structural response.

Chapter 7 presents the modeling and results by applying the SDOF model on the 2D panel and 3D panels. The SDOF model has been applied for the $3[m]$ by $3[m]$ for the load from the OTG and the rigid load pulse as these loads are viewed as the most critical. For the 2D model, an SDOF analysis was carried out using the input parameters from the rigid load pulse obtained at the same impact velocity as for the experiment in (Faltinsen, 2000).

In chapter 8, the results and applied methods are discussed in terms of their applicability in assessing loads and responses of semi-submersibles. In particular, the ALE approach for simulating drop tests to estimate pressure pulses from a wave hitting a semi submersible will be discussed.

Chapter 9 is the final chapter in the thesis and includes the conclusions drawn from the results. There are many topics that should have been looked into related to the work. These

topics are recommended to look further into in a section for further work.

Chapter 2

Theory

2.1 Wave Theory

2.1.1 Linear Wave Theory

Even though slamming loads on semi-submersibles will be dominated by large amplitude waves, which in general don't comply with linear theory, linear theory can give viable estimates when used appropriately. According to linear wave theory, the velocity potential for a cosine wave can be given in the form as seen in equation 2.1. The wave theory in the thesis is based upon the wave theory described in (Faltinsen, 1993) with waves propagating in the positive x-direction.

$$\phi = \zeta_A \frac{g}{\omega} \frac{\cosh(k(h+z))}{\cosh(kh)} \cos(\omega t - kx) \quad (2.1)$$

The most important parameters for establishing the loads on a structure is the dynamic pressure term and the velocity components. For a wave with the same velocity potential as in equation 2.1, the dynamic pressure is given by equation 2.2. The first order velocity components in the x and z direction are given in equations 2.3 and 2.4 respectively.

$$p_d = \rho g \zeta_A \frac{\cosh(k(h+z))}{\cosh(kh)} \sin(\omega t - kx) \quad (2.2)$$

$$u = \zeta_A \omega \frac{\cosh(k(h+z))}{\cosh(kh)} \sin(\omega t - kx) \quad (2.3)$$

$$w = \zeta_A \omega \frac{\cosh(k(h+z))}{\cosh(kh)} \sin(\omega t - kx) \quad (2.4)$$

A linear wave in finite water travels at a speed independent of its wave height. The wave celerity in finite water is given by equation 2.5.

$$C = \frac{g}{\omega} \tanh(kh) \quad (2.5)$$

Linear theory is inaccurate when z is larger than 0, which is problematic as it is typically the wave crest which hits the platform. Using lower order wave theory involves some errors, both in terms of velocities and wave amplitudes. Some of these errors could be accounted for by using correction factors.

2.1.2 Velocity Estimates by Wheeler Stretching

Wheeler stretching was proposed in (Wheeler et al., 1969) as a simple method to account for nonlinear effects above the mean water line. The method involves estimating an effective height at which the linear wave properties are calculated as seen in equation 2.6. The principles of the wheeler stretching estimate may be seen in figure 2.1. It is to note that wheeler stretching is considered to be unconservative compared to other methods.

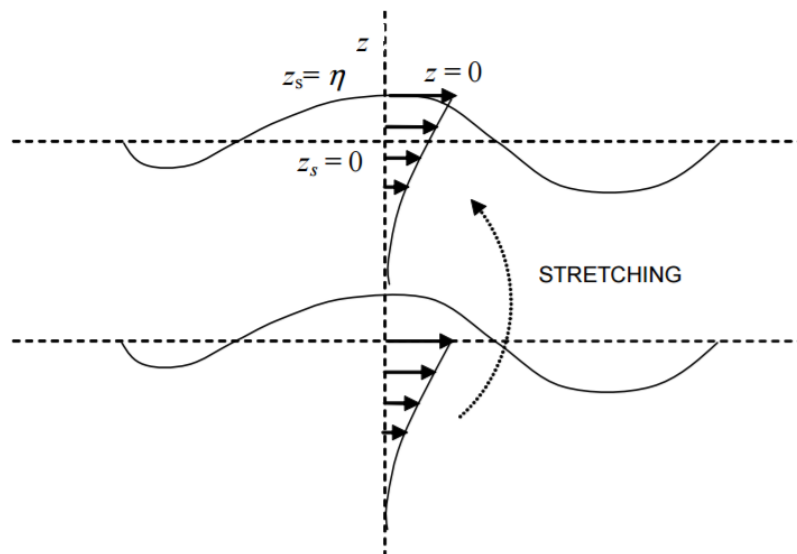


Figure 2.1: Principles of an effective height used in wheeler stretching (DNV, 2014b)

$$z = \frac{z_s - \zeta}{1 + \zeta/h} \quad (2.6)$$

2.1.3 Velocity Estimates by the Second Order Kinematics Model

The second order kinematics model is based on a Taylor series expansion. According to the recommended practice given in (DNV, 2014b), the particle velocity over the mean water line can be given as in equation 2.7. $u^{(2+)}(0)$ and $u^{(2-)}(0)$ are the velocities from second order sum and difference frequency velocity profiles. The principles of the calculation can be seen in figure 2.2.

$$u(z) = u^{(1)} = u^{(1)}(0) + \left(\frac{\partial u^{(1)}}{\partial z} \right) \Big|_{z=0} z + u^{(2+)}(0) + u^{(2-)}(0) \quad (2.7)$$

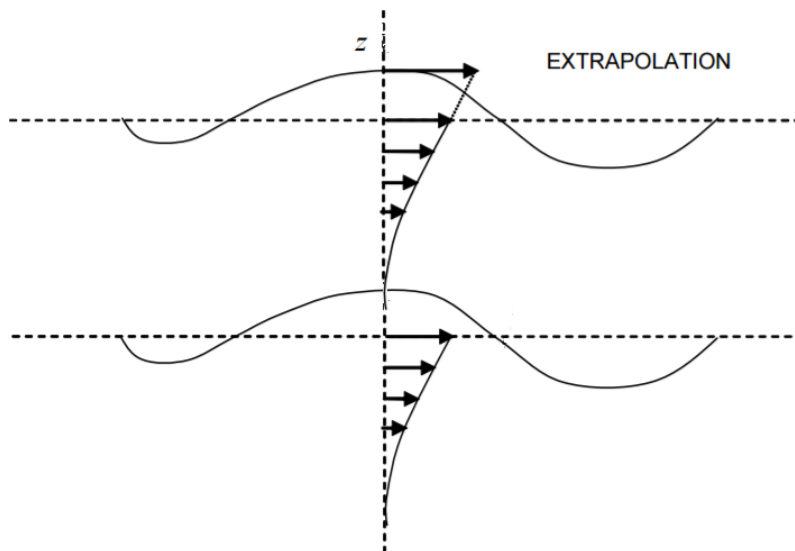


Figure 2.2: Principles of a horizontal velocity calculation according to the second order kinematics model (DNV, 2014b)

2.1.4 Energy Content in Waves

According to (Faltinsen, 1993), the energy contents of a fluid volume in a wave can be given as in equation 2.8, where τ is used as a symbol for volume integration.

$$E(t) = \rho \int \int \int \left(\frac{1}{2} V^2 + gz \right) d\tau \quad (2.8)$$

In a linear wave, the total energy of a wave is given as in equation 2.9. A loading pulse is related to the amount of energy transferred upon impact and the energy contents of the wave could thus be of interest when estimating the load pulse.

$$E = \frac{1}{2} \rho g \zeta_a^2 \quad (2.9)$$

2.1.5 Wave Breakage and Shoaling

When a wave breaks, the back of the wave moves faster than the front of the wave. The pontoons might simulate a shallow end, causing the wave height to increase, increasing the likelihood for the wave to break. However, a wave doesn't necessarily have to break when entering shallow waters, it may also break while still in deep waters. According to (Kjeldsen and Myrhaug, 1978) there are 4 different criteria for waves to break, all of which are listed below.

1. A maximum wave angle at the wave crest of 120°
2. The velocity of the fluid particle near the wave crest exceeding the wave celerity c
3. The vertical downward particle acceleration close to the wave crest exceeds $\frac{g}{2}$
4. A wave steepness $s = \frac{H}{\lambda}$ exceeding the critical steepness $s = \frac{1}{7}$

In terms of loads, there are two reasons we are concerned with breaking waves. A breaking wave will have larger fluid velocities than a non-breaking wave, leading to higher pressures. In addition, the mechanics of a breaking wave will change the angle of impact, which may lead to higher loads on the structure if the relative angle between the front of the wave and the structure itself is reduced.

Equation 2.10 is obtained by conservation of wave energy when a wave enters shallow water. The equation illustrates the change in wave height due the shoaling effect. H_0 denotes the wave height in the deep region and H_2 denotes the new wave height in the shallow region. Moreover, C_0 is the wave celerity in deep water and C_{g2} is the group velocity in the shallow region. The wave period remains constant as the wave enters more shallow water. The equation describes how the wave height increases as a wave enters shallow waters.

$$H_2 = H_0 \sqrt{\frac{C_0}{2C_{g2}}} \tag{2.10}$$

The geometry of a breaking wave is more complex than the geometry of a non-breaking wave. The angle of front of the wave might approach 0°, leading to large pressures on structures. The geometry of a breaking wave according to (Kjeldsen et al., 1979) can be seen in figure 2.3.

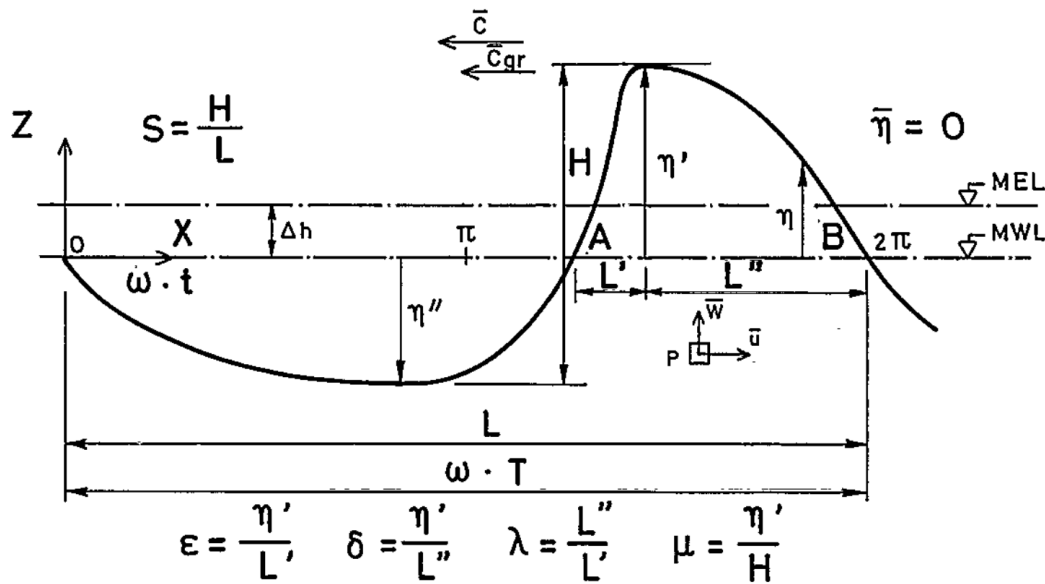


Figure 2.3: Geometry of a breaking wave as seen in (Kjeldsen et al., 1979)

2.2 Estimates of Load Pulses on Offshore Structures

DNV GL has released an offshore technical guideline related to slamming loads on semi-submersibles related to both the magnitude as well as the loading duration of the pressure pulse, given in (GL, 2016b). The predicted load pulses are recognised by short rise times and a narrow pressure peak. The method is based upon running air gap analyses in a series of sea states and applying the relative upwelling in order to estimate the pressure-time series on the structure.

2.2.1 Sea States Given by Steepness Criterion and Probability Contours

The loading conditions for a semi-submersible are most critical in steep and high seas. According to (GL, 2016a), the environmental parameters in survival condition may be given in terms of a contour curve or the steepness criterion. This is called the contour line method and gives the significant wave height H_S for every zero mean crossing period T_Z . For operation in specific locations, the contour line will typically be given for different annual probabilities, such as in figure 2.4. The solid line shows the contour for an annual probability of 10^{-2} whereas the dashed line shows the contour for an annual probability of 10^{-4} . The dotted line shows a plot of the DNV GL steepness criterion, given in (DNV, 2014b).

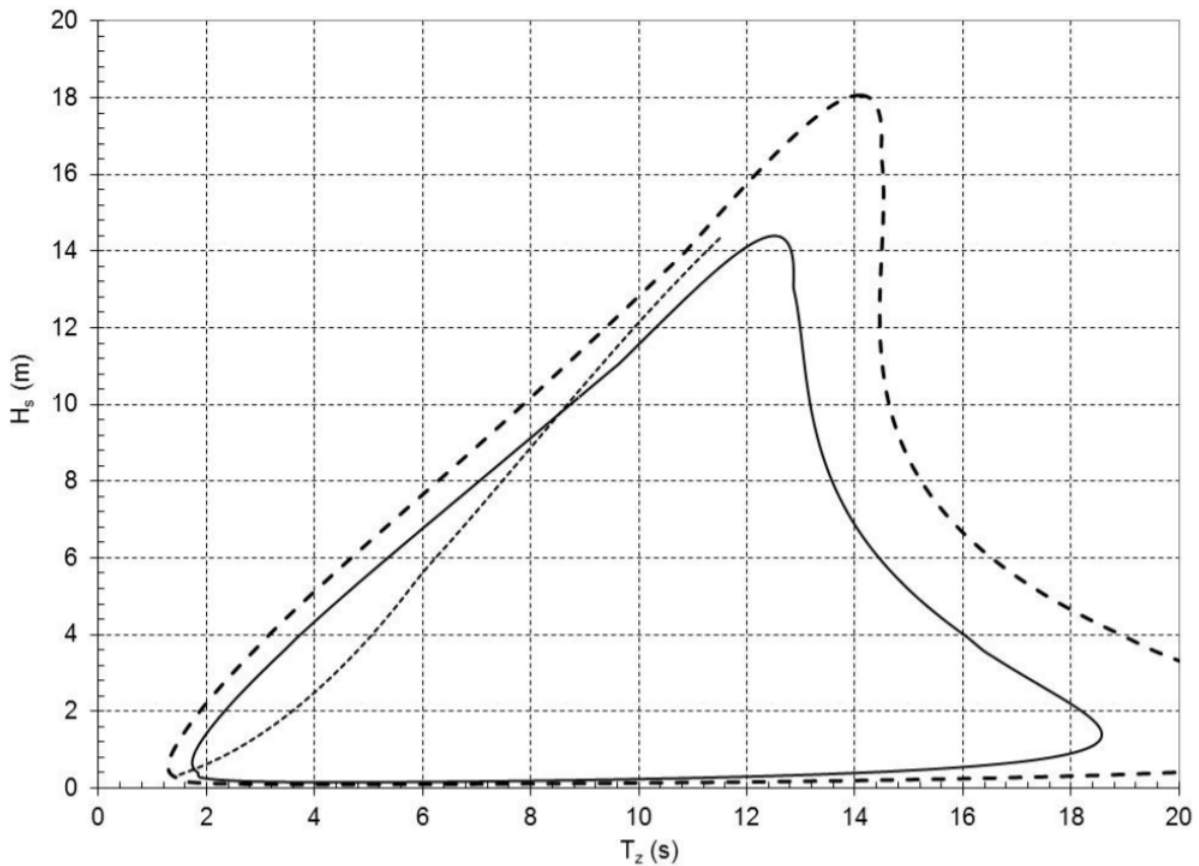


Figure 2.4: Example of a design contour on the Norwegian Continental Shelf (GL, 2016a)

$$S_S = \frac{2\pi H_S}{g T_Z^2} \quad (2.11)$$

The steepness is given by two different values of S_S which are given above and below certain zero mean crossing periods, T_Z . For T_Z values between 6 and 12, you linearly interpolate between the two functions.

$$S_S = \frac{1}{10} T_Z < 6$$

$$S_S = \frac{1}{15} T_Z > 12$$

2.2.2 Equations of Motion

A semi-submersible in a given sea state can be modelled as a mass-spring system subjected to excitation forces. According to (Faltinsen, 1993), the coupled equations of motion for the k^{th} degree of freedom can be written as in equation 2.12.

$$\sum_{k=1}^6 [(M_{jk} + A_{jk})\ddot{\eta}_k + B_{jk}\dot{\eta}_k + C_{jk}\eta_k] = F_j e^{-i\omega_e t} \quad (2.12)$$

The response of a system subjected to a complex load on the form given in equation 2.12 will yield a response of the form in equation 2.13 where η_{k0} is the magnitude of the response.

$$\eta_k = \eta_{k0} e^{i\omega_e t}$$

$$\dot{\eta}_k = \eta_{k0} i\omega_e e^{i\omega_e t} \quad (2.13)$$

$$\ddot{\eta}_k = -\omega_e^2 \eta_{k0} e^{i\omega_e t}$$

Applying the complex form given in equation 2.13 allows one to rearrange the equation into equation 2.14.

$$\sum_{k=1}^6 [-(M_{jk} + A_{jk})\omega_e^2 + B_{jk}i\omega_e + C_{jk}] \eta_{k0} = F_{j0} \quad (2.14)$$

If the degrees of freedom are uncoupled, the amplitude of the response can be found by calculating the absolute value of the complex equation as seen in equation 2.15. In a linear analysis, the excitation force is linearly dependent on the wave amplitude. Thus, by dividing with η_j , you are left with an expression for the system's RAO or response amplification operator.

$$RAO = \left| \frac{F_{j0}}{\eta_{j0} \sqrt{(C_{jj} - (M_{jj} + A_{jj})\omega_e^2)^2 + B_{jj}^2 \omega_e^2}} \right| \quad (2.15)$$

The similar approach can be done for the 6 degree of freedom coupled system by inverting the dynamic equation matrix instead. The coupled responses are thus given as in equation 2.16.

$$\eta_0 = \left(\sqrt{(\mathbf{C} - (\mathbf{M} + \mathbf{A})\omega_e^2)^2 + \mathbf{B}^2 \omega_e^2} \right)^{-1} \mathbf{F}_0 \quad (2.16)$$

2.2.3 Calculating Air Gap by the Simplified Approach

According to the (Kazemi and Incecik, 2007) , the instantaneous air gap can be calculated from equation 2.17. a_0 is defined as the static air gap, $z(x, y, t)$ is the vertical displacement of the evaluated point on the structure and $\zeta(x, y, t)$ is the surface elevation. The principles can be studied more closely in figure 2.5.

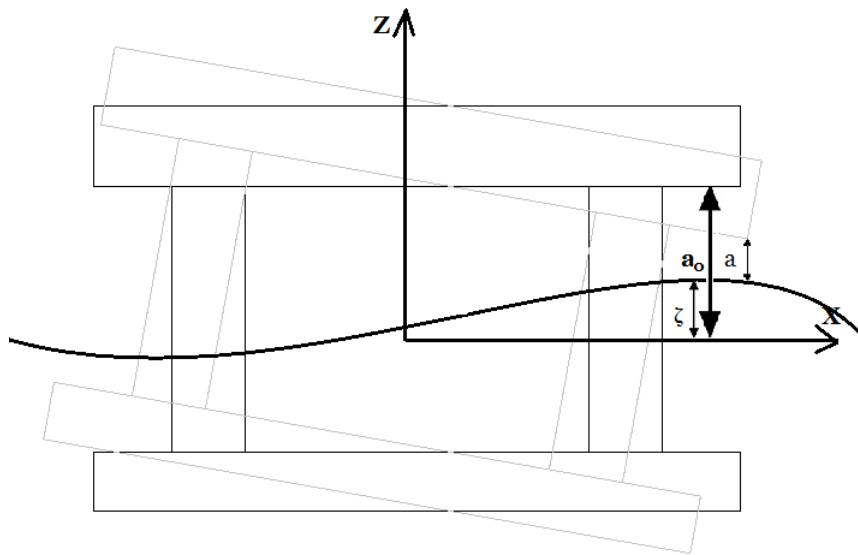


Figure 2.5: Principle of an Air Gap Analysis

$$a(x, y, x) = a_0 + z(x, y, t) - \zeta(x, y, t) \quad (2.17)$$

The actual surface elevation can be viewed as a sum of many components, as seen in equation 2.18. In addition to the linear incident waves $\zeta_I^{(1)}$, radiation and diffraction waves, $\zeta_{R,D}^{(1)}$ surrounding the floating structure are to be considered as well. $\zeta^{(2)}$ are contributions due to second-order effects which consists of sum and frequency interaction effects. Higher order terms could be taken into account as well, but are usually neglected in the simplified approach.

$$\zeta = \zeta_I^{(1)} + \zeta_{R,D}^{(1)} + \zeta_I^{(2)} + \zeta_{R,D}^{(2)} \quad (2.18)$$

In a long crested sea state, the random linear wave can be assumed as a standard wave on the form as in equation 2.19.

$$\zeta_1 = \sum_{i=1}^I \zeta_{A_i}(\omega_i) \cos(\omega_i t + \epsilon_i) \quad (2.19)$$

The vertical displacement of the structure may be written as in equation 2.20. For small displacements, $\sin(\phi) \approx \phi$.

$$z(x, y, t) = \eta_3(t) - x \sin[\eta_5(t)] + y \sin[\eta_4(t)] \quad (2.20)$$

In linear theory, the motions of a semi submersible can be calculated using the semi-submersible's RAO and is thus linearly dependent of the wave amplitude. By adding all of the contributions from the waves in a sea state, the linear motions of the semi-submersible can be calculated as in equation 2.21. For a sea state with N zero mean crossings, the maximum wave height is given by equation 2.22 as given in (Veritas, 2011b).

$$\eta_3 = \zeta |RAO| \cos(kx - \omega t + \epsilon) \quad (2.21)$$

$$\frac{H_{max}}{H_S} = \sqrt{\frac{1}{2} \ln(N)} \quad (2.22)$$

2.2.4 Applying Asymmetry Factors

Asymmetry factors are used to scale waves where the wave crests are larger than the wave troughs. The asymmetry factor is equal to the relationship between the crest and the trough. In (GL, 2016a), the recommended asymmetry factors vary depending on the direction of the wave impact as well as the position on the platform which is being analysed. For areas in which the wave hits head on, the asymmetry factors α should equal 1.3. When the structure is hit from the side, an asymmetry factor of 1.2 is used as indicated figure 2.6.

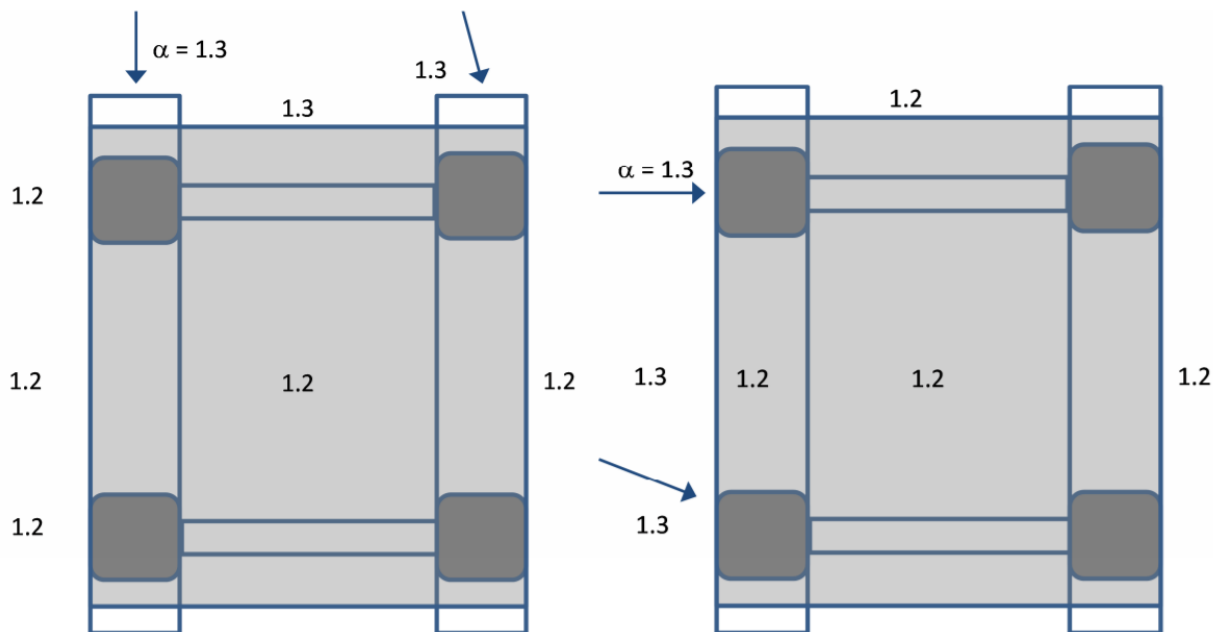


Figure 2.6: Wave asymmetry factors w.r.t. to position and wave direction (GL, 2016a)

2.2.5 Air Gap Calculations in Wadam

According to (Veritas, 2008), Wadam is a hydrodynamic software developed by DNV GL as part of the Sesam software package. The software is based on linear wave theory where the waves propagate in the β direction as indicated in figure 2.7 where the surface elevation is given according to equation 2.23.

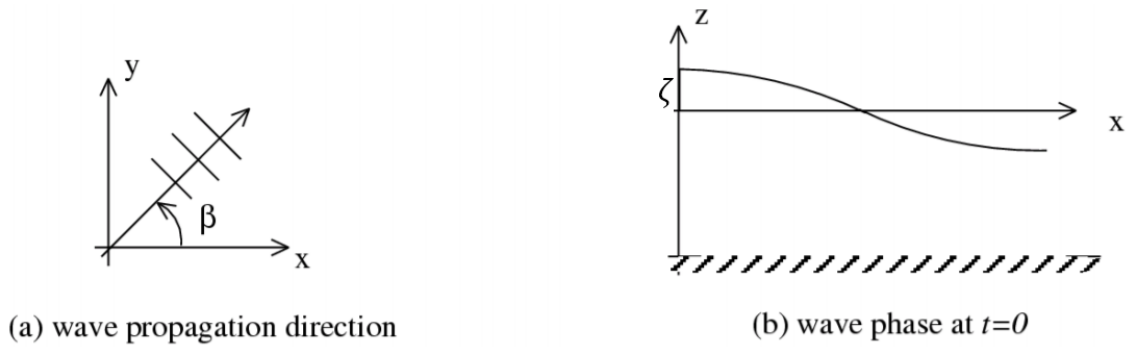


Figure 2.7:

$$\zeta = \zeta_A \cos(\omega t - k(x \cos \beta + y \sin \beta)) \quad (2.23)$$

The wave loading on the structure is estimated by the panel method. Damping is commonly accounted for by either defining the damping matrix or by applying a composite model. A composite model consists of both a panel model and a Morison model where the Morison model adds damping to the structure. The volume from the Morison model is included when the total displacement is calculated. Hence, the diameter and drag coefficient should be scaled so that the drag resistance is correct while the total added displacement is negligible. Wadam outputs the results in terms of RAOs for each direction. The RAOs for specific points of the structure may be obtained by adding sampling points. These RAOs may then be post processed in order to estimate the resulting air gaps by subtracting the surface elevation in each point.

2.2.6 Loads Based on Offshore Technical Guidelines

In (GL, 2016b) there are design guidelines for how large horizontal impact loads should be considered when designing a semi-submersible. The paper describes maximum loads given from the ULS condition, both in terms of peak pressures as a function of the relative upwelling as well as the time history of the load. In figure 2.8, design criteria for the peak pressures are given for the vertical position you are assessing divided by the ULS-upwell. The upwell is here considered as the relative motion between the wave and the vertical displacement of the platform, given by equation 2.24.

$$\chi(x, y, t) = \zeta(x, y, t) - z(x, y, t) \quad (2.24)$$

According to (GL, 2016a), the upwelling corresponding to the 90 percentile should be used in design of semi-submersibles. According to (Veritas, 2011b), the p-fractile extreme value may be calculated according to equation 2.25.

$$\frac{H_p}{H_S} = \sqrt{\frac{1}{2} \ln(N)} \left(1 - \frac{\ln(-\ln(p))}{\ln(N)} \right)^{\frac{1}{2}} \quad (2.25)$$

(GL, 2016b) describes the pressure-time series of a wave hitting an offshore structure in terms of the relative upwelling. The guidelines recommend to use different rise times and apply the rise time yielding the worst structural response. As a simplification, the thesis considers the peak pressure occurring approximately 0.012[s] after the wave hits the structure. This can be seen in the figure 2.9.

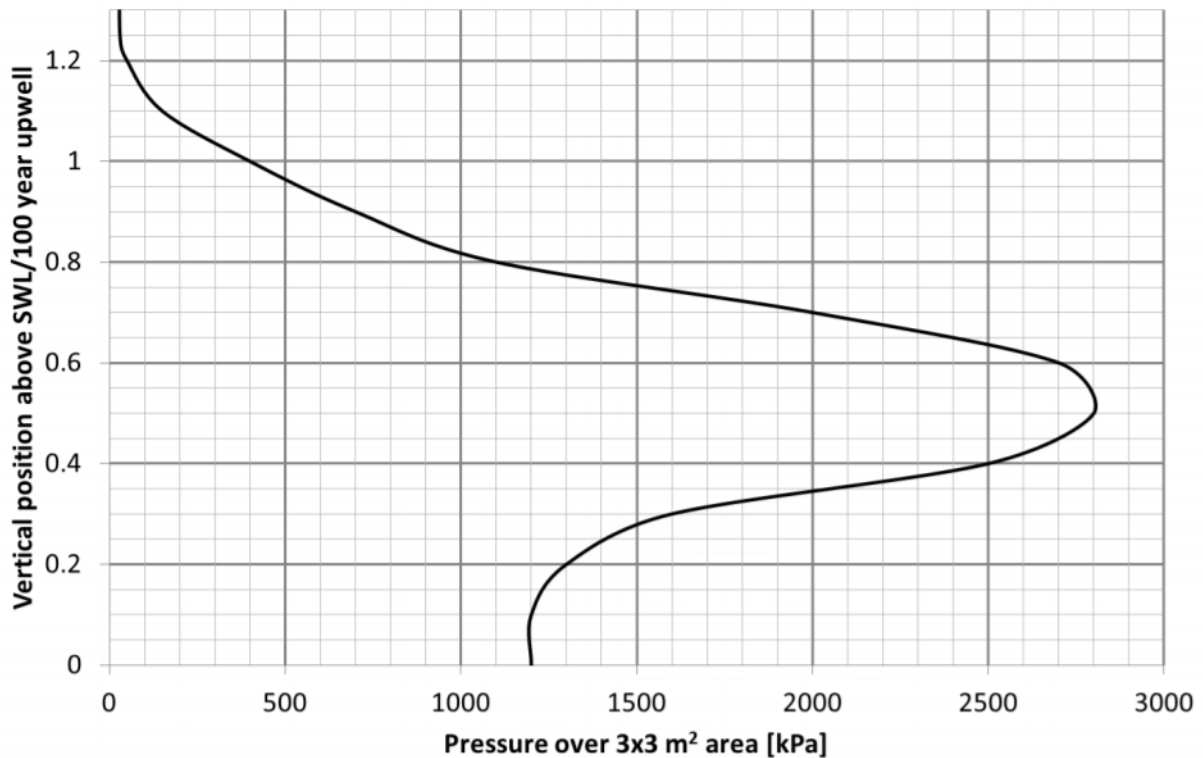


Figure 2.8: ULS peak pressures for vertical positions in terms of relative upwelling as given in (GL, 2016b)

The relative upwelling is calculated from the relationship between the static vertical position under review and the upwelling as in equation 2.26. z_{local} is the position from the top of the deckbox to the middle of the plate which is to be analysed.

$$upwelling_{relative} = \frac{a_{static} + z_{local}}{\chi_{max}} \quad (2.26)$$

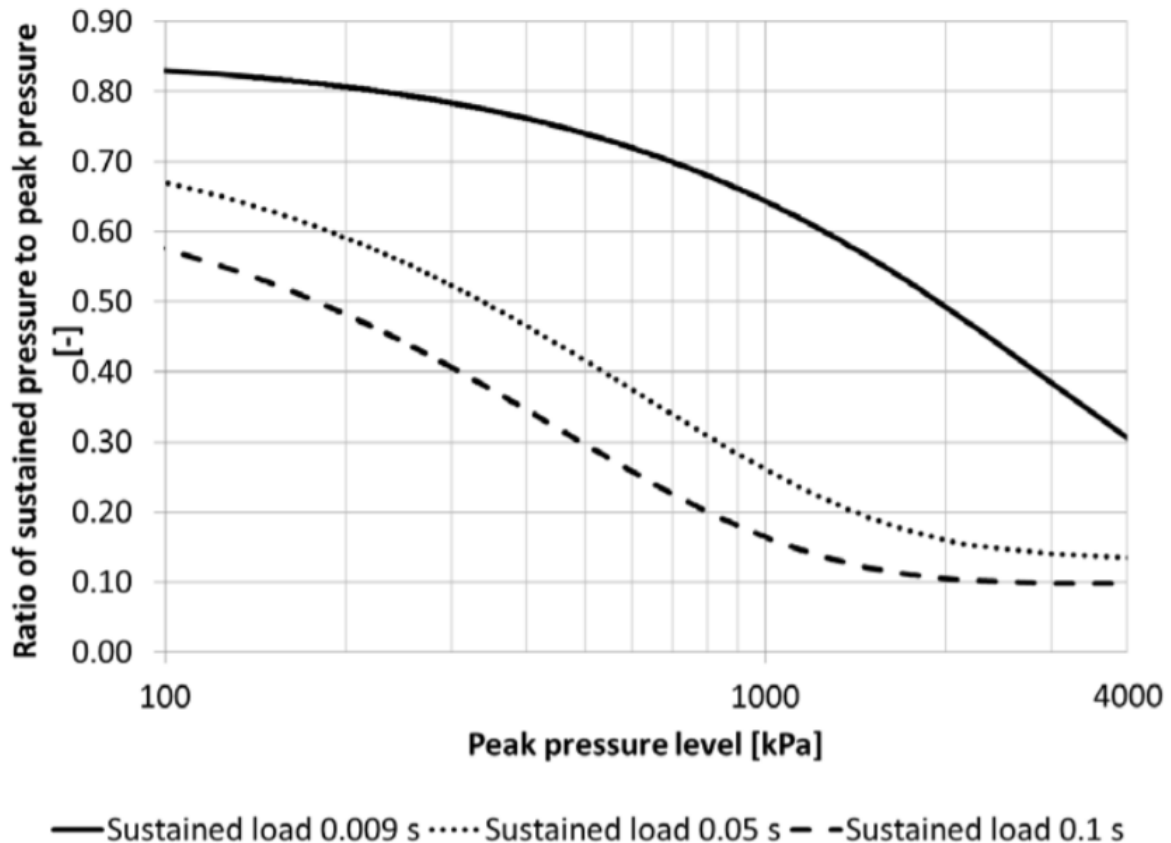


Figure 2.9: Temporal Pressure w.r.t. peak pressure. (GL, 2016b)

Furthermore, the guideline also has a graph displaying the pulse development of the wave impact that can be seen in figure 2.10. It is recommended to test different rise times and apply the rise time yielding the worst structural response. In the guidelines, rise times between 0.005[s] and 0.015[s] are suggested. For simplicity, only the rise time equal to 0.012[s] is tested in the thesis even though more rise times theoretically should have been tested. The total duration of the load pulse is found by extrapolating the load curve and found to equal 0.2[s].

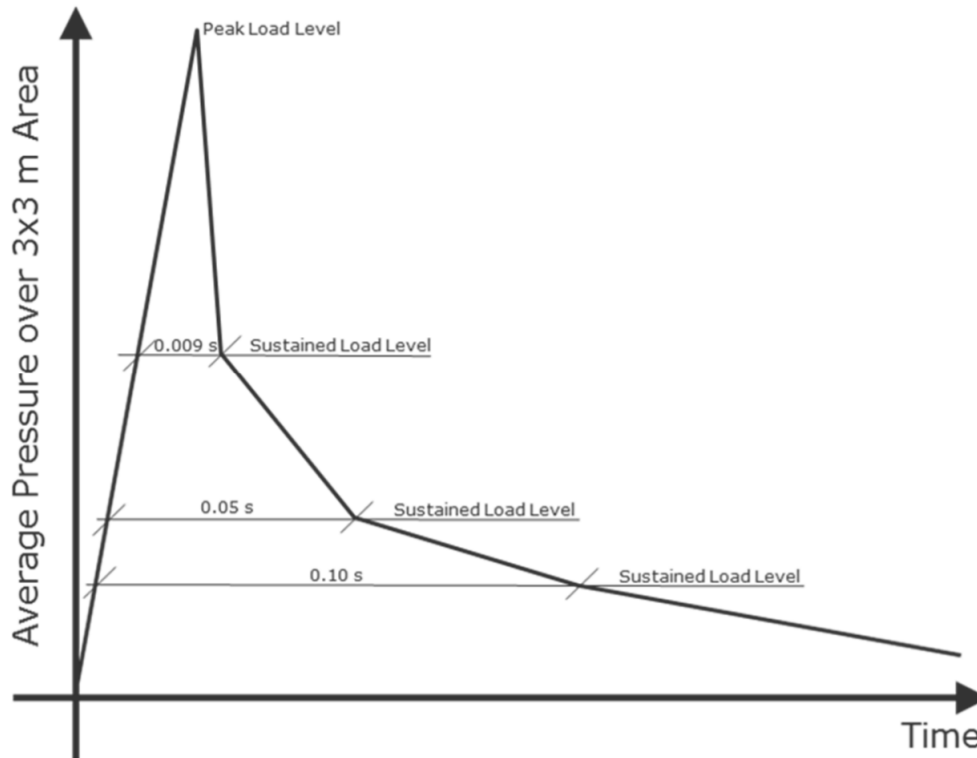


Figure 2.10: Description of the idealised slamming pulse (GL, 2016b)

For further analysis, the total impulse could be relevant. The load impulse is related to conservation of momentum, and if the duration of the load is short compared to the natural period of the structure, it could be used to make a simple estimate of the maximum structural response. From numerical integration, the total impulse as a function of the pressure peak was estimated by equation 2.27 and found to be approximately equal to $0.041 p_{peak}$.

$$I = \int_0^t p(t) dt = \sum_{i=1}^N I_i \Delta t_i \approx 0.041 p_{peak} \quad (2.27)$$

2.2.7 Loads Based on Recommended Practices

According to (DNV, 2014b), horizontal loads due to wave impact consists of three components, a drag force, inertia forces and the slamming force where the slamming force has a short duration. The slamming force and drag force is proportional to u^2 . Equation 2.28 is given in (Kaplan et al., 1995) and describes the horizontal wave in deck force in terms of added mass, change in added mass and drag. c is the vertical wetted length, B is the width, ρ is the density of water and u is the vertical particle velocity in the water. Assuming that the breadth B is much larger than the vertical wetted length c , the added mass

component $M_{a,x}$ can be calculated according to equation 2.29.

$$F_h(t) = M_{a,x}\dot{u} + \frac{dM_{a,x}}{dt}u + \frac{1}{2}\rho c C_D B u |u| \quad (2.28)$$

$$M_{a,x} = \frac{2}{\pi} \rho c^2 B \quad (2.29)$$

(DNV, 2014b) also describes a simplified formula for estimating the horizontal wave load. The force is calculated by equation 2.30 where A is the projected area, V is the particle velocity and C_h is the load coefficient which is to be taken as 2.5 for a head on hit, 1.9 for a diagonal hit and 3.5 for low impact heights, accounting for multiple obstacles.

$$F_h = \frac{1}{2} \rho C_h V^2 A \quad (2.30)$$

2.3 Slamming

2.3.1 General Slamming Theory

According to (Faltinsen, 1993), the slamming pressure on a structure can be calculated approximately by differentiation of the velocity potential as in equation 2.31.

$$p = -\rho \frac{\partial \phi}{\partial t} \quad (2.31)$$

For a flat plate, the velocity potential can be written as in equation 2.32 where $2c(t)$ is the total length of the wetted plate at time t and $V(t)$ is the impact velocity at time t . It is to be noted that $c(t)$ isn't differentiable for contact between two flat surfaces if the angle of impact is 0° . Thus, for analytical solutions, the angle of impact must either be larger than 0° , the water profile must not be plain, or the plate may have an initial imperfection.

$$\phi = -V(t) \sqrt{c(t)^2 - x^2} \quad (2.32)$$

The equation for the total pressure due to the wave impact is given in equation 2.33 and is

obtained by combining equation 2.31 with equation 2.32. The first pressure term depends on the change in velocity. This may be viewed as the added mass pressure. Added mass is understood as the pressure component that is in phase with the acceleration of the body and may in general be calculated according to equation 2.34. The second term depends on the change in wetted surface area and this is denoted as the slamming term.

$$p = \rho \frac{dV}{dt} \sqrt{c^2 - x^2} + \rho V \frac{c}{\sqrt{c^2 - x^2}} \frac{dc}{dt} \quad (2.33)$$

$$p = -M_a a \quad (2.34)$$

By conservation of momentum during water impact, (Von Karman, 1929) found that the maximum pressure could be given by equation 2.35. The maximum pressure along the surface is located in the middle of the plate and by inserting the coordinates for the middle of the plate in equation 2.35, equation 2.36 is obtained.

$$p(\chi, \alpha) = \frac{v_0^2 \cot \alpha}{1 + \frac{\rho g \pi \chi^2}{2W}} \rho \pi \chi \quad (2.35)$$

$$p_{max}(\alpha) = \frac{\rho v_0^2}{2} \pi \cot \alpha \quad (2.36)$$

The parameter v_0 is equal to the velocity of the plate, χ is the local position on the plate and α is the angle between the water and plate. W denotes the width of the plate. It is to be noted that according to these equations, the slamming pressures goes to infinity as the angle approaches 0, as is also indicated by a non-differentiable $c(t)$ in equation 2.33.

2.3.2 Experimental Drop Test

In (Huera-Huarte et al., 2011), several experimental drop tests are described in detail. The experimental set-up consists of an adjustable rig capable of adjusting both the angle of impact as well as the impact velocity of a 0.3[m] by 0.3[m] rigid plate.

In (Huera-Huarte et al., 2011), the forces are plotted for a single force factor, denoted C_S , which expresses the total force on the structure as in equation 2.37.

$$F = C_S \frac{1}{2} \rho V^2 \quad (2.37)$$

The coefficient is decided from two parameters, time and angle of impact. The time is nondimensionalised using equation 2.38 where the length is to be taken as the penetration length. The force coefficient varies with time according to equation 2.39.

$$\delta t^* = \frac{v_0 \delta t}{L} \quad (2.38)$$

$$C_S^{\delta t^*} = 0.79 \delta t^{*-1.4} \quad (2.39)$$

The force coefficient's dependency on angle of impact is given in equation 2.40. The relationship holds for angles greater than 5° . The force coefficient with respects to both angle of impact and time is plotted in figure 2.11. Also included in the plot are results from drop tests carried out in (Tveitnes et al., 2008).

$$C_S^\alpha = 124.25 \alpha^{-1.086} \quad (2.40)$$

Also to note is how the results are scattered for angles smaller than 5° , indicating a large degree of uncertainty in this region.

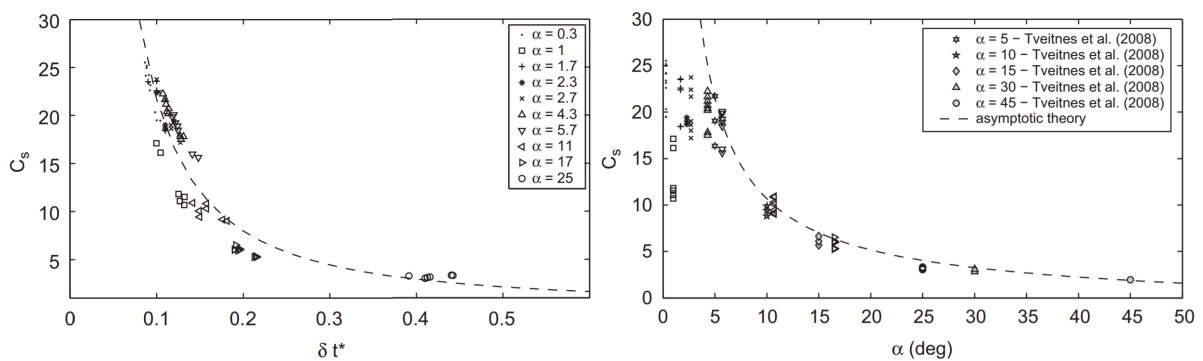


Figure 2.11: C_S plotted as a function of δt^* and α (Huera-Huarte et al., 2011)

As both graphs start in the same position, i.e. $C_s = 30$, the graphs may be used to approximate a two-variable equation describing the force coefficient during the impact. The equation holds for both graphs and may be seen in equation 2.41.

$$C_s = \frac{C_s^\alpha \cdot C_s^{\delta t^*}}{30} = 3.27\alpha^{-1.086}\delta t^{*-1.4} \quad (2.41)$$

Figure 2.12 shows the measured results from a drop test with an impact angle of 2.7° . The force development of the slamming pulse is dominated by a large peak with rapid build up and decay. The duration of the peak is low, in the range of 5 to 10[ms]. The total duration of the relevant pulse is shorter than 25[ms]. The shape of the load is not unlike that of the load given from the OTG in figure 2.10. The duration is shorter, but the penetration length is likely shorter than the length of the wave segment hitting an offshore structure. One should note that the slamming coefficients given in equation 2.39 might be too conservative given that the approximation w.r.t. time lies above the force trough seen in the plot in figure 2.12.

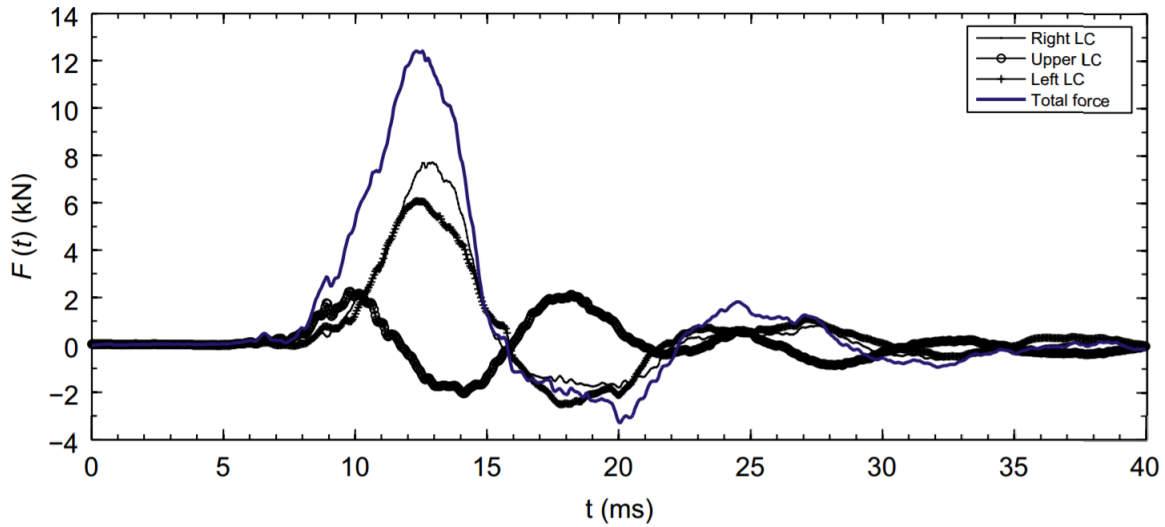


Figure 2.12: Measured force development w.r.t time (Huera-Huarte et al., 2011)

2.4 Hydroelastic Structure Interaction

2.4.1 Criteria for Hydroelastic Calculations

For large deformations due to hydrodynamic forces, hydroelastic effects should be taken into account. Hydroelastic effects occur when structural deformations are so large that they

affect the hydrodynamic flow. Typically, the effects would lead to a decreasing pressure, and thus, not calculating hydroelastically is generally a conservative approach as stated in (DNV, 2014b). In (DNV, 2014b), the criteria for when hydroelastic effects are to be considered is given by equation 2.42. L is the length of the beam, V_R is the relative velocity between the beam and the wave and α is equal to the angle of impact.

$$\sqrt{\frac{EI}{\rho L^2}} \frac{\tan \alpha}{|V_R|} < 0.25 \quad (2.42)$$

2.4.2 Analytical Hydroelastic Calculations

In (Faltinsen, 2005), analytical hydroelastic responses are described with reasonable agreement with the same test results as described in section 4.1.1. In the analytical calculations, pressures are not considered. Instead, the beam is given an initial velocity equal to the drop velocity of the beam. The theory goes into the free vibration phase after the initial slamming. The free vibration phase is given in terms of equation 2.43. The theory is based on two-dimensional beam theory, hence, 3D effects are ignored. The pressures on the plate are given in terms of the added mass force arising from the deformation of the panel.

$$M_B \frac{\partial^2 w}{\partial t^2} + EI \frac{\partial^4 w}{\partial x^4} = p(x, w, t) \quad (2.43)$$

The mode shape of the response of the beam is assumed to be given as a modal sum where each mode follows the cosine pattern as $\psi_n = \cos\left(\left(\frac{\pi}{2} + n\pi\right)x\right)$. The model neglects damping so that the relevant terms are given as the mass, M , added mass, M_a , and the restoring coefficient C . Reference is made to section 2.5.3 where the generalised formulas for a single degree of freedom dynamic system are listed. The coefficients for the first and most prominent eigen mode are given in equations 2.44 to 2.46.

$$C_1 = EI \left(\frac{\pi}{L}\right)^4 \int_{-L/2}^{L/2} \cos^2\left(\frac{\pi}{L}x\right) dx = 0.5\omega_1^2 M_B L \quad (2.44)$$

$$M_1 = M_B \int_{-L/2}^{L/2} \cos^2\left(\frac{\pi}{L}x\right) dx = 0.5M_B L \quad (2.45)$$

$$M_a = \rho \frac{2}{\pi} \int_{-L/2}^{L/2} \sqrt{\left(\left(\frac{L}{2}\right)^2 - x^2\right)} \cos\left(\frac{\pi}{L}x\right) dx \approx \rho \cdot 0.18L^2 \quad (2.46)$$

ω_1 is equal to the dry natural frequency of the beam beam and is given by equation 2.47. This is not to be confused with the wet natural frequency which includes added mass and is given by equation 2.48.

$$\omega_1 = \left(\frac{EI}{M_B}\right)^{1/2} \left(\frac{\pi}{L}\right)^2 \quad (2.47)$$

$$\omega_w = \left(\frac{C_1}{M_1 + M_a}\right)^{1/2} \quad (2.48)$$

2.4.3 Hydroelastic Calculations in LS-Dyna

In (Stenius et al., 2011), the loads on a catamaran were estimated hydroelastically using LS-Dyna software. It studies the pressure pulse development both for an elastic and a rigid structure for different deadrise angles as well as different impact velocities. The panel deflection is plotted for a hydroelastic plate versus a rigid/quasi-static plate in figure 2.13.

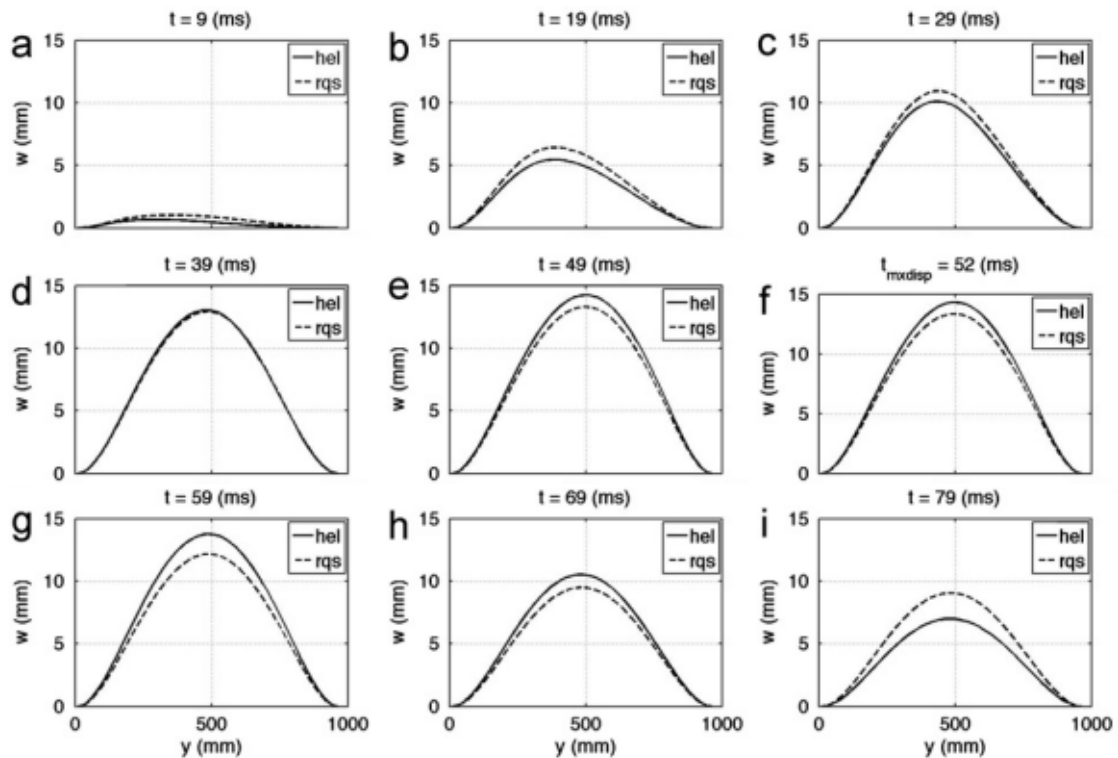


Figure 2.13: Hydroelastic versus rigid quasi static deflection (Stenius et al., 2011)

The rise time for the maximum deflection when calculating hydroelastically is longer than for the rigid estimates. However, the maximum deflection achieved for hydroelastic calculations are larger. This contrasts the theory stated in (DNV, 2014b), where it is stated that neglecting hydroelastic effects in general is conservative.

2.4.4 ALE

ALE is the abbreviation for arbitrary Lagrangian Eulerian, which is a method commonly applied for solving fluid structure interaction problems. According to (Donea et al., 1982), the method consists of two different domains, a physical domain that changes with time, the Lagrangian, as well as a reference domain that is constant with time, the Eulerian. According to (Yang et al., 2016), the ALE-formulation is based upon the relation given in equation 2.49. Here, X_i is the Lagrangian coordinate, ξ the referential coordinate and x_i is the Eulerian coordinate. The parameter w_i is the relative velocity between the material u_i and mesh v_i .

$$\frac{\partial f(X_i, t)}{\partial t} = \frac{\partial f(\xi, t)}{\partial t} + w_i \frac{\partial f(x_i, t)}{\partial x_i} \quad (2.49)$$

Furthermore, (Yang et al., 2016) also gives ALE-formulation defined by conservation of mass, momentum and energy. The equation for conservation of mass is given in equation 2.50, the equation for momentum conservation is given in equation 2.51 and the conservation of energy is given in equation 2.52.

$$\frac{\partial \rho}{\partial t} \Big|_{\xi} + \rho \frac{\partial v_i}{\partial x_i} + w_i \frac{\partial \rho}{\partial x_i} = 0 \quad (2.50)$$

$$\rho \frac{\partial v_i}{\partial t} \Big|_{\xi} + \rho w_i \frac{\partial v_i}{\partial x_i} = w_i \frac{\partial \sigma_{ij}}{\partial x_j} + \rho b_i \quad (2.51)$$

$$\rho \frac{\partial E}{\partial t} \Big|_{\xi} + \rho w_i \frac{\partial E}{\partial x_i} = \sigma_{ij} \frac{\partial v_i}{\partial x_j} - \frac{\partial q_i}{\partial x_i} \quad (2.52)$$

The density, body force, thermal flux and total energy are denoted by ρ , b_i , q_i and E respectively.

2.4.5 ALE in LS-Dyna

There are some limitations to the ALE approach in the LS-Dyna software. For instance, the ALE solver in LS-Dyna is not a full Navier Stokes solver and hence, it is not capable of calculating boundary layer effects such as drag, according to (Group et al., 2012). Not including the drag force in the simulation might give unconservative results. Both (Bea et al., 2001) dealing with wave in deck loads on offshore jackets and (BOM) which describes the Kaplan model for load prediction due to horizontal wave impact, lists drag as an important component. Thus, the additional loading due to drag forces should be addressed.

In LS-Dyna, equations of state, denoted as EOS, are commonly used in order to describe how pressure in the fluid changes with respects to how the volume of the fluid changes. The equation of state for fluids are commonly defined either according to a linear polynomial model or according to a Gruneisen model. Simulations of FSI drop tests are conducted in (Lee et al., 2010) where the linear polynomial model was applied. The pressure in compression is defined according to the equation 2.53 while the pressure in tension is defined according to equation 2.54. The parameter μ represents relative density defined as $\frac{\rho_0}{\rho} - 1$.

$$p = C_0 C_1 \mu + C_2 \mu^2 + C_3 \mu^2 + (C_4 \mu + C_5 \mu^2 + C_6 \mu^2) E \quad (2.53)$$

$$p = C_1 \mu + (C_4 \mu + C_5 \mu^2 + C_6 \mu^2) E \quad (2.54)$$

The linear polynomial EOS are only viable for linear deformations. For large deformations, the Gruneisen EOS should be applied, such as for water impacts at high velocities. The pressure for by the EOS Gruneisen model are given in equation 2.55. It is a function of the shockwave velocity $v_s(v_p)$ where v_p is the particle velocity. According to (LSTC, 2015), C is the intersect of the y-axis and the $v_s(v_p)$ curve in which S_1 , S_2 and S_3 are unitless parameters describing the slope of the curve. Commonly, C taken as the speed of sound in the material. γ_0 is a unitless Gruneisen gamma while a is a unitless volume correction for γ_0 and E is the internal energy.

$$p = \frac{\rho_0 C^2 \mu [1 + (1 - \frac{\gamma_0}{2})\mu - \frac{a}{2}\mu^2]}{[1 - (S_1 - 1)\mu - S_2(\frac{\mu^2}{\mu+1}) - S_3(\frac{\mu^3}{(\mu+1)^2})]^2} + (\gamma_0 + a\mu)E \quad (2.55)$$

Applied coefficients used to describe the EOS for water varies in the literature; some combinations of parameters are more suitable to describe some problems than others. EOS Gruneisen parameters from a selection of reports dealing with pressure pulses in water the are tabulated in 2.1. V_0 and E_0 is the initial volume fraction and internal energy respectably.

Table 2.1: Gruneisen EOS from literature

C	S1	S2	S3	Gamma0	A	E0	V0	Reference
1480	2.56	-1.986	0.227	0.5	0	0	1	(John, 1998)
1480	1.41	0	0	1	0	1.89E+06	1	(Kim and Shin, 2008)
1480	2.56	1.986	1.2268	0.5	0	0	0	(Liu et al., 2002)

In the modelling, the mesh for air and water should have merged nodes at the boundaries. There are commonly two different approaches used in modelling. The simplest approach is to use ALE with a single material and void, with the air mesh approximated as an initial void. Due to its low relative density, the error in modelling by this approach is relatively small. The other approach is to model the air and water meshes as a multimaterial ALE group.

In the case of high velocity water impacts, nodes might reach out-of-range velocities causing errors in the calculations and premature termination of the analyses. Hence, several different parameters should be tested. Which ALE procedure and which EOS to use will depend upon the problem formulation.

2.4.6 Penalty Algorithm

The penalty algorithm is a common approach to apply when solving ALE problems and is commonly applied in FSI problems in LS-Dyna. According to (Aquelet et al., 2006), the penalty algorithm requires one master part and one slave part. In an FSI problem describing an impact between two parts, the nodes in the moving part are defined as slaves while the nodes in the stationary part are defined as master nodes. Hence, for a drop test in

which a plate is dropped into water, the nodes in the plate are to be slave nodes while the nodes in the fluid mesh are to be defined as master nodes. The penalty algorithm adds a resisting force to the slave node which is proportional to the penetration through the master element, analogous to a spring stiffness as seen in equation 2.56. k is the spring stiffness and d is the penetration length into the element. The spring stiffness is calculated from the bulk modulus, K , representing the compressibility of the material as well as the volume, V , and area, A of the master element. The factor p_f is a scale factor between 0 and 1. The principles of the calculations can be seen in figure 2.14.

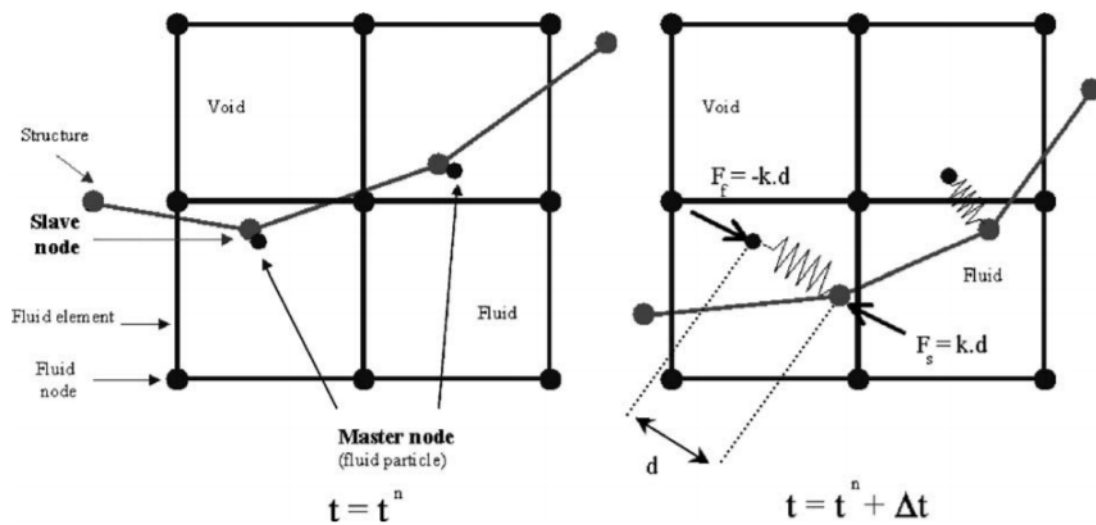


Figure 2.14: Principles of the penalty algorithm (Aquelet et al., 2006)

$$F_S = -k \cdot d = -p_f \frac{KA}{V} \cdot d \quad (2.56)$$

2.5 Structural Analysis

2.5.1 Failure Modes of Plates

A stiffened plate consists of 3 different components; stiffeners, girders and a plate. According to (DNV, 2014a), there are mainly four different matters in which a stiffened plate may fail, all of which are visualised in figure 2.15. For a stiffened plate, collapse may occur due to either a stiffener, girder or both collapsing. The failure mode may include either elastic or plastic deformations of the remaining structural components. A single degree of

freedom (SDOF) model may be used if on only a single component fails by the assumption that dynamic interaction between the plate and flange can be neglected. Should however collapse occur in both a stiffener and girder, a multiple degree of freedom (MDOF) analysis is required. By plastic deformation it is understood that the maximum deflection exceeds the elastic deformation limit of the component.

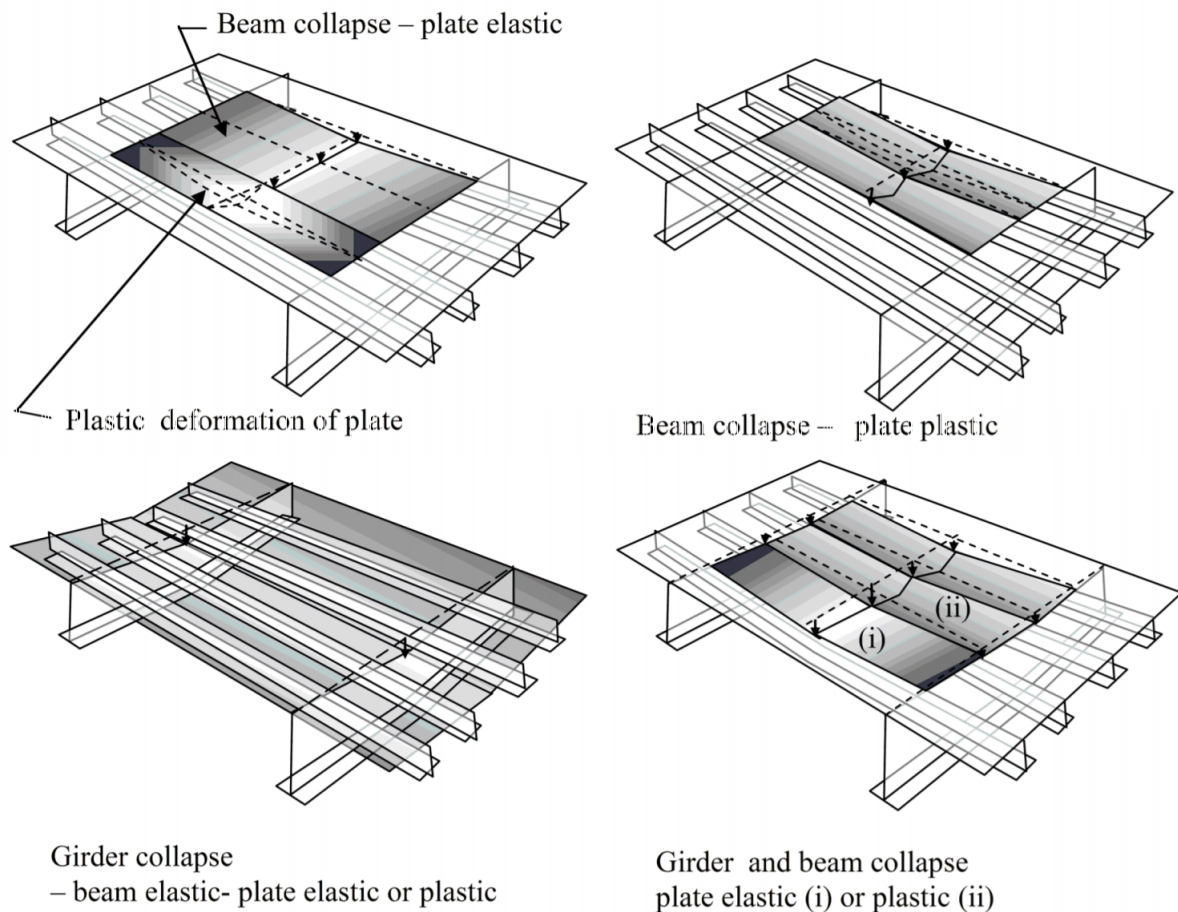


Figure 2.15: Different failure modes for a stiffened plate. (DNV, 2014a)

2.5.2 Resistance Model for Stiffened Plate

A resistance model for stiffened plates is given in (Standard, 2004) and it gives the relationship between plastic resistance and deformation. The plastic resistance is given in figure 2.16 and should be accounted for for large deformations.

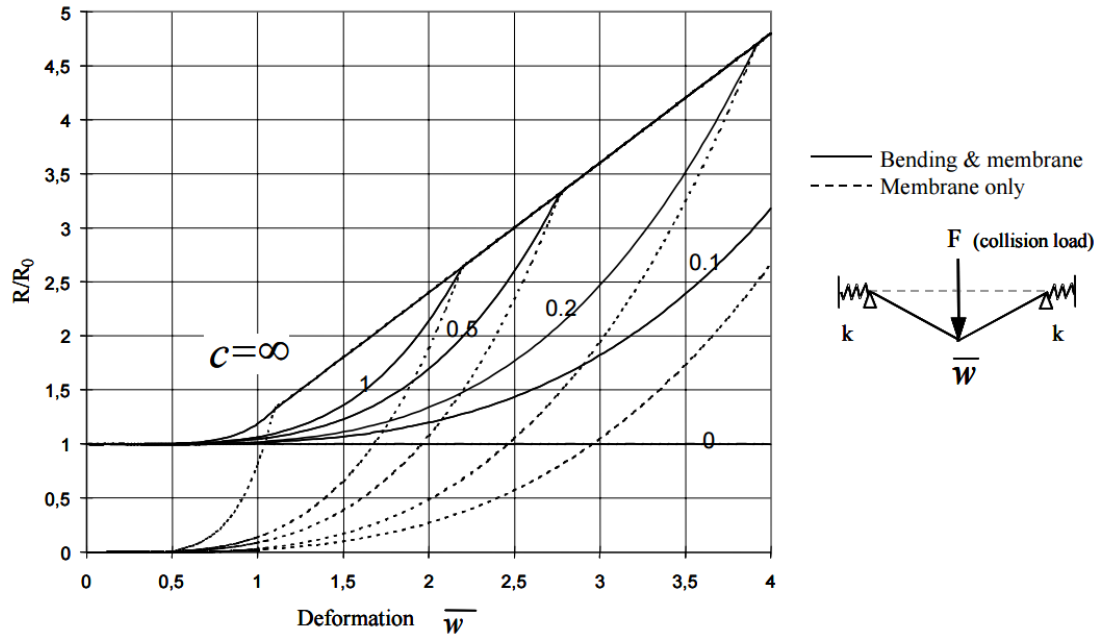


Figure 2.16: Plastic resistance according to (Standard, 2004)

For a beam subjected to a constant pressure, the plastic resistance is given as in equation 2.57. Assuming that the stiffeners are uniform so that plastic hinges may be formed at the girders, c_1 may be taken as 2. W_P is the plastic section modulus and for a stiffened plate. It may be calculated according to equation 2.58, assuming the effective section lies at the web toe on the stiffener.

$$R_0 = \frac{8c_1\sigma_y W_P}{l} \quad (2.57)$$

$$W_P = A_S z_g \quad (2.58)$$

The non-dimensional deformation is given as in equation 2.59. c may be established according to equation 2.60 where k_1 is calculated according to equation 2.61. k_{node} is the axial stiffness of the node with the evaluated member removed.

$$\bar{w} = \frac{w}{c_1 w_c} = \frac{Aw}{c_1 1.2 W_P} \quad (2.59)$$

$$c = \frac{4c_1 k_1 w_c^2}{\sigma_y A l} \quad (2.60)$$

$$\frac{1}{k_1} = \left(\frac{1}{k_{node}} + \frac{l}{2EA} \right) \quad (2.61)$$

2.5.3 SDOF Analysis

In an SDOF analysis, it is assumed that the dynamic deformation pattern is approximately equal to the static deformation pattern. The deformation is given as a function of length and time according to equation 2.62 where $\phi(x)$ is the displacement shape function $y(t)$ and is equal to the displacement magnitude.

$$w(x, t) = \phi(x)y(t) \quad (2.62)$$

By applying the deformation shape, the dynamic equation may be solved in generalised form as in equation 2.63. The equation for generalised mass is given in equation 2.64, generalised stiffness is given in equation 2.65, where N is the normal force yielding membrane stiffness, and the generalised force is given in equation 2.66.

$$\bar{m}\ddot{y} + \bar{k}y = \bar{f}(t) \quad (2.63)$$

$$\bar{m} = \int_l m\phi(x)^2 dx + \sum_i M_i\phi_i^2 + \sum_i K_i\phi^2 \quad (2.64)$$

$$\bar{k} = \int_l (EI\phi_{,xx}(x)^2 + N\phi_{,x}(x)^2) dx \quad (2.65)$$

$$\bar{f}(t) = \int_l q(t)\phi(x) dx + \sum_i F_i\phi_i \quad (2.66)$$

Commonly, the structural response for an SDOF model may be calculated using pulse response diagrams or Biggs charts. Typically, Biggs charts are given in terms of a defined loading pulse shape. Response curves are given in terms of the structure's stiffness and the maximum response is calculated for the structure's eigen period relative to the total loading duration. A typical Biggs chart as given in (DNV, 2014a) can be viewed in figure 2.17.

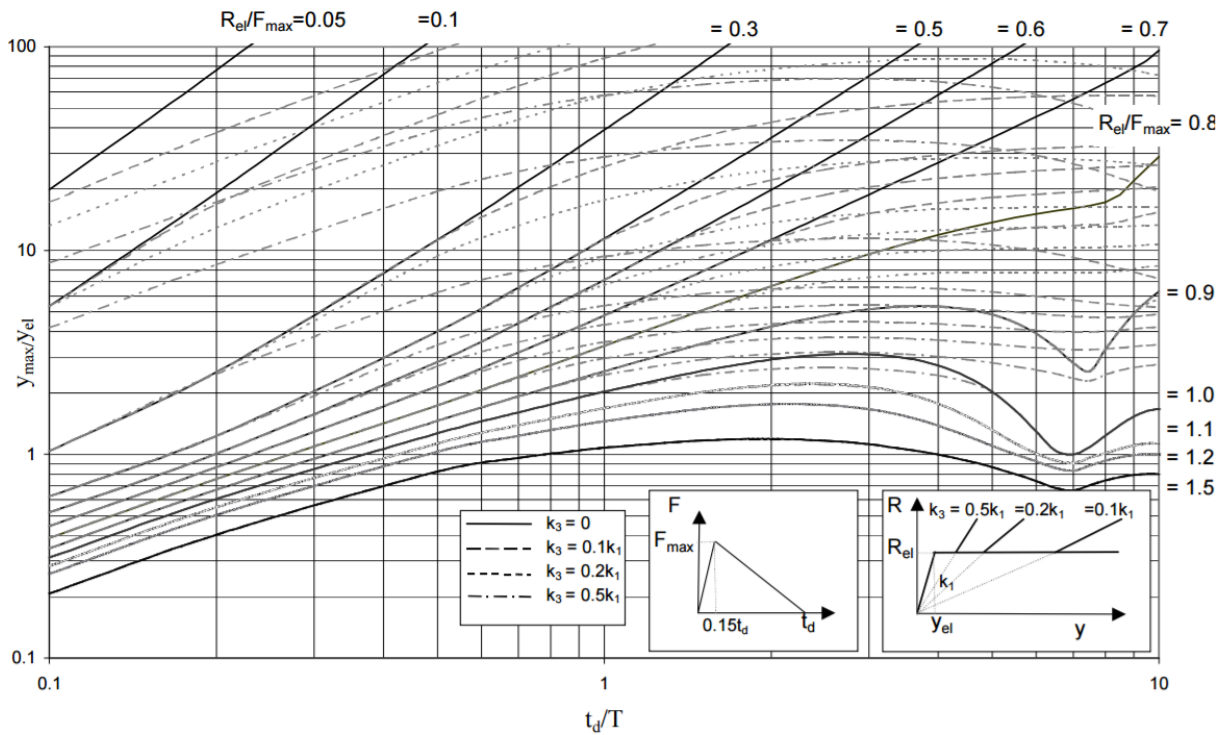


Figure 2.17: A typical Biggs chart as given in (DNV, 2014a)

2.5.4 Methods for Calculating Dynamic Response

According to (DNV, 2014a), the dynamic response of a structure may fall into three categories depending on the relationship between the duration of the load pulse and the structure’s eigen period.

The impulsive domain is defined by equation 2.67. A structure in the impulsive domain is able to withstand large peak pressures as the structural response is governed by the pressure impulse given by equation 2.68.

$$\frac{t_d}{T} < 0.3 \tag{2.67}$$

$$I = \int_0^{t_d} F(t) dt \tag{2.68}$$

The structural response may be calculated iteratively by equation 2.69 where $R(w)$ equals the relationship between force and deformation and m_{eq} is equal to the equivalent mass. A

rough estimate of deformation for short pulses may according to (Larsen, 2014) be estimated as in equation 2.70.

$$I = \sqrt{2m_{eq} \int_0^{w_{max}} R(w) dw} \quad (2.69)$$

$$w_{max} = \frac{I}{\sqrt{km}} \quad (2.70)$$

The dynamic domain is defined by equation 2.71. In order to find the response in the dynamic domain, the dynamic equations given by 2.63 must be integrated numerically. Results may then be presented in terms of Biggs charts.

$$0.3 < \frac{t_d}{T} < 3 \quad (2.71)$$

According to (Larsen, 2014), the constant mean acceleration method is possibly the most commonly used time integration scheme for dynamic problems. The method is implicit and based on applying the mean of the initial acceleration and the final acceleration for each time step. For each time step, the displacement, acceleration and velocity are solved according to equations 2.72 to 2.74. The method is unconditionally stable and the time steps may thus be decided solely by the accuracy requirement.

$$u_{i+1} = \frac{P_{i+1} + m\ddot{u}_i + \left(\frac{4}{h}m + c\right)\dot{u}_i + \left(\frac{4}{h^2}m + \frac{2}{h}c + k\right)u_i}{\left(\frac{4}{h^2}m + \frac{2}{h}c + k\right)} \quad (2.72)$$

$$\ddot{u}_{i+1} = 4\left(\frac{u_{i+1} - u_i - \dot{u}_i h}{h^2}\right) - \ddot{u}_i \quad (2.73)$$

$$\dot{u}_{i+1} = \dot{u}_i + \frac{1}{2}(\ddot{u}_i + \ddot{u}_{i+1})h \quad (2.74)$$

The quasi-static domain is defined by equation 2.75 and is recognised by responses close to static deformations. For a short rise time, the solution may be found by iteration using equation 2.76.

$$\frac{t_d}{T} > 3 \quad (2.75)$$

$$w_{max} = \frac{1}{F_{max}} \int_0^{w_{max}} R(w) dw \quad (2.76)$$

2.5.5 Added Mass

Added mass is equal to the pressure acting in phase with an objects acceleration and must be considered in a dynamic analysis. In addition to the theoretical model for calculating generalised added mass as described in section 2.4.2, there are three different means of establishing the added mass which are discussed in this thesis. The added mass may be established from DNV GL's recommended practice (DNV, 2014b) where the added mass is given for a series of geometries. The tabulated added mass for a fully submersed rectangular plate may be seen in figure 2.18.

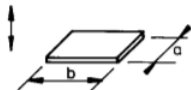
Body shape	Direction of motion	C_A				V_R
		b/a	C_A	b/a	C_A	
Rectangular plates 	Vertical	1.00	0.579	3.17	0.840	$\frac{\pi}{4} a^2 b$
		1.25	0.642	4.00	0.872	
		1.50	0.690	5.00	0.897	
		1.59	0.704	6.25	0.917	
		2.00	0.757	8.00	0.934	
		2.50	0.801	10.00	0.947	
		3.00	0.830	∞	1.000	

Figure 2.18: Added mass for a 2D plate as given by (DNV, 2014b)

In (Meyerhoff, 1970), added mass for a flat oscillating plate is calculated for relative aspect ratios by potential theory. A non-dimensional added mass J is given in table 2.2 for different aspect ratios χ . J may be estimated according to equation 2.77. Here, B and L are taken as half the width and half the length.

Table 2.2: Non dimensional added mass by dipole singularities as described in (Meyerhoff, 1970)

χ	0.1	0.125	0.16	0.2	0.25	0.315	0.4	0.5	0.63	0.8	1
J	0.947	0.934	0.917	0.897	0.872	0.840	0.801	0.757	0.704	0.694	0.579

$$J = \frac{M_a}{2\pi\rho B^2 L} \quad (2.77)$$

Good agreement is seen between the added mass for various aspect ratios from (Meyerhoff, 1970) and (DNV, 2014b). It is however to note that the results are found for a rigid plate in which the entire plate is oscillating in water equally. Adjustments to the added mass factor should be made to account for non-uniform oscillation, as for a deformable plate. In (Faltinsen, 2005), the mean relative velocity potential over the plate's length was calculated as $\frac{2}{\pi} \approx 0.64$ for simply supported boundary conditions.

Finally, the added mass factor may be established from the difference between the dry and wet oscillation period measured in drop tests. The method does not hold for large deformations where other effects can lead to a change in dry and wet period.

There are two ways of defining the added mass factor. Some include the dry mass in the added mass factor while others treat it separately. In this thesis, it is treated separately so that $M_{total} = M_{dry}(1 + C_A)$ where C_A is equal to the added mass factor.

2.5.6 Nonlinear Strain

For panels and beams undergoing large deformations, linear stress and strain analyses are no longer valid. For a beam with the deflection function $w(x)$, the strain can be given as in equation 2.78.

$$\epsilon_x = \frac{du}{dx} + \frac{1}{2} \left(\frac{dw}{dx} \right)^2 - z \cdot \frac{d^2w}{dx^2} \quad (2.78)$$

The material properties in LS-Dyna are to be given in effective strain while the properties are given in true strain. The effective plastic strain is calculated according to equation 2.79. Three different types of nonlinear structural steel are applied in the thesis, all of which are collected from (Veritas, 2013).

$$\epsilon_{effective} = \epsilon_{true} - \frac{\sigma_{true}}{E} \quad (2.79)$$

Table 2.3: Nonlinear material parameters for S235 steel

	$\sigma_{true}[MPa]$	$\epsilon_{true}[]$	$\epsilon_{effective}[]$
Yield 1	236.2	0.004	0.0029
Yield 2	243.4	0.0198	0.0186
Ultimate	432.6	0.1391	0.1370

Table 2.4: Nonlinear material parameters for S355 steel

	$\sigma_{true}[MPa]$	$\epsilon_{true}[]$	$\epsilon_{effective}[]$
Yield 1	357	0.004	0.0023
Yield 2	366.1	0.0197	0.0180
Ultimate	541.6	0.1391	0.137

Table 2.5: Nonlinear material parameters for S420 steel

	$\sigma_{true}[Mpa]$	$\epsilon_{true}[]$	$\epsilon_{effective}[]$
Yield 1	420	0.004	0.0020
Yield 2	421.3	0.01	0.008
Ultimate	500	0.12	0.1176

2.5.7 Strain Rate Hardening

According to (Veritas, 2013), impact loads with low duration may lead to strain rates that exceed $0.1[s^{-1}]$. At these strain rates, strain rate hardening effects could become prominent. Considering the Cowper-Symonds model, the dynamic stress can be calculated according to equation 2.80. For structural components on offshore platforms, the factors $C = 4000[s^{-1}]$ and $p = 5[]$ are proposed if no other information is available. In (Manual and Volume, 2015), it is stated that material type 24 may account for linear piecewise plasticity by the Cowper-Symonds model and is thus a suitable material type for analysing the response.

$$\sigma_{dynamic} = \sigma_{static} \left(1 + \left(\frac{\dot{\epsilon}}{C} \right)^{\frac{1}{p}} \right) \quad (2.80)$$

2.5.8 Eigen Period for a Beam in Tension

Large strains may lead to membrane forces in the beam. Membrane forces arise as a result of mean strains equivalent to as if the beam was under tension. According to (Larsen, 2015), the tension force affects the natural eigen period of the beam. As can be seen in equation, 2.81, an increase in tension force N will decrease the natural period of the structure.

$$T = \frac{2l}{n\sqrt{\frac{N}{m} + \frac{n^2\pi^2}{l^2} \cdot \frac{EI}{m}}} \quad (2.81)$$

Chapter 3

Global Air Gap Analysis of Semi-Submersible

3.1 Semi-Submersible Parameters

3.1.1 Modelling

The negative air gaps are decided by running an air gap analysis. The model was created as a composite model, which consists of both a panel model and a Morison model. Both models were created using the modelling tool Genie in the Sesam software package. The model was developed as a generic semi-submersible model which may be seen in figure 3.1. Only a quarter of the model was created and was imported into HydroD as a two-plane symmetry model. As we are interested in structural responses for a ULS condition, the platform deck is raised in order to increase the static air gap as common for platforms facing extreme conditions. The water depth in the location is taken to be equal to 300 meters.

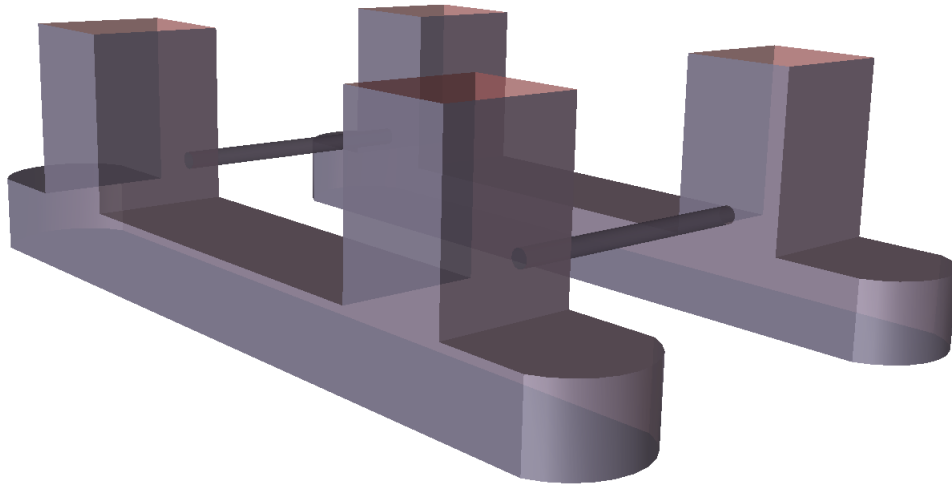


Figure 3.1: The typical semi-submersible model used in the air gap analysis

The critical air gap is to be measured at a series of points surrounding the semi-submersible. 19 sampling points were placed around the semi-submersible. Due to symmetry, the sampling points are only placed on the front and one of the platform's long sides as seen in in figure 3.2. The set of incoming waves are propagating in directions between 0° and 180° with a step size of 15° . For each direction, the RAO for the structure's motion as well as the wave elevation is saved.

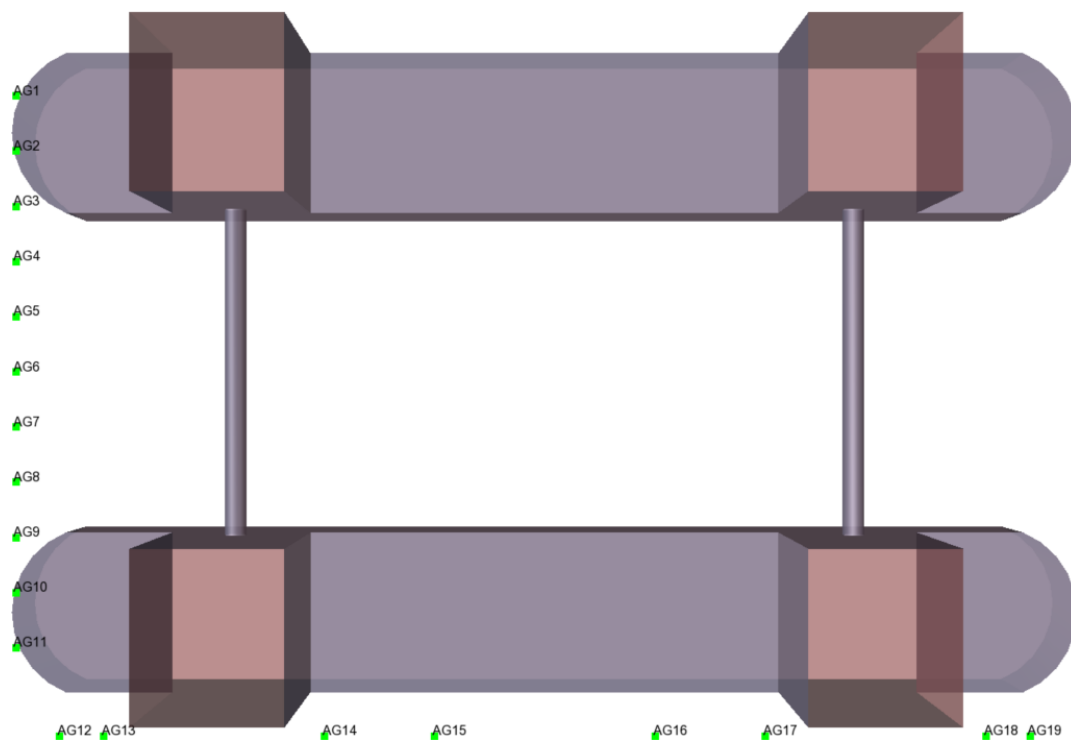


Figure 3.2: The 19 air gap points used in the air gap analysis

In order to obtain the responses in the various sea states, the RAOs were postprocessed in the data processing software postresp to obtain the response spectrum. To remain conservative, the asymmetry factor is taken as 1.3 for all locations and all incoming wave directions. In addition, a wave spreading of $\cos 10$ was used.

Table 3.1: Locations for air gap sampling points

Point	x	y	z	Point	x	y	z
AG1	-48	25	0	AG11	-48	-25	0
AG2	-48	20	0	AG12	-44	-33	0
AG3	-48	15	0	AG13	-40	-33	0
AG4	-48	10	0	AG14	-20	-33	0
AG5	-48	5	0	AG15	-10	-33	0
AG6	-48	0	0	AG16	10	-33	0
AG7	-48	-5	0	AG17	20	-33	0
AG8	-48	-10	0	AG18	40	-33	0
AG9	-48	-15	0	AG19	44	-33	0
AG10	-48	-20	0				

The chosen design parameters for the semi-submersible are tabulated in table 3.2. B_p is the breadth of the pontoons and R_x , R_y and R_z is the radius of gyration about the denoted axis. The location of the centre of gravity, CG , is measured above the mean water line.

Table 3.2: General parameters for test semi-submersible

$L[m]$	$B[m]$	$D[m]$	$a_{static}[m]$	$B_p[m]$	$R_x[m]$	$R_y[m]$	$R_z[m]$	$CG[m]$	$m[kg]$
100	60	15	13	15	28	31	34	25	$30.8e + 10^6$

The properties of the Morison component of the model, which adds damping to the semi-submersible, are described in table 3.3. As suggested in section 2.2.5, the parameters are scaled to add only a small additional volume to the structure since the volume already is accounted for in the panel model.

Table 3.3: Parameters for Morison model

	Virtual diameter[m]	C_D []
Pontoons	0.0165	400
Braces	0.02	70

The air gap for the semi-submersible was checked for 23 different sea states, all given by the DNV steepness criteria as described in equation 2.11 in section 2.2.1. The definitions of the sea states used can be seen in table 3.4. For each of the sea states, σ_a was taken as 0.07 and σ_b was taken as 0.09. Each sea state is assumed to last for a total of 3 hours, i.e. a total of 10800 [s].

Table 3.4: Jonswap spectra defined by the DNV steepness criteria for use in air gap analysis

Run ID	T_z	γ	Hs	Run ID	T_z	γ	Hs
1	6	5	5.62	13	12	3.15	14.98
2	6.5	5	6.34	14	12.5	3.14	16.25
3	7	5	7.14	15	12.9	3.15	17.3
4	7.5	5	7.96	16	13.5	2.18	17.2
5	8	5	8.78	17	14	1.6	17.1
6	8.5	5	9.6	18	15	1	16.6
7	9	5	10.42	19	16	1	15.7
8	9.5	5	11.22	20	17	1	14.4
9	10	5	12	21	18	1	12.4
10	10.5	4.59	12.76	22	19	1	8.2
11	11	4.04	13.48	23	21	1	8.2
12	11.5	3.51	14.16				

3.1.2 Post Processing RAOs

The resulting RAOs were post processed by creating a script for postresp that may be viewed in appendix E. The script calculated RAOs for the combined motions for each direction as well as the relative upwelling RAO. The most likely maximum response was also calculated for all sea states listed in table 3.4. The sea states were taken to be short crested with a wave spreading power of 10. The sea state and direction leading to the largest negative air gap

for each sampling points were plotted in order to establish the most critical combination of wave direction, sea state and location. A run was also conducted for long crested sea states with zero wave spreading.

The upwelling was calculated according to equation 2.24 in section 2.2.6. Since the outputted response is given in terms of the most likely response, and the recommended practice is to utilise the 90% fractile, the response is multiplied with the factor given in equation 3.1.

$$\frac{H_{0.9}}{H_{max}} = \left(1 - \frac{\ln(-\ln(p))}{\ln(N)}\right)^{\frac{1}{2}} \quad (3.1)$$

3.2 Air Gap Results

The purpose of the air gap analysis is to map the points experiencing the largest negative air gaps assuming that the points with the largest negative air gaps experiences the largest loads. In (GL, 2016b), the pressure pulse is estimated by the size of the relative upwelling were larger negative air gaps in general yield larger loads. The largest air gaps for all sea states were observed at sampling point 11, located in front of the column above the pontoon. The largest negative air gap was observed in sea state 15 with an the incoming waves propagating in a direction of 30° with the negative air gap equal to -5.75[m]. The second largest negative air gap for the same location was measured to equal -5.56[m] in sea state 16 and the third largest was measured to equal -5.4[m] in sea state 6. Both occurred for waves propagating in a direction of 30°. The maximum negative air gap for all locations may be observed in figure 3.3. The most critical negative air for each location are tabulated in table C.1 in appendix C. The negative air gaps are given in terms of the magnitude and relative upwelling for the most critical sea state and incoming wave direction.

A plot of the negative air gap by the front of the semi-submersible at head sea with zero wave spreading may be seen in figure 3.4. The air gap is symmetrical about the neutral axis and one can see that the magnitude of the negative air gap increases as one approaches the centre of the columns.

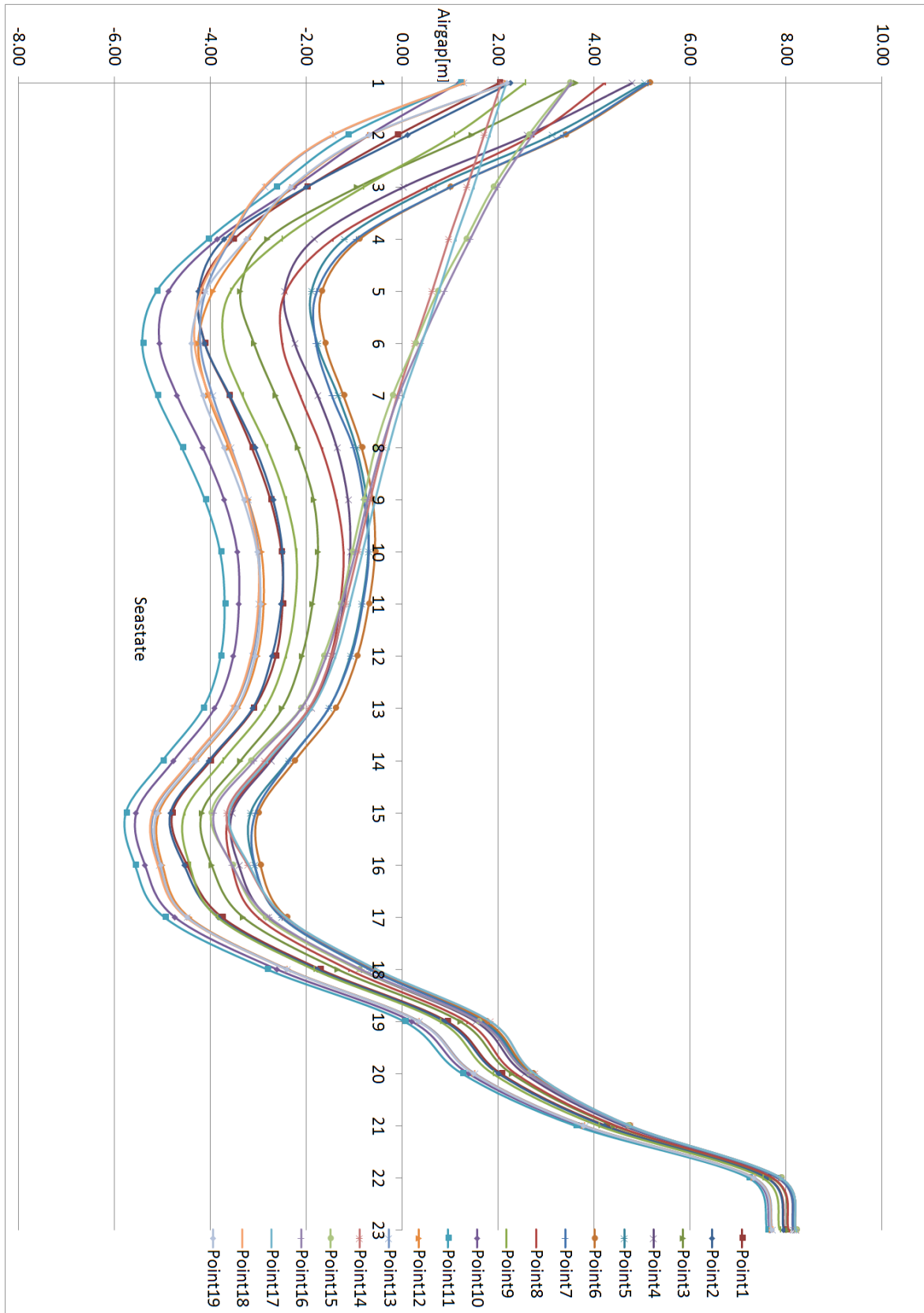


Figure 3.3: Maximum negative air gap measured by sampling point and sea state

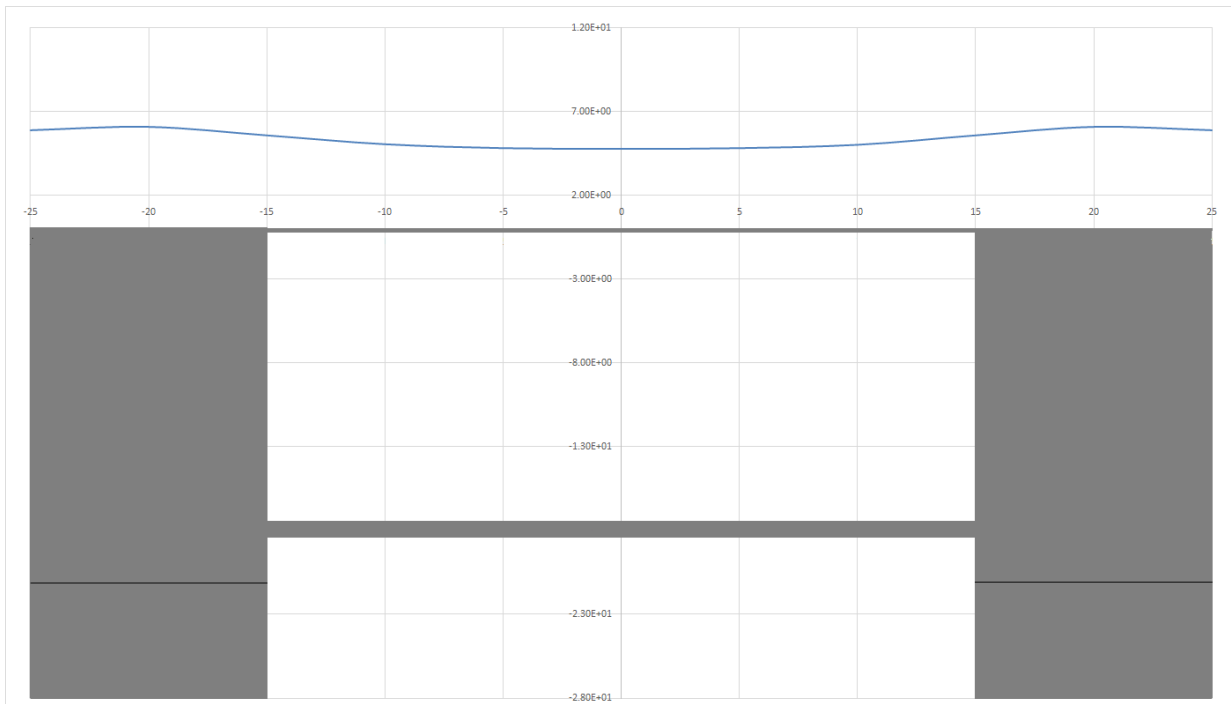


Figure 3.4: Negative air gap at the front of the semi-submersible at head sea with 0 wave spreading

3.3 Particle Velocities

Aside from the loading model from the OTG, the loading models are in general based upon calculating the particle velocity in the wave. Sea state 6 and 15 are evaluated as they are the most critical in terms of negative air gap. In addition, the two conditions are of interest as condition 15 may yield large loads due to the large significant wave heights while sea state 6 may cause large loads due to a high peak frequency in the sea state. The approximate wave parameters for sea state 6 and 15 using the peak frequency as a basis are given in table 3.5.

Table 3.5: Approximate wave parameters for sea state 6 and 15

	ω_p	α	$H_s[m]$	$H_{max}[m]$	$\zeta_{a_{upper}}$	k_{peak}	$a[m]$	$z_{global}[m]$
Sea state 6	1.04	1.3	9.6	11.96	6.24	0.11	-5.40	3.87
Sea state 15	0.687	1.3	17.3	20.91	11.245	0.048	-5.75	9.35

The loaded plate is assumed to be located directly above the deck box and with a height of 3[m]. The outer plate above the deck box is assumed to consist of the same 3[m] by 3[m]

stiffened plate for the entire platform. The wave height is assumed to equal the most likely highest wave in the sea state and the dominating wave frequency is assumed to equal the peak frequency of the sea state. The peak frequency for the sea state is calculated from the zero mean crossing period of the sea state by equation 3.2.

$$\omega_p = 1.41 \frac{2\pi}{T_Z} \quad (3.2)$$

The wave is assumed to be a linear wave with an asymmetry factor of 1.3. As previously discussed, errors are expected when applying linear theory for nonlinear problems such as tall and steep waves. The velocities are subsequently estimated in terms of wheeler stretching described in section 2.1.2 and the second order kinematics model described in section 2.1.3. The second order sum and difference frequency effects are neglected.

The vertical position of the centre of plate is measured by adding the height of the centre of the plate from the deckbox with the static air gap and the maximum free surface elevation as in equation 3.3. The maximum wave height is taken as the most probable largest wave in the sea state and for the case of the 3[m] by 3[m] plate, z_{local} is taken as 1.5[m]. It is assumed that the largest negative air gaps occurs when the displacement of the sampling point is close to its maximum displacement, meaning that the structure's velocity is approximately 0[m/s]. Hence, only the particle velocity of the fluid is considered in the thesis.

$$z_{global} = z_{local} + a + \zeta_{max} \quad (3.3)$$

3.3.1 Velocity Estimates by Wheeler Stretching

The depth of the location is 300 [m] and the approximate wave properties are taken from table 3.5. The velocity and acceleration to be used in load estimates by Wheeler stretching are given in table 3.6.

Table 3.6: Relative location, particle velocity and acceleration given by Wheeler stretching

Sea state	$z_{wheeler}$ [m]	u [m/s]	a_x [m/s ²]
6	-2.32	5.03	5.23
15	-1.83	7.08	4.86

3.3.2 Velocity Estimates by the Second Order Kinematics Model

The velocities and accelerations based upon the second order kinematics model is given in table 3.7. The values are conservative compared to those obtained by Wheeler stretching.

Table 3.7: Relative location, particle velocity and particle acceleration given by the second order kinematics model

Sea state	$z[m]$	$u(0)[m/s]$	$\frac{\partial u}{\partial z}[m/s]$	$u(z)[m/s]$	$a_x[m/s^2]$
6	3.87	6.49	0.71	9.25	9.62
15	9.35	7.73	0.37	11.19	7.69

3.3.3 Sea State Properties

If the wave is breaking, the particle velocity at the peak of the wave crest exceeds the wave celerity leading to higher loads than for a non-breaking wave. The properties of the mean wave in the sea state are given in table 3.8.

Table 3.8: Wave properties of a non-breaking wave

Sea state	$C[m/s]$	$l_0[m]$	$Duration[s]$
6	9.43	4.75	1.98
15	14.28	10.24	1.39

Assuming the wave doesn't break, the area of the wave hitting the plate is estimated as a trapezoid with an height equivalent of that of the plate, i.e. $3[m]$. The area is calculated according to the descriptions given in figure 3.5 and calculated according to equation 3.4.

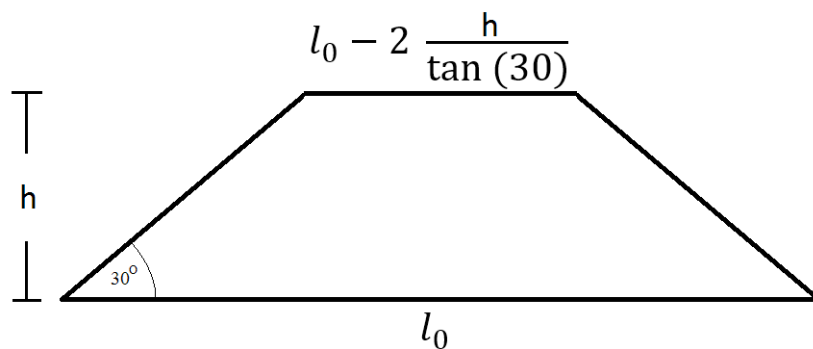


Figure 3.5: Estimated are of non-breaking wave

$$A = h \left(l_0 - \frac{h}{\tan(30^\circ)} \right) \quad (3.4)$$

From figure 3.5 it is seen that the area of the design wave in sea state 15 is equal to $15.13[m^2]$. The energy content in section of the most critical design wave hitting the structure is calculated as in table 3.9.

Table 3.9: Wave energy content for the most critical sea state

$E_{particle}[kJ/m^3]$	$A[m^2]$	$s[m]$	$Energy[kJ]$
64183.63	15.13	0.50	485.62

Using the total breadth of the plate equal to $3[m]$, the total energy contents of the wave segment which hits the stiffened plate is $2.91[MJ]$.

Chapter 4

Verification of FSI-Model by 2D-Experiments

4.1 Experimental Layout

(Faltinsen, 2005) describes a drop test in which a plate equivalent to a beam is dropped into water. The plate is modelled as a two dimensional beam with a length of 500 [mm] with pressure gauges placed in various locations underneath the plate. The pressure gauges have a sampling frequency of up to 500[khz]. The drop test was conducted for two different materials, steel and aluminium with their material properties listed in table 4.1. Only the steel plate is evaluated in the thesis. The test rig has a total mass of 385[kg] ensuring a sufficient momentum so that the rig's rigid body velocity remains relatively constant upon water impact.

Table 4.1: Parameters for deformable plates used in drop tests (Faltinsen, 2005)

Parameter	Steel plate	Aluminium plate
Structural mass $M_B [kg/m^2]$	62	21
Modulus of elasticity $E [Pa]$	2.10E+11	7.00E+10
Plate length $L [m]$	0.5	0.5
Plate breadth $B [m]$	0.1	0.1
Bending stiffness $EI [N^2 m]$	8960	17060
Structural mass parameter $M_B / (\rho L)$	0.124	0.042
Spring stiffness parameter $k_\theta L / (2EI) []$	2.85	1.5
Distance from neutral axis to strain measurements $z_a []$	0.004	0.01375

The experimental setup of the plate consists of three plates, the main plate at the bottom connected to a rigid reference plate via boundary springs. The middle plate is connected to the top plate via force transducers as indicated in figure 4.1.

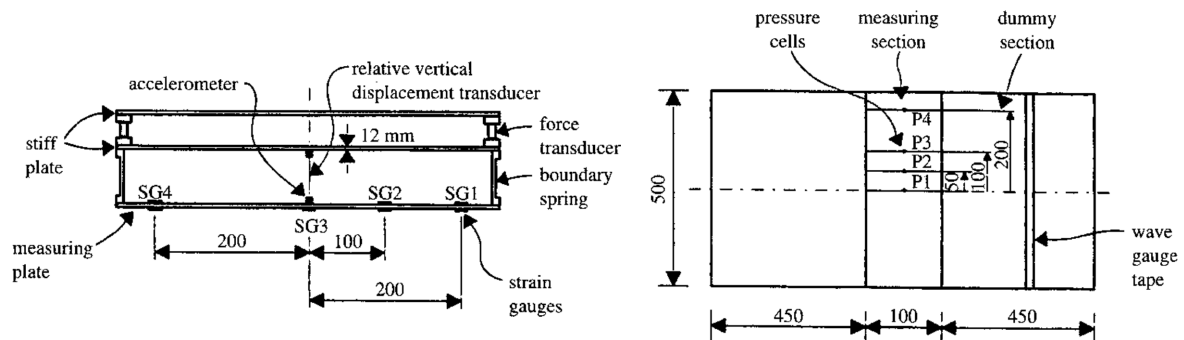


Figure 4.1: Experimental setup of the drop test described in (Faltinsen, 2005)

4.1.1 Experimental Results

The results from the drop tests shows the development of surface pressures on the structures as well as strains over the structure. Figure 4.2 shows the pressure development of the steel plate from table 4.1 dropped at a velocity of 2.94[m/s]. It is to be noted that large pressure peaks may be observed during the impact, but if the duration is short, the pressure peak will have a negligible impact on overall structural behaviour as it is mainly the overall pressure impulse, i.e. pressure integrated w.r.t time which determines the structural response. After impact, an added mass force may be observed, leading to an increased

period in the region where the force is acting. After 0.01[s], cavitation occurs as the pressure equals the ventilation pressure.

As air is sucked in from the free surface, added mass approaches 0, reducing the natural period of the system. Analytical results are no longer valid after this point. However, the maximum strains and pressures occur during the first half period, thus the ongoing oscillation is of limited interest. Also to note is that the analytical added mass slightly over predicts the wet period measured experimentally.

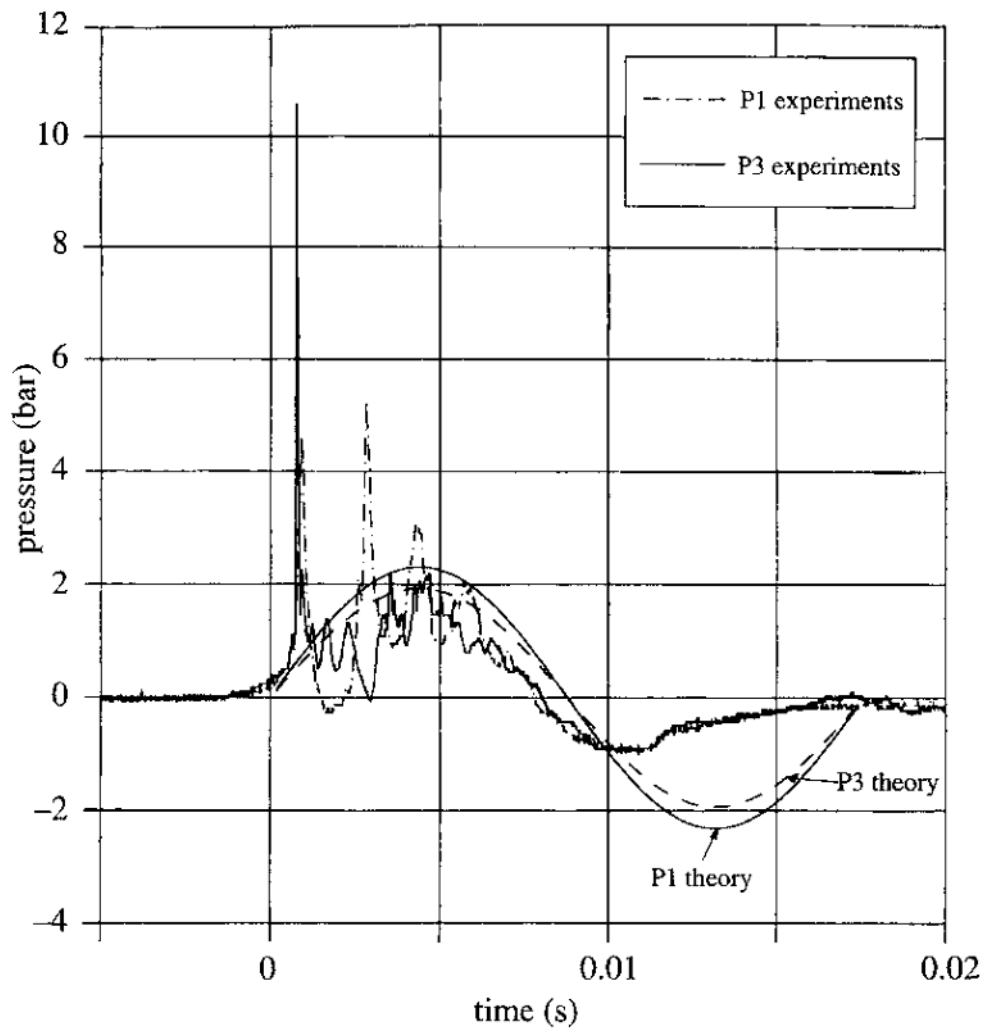


Figure 4.2: Pressures measured in the middle and at $\frac{z_a}{L} = \frac{1}{10}$ (Faltinsen, 2005)

The structural strain of the plate with the same parameters may be seen in figure 4.3. By inspection of the figure, one can observe that the theoretical natural period of the structure approximately equals 0.018[s]. The theoretical natural period is slightly larger than the periods observed for the practical drop tests. In addition, the theoretical strains are larger, approximately equal to $1.85e^{-3}$ [] whereas the measured strain is equal to $1.58e^{-3}$ [].

to note that the plate is oscillating with its dry natural period after the initial deflection due to ventilation.

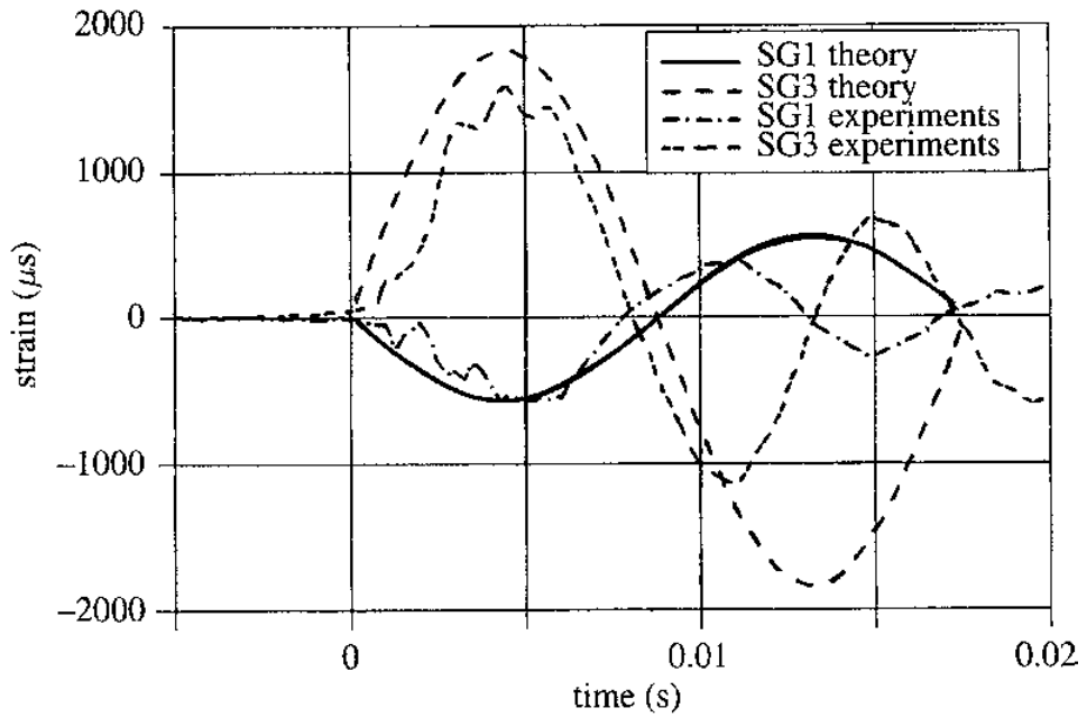


Figure 4.3: Structural strain measured in the middle and at $\frac{z_a}{L} = \frac{1}{10}$ (Faltinsen, 2005)

4.2 Finite Element Modelling of Drop Tests

4.2.1 Water and Air Modelling in LS-Dyna

The fluids are modelled as Eulerian null materials while the steel plate that is interacting with the fluid is a Lagrangian element. The fluid elements are modelled as master elements with the plate modelled as slave elements. For each drop test, the node's of the fluid mesh overlaps the nodes of the plate mesh. The material properties of the different types of fluid applied in the simulations in LS-Dyna are given in table 4.2.

Table 4.2: Material properties applied in LS-Dyna

	Material type	Density ρ [kG/m^3]	Viscosity μ []	Pressure cutoff [Pa]
Air	Null	1.23	1.00E-03	-1.00E+11
Fresh water	Null	1000	1.84E-05	0
Salt water	Null	1025	1.67E-03	0

The modelling involved some trial and error in order to find the most suitable EOS which both resulted in stable analyses as well as matching the properties of the real material. The plate, air and water were all modelled as EOS Gruneisen materials with the properties described in table 4.3.

Table 4.3: EOS applied for water, air and steel

	C	S1	S2	S3	Gamma0	A	E0	V0
Water	1480	2.56	-1.986	0.227	0.5	0	0	0
Air	343.7	0	0	0	1.4	0	0	0
Steel	4570	1.5	0	0	1.93	0	0	0

4.2.2 2D Panel Model

In general, the drop test consists of three different parts, air, water and the plate. The analysis is set up according to ALE theory where the plate is modelled according to Lagrangian theory while the water and air is modelled according to Eulerian theory. The fluid mesh consists of water and air where the air mesh is modelled as an initial void. In order to ensure valid results, the input data must be correct. It was chosen to validate the input data by recreating the experimental configuration in the drop test described in (Faltinsen, 2005) and comparing the two results.

For the first runs, the tests were run in 2D, where the breadth of the plate was modelled to equal 10[mm] with all motion constrained in the out-of-plane direction. The components on the plate were modelled as four node-shell elements with the water and air elements modelled as 8 node-solid elements. In the drop test in (Faltinsen, 2005), the drop was conducted at a height of 0.5 [m], yielding a velocity of approximately 2.94[m/s]. For the subsequent analyses, half the model was used with symmetry conditions at the middle in order to save computational time where the middle nodes were constrained for rotation and translation in the x-direction.

Two different test rigs were tested, modelled with different methods of obtaining the desired rotational stiffness of 502.44[Nm/rad]. The first test rig may be viewed in figure 4.4. The spring was modelled as a beam with one clamped end to the rigid upper plate and the other end connected to the lower plate. The desired rotational of 502.44[Nm/rad] stiffness was achieved by the means of the stiffness coefficient method which gives the rotational

stiffness by equation 4.1.

$$k_{\theta} = \frac{4EI}{l} \quad (4.1)$$

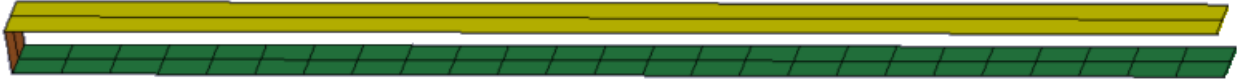


Figure 4.4: Set up of 2D plate structure in LS-Dyna with elastic spring

For the second rig, the boundary of the lower plate was modelled using a joint with rotational stiffness of $502.44[Nm/rad]$. The jointed connection must be between two rigid element types, hence, the edge of the bottom plate is modelled as a short, rigid element. A small imperfection angle of 0.05° was also added so that the middle of the plate hit the water just before the rest of the plate. The setup may be seen in figure 4.5.

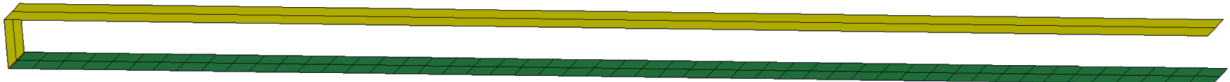


Figure 4.5: Setup of 2D plate structure in LS-Dyna with rotational spring

The default continuum treatment was chosen to be the Eulerian obsolete with the second order Van Leer + half index solver. The finest mesh used on the steel plate had a breadth of 5 [mm] and a length of 5 [mm]. The finest mesh used on the water elements had a length and breadth of 5 [mm] and a height of 2.5 [mm]. The element type for the shells was chosen as S/R Hughes-Liu elements with 5 integration points. Further increasing the mesh density by setting the breadth and length to 2.5[mm] did not change the outcome of the analyses noteworthy.

Two different means of extracting the slamming loads were tested. The first method involved extracting the nodal forces on the Lagrangian elements while the other involved FSI-sensors on the Lagrangian elements which extracts the pressure in the Eulerian fluid. The downside to extracting the nodal forces is that nodal forces may not be extracted for rigid element types. However, the two methods yielded the same pressure impulse for the deformable plate, indicating that the FSI-sensor method was a valid approach for extracting loads on

the plate. Thus, the pressure pulses were ultimately extracted with FSI-sensors for both the deformable and non-deformable plate.

Results were checked against the results in (Faltinsen, 2005), with an emphasis on obtaining both the correct magnitude and period of the response. The added mass equivalent to the response calculated in LS-Dyna is estimated from the relationship between the wet and dry natural period as in equation 4.2 where \bar{M} is equal to 15.5[kg]. Generalised mass i used for simplified comparisons between the analytical solution and the solution from LS-Dyna. For large deformations where membrane forces become prominent, this approximation will yield inaccurate results.

$$\bar{M}_a = \bar{M} \left(\left(\frac{T_{wet}}{T_{dry}} \right)^2 - 1 \right) \quad (4.2)$$

The elemental properties of the plate are given in table 4.4. n_B and n_L are the number of elements over the breadth and length of the plate. The linear material properties applied in the analyses are listed in table 4.5 and the nonlinear parameters are given in table 4.6.

Table 4.4: Properties for the finite element model used in the 2D drop test verification study

Part	$B[m]$	$L[m]$	n_B	n_L	$t[mm]$	Tested Materials
Plate	0.02	0.25	2	50	8	1,3,4
Spring	0.02	0.1	2	1	8	2
Heavy plate	0.02	0.25	2	1	8	5

Table 4.5: Linear material properties used in 2D drop tests

Material	Material type	$\rho[kg/m^3]$	$E[GPa]$	$\nu[]$
1	Elastic	7850	210	0.3
2	Elastic	7850	15	0.3
3	Elasto-plastic	7850	210	0.3
4	Rigid	7850	210	0.3
5	Rigid	9.62E+05	210	0.3

Table 4.6: Nonlinear material properties used in 2D drop tests

Material	$\sigma_1 [MPa]$	$\epsilon_1 []$	$\sigma_2 [MPa]$	$\epsilon_2 []$	$\sigma_3 [MPa]$	$\epsilon_3 []$	$C []$	P
3	236.2	0.0029	243.4	0.0186	432.6	0.137	0	0

4.2.3 Analytical Plate Properties for Verification Study

For the panel described in section 4.2.2, the generalised properties are estimated according to the equations and methods listed in section 2.4.2. The generalised stiffness contribution for a rotational boundary stiffness is not known. However, the generalised stiffness contribution for a vertical spring is known and given as in equation 4.3.

$$\bar{k}_i = K_i \phi^2(x_i) \quad (4.3)$$

The additional added generalised stiffness contribution was estimated from an analogy for a simply supported beam. First the maximum deflection for a simply supported beam subjected to a point load in the middle of the beam was set equal to the maximum for a beam subjected to an end moment as seen in equation 4.4.

$$\frac{M_e L^2}{16EI} = \frac{FL^3}{48EI} \quad (4.4)$$

The point load was set equal to that of a vertical spring with a generalised displacement, $F_i = K_i \phi(x_i)$, while the end moment was set equal to a rotational spring with a generalised rotation, $M_j = k_{j\theta} \frac{\partial \phi}{\partial x}(x_j)$. By inserting these values in equation 4.4, the added generalised stiffness in equation 4.5 was obtained.

$$\bar{k}_i = K_i \phi^2(x_i) = \frac{3}{L} k_{j\theta} \frac{\partial \phi}{\partial x}(x_j) \phi(x_i) \quad (4.5)$$

The added mass is calculated using the same analytical theory as described in section 2.4.2 with the calculations shown in equation 4.6.

$$\bar{M}_A = \rho \cdot 0.18L^2 = 1000 \cdot 0.18 \cdot 0.5^2 = 45 \quad (4.6)$$

The properties of the plate are listed in table 4.7 and they comply with the values found for the lowest eigen modes found in (Faltinsen, 2005). Both the model with and without rotational stiffness are listed. As in (Faltinsen, 2005), only the model with the rotational boundary stiffness is used in simulations of the experimental drop tests.

Table 4.7: Analytical properties of the flat plate subjected to drop tests

k_θ	\bar{m}	\bar{M}_A	\bar{k}	T_{dry}	T_{wet}
0	15.5	45	3491141.82	0.013	0.026
102144	15.5	45	7341879.82	0.009	0.018

4.3 Results from Drop Test Simulations

The material properties for water appear to have been modelled such that the water behaves as one would expect when hit by a plate. In figure 4.6, one can clearly see how the water rises as the plate enters the water. The figure was created by plotting the volume fraction with red representing only water and blue representing air. As time passes, one can also observe that the plate is increasingly submerged.

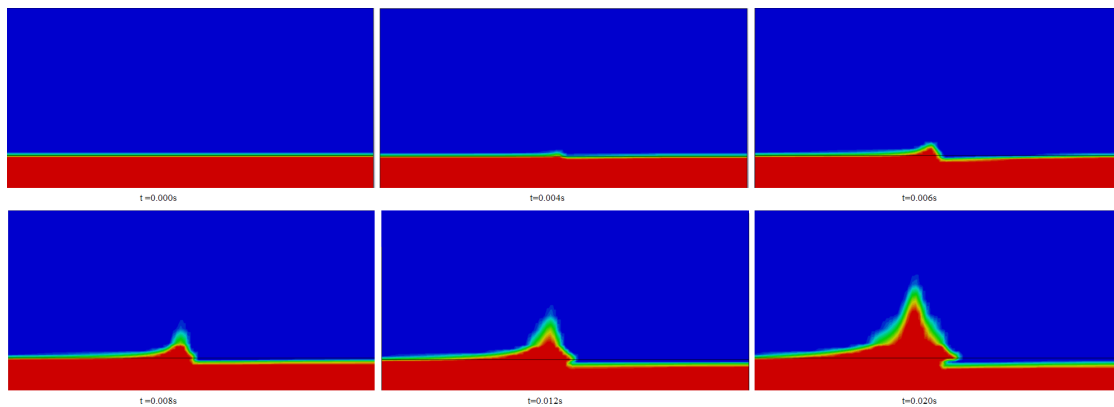


Figure 4.6: Water rise due to water entry of elastic plate at a velocity of 2.94 [m/s]

Of the two different tested plate configurations, the plate with the rotational spring modelled as a plate yielded the results which was the best fit with the theory described in (Faltinsen, 2005). In linear theory, membrane stiffness is neglected and the model with the rotational joint connected to the rigid beam, seen in figure 4.5, yielded large membrane stress. The elastic spring in the model in figure 4.4 doesn't carry large shear forces during the deformation. This leads to small membrane stresses in the plate. Hence, the model with

the elastic spring had the best correspondence with the analytical model out of the two rigs and the model with the rotational joint was discarded for further analyses.

The natural period of the plate is found graphically by measuring the duration of the first half period and multiplying by two to get the total period. By measuring the eigen period in figure 4.7 at an impact velocity of $2.94[m/s]$ the eigen period is found to be approximately $0.018[s]$, the same as the analytical eigen period. There are however some discrepancies in terms of the wet and dry natural period. The dry natural period was slightly lower than the analytical dry natural period, $0.008[s]$ versus $0.009[s]$. The mode shape for the maximum deflection in LS-Dyna is similar to the cosine function chosen for the analytical calculations. A comparative plot of the mode shapes may be seen in appendix F in figure F1.

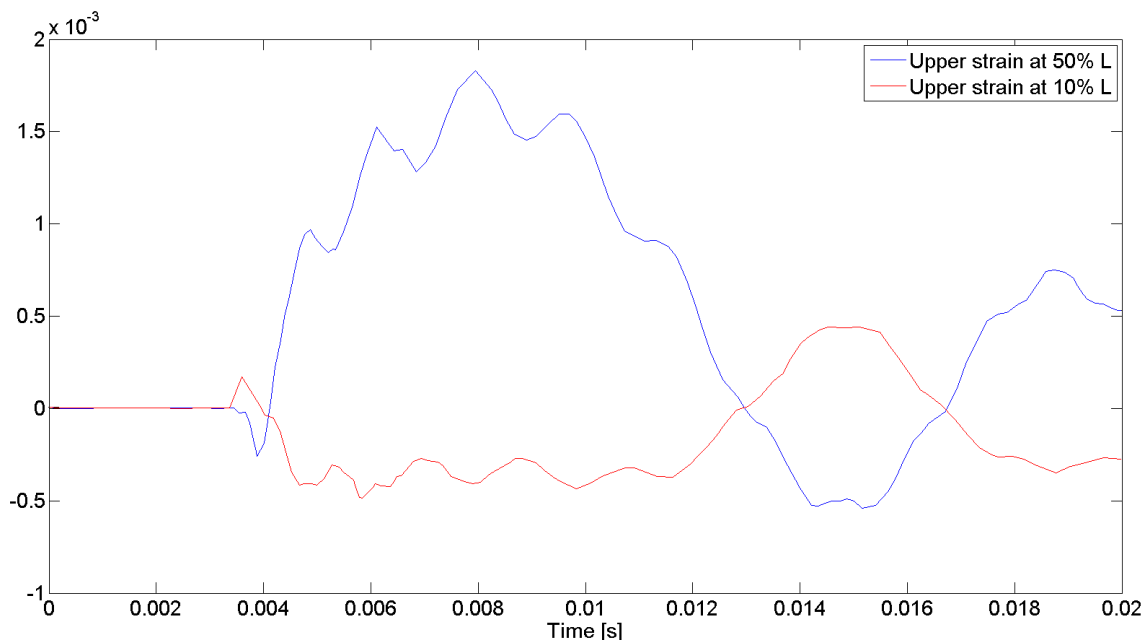


Figure 4.7: Upper x-strains measured at $x/L = 0.1$ and 0.5

The maximum strain in the middle of the plate was measured to equal $1.8e-3$, which is in the same order of magnitude as what was measured in tests and found analytically in section 4.1.1 adding credibility. The analytical solution yielded a maximum strain of $1.85e-3$ and the measured maximum was $1.58e-3$. Similarly, the maximum size of the strain at 10% of the plate's length was measured to be equal to $0.5e-3$, the same as measured at 10% of the length in Faltinsen (2000). In figure 4.8, the pressure time series is shown at the middle and 10% of the plate's length. The pressure distribution at both locations are similar in magnitude to the ones estimated at point 1 and point 3 in (Faltinsen, 2005). Reference is made to figures

4.3 and 4.2 in section 4.1.1 where the results from the experimental drop tests can be viewed.

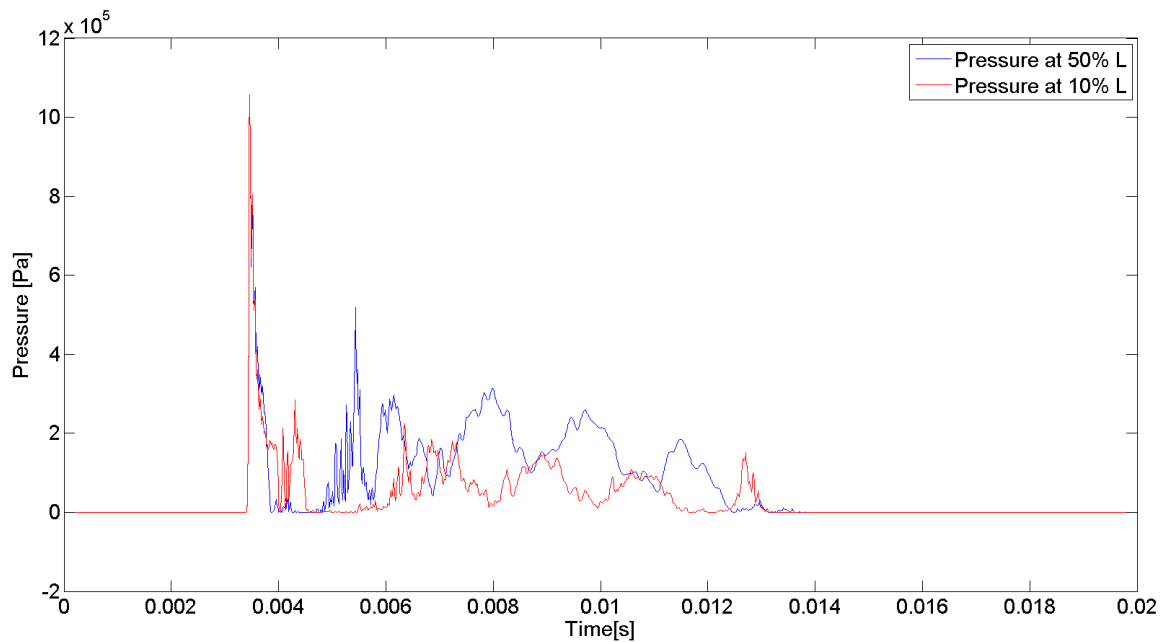


Figure 4.8: Pressure distribution at $L = 50\%$ and $L = 10\%$ for the deformable plate based on the experimental drop test described in (Faltinsen, 2005) with an impact velocity of 2.94 m/s

Overall, the two dimensional drop tests showed promising results. The pressure peaks were in the same range as estimated in the (Faltinsen, 2005). The pressure development for the deformable plate follows a sine-curve with an amplitude of approximately 2 bar, approximately the same as what was seen from analytical and experimental results. For the pressure distribution at the middle and 10% of the plate's length as seen in figure 4.8, one can observe that the pressures varies with lower periods than the overall mean period. In addition, it is to be noted that the pressures at the middle of the plate are larger than the pressures closer to the edge.

Chapter 5

FEM Studies of 2D and 3D Panels

5.1 2D Panels

For the analysis of the 2D panels, the same model as applied in chapter 4 is used where the same two-dimensional plate is dropped into fresh water.

5.1.1 Pressures and Deformations for Drop Velocity of 3[m/s]

The mean pressure over the plate surface is given in figure 5.1. One can observe that the initial mean pressure pulse for the rigid panel is larger than for the deformable panel. The second pressure surge has a duration of approximately 0.09[s], half the analytical wet eigen period for the plate, indicating that the second pressure surge is proportional to the acceleration and may be viewed as an added mass force.

For the deformable column, the impulse is approximately equal to $0.0010p_{max}$ and the impulse is equal to $0.0008p_{max}$ for the rigid panel drop.

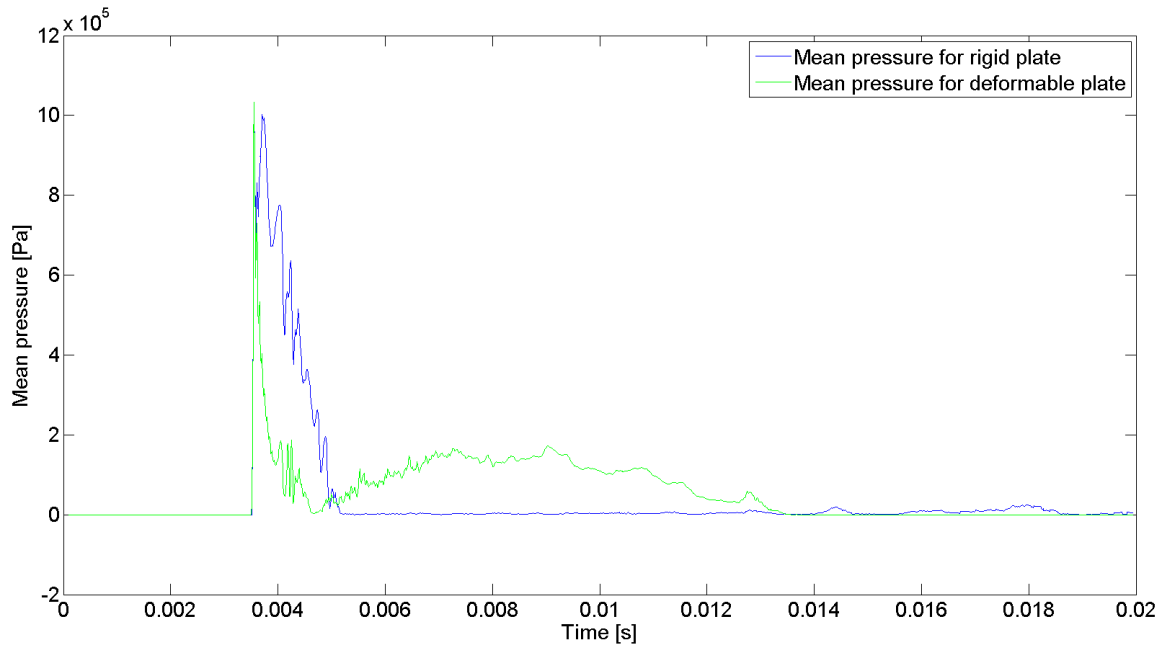


Figure 5.1: Mean pressure development for two-dimensional drop test with an impact velocity of 2.94[m/s]

The duration of the initial loading period for the deformable panel is equal to 0.0015[s] and the panel oscillates with a period of approximately 0.018[s], defining the initial load as within the impulsive domain. The total duration of the loading is equal to 0.011[s], placing it in the dynamic domain as the duration is 61% of the eigen period. Accounting for the modal shape, the total load impulse of the rigid drop test equals $268[N/m^2 s]$ while the total load impulse for the deformable drop test is equal to $343[N/m^2 s]$.

For the initial pressures, the spatial pressure distribution is approximately uniform for the majority of the plate's length. However, the pressure may vary substantially for larger deformations, with the largest pressures at the centre of the plate and the lowest near the end of the plate. Figure 5.2 shows the pressure distribution for the deformable and non-deformable plate immediately after impact. As one would expect, as no deformation has occurred, the pressure is approximately equal for the two cases.

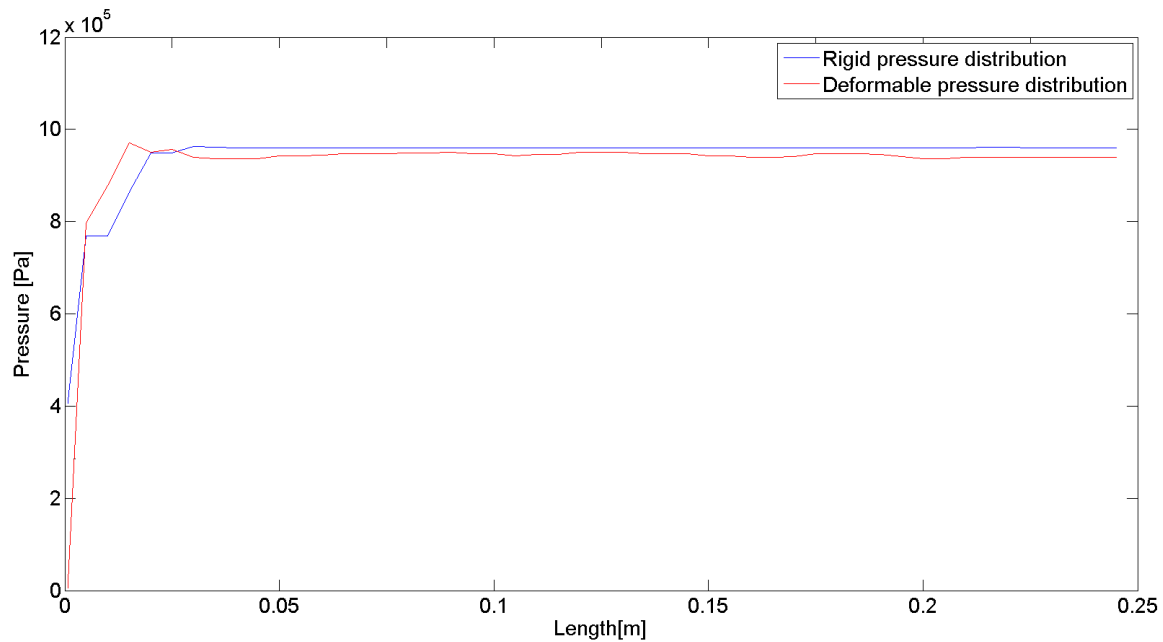


Figure 5.2: Pressure distribution upon water impact for deformable and non-deformable plate

5.1.2 Velocity Dependency

The rig was dropped at velocities of 0.75 m/s , 1.5 m/s and 6 m/s . The results from LS-Dyna show a linear relationship between the mean magnitude of the pressure and the velocity. For single FSI-sensors, short and large pressure peaks are observed, but these may be neglected in load and response analyses due to their short duration. At an impact velocity of 0.75 m/s , the maximum mean pressure equals 2.76 bar. For the drop test with the velocity of 1.5 m/s , the pressure is measured to equal 5.74 bar and for the drop velocity of 6 m/s , the maximum mean pressure is estimated to equal 21 bar. The pressure development may be seen in appendix F in figures F.2 to F.4. One can see that the overall shape is similar for all impact velocities and that it is mainly the magnitude of the pressure which changes for increased drop velocities.

5.1.3 Elasto-Plastic Plate Response

In order to investigate how material and geometric nonlinearities affect the pressure on the panel, nonlinear drop tests are carried out as well. For investigating how nonlinear material properties affect the pressure distribution of the, material model S235 was used. The

nonlinear material properties for S235 steel are given in table 4.6 as seen in section 4.2.2. The mean pressure development for a drop velocity of $9[m/s]$ may be seen in figure 5.3 and the pressure pulse at a drop velocity of $12[m/s]$ may be seen in figure 5.4.

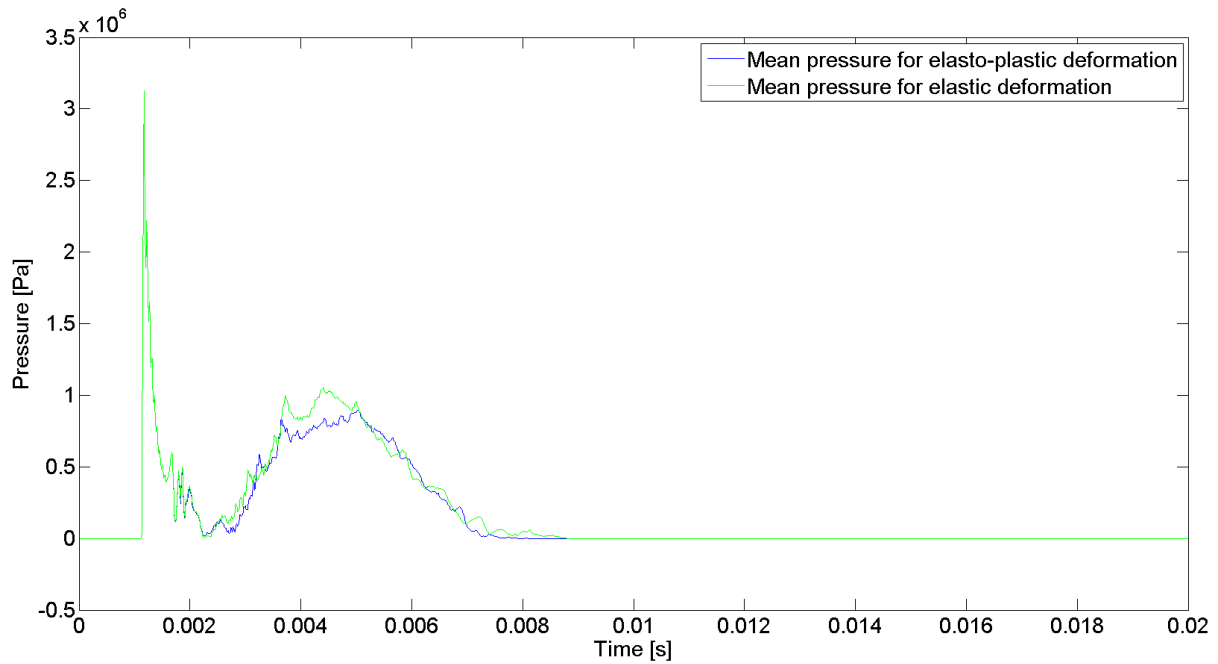


Figure 5.3: Mean pressure time series for a drop velocity of $9[m/s]$

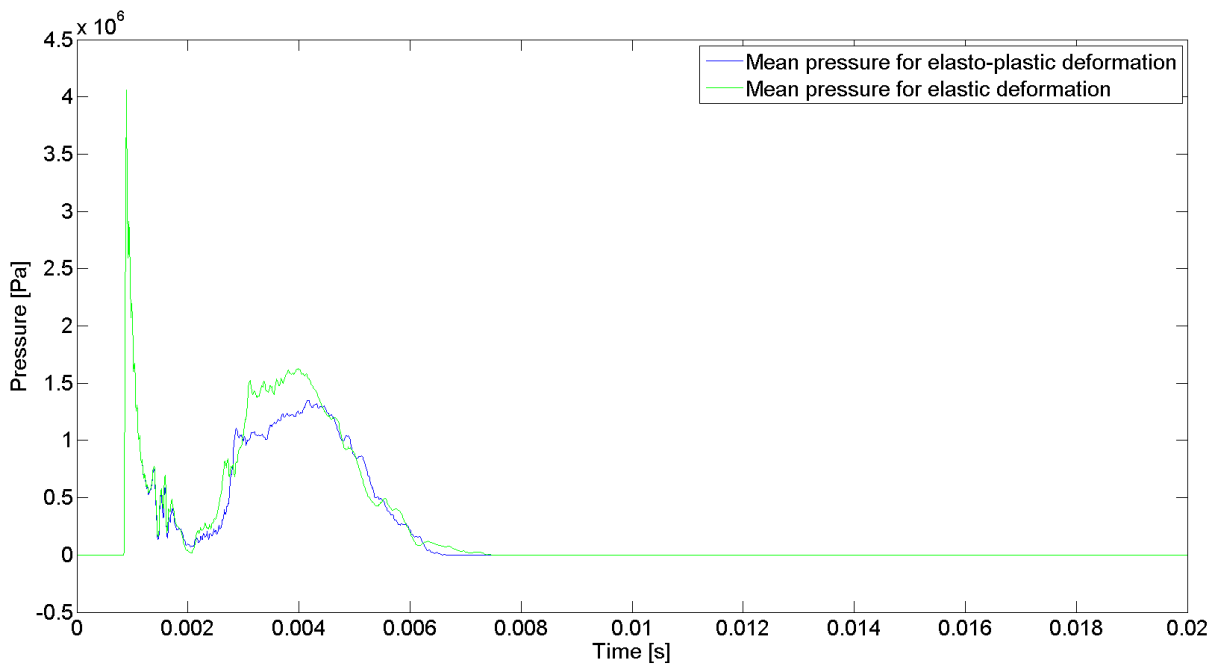


Figure 5.4: Mean pressure time series for a drop velocity of $12[m/s]$

The duration of the second pressure surge is approximately equal for both the elastic and elasto-plastic plate, but noticeably shorter than for lower impact velocities. The peak of the second pressure surge is larger for the elasto-plastic plate response than for the elastic plate. For a drop velocity of $12[m/s]$, the difference between the two pressure time series is greater. This is due to larger pressures leading to larger plastic deformations. The duration of the pressure pulse is shorter than for the previous case and the difference between the second pressure peak is larger.

The deformation of the plate for impact velocities of $9[m/s]$ and $12[m/s]$ may be seen in figure 5.5 and figure 5.6. Both cases show permanent plastic deformation. The permanent deformation causes a new equilibrium position in which the plate is oscillating about. For higher velocities and larger resulting deformations, the deviation for the new equilibrium position increases. The pressure and deformation for a drop velocity of $18[m/s]$ is given in appendix F in figure E.6 and figure E.7 respectively.

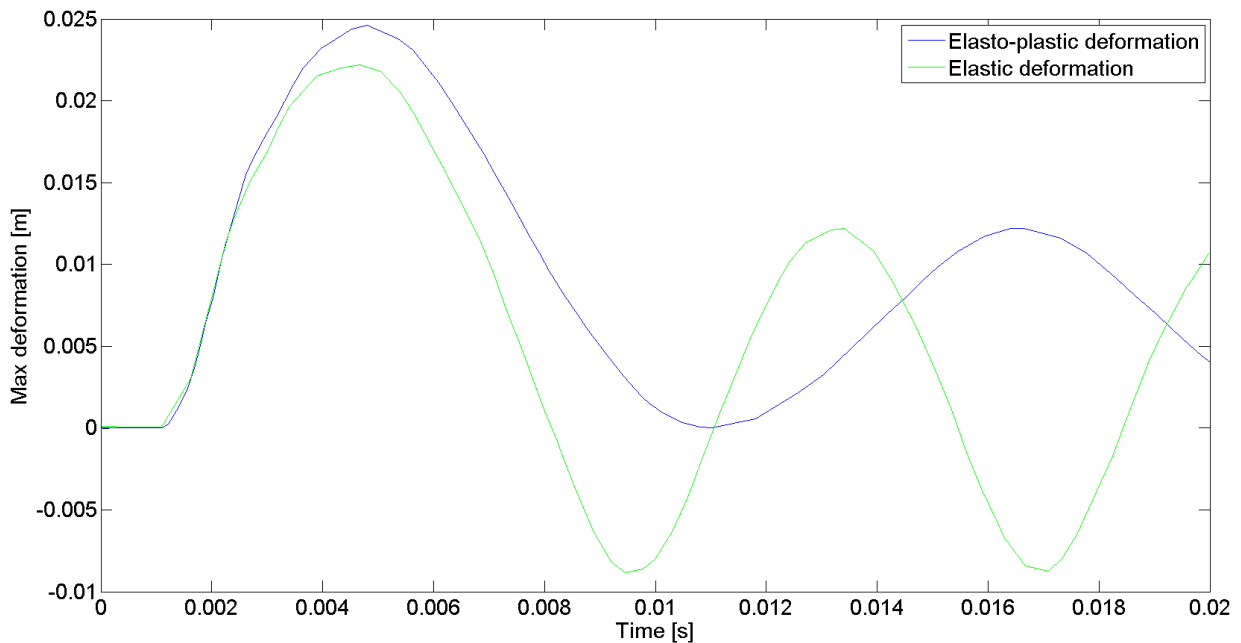


Figure 5.5: Elastic and elasto plastic deflection at a drop velocity of $9[m/s]$

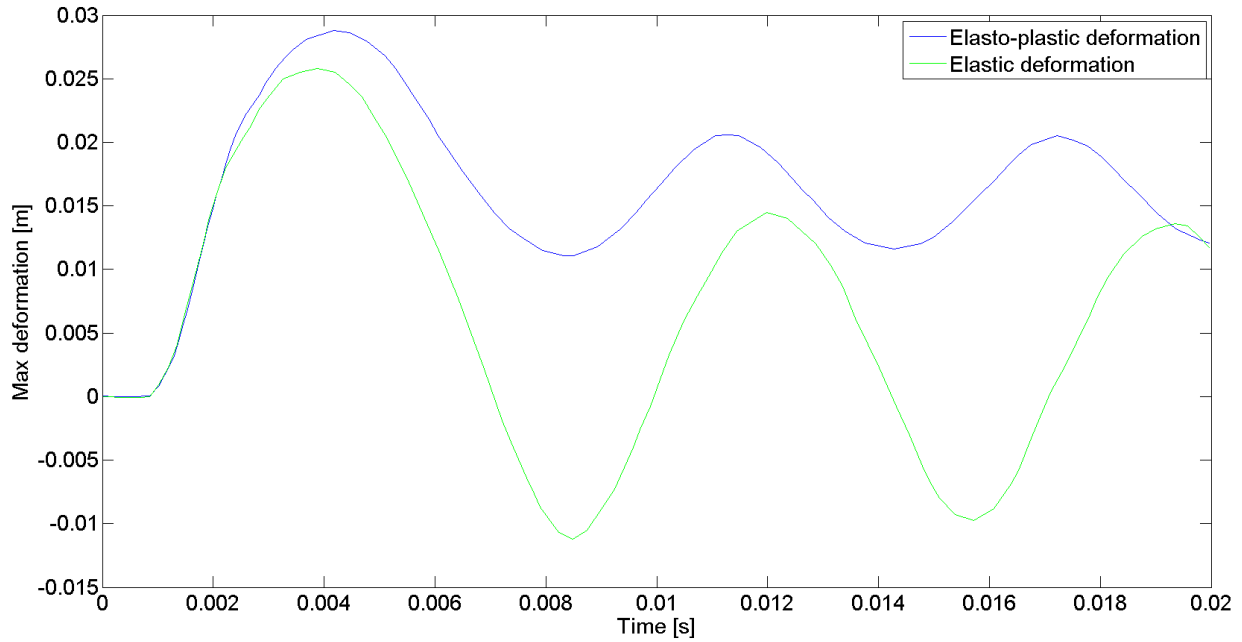


Figure 5.6: Elastic and elasto-plastic deflection at a drop velocity of 12[m/s]

5.1.4 2D Drop Test Summary

The most relevant results from the drop tests are tabulated in table 5.1. Key results to note are that values for low impact velocities have a good agreement with linear analytical theory. For higher impact velocities, nonlinear effects become prominent and linear theory no longer holds. Key trends are lower eigen periods. This may both be due to a reduction in added mass for higher velocities as well as increased membrane forces that are negligible at low impact velocities.

Purely elastic materials are denoted as E while materials with elasto-plastic material behaviour are denoted as E-p. Other key results are that the initial peak is equal for both elastic and elasto-plastic behaviour while the second pressure peak is lower for elasto-plastic behaviour with larger discrepancies for higher velocities. The estimate of the generalised added mass $\overline{M}_a[kg]$ is calculated according to equation 5.1 which is increasingly inaccurate for increased velocities.

$$\overline{M}_a = \overline{M} \left(\left(\frac{T_{wet}}{T_{dry}} \right)^2 - 1 \right) \quad (5.1)$$

Table 5.1: Key results from drop tests based on the test rig in (Faltinsen, 2005)

$v[m/s]$	Material	$w_{max}[mm]$	$p_{peak}^{(1)}[bar]$	$p_{peak}^{(2)}[bar]$	$T_{wet}[s]$	$T_{dry}[s]$	$\overline{M}_a[kg]$
0.75	E	2.87	2.8	0.5	0.018	0.009	46.5
1.5	E	4.8	5.5	1	0.018	0.008	63.0
2.94	E	8.1	10.1	1.8	0.018	0.008	63.0
6	E	17.6	21	5	0.016	0.008	46.5
9	E	22.3	32	10.1	0.014	0.007	46.5
9	E-p	24.7	32	9	0.014	0.006	68.9
12	E	26	40	17	0.012	0.007	30.1
12	E-p	29	40	14	0.012	0.006	46.5
18	E	31.3	60	32	0.010	0.006	27.6
18	E-p	39.5	60	20	0.010	0.006	27.6

5.2 3D Panels Exposed to Slamming Loads

5.2.1 Modelling of 3D Panels

The stiffened panel is modelled in correspondence with DNV GL's offshore technical guidelines in (GL, 2016b) where a 3[m] by 3[m] meter plate is to be evaluated when loads and responses due to wave impacts are considered. The stiffened plate is initially designed according to a typical stiffened panel structure for semi-submersibles. The section modulus for the stiffener and plate was checked against the criteria given in (Veritas, 2011a). The thickness of the plate is to be estimated from equation 5.2 while the section modulus of the stiffener is to be calculated according to equation 5.3 and is not to be taken as less than $15cm^3$. The plate is viewed as a primary structural member, and is checked against the thickness criterion in 5.4 where t_0 is taken as 7[mm]. The steel type is taken as S355 steel with a yield strength of 355[MPa].

$$t = \frac{15.8k_a s \sqrt{p_d}}{\sqrt{\sigma_{pd1} k_{pp}}} [mm] \quad (5.2)$$

$$Z_S = \frac{l^2 s p_d}{k_m \sigma_{pd2} k_{ps}} 10^6 [mm^3] \quad (5.3)$$

$$t > \frac{14.3 t_0}{\sqrt{f_{yd}}} \quad (5.4)$$

Calculations were performed with design pressures given in terms of simplified wave loads from (DNV, 2014b). The fixation parameter k_p is chosen conservatively, i.e., the boundary is approximately simply supported. The material factor for steel is taken as 1.15.

The analysis of the stiffened is executed using FEM in LS-Dyna where the entire panel is modelled. The design pressure given in (Veritas, 2011a) is gradually loaded normal to the panel. A simple approach for the stiffeners were carried out where flanges were added to the webs so that the stiffeners' moment of inertia matched that of the selected bulb flats. The resulting Von Mises stresses were then inserted into equation 5.2 and 5.3.

The stiffened plate has a length and width of 3 meters. Stiffener spacing was chosen to be equal to 500 [mm] and the stiffener profile was chosen as HP180x10 with its parameters listed in 5.2. Plate thickness was chosen to 8 [mm], fulfilling the requirement given by equation 5.4 which yields a minimum plate thickness of 7.8[mm]. The plate will act as a bottom flange, and when viewed as a two dimensional beam, the cross section can be considered equal to the cross section in figure 5.7. With 5 stiffeners in the deformable section and a steel density of 7850[kg/m^3], the total mass of the stiffened panel is equal to 3210[kg].

Table 5.2: Properties of the chosen bulb flat

$H[mm]$	$W[mm]$	$C[mm]$	$R[mm]$	$A[cm^2]$	$z_g[cm]$	$I[cm^4]$	$Z[cm^3]$
180	10	25	7	22.46	10.6	717	67.8

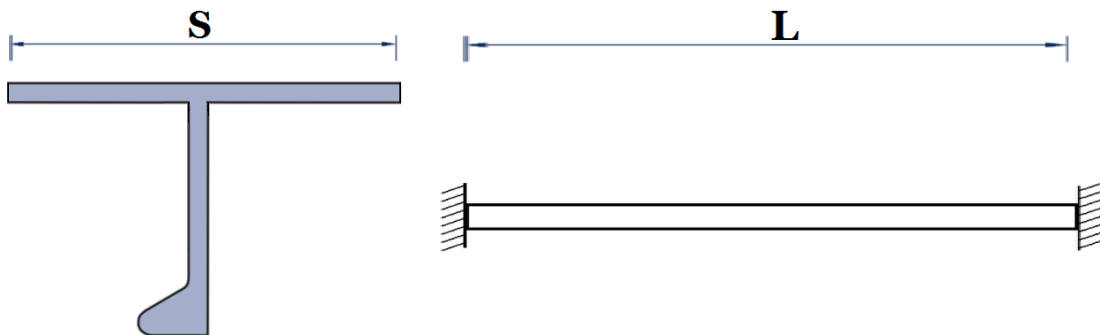


Figure 5.7: Cross section of the beam model of the stiffened plate

The full three-dimensional finite element model of the stiffened plate may be viewed in

figure 5.8 with the properties of the approximation given in table 5.3. For a stiffened plate, the boundary conditions are somewhere between clamped and simply supported. By fixing all of the sides for vertical translation, some rotational stiffness is added to all of the edges. Moreover, as the wave is assumed to be hitting the surrounding plates as well, symmetry could be justified about the girders, leading to a deformation angle of approximately 0° . Approximately clamped boundary conditions could thus be justified and are applied at the edges in the x-direction of the structure. Pinned boundary conditions are applied for the edges in the y-direction.

Table 5.3: Approximate bulb flat stiffener parameters

$H_{web}[mm]$	$t_{web}[mm]$	$W_{flange}[mm]$	$t_{flange}[mm]$
165	10	27.4	30

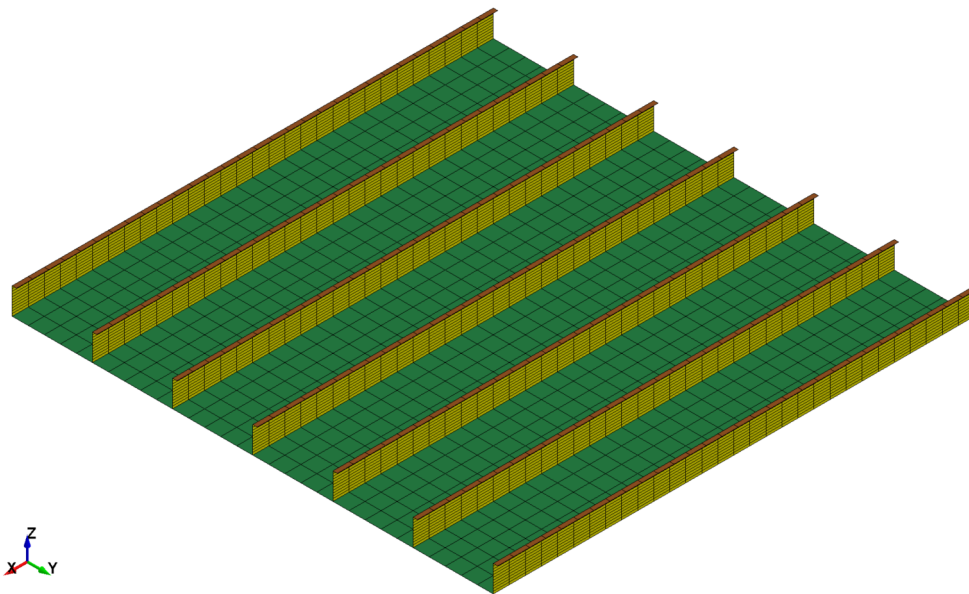


Figure 5.8: Finite element model of the stiffened plate

5.2.2 Calculating Added Mass

When simulating drop tests of deformable plates, the added mass is assumed to be included in the loading conditions as pressures proportional to the acceleration can be observed. When loading a comparable plate with the same pressure time history, the added mass should hence be included in the calculations.

Added mass is included by increasing the density by the same factor as the added mass

contributes to the total dynamic mass of the system. The mass of the 3[m] by 3[m] plate is found to equal 565[kg]. The same factor used to account for plate deformation as opposed to a full oscillating plate of 0.64 as given in (Faltinsen, 2005) is used. The added mass for a quadratic plate from (Meyerhoff, 1970) and the assumed relative effective length of 0.64 yields an added mass of 8070[kg] where the calculations may be viewed in table 5.4. Thus, the added mass is 14.28 times the actual mass of the plate.

The total mass of the stiffened plate is equal to 830[kg]. The added mass of 8070[kg] is thus approximately 10 times the mass of the stiffened plate.

Table 5.4: Added mass calculation for 3D stiffened panel

$B[m]$	$L[m]$	χ	J	$\rho[kg/m^3]$	$M'_a[kg]$	f	$M_a[kg]$
1.5	1.5	1	0.579	1025	12585	0.64	8070

5.2.3 Elemental and Material Properties of Model

The elemental properties of the plate subjected to load pulses are given in table 5.5. The subscript a denotes that the material uses the material density that accounts for added mass.

Table 5.5: Elemental properties of stiffened panel subjected to load pulse

Part	$B[m]$	$L[m]$	n_B	n_L	$t[mm]$	Tested Materials
Plate	3	3	30	30	8	1a,2a,3a
Web	0.165	3	11	30	10	1,2,3
Flange	0.0274	3	1	30	30	1,2,3

The linear material properties used in the analysis are listed in table 5.6 with the nonlinear properties listed in table 5.7. Also here, the subscript a denotes the material density accounting for added mass.

Table 5.6: Linear material properties used for stiffened 3[m] by 3[m] panel

Material	Material type	$\rho_a[kg/m^3]$	$\rho[kg/m^3]$	$E[GPa]$	$\nu[]$
1	Elastic	1.12E+05	7850	210	0.3
2,3	Elasto-plastic	1.12E+05	7850	210	0.3

Table 5.7: Nonlinear material properties used for stiffened 3[m] by 3[m] panel

Material	$\sigma_1 [MPa]$	$\epsilon_1 []$	$\sigma_2 [MPa]$	$\epsilon_2 []$	$\sigma_3 [MPa]$	$\epsilon_3 []$	$C []$	P
2	357	0.0023	366.1	0.018	541.6	0.137	0	0
3	357	0.0023	366.1	0.018	541.6	0.137	4000	5

5.2.4 Loads Based on RP-C205

For the simple force estimate, the load coefficient C_h is taken as 2.5, both for direct and diagonal hits as a conservative estimate as opposed to 1.9 which is to used for a diagonal hit in the RP. For the added mass calculation, the vertical wetted length $c(t)$ is approximated assuming the wave is about to break. Since a wave breaks when the crest angle exceeds 120° , an approximation of the wetted height could be given in terms of an incoming wave angle of 30° , wave celerity, air gap and an assumption that the geometry of the crest of the wave is similar to that of a triangle. The drag coefficient C_D for a thin plate is given as 1.9 in (DNV, 2014b).

Reference is given to figure 5.9 where the geometric properties of a breaking non-wave are given. The total loading duration is calculated as in equation 5.5. The wetted length c is calculated according to equation 5.6 where l is the height of the plate.

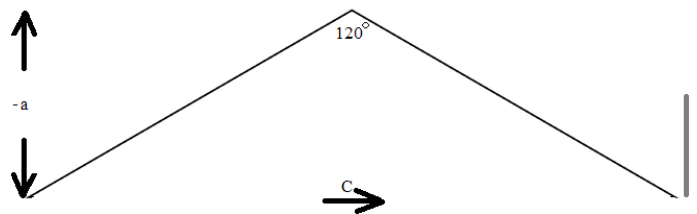


Figure 5.9: Stokes wave approximation used for estimated wetted length

$$t_{load} = \frac{-a \cdot 2 \tan(60^\circ)}{C} \quad (5.5)$$

$$c = \frac{Ct}{\tan(30^\circ)} \leq l \quad (5.6)$$

Thus, the added mass and change in added mass may be calculated according to equation 5.7 and equation 5.8 respectively.

$$M_{a,z} = \frac{2}{\pi} \rho \left(\frac{Ct}{\tan(30^\circ)} \right)^2 \quad (5.7)$$

$$\frac{dM_{a,z}}{dt} = \frac{2}{\pi} \rho \frac{2C^2 t}{\tan^2(30^\circ)} \quad (5.8)$$

The resulting loads may be viewed in table 5.8 based on the velocity estimates given in table 3.6 and 3.7. $p_{Wheeler}$, p_{SOK} and p_{mean} are pressures based on velocity estimates by Wheeler stretching, the second order kinematics model and the mean of the two methods respectively. The loads are static and are applied gradually in LS-Dyna to reduce dynamic effects.

Table 5.8: Design loads based on recommended practices

Sea state	C_S	$p_{Wheeler}[kPa]$	$p_{SOK}[kPa]$	$p_{mean}[kPa]$
6	1.9	24.61	83.35	51.04
15	1.9	48.75	121.95	62.72

This approximation is for a constant pressure acting on the plate with dynamic effects are neglected. The load model assuming the wave is about to break for sea state 6 is given in table 5.9 and the resulting loads for sea state 15 are given in table 5.10. From the tables, it is apparent that sea state 15 is more critical than sea state 6, given the RP-loading model.

Table 5.9: Pressure time series for sea state 6

$c[m]$	$t[s]$	$M_{a,z}[kg/m]$	$\frac{dM_{a,z}}{dt}[kg/ms]$	$p[kPa]$
1.08	0.20	762.27	7681.79	155.90
2.16	0.40	3049.09	15363.57	162.68
3.00	0.60	5872.82	0.00	102.19
3.00	0.79	5872.82	0.00	102.19
3.00	0.99	5872.82	0.00	102.19
3.00	1.19	5872.82	0.00	102.19
3.00	1.39	5872.82	0.00	102.19
3.00	1.59	5872.82	0.00	102.19
2.16	1.79	3049.09	-15363.57	31.17
1.08	1.98	762.27	-7681.79	24.38

Table 5.10: Pressure time series for sea state 15

$c[m]$	$t[s]$	$M_{a,z}[kg/m]$	$\frac{dM_{a,z}}{dt}[kg/ms]$	$p[kPa]$
1.15	0.14	862.41	12369.17	248.12
2.30	0.28	3449.64	24738.34	253.89
3.00	0.42	5872.82	0.00	137.00
3.00	0.56	5872.82	0.00	137.00
3.00	0.70	5872.82	0.00	137.00
3.00	0.84	5872.82	0.00	137.00
3.00	0.98	5872.82	0.00	137.00
3.00	1.12	5872.82	0.00	137.00
2.30	1.26	3449.64	-24738.34	13.08
1.15	1.39	862.41	-12369.17	7.31

5.2.5 Response Based on RP-C205

The maximum displacement of the plate was found at the bottom of the middle stiffener to equal 3.2[mm] with the plot of maximum deflection versus time may be seen in figure 5.10.

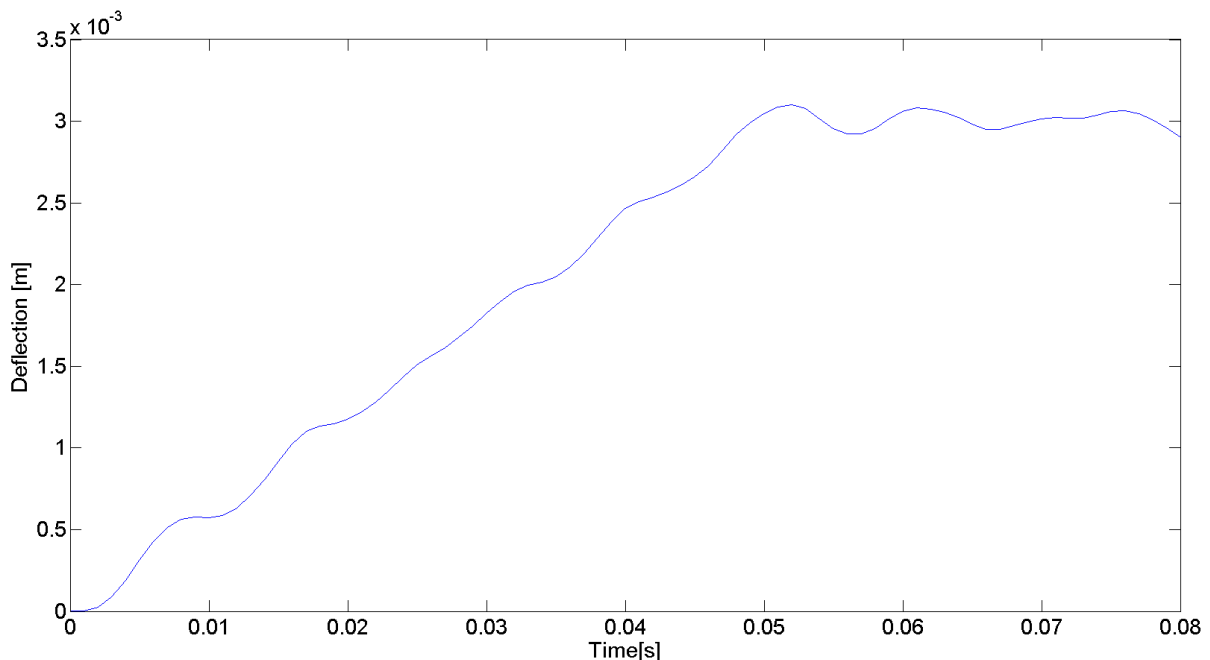


Figure 5.10: Deflection of the stiffened clamped plate subjected to the rigid design load pulse from FEA

The Von Mises stress from the FEA in LS-Dyna are given in figure 5.11. The maximum Von Mises stress in the stiffener is equal to $217.4[MPa]$ and the maximum Von Mises stress in the plate is equal to $78.9[MPa]$.

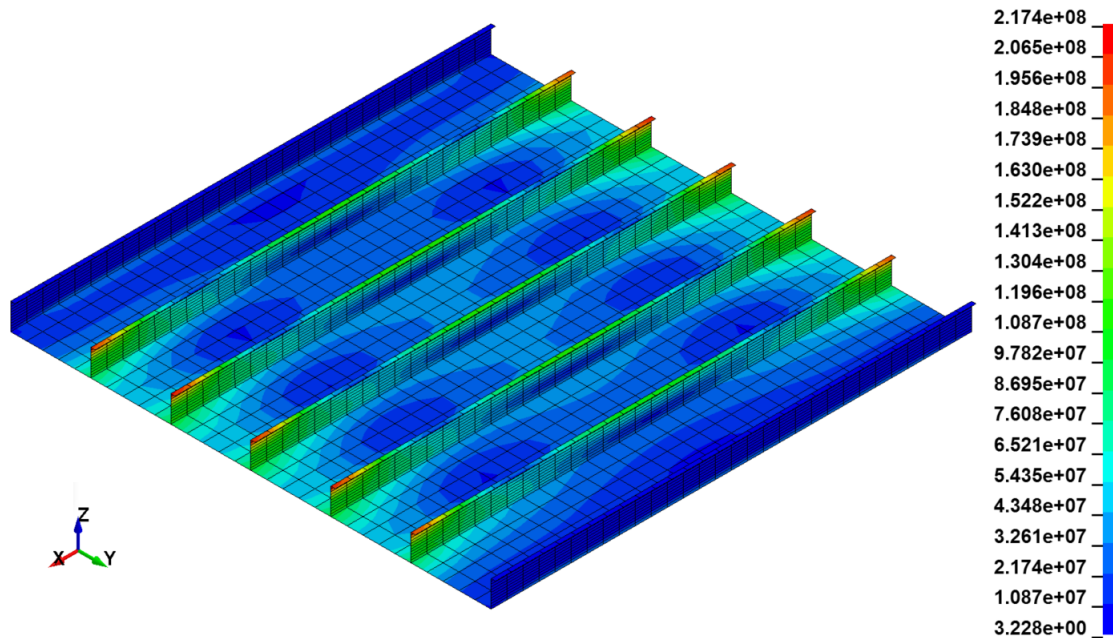


Figure 5.11: Maximum Von Mises stress from maximum static design wave load

The stresses in the flange are checked against the criteria for thickness and section modulus in equation 5.2 and 5.3 with the results tabulated in table 5.11 and table 5.12. The selected plate thickness satisfy the minimum requirement. However, the stiffener does not satisfies the minimum requirements given the most conservative wave loading condition. However, this is for the ULS-condition loading with the most conservative water particle velocity and we are interested in investigating large, nonlinear deformations of the structure. The plate and stiffeners can thus be viewed as an accurate representation of a stiffened plate even though it is undersized for the environmental conditions.

Table 5.11: Values for thickness calculations by equation 5.2 with design stresses given by (DNV, 2014b)

$t[mm]$	$k_a[]$	$p_d[kPa]$	$\sigma_{pd}[MPa]$	$k_{pp}[]$
7.02	1.00	122.00	308.70	0.50

Table 5.12: Values for section modulus calculations by equation 5.3 with design stresses given by (DNV, 2014b)

$Z_s[cm^3]$	$p_d[kPa]$	k_m	$\sigma_{pd}[MPa]$	k_{ps}
554.90	122.00	12	91.70	0.9

For the dynamic loading condition, the maximum deflection is located at the middle of the plate and is equal to 6.5[mm]. The maximum deflection versus time based on this loading condition be viewed in figure 5.12.

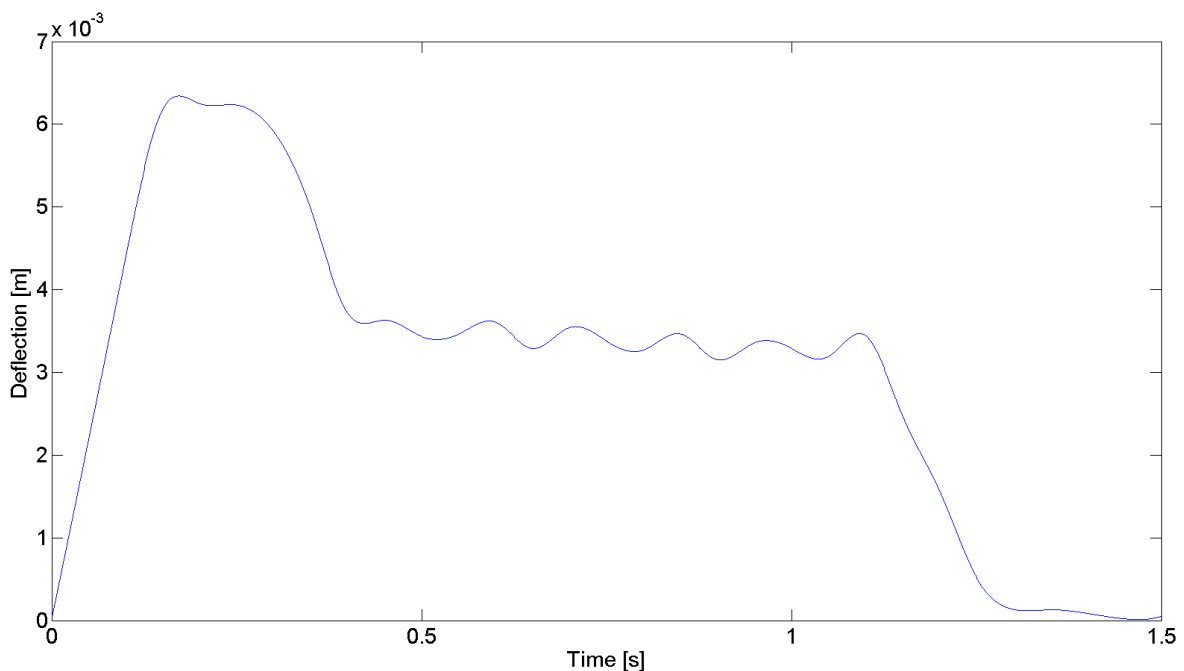


Figure 5.12: Maximum deflection measured for the dynamic loading condition based on the RPC

5.2.6 Loads Based on OTG-14

The same relative upwelling found in section 3.2 is used in the loading model. In (GL, 2016b), the largest pressures occur for relative upwelling values approximately equal to 0.5. As the loaded plates are positioned high up on the platform, with relative upwelling values close to 1, the load increases for decreasing relative upwelling values. Hence, the positions and sea states with the lowest relative upwelling are considered to be the most critical. The pressures are obtained graphically from the relative upwelling in figure 2.8 in section 2.2.6. It is assumed that the peak pressure occurs after 0.012 [s]. The peak pressure from the

offshore technical guidelines for sea state 6 and sea state 15 are given in table 5.13.

Table 5.13: Peak pressure based on OTG 14

Sea state	$\chi[m]$	Relative upwelling	$p_{max}[kPa]$
6	15.81	0.79	1150
15	16.23	0.77	1200

The lowest sustained pressure is found to equal 14% of the peak pressure, the second is equal to 23 % of the peak pressure and the third is equal to 61 % of the maximum load. The pressure-time series of the load for sea state 6 is plotted in appendix D with the pressure-time series for sea state 6 given in figure D.1. The pressure time series for sea state 15 is given in figure 5.13. As the pressure peak is larger for sea state 15 than for sea state 6, this is the sea state which is evaluated in further analysis. The total pressure impulse in this sea state is equal to 49.2[kPAs].

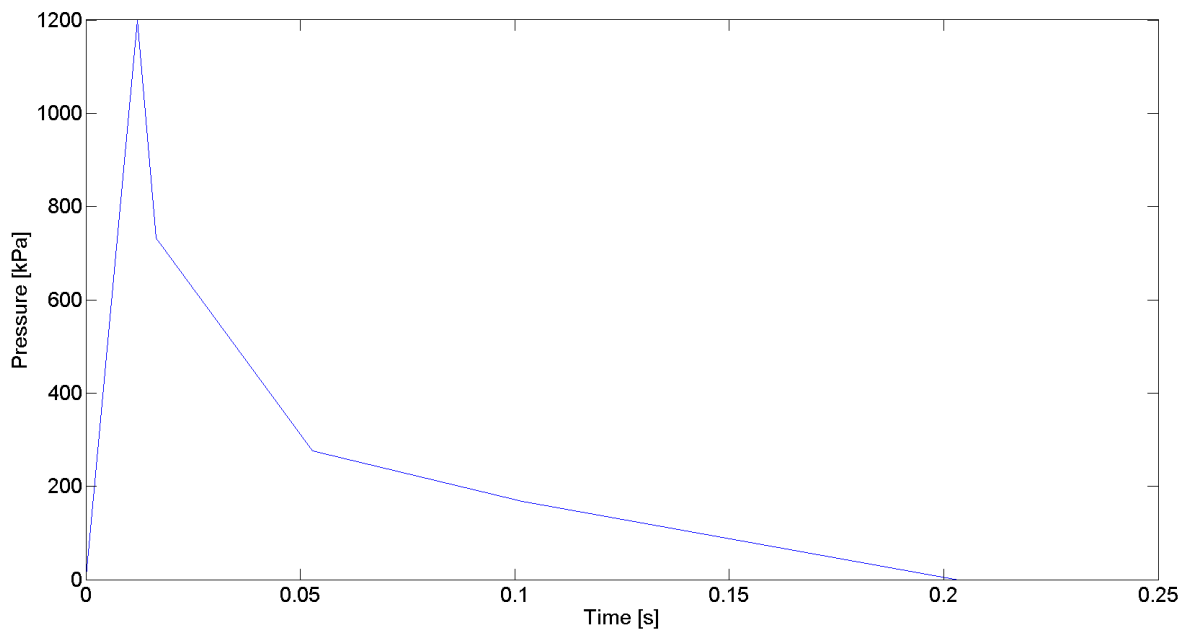


Figure 5.13: Pressure development based on OTG for sea state 15

5.2.7 Response Based on OTG-14

The loading condition based on the offshore technical guidance are characterised by a short rise time, a large pressure peak and a relatively longer decay time. The loading based on the OTG yielded much larger deformations than what was seen from the RP loading condition. For pure elastic response, the maximum deflection from the FEA is measured as 40[mm].

The maximum deflection is found to equal 216[mm] for pure elasto-plastic response. When strain rate hardening is considered, the maximum deflection is estimated to equal 175[mm]. It can hence be seen that strain rate hardening has a large influence on the overall response of the structure. The model with strain rate hardening is considered to be the most realistic representation of the material model and the stresses are evaluated for this material model. The stress distribution may be seen in figure 5.15.

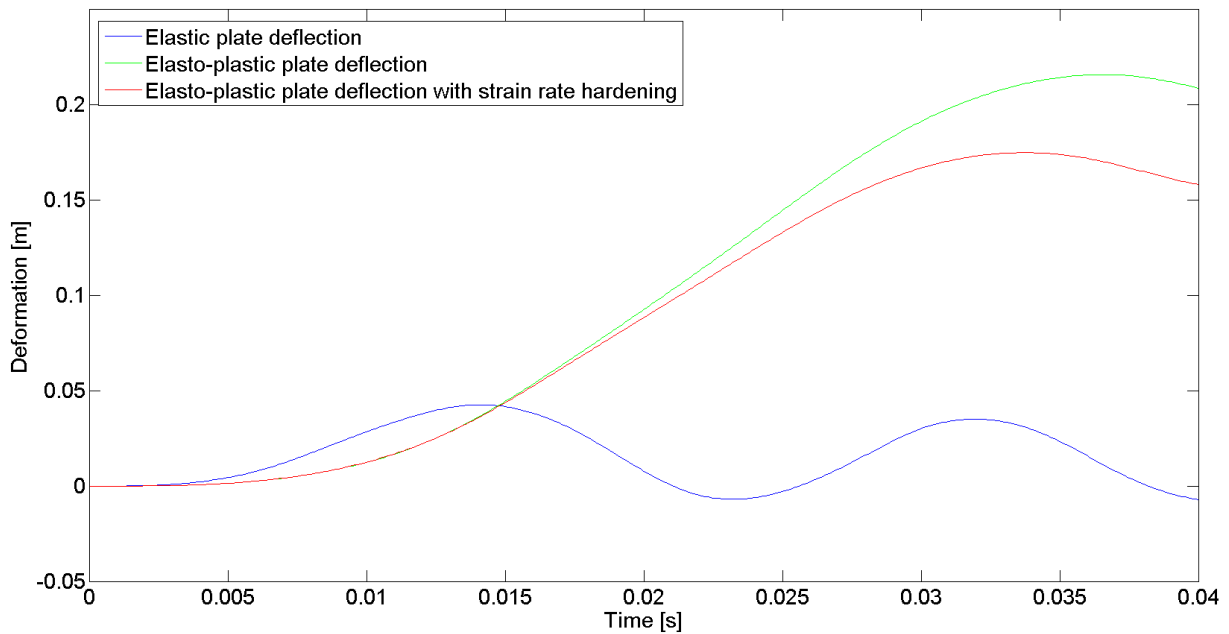


Figure 5.14: Maximum deflection measured for the dynamic loading condition based on the OTG

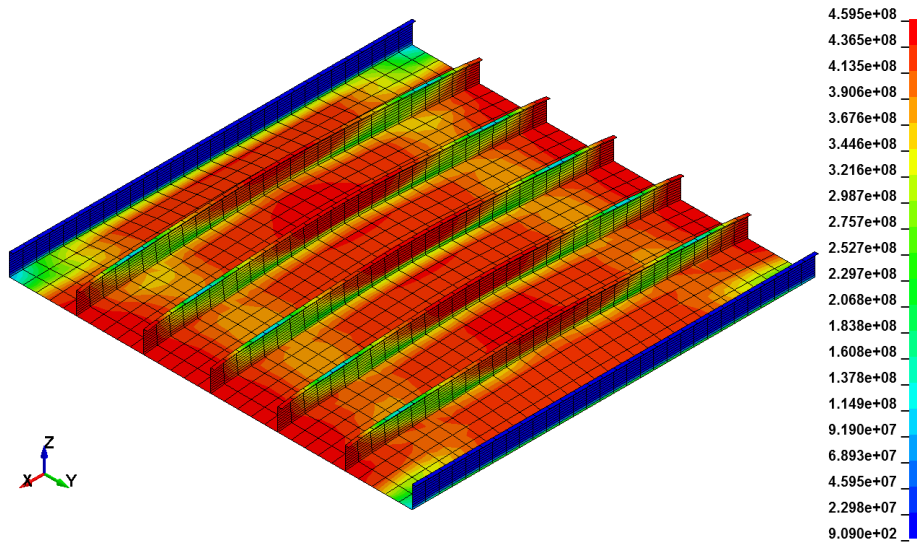


Figure 5.15: Von Mises stress at maximum deflection with OTG loading

When the deflection has reached its maximum of 175[mm], the maximum Von Mises stress is located in the plate and equal to 459.5[MPa]. This is beyond yield, but less than the ultimate strength of the material of 540[MPa].

5.3 3D Panel Drop Tests

5.3.1 Water and Air Modelling

For the drop tests applied in 3D, the drop tests are considered to be conducted in salt water with the material properties as given in table 5.14.

Table 5.14: Fluid properties applied in LS-Dyna

	Material type	Density ρ [kg/m ³]	Viscosity μ [Pa·s]	Pressure cutoff [Pa]
Air	Null	1.23	1.00E-03	-1.00E+11
Salt water	Null	1025	1.67E-03	0

The plate, air and water were modelled with the same EOS Gruneisen properties as for the two-dimensional drop tests with the properties given in table 5.15.

Table 5.15: EOS applied for water, air and steel

	C	S1	S2	S3	Gamma0	A	E0	V0
Water	1480	2.56	-1.986	0.227	0.5	0	0	0
Air	343.7	0	0	0	1.4	0	0	0
Steel	4570	1.5	0	0	1.93	0	0	0

5.3.2 FEM Model of 3D Panel

As was the case for the 2D tests, the first 3D tests involved recreating the parameters for the drop test described in (Faltinsen, 2005). The model was developed using the same material parameters as described in section 4.2.1. Each element on the Lagrangian panel was fitted with nodal force sensors. As drop tests carried out in 3D are computationally demanding, the three dimensional drop tests was carried out using NTNU's super computer "Vilje".

The same plate structure as seen in figure 5.8 was modified to conduct a full scale model test. As was the case for the two-dimensional drop tests, the boundary is represented by shell elements connected to a heavy rigid plate to ensure a small reduction in the plate's overall velocity, as would be realistic for a plate on a semi-submersible experiencing loads due to wave impact. The boundary shell elements were modelled to be 8[mm] thick and the modulus of elasticity is the same as for standard steel 210[GPa]. The configuration may be viewed in figure 5.16 and is modelled to match the parameters of the stiffened plate to be loaded by pressure pulses as described in section 5.2.1.

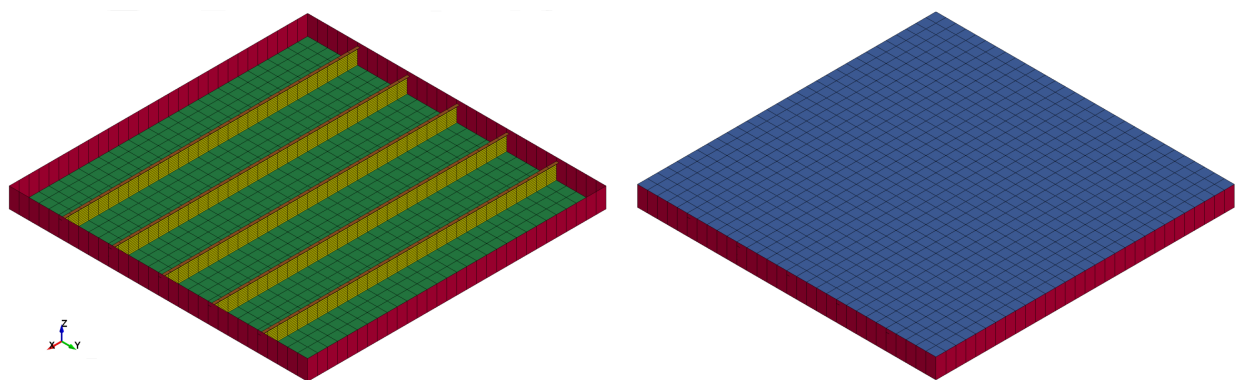


Figure 5.16: Finite element model of the stiffened plate drop rig

The elemental properties are given in table 5.16. Material 1 is purely elastic while material

2 is an elasto-plastic material while strain rate hardening is included in material 3.

Table 5.16: Elemental properties for the 3D dropped panel rig

Part	$B[m]$	$L[m]$	n_B	n_L	$t[mm]$	Tested Materials
Plate	3	3	30	30	8	1, 2, 3, 4
Web	0.165	3	11	30	10	1, 2, 3
Flange	0.0274	3	1	30	30	1, 2, 3
Boundary plate	0.2	3	1	30	8	1
Heavy plate	3	3	30	30	8	6

The linear material properties applied are given in table 5.17 and the nonlinear material properties are listed in table 5.18.

Table 5.17: Linear material properties applied in the 3D panel drop rig

Material	Material type	$\rho[kg/m^3]$	$E[GPa]$	$\nu[]$
1	Elastic	7850	210	0.3
2,3	Elasto-plastic	7850	210	0.3
4	Rigid	7850	210	0.3
5	Rigid	9.62E+05	210	0.3

Table 5.18: Nonlinear material properties applied in the 3D panel drop rig

Material	$\sigma_1[MPa]$	$\epsilon_1[]$	$\sigma_2[MPa]$	$\epsilon_2[]$	$\sigma_3[MPa]$	$\epsilon_3[]$	$C[]$	P
2	357	0.0023	366.1	0.018	541.6	0.137	0	0
3	357	0.0023	366.1	0.018	541.6	0.137	4000	5

5.3.3 Pressure Development and Relative Volume for 3D Drop Tests

As with the two dimensional case, the drop tests were also conducted for both a deformable and non-deformable plate to compare the resulting pressures. The pressure development may be seen in figure 5.17.

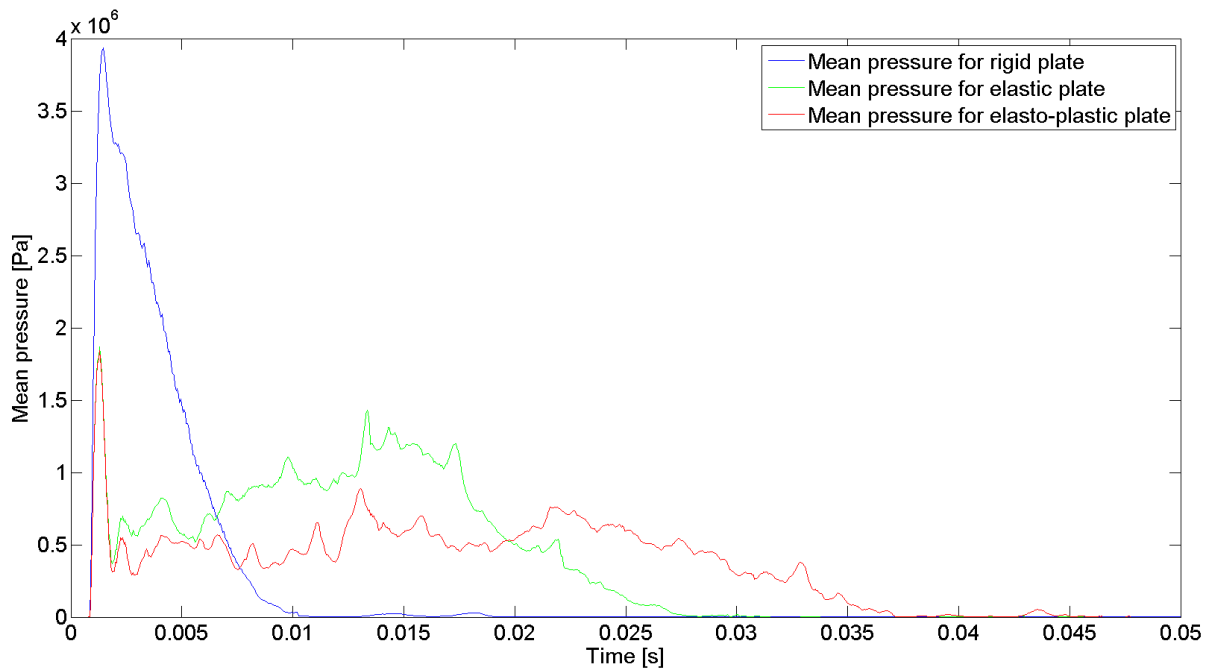


Figure 5.17: Pressure time history for 3D drop test into sea water at the design wave condition

When dropped at the velocity given from the SOKM, the peak pressure for the rigid panel was estimated to be approximately identical to the 2D drop test's peak pressure at the same velocity and water properties, i.e. $3.9[MPa]$. However, the duration of the sustained load was longer, approximately $0.009[s]$ compared to $0.002[s]$ for the rigid drop test. For the deformable plate, the mean peak pressure was estimated to equal $1.95[MPa]$, half the duration of the "rigid pressure pulse". The elasto-plastic response of the plate is large and one can observe an increased eigen period more clearly than for the two dimensional case. As was the case i for the two-dimensional response, the second pressure peak is lower for the elasto-plastic deformation than for the elastic deformation.

The duration for the full scale drop test is approximately 4 times the duration of the 2D drop test. The increased duration may be due both the increased surface area, different boundary conditions or a combination of the two. The duration of the measured pressures on the elastic and elasto-plastic plate is approximately half the plate's natural period. Hence, the impulse may not be used to calculate the response by the simplified method as the relative duration is larger than 30%. However, it could still be of interest in terms of evaluating conservation of momentum. The pressure impulse for the rigid plate is equal to $13[kPas]$, for the elastic plate, the pressure impulse is equal to $19[kPas]$ and for the elasto-plastic plate, it is equal to $22[kPas]$. Hence, the load impulses are lower for the drop

tests than the pressures from the OTG, where the pressure impulse was equal to $49.2[kPas]$. By measuring the duration of the pressure during the deformation phase of the plates in figure 5.17, estimates of the plates' natural period can be made. The period of the elastic plate is approximately equal to $0.05[s]$ while the natural period for the elasto-plastic plate is approximately equal to $0.07[s]$.

The mean spatial pressure distribution is seen to be greater near the middle of the plate than by the edges causing a greater moment than for a uniform pressure. When evaluating half the plate's length, it is seen that the resultant force acts at 30% of the plate's length. The mean spatial distribution of the pressure pulse may be seen in figure 5.18. From the moment analysis, an equivalent load accounting for the non-uniform pressure distribution could be obtained by applying a pressure between 10% and 90% of the plate's length while increasing the load by a factor equivalent of the reduced area, equal to 1.2^2 .

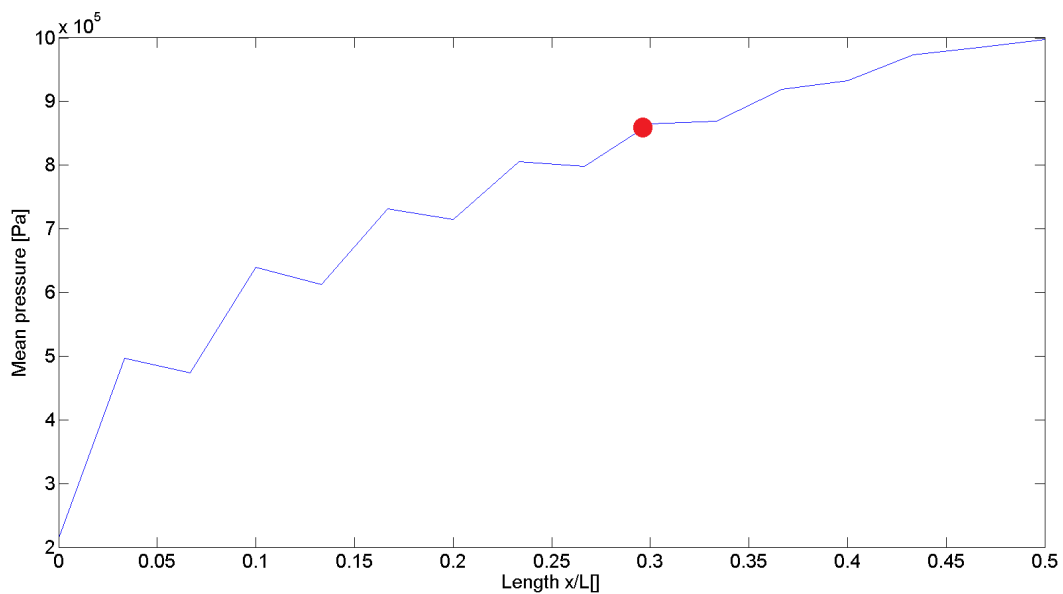


Figure 5.18: Mean spatial pressure distribution seen at the middle of 3D rigid panel

The relative volume fraction of the fluid elements is a good indication on how the plate deforms. This may be seen in figure 5.19.

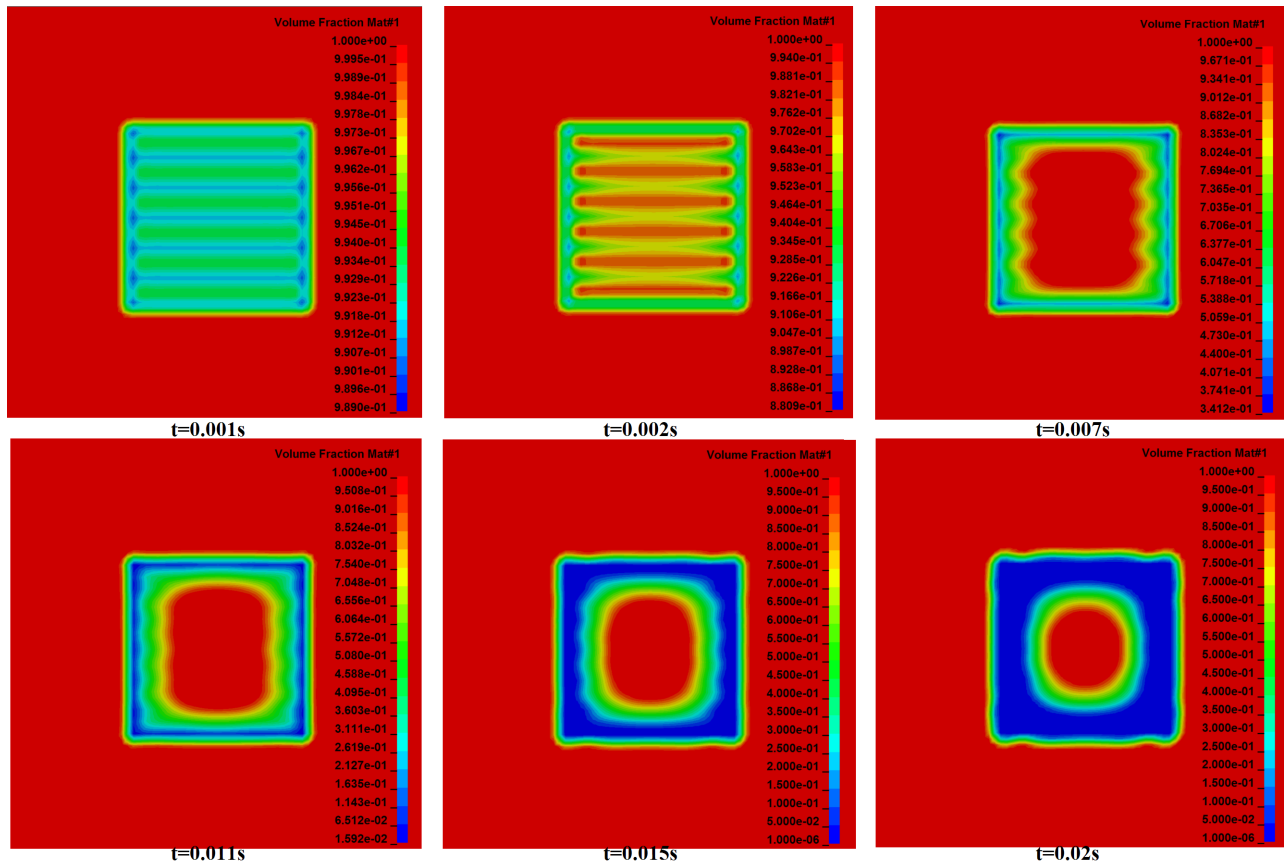


Figure 5.19: Relative volume fraction of the fluid upon impact

The deformable section of the plate deforms as the velocity relative to the deforming section and boundary equals the drop velocity. Upon impact, larger deformation may be seen between the stiffeners than the rest of the structure. One could observe that the deformation approaches the final deformation shape with a sine function in both the x- and y-direction. The indicated deflection shape is of interest as it indicates that the assumption of a constant deflection shape is inaccurate and may lead to inaccurate results when applied in an SDOF analysis.

5.4 Drop Test Responses

5.4.1 Response Based on Hydro-Elasto-Plastic Behaviour

The maximum deflection for the elastic material properties is equal to $140[mm]$. For the elasto-plastic response with strain rate hardening, the maximum deflection was equal to

210[mm]. With strain rate hardening, the maximum estimated deflection is equal to 250[mm]. The deformations may be seen in figure 5.20.

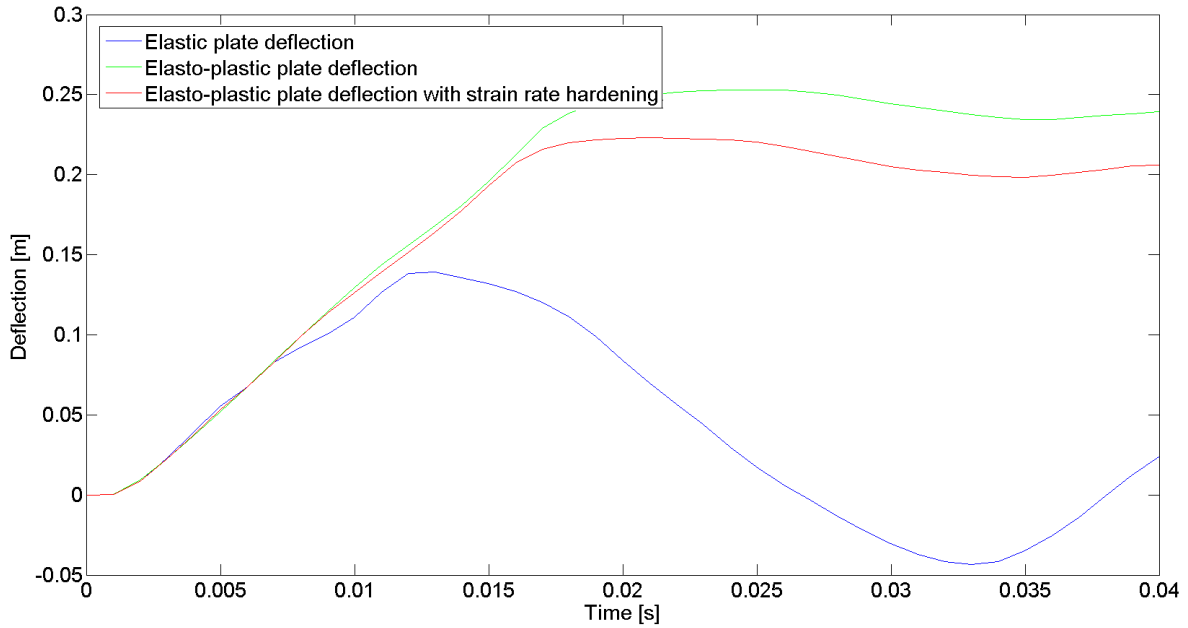


Figure 5.20: Maximum deflection at an impact velocity of 11.19[m/s] for deformable plate

Both the magnitude and distribution of the stresses were different for the rigid and deformable plate. The maximum Von Mises stress for the deformable plate dropped with strain rate hardening is equal to 466[MPa]. The stress distribution may be viewed in figure 5.21 and it is clear that a large part fo the stress is concentrated in the plate.

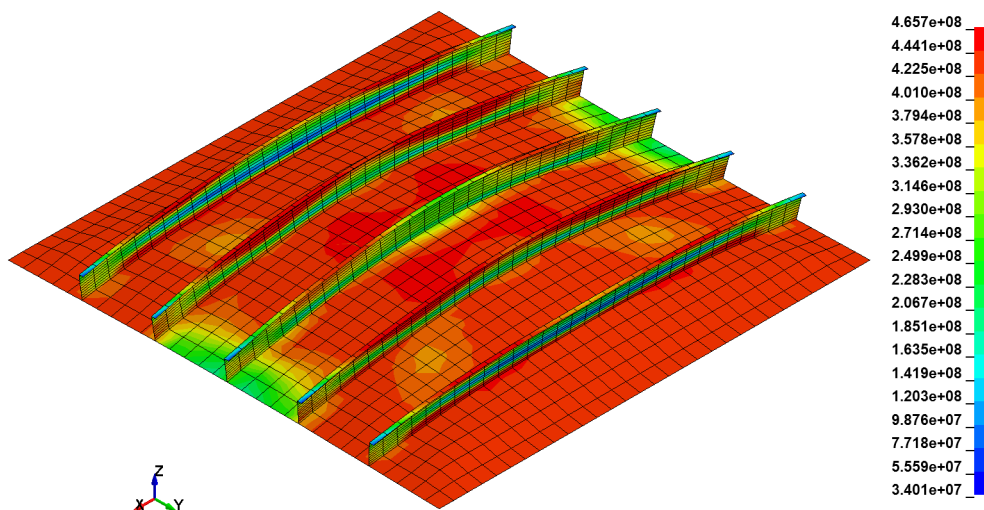


Figure 5.21: Von Mises stress at maximum deflection for elasto-plastic drop test with strain rate hardening

5.4.2 Response Based on "Rigid Drop Pulse"

A plot of the deformation versus time for the plate subjected to a rigid load pulse may be seen in figure 5.22.

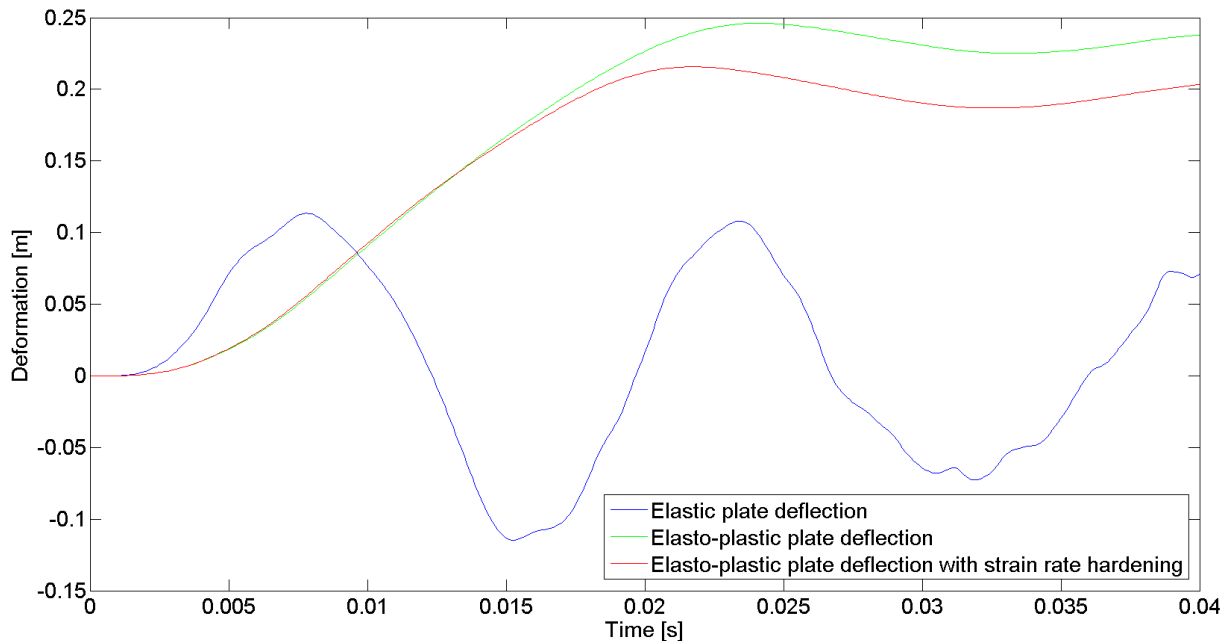


Figure 5.22: Maximum deflection at an impact velocity of $11.19[m/s]$ for rigid drop pulse

For the elastic plate subjected to the rigid load pulse, the maximum deflection obtained is equal to $115[mm]$. For the case with the elasto-plastic plate with strain rate hardening, the maximum deformation was measured to equal $215[mm]$ and the maximum deformation for the elasto-plastic deformation is found to equal $250[mm]$.

For the plate subjected to the rigid loading pressure, the stresses at the maximum deflection of $215[mm]$ may be seen in figure 5.23. The stress distribution is less uniform than what was found in the drop test. Large stresses are observed at the bottom of the stiffener webs. The maximum stress is found to equal $442[MPa]$ and is found in the middle stiffener web and surrounding plate flange, approaching the ultimate stress of the material.

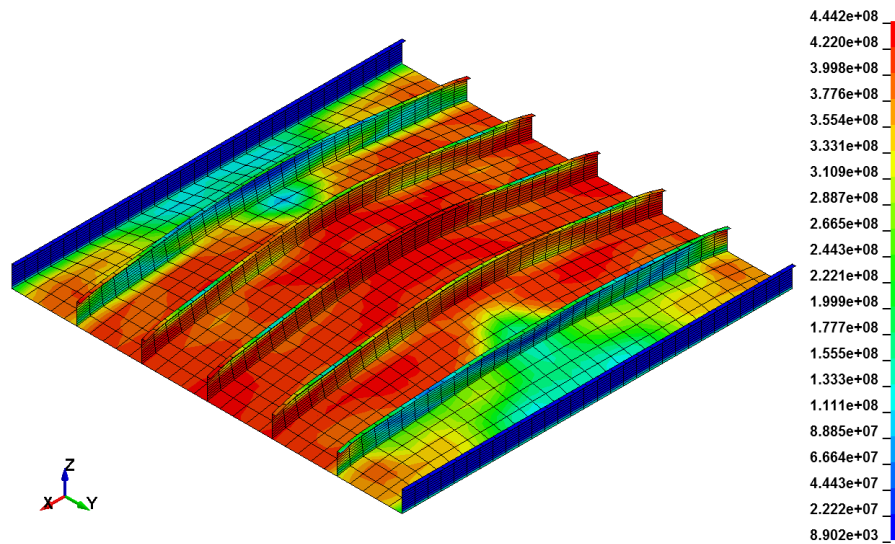


Figure 5.23: Von Mises stress at maximum deflection for elasto-plastic plate test with strain rate hardening subjected to the rigid drop pressure

5.4.3 Pressure Peak from Experimental Drop Test

From the experimental drop tests in (Huera-Huarte et al., 2011), following the asymptotic theory, the maximum loading coefficient C_S of 30 is found for an angle of impact equal to 5° . Experimental data at impact angles close to 0° show load coefficients in the range of 20 and 25. The model yields a maximum pressure between 1200 and 1900[kPa] for the SOK model and 900 and 1300[kPa] for the Wheeler stretching model. The peak pressures are tabulated in table 5.19 and are in the same range as found for deformable drop tests and the loads from (GL, 2016b).

Table 5.19: Peak pressures given by the loading model from (Huera-Huarte et al., 2011),

Sea state	$p_{C_h=20}$ [kPa]	$p_{C_h=25}$ [kPa]	$p_{C_h=30}$ [kPa]
6	877	1097	1316
15	1284	1605	1926

5.4.4 Comparing the Loading Models and Experimental Data

The platform in which the experimental tests are based on are confidential and are merely meant as a basis for validating the obtained loading results. The dimensions of the platform are in the same order of magnitude as for the test-platform, but the dimensions are not equal

due to the non-disclosure agreement.

As was the case for the air gap analysis run in Wadam, the most critical location is found to be surrounding the columns. The most critical direction was found to be during head sea as opposed to an incoming angle of 15° . The maximum scaled negative air gap was found to be approximately $10[m]$, 25% larger than what was found from the analyses in Wadam.

The model in the model tests was fitted with pressure panels measuring the peak pressures from the wave impacts. The maximum pressure peak was measured above the front column and was measured to be equal to $1600[kPa]$ and is found in the approximately same sea state as the critical air gap for the Wadam runs, sea state 16. The peak pressure is approximately 25% larger than the peak pressure found using the approach from the OTG. The pressures from the OTG are in the same range as the pressures found using the loading model from the experimental drop tests in (Huera-Huarte et al., 2011) indicating that peak pressures in the same order of magnitude for wave impacts could be obtained in drop tests. The peak pressure from the simulated drop tests are rger.

When comparing the load results from those based on the RP, the total load impulse is in the same order of magnitude as for the OTG. The maximum pressures are estimated to be approximately 10% of the peak pressures estimated from the OTG. At the same time, the duration of the load using the model is estimated to be approximately ten times the duration found from the OTG.

5.4.5 Summary FEA Response Estimates

For the applied material model, the stresses for the loading conditions based upon the RP, the stresses are below yield. For the analysis with the loading condition based upon the OTG, the stresses are above yield which leads to large deformations. Strain rate hardening is also of high importance as it leads to a reduction in overall deformation of to 30% compared to pure elasto-plastic plate response.

The response from drop tests with deformable panels was approximately the same as when using the loading model from (GL, 2016b). This indicates that despite poor agreement in terms of the pressure pulses, the model could capture some key effects. Also interesting to note is that the response when loading the pulses from the drop test of rigid panels on deformable panel was close to that obtained in the drop test of the deformable panel.

Chapter 6

Steel Columns

6.1 Finite Element Modelling

6.1.1 Water and Air modelling

The same fluid properties as applied for the 3D drop tests are applied for the column drop tests as well with the fluid properties give in table 6.1.

Table 6.1: Fluid properties applied in LS-Dyna

	Material type	Density $\rho[kG/m^3]$	Viscosity $\mu[]$	Pressure cutoff [Pa]
Air	Null	1.23	1.00E-03	-1.00E+11
Salt water	Null	1025	1.67E-03	0

The EOS used for steel, air and water are the same in all drop tests, and may be seen in table 6.2.

Table 6.2: EOS applied for water, air and steel

	C	S1	S2	S3	Gamma0	A	E0	V0
Water	1480	2.56	-1.986	0.227	0.5	0	0	0
Air	343.7	0	0	0	1.4	0	0	0
Steel	4570	1.5	0	0	1.93	0	0	0

6.1.2 Stiffened Column Model

To investigate the effect of hydroelasticity on more complex structures, drop tests are to be conducted for offshore columns. S420 steel is used as columns are more exposed to large loads than the plates above the main deck. Higher strength steel is thus used to compensate for higher loads. Internal structural components are modelled using the S355 steel type.

The column model is loosely based on the columns for existing semi-submersibles. The column is modelled with a height of 30[m] and a width of 18[m]. The outer plates are stiffened by HP200X10 stiffeners with a spacing of 600[mm], internal decks, ring stiffeners as well as internal bulk heads. To model the mass of the rest of the semi-submersible, a heavy, rigid plate is connected to the rear of the column model. An isometric view of the the finite element model, without the heavy rigid plate applied in the structural analysis of the column, may be seen in figure 6.1 as the green square.

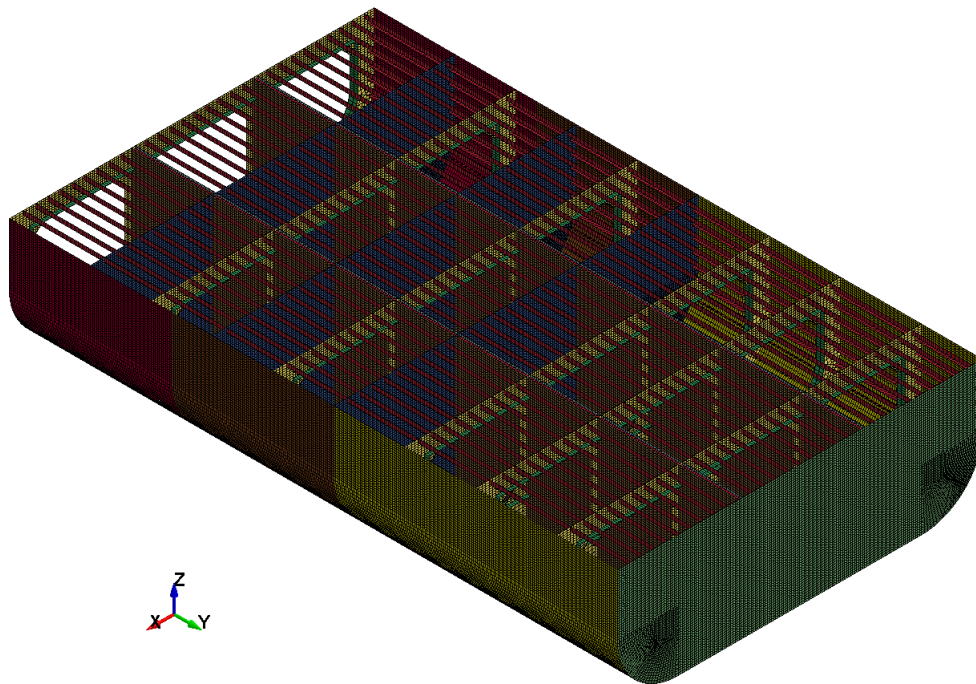


Figure 6.1: Finite element model of the column

The material parameters for S420 steel used for the outer plates are given in table 2.5 while S355 steel are used for the internal components with the parameters listed in table 2.4. The loads and structural responses are to be evaluated on a 6[m] by 6[m] segment on the column. The loading condition on the column isn't necessarily largest for the same critical sea state as evaluated for the plate which is located above the deck box. As the point of

interest is located closer to the mean water line, more waves will hit the structure during its lifetime. To investigate the effect of large deformations, an impact velocity of 20[m/s] could be used to represent water particle velocities of the same magnitude. The area that is to be loaded may be viewed in figure 6.2.

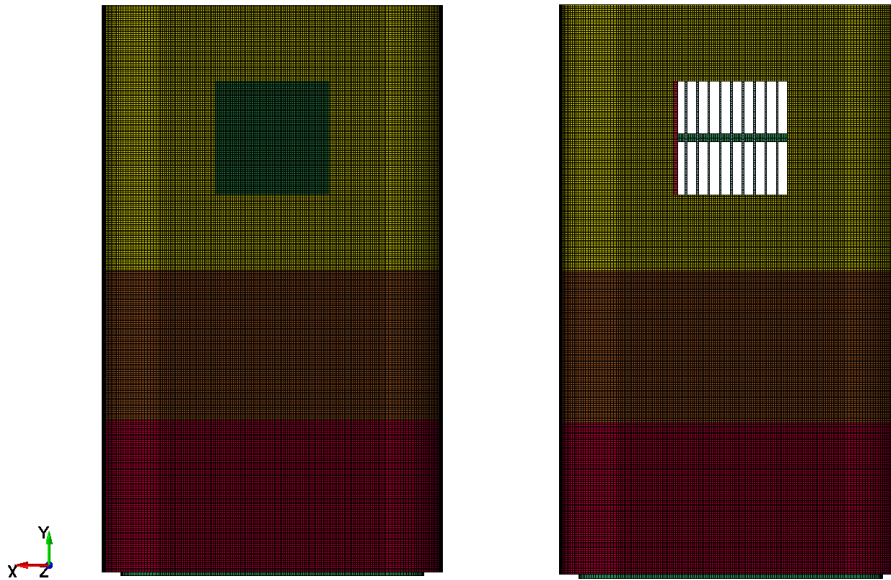


Figure 6.2: Loaded area of column

The outer plate is 16[mm] thick and the density of steel is equal to 7850[kg/m³] yielding a dry mass of the outer plate of 4520[kg]. Meyerhoff's formula yields an added mass equal to 100680[kg]. When accounting for the difference in velocity potential for a fully oscillating plate versus that of a deforming plate, assumed to equal 0.64, the added mass equals 64400[kg] yielding an added mass factor of 14.3. The added mass factor is only applied for the area exposed to the loading. The calculation may be viewed in table 6.3.

Table 6.3: Calculation of added mass on the 6[m] by 6[m] panel using Meyerhoff's formula

$B[m]$	$L[m]$	χ	J	$\rho[kg/m^3]$	$M'_a[kg]$	f	$M_a[kg]$
3	3	1	0.579	1025	100681	0.64	64400

The elemental properties of the columns are given in table 6.4. In the rounded regions of the columns, the number of elements are higher in order to properly describe the geometry of the structure. n_B and n_L are the number of elements in the breadth and length of the part.

Table 6.4: Elemental properties for steel columns.,

Part	$B[m]$	$L[m]$	n_B	n_L	$t[mm]$	Tested Materials
Upper plate	18	14	180	140	16	1,3
Loaded section	6	6	60	60	16	1,3,5
Middle plate	18	8	180	80	17	1
Lower plate	18	8	180	80	18	1
Ring stiffener	6	18	60	180	10	2
Ring stiffener web	16	0.4	160	2	10	2
Deck	6	18	60	180	16	2
Web	0.2	30	1	300	10	2
Flange	0.1	30	1	300	30	2
Bulkhead	6	30	60	300	10	2
Heavy plate	18	30	180	300	10	4

The linear material properties are listed in table 6.5. Material type 5 has an increased density accounting for added mass and is used for the non-coupled analysis where the plate is loaded by the pressure obtained from rigid drop tests. The nonlinear material properties are listed in table 6.6.

Table 6.5: Linear material properties for steel columns

Material	Material type	$\rho[kg/m^3]$	$E[GPa]$	$\nu[]$
1,2	Elasto-plastic	7850	210	0.3
3	Rigid	7850	210	0.3
4	Rigid	9.62E+05	210	0.3
5	Elasto-plastic	1.201E+05	0.3	

Table 6.6: Nonlinear material properties for steel columns

Material	$\sigma_1[MPa]$	$\epsilon_1[]$	$\sigma_2[MPa]$	$\epsilon_2[]$	$\sigma_3[MPa]$	$\epsilon_3[]$	$C[]$	P
1	420	0.002	421.3	0.008	500	0.1176	4000	5
2,5	357	0.0023	366.1	0.018	541.6	0.137	4000	5

6.2 Results from Drop Test Simulations

6.2.1 Pressure Pulse Histories

At a drop velocity of $20[m/s]$, the maximum rigid pressure was found to equal $72[bar]$ while the maximum pressure for the deformable plate section of the column was found to equal $40[bar]$. The duration of the rigid load pulse is equal to $0.01[s]$. The eigen period for the panel appears to lie between $0.16[s]$ and $0.18[s]$, noticeably longer than for the smaller plates. The pressure may be seen in figure 6.3. The "rigid drop impulse" is found to equal $37.356[kPas]$ while the total impulse for the "deformable pressure impulse" is found to equal $45.231[kPas]$.

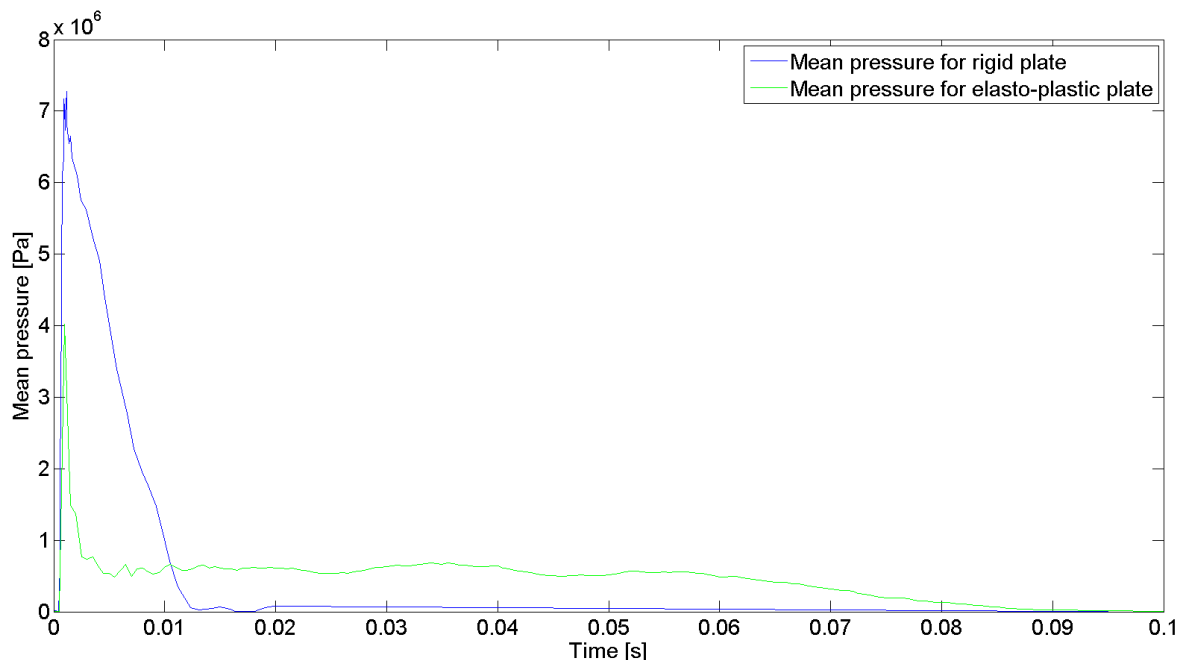


Figure 6.3: Pressure time series for the $6[m]$ by $6[m]$ plate on the column

6.2.2 Structural Deformations

The maximum deformation found for the column subjected to the pressure pulse found from the rigid drop test was equal to $0.635[m]$. For the coupled analysis, the maximum deformation was found to equal $0.652[m]$, 2% larger than for the "rigid pulse".

Structural responses for a modified rigid pulse is estimated as well, where the modified pressure accounts for the pressure not acting uniformly over the plate's area. In the model, the majority of the pressure is assumed to be between 10% and 90% of the panel's length and

the pressure is thus applied here. To maintain the same force on the plate despite of the reduced loading area, the pressure is multiplied by the same factor in which the area is reduced, i.e. 1.2^2 . The deformation curve may be seen in figure 6.4 where the modified pressure yields a maximum deformation $0.691[m]$.

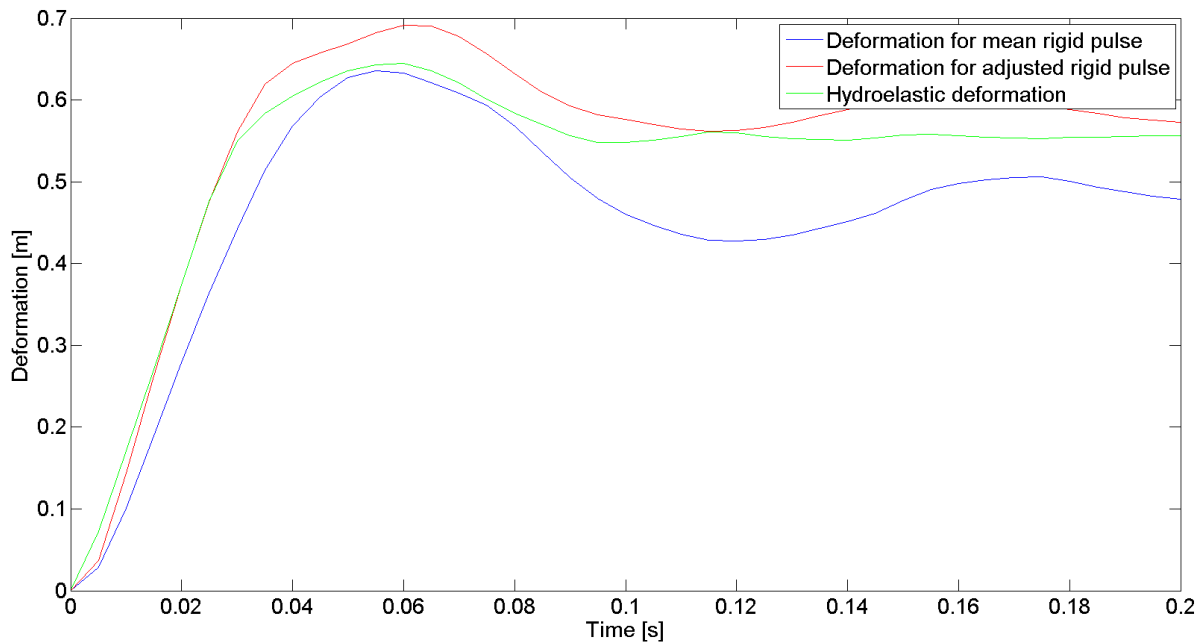


Figure 6.4: Maximum deformation found for the column subjected to loading at an impact velocity of $20[m/s]$

The deflection curves are quite similar up until the maximum deflection, indicating that the estimated added mass is a good approximation for the structure. After the initial deformation, the structure oscillates with the wet eigen period while ventilation has occurred for the coupled analysis, causing the structure to oscillate with the dry eigen period.

As was the case for the 3D stiffened panel, the deflection shape is not equal to the final deformation shape throughout the deformation phase. This can be seen in figure 6.5 where the relative displacement of the plate interacting with the fluid is plotted at different points of time. It is clear that the deformation occurs slower near the stiffened region. One can also observe how the deformation shape approaches a shape dominated by a single mode, such as a sinusoidal mode.

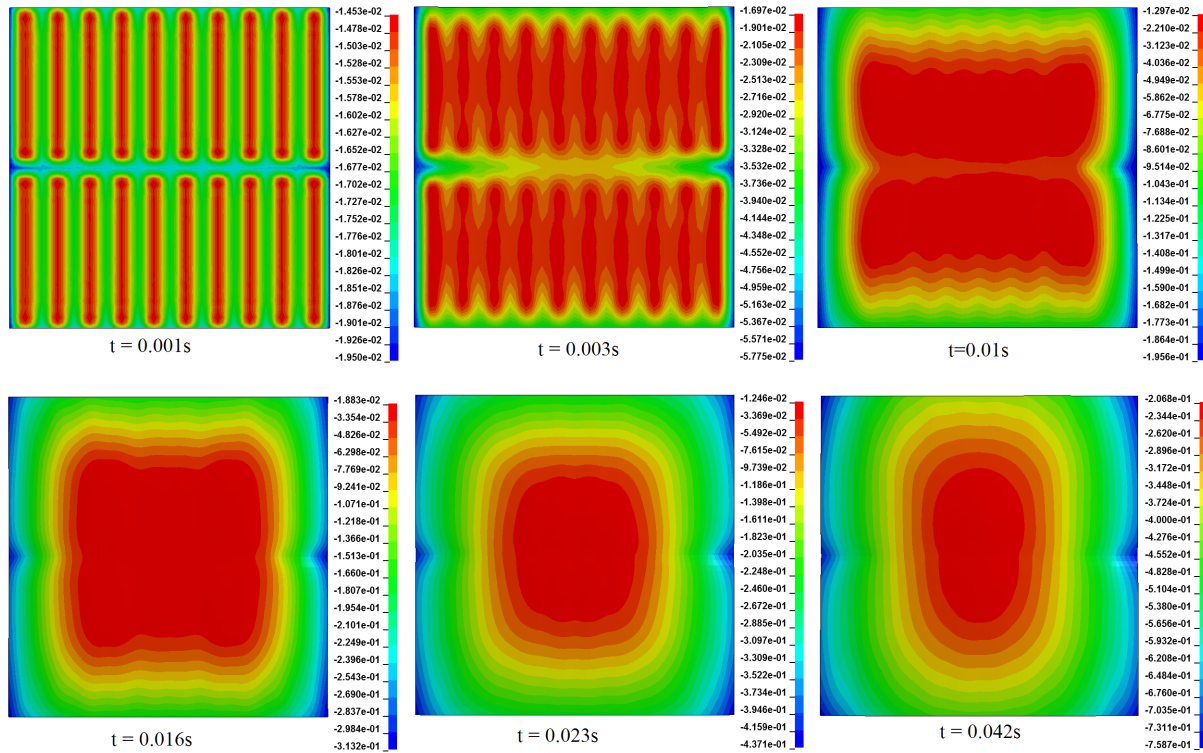


Figure 6.5: Relative displacement for deformable stiffened plate on column dropped into sea water at a velocity of $20[m/s]$

6.2.3 Response Based on Hydro-Elasto-Plastic Behaviour

At the point of maximum deflection equal to $0.635[m]$, the maximum Von Mises stress found is equal to $535.0[MPa]$ and a large part of the stresses are in the plates. Failure occurs in the surrounding ring stiffeners, as the ring stiffeners buckle due to the large external loading. The maximum strain is located in the ring stiffener beneath the loaded area. A maximum plastic strain of $0.25[]$ is observed near the edge of the buckling ring stiffener, which would indicate failure in the ring stiffener. The distribution of the Von Mises stress may be viewed in figure 6.6.

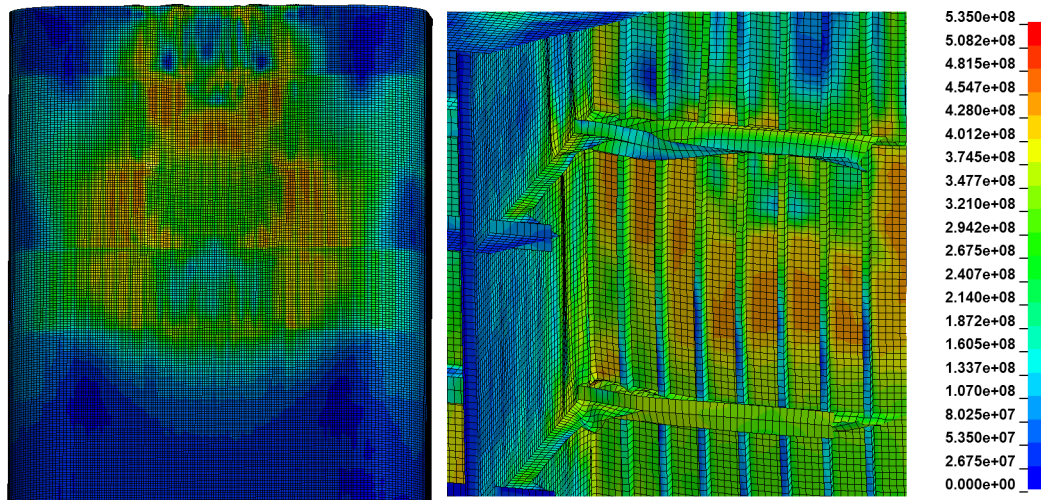


Figure 6.6: Von Mises stress in column at maximum deflection the coupled analysis

6.2.4 Response Based on "Mean Rigid Drop Pulse"

Overall, the structural responses and stresses are quite similar to those obtained for the coupled, hydroelastic analysis. For the column subjected to the rigid load pulse, the maximum stress was found to equal $535.6[MPa]$ with large stresses measured in the outer plating. Buckling is seen in the internal ring stiffeners, both the stiffener located by the loading and the surrounding ring stiffeners. The stress distribution may be seen in figure 6.7. The maximum strain is located in the ring stiffener by the loaded segment equal to 0.29, which would cause failure in the ring stiffener.

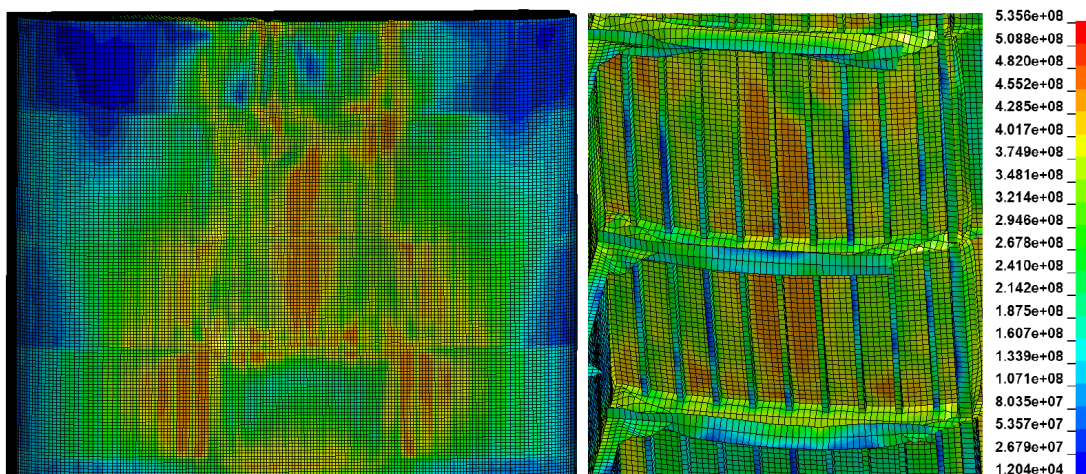


Figure 6.7: Von Mises stress in column at maximum deflection for "mean rigid load pulse"

6.2.5 Response Based on "Adjusted Rigid Drop Pulse"

The maximum Von Mises stress found for the "adjusted rigid drop pulse" is found to equal $540[MPa]$ and is located in the buckling ring stiffener. Overall, the same response patterns as for the "mean rigid drop pulse" and hydroelastic response are seen where the response may be viewed in figure 6.8.

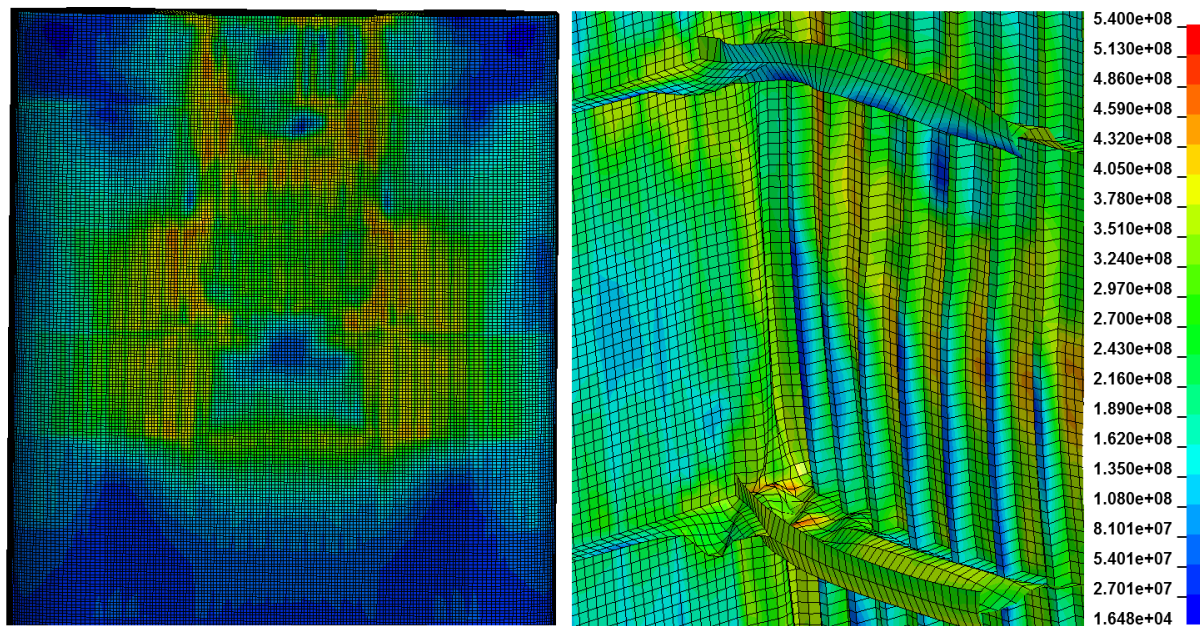


Figure 6.8: Von Mises stress in column at maximum deflection for "adjusted rigid load pulse"

6.3 Results from OTG Loading

6.3.1 Pressure Pulse from OTG

In (GL, 2016b), the maximum pressure when evaluating the structural integrity of girders over an area of $6[m]$ by $6[m]$ is equal to $2300[kPa]$. The pressure pulse curve may be seen in figure 6.9. The pressure pulse is seen to be more narrow than the pressure pulse which was used in loading the $3[m]$ by $3[m]$ stiffened panel.

With a pressure peak equal to $2300[kPa]$, the peak is equal to 57.5% of what was obtained from the deformable panel drop test and 33% of the rigid panel drop test. The total impulse is however larger and equal to $68.58[kPas]$.

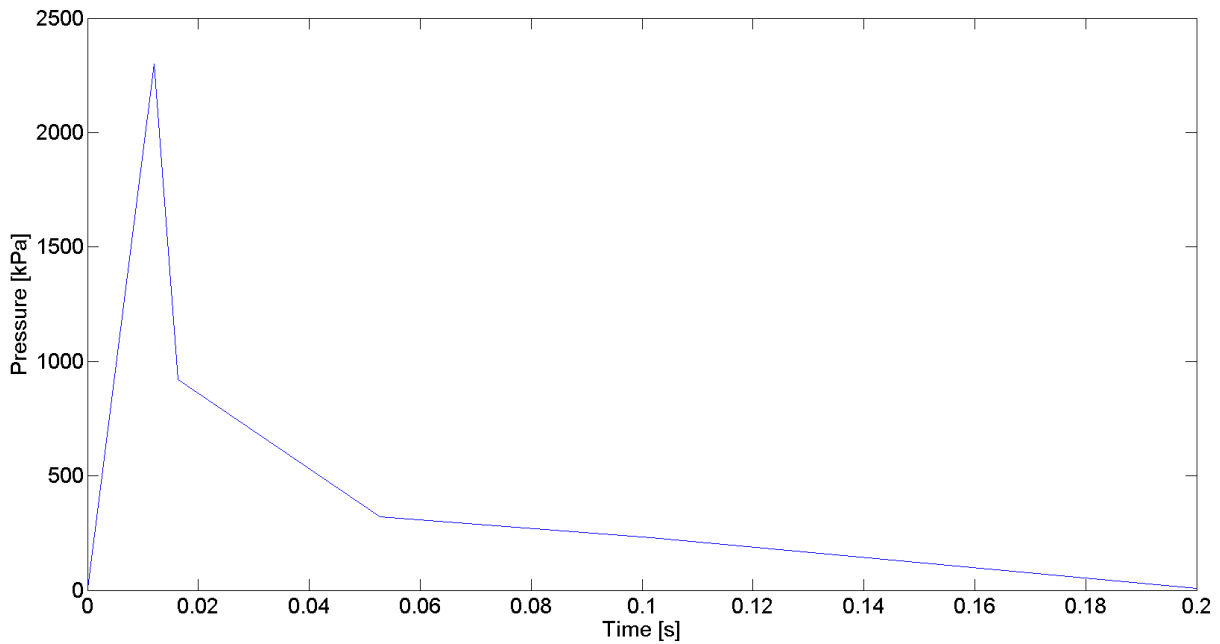


Figure 6.9: Pressure pulse curve for OTG loading of steel column based on maximum girder loading of a 6[m] by 6[m] area

6.3.2 Response based Pressure Pulse from OTG

The maximum deflection found for the loading from the OTG was equal to 0.681[m], which is 4% larger than found from the coupled analysis. The plot of the maximum deflection versus time may be seen in figure 6.10. By this loading model, the structure uses a longer amount of time in order to reach its maximum deformation. The loading models from the drop tests all reached maximum deformation after approximately 0.06[s] while the maximum deformation from this loading model was reached approximately 0.09[s]. This is close to half the wet eigen period found from the drop test with the deformable panel.

The deformation reaches its second maxima after approximately 0.19[s] indicating an eigen period that is reduced to approximately half due to nonlinear response.

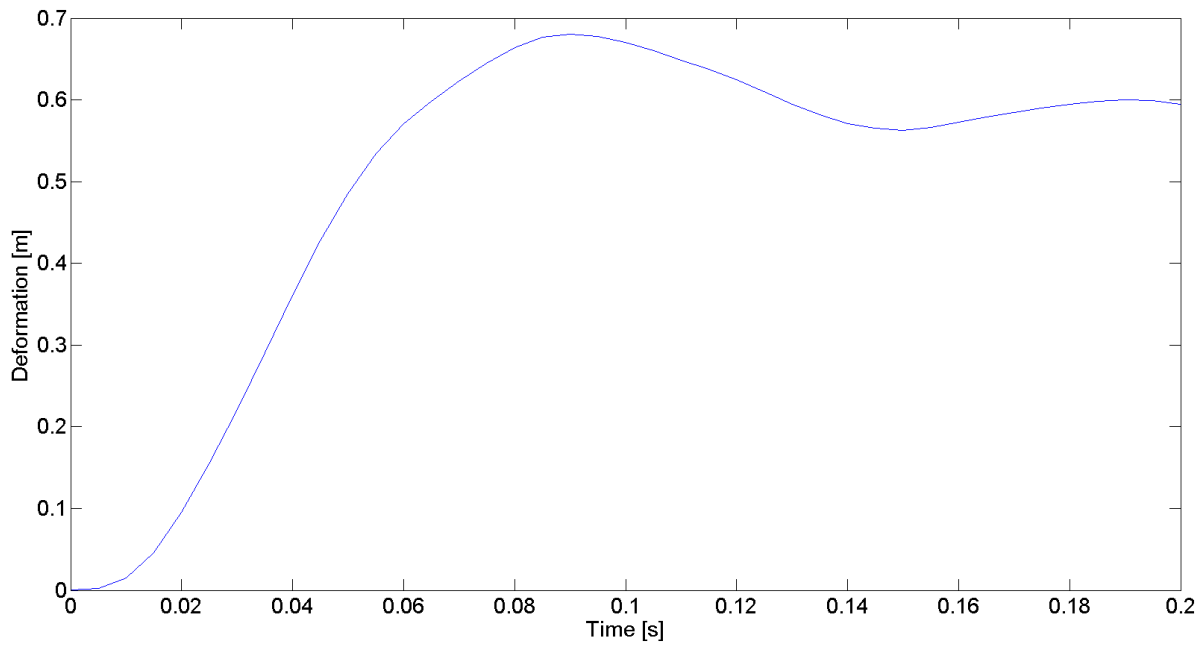


Figure 6.10: Maximum deflection of steel column with loading condition from OTG-14

The maximum Von Mises stress is found to equal $540.1 [MPa]$, the same maximum stress as found for the "modified rigid load pulse". The response follows the same overall pattern, with large stresses in the outer plate and buckling in the ring stiffener. The stress distribution may be seen in figure 6.11.

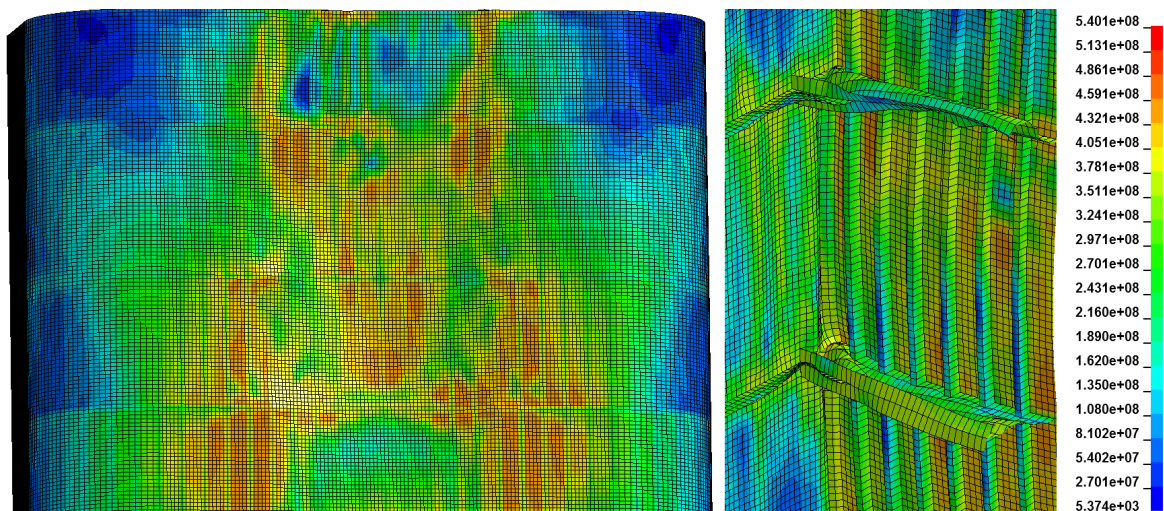


Figure 6.11: Maximum Von Mises stress distribution for OTG loading on the steel column

Chapter 7

SDOF Analysis

7.1 SDOF Analysis of Test Rig

The same generalised parameters as obtained in section 4.2.3 are used in the SDOF analysis of the 2D test rig with the generalised parameters tabulated in table 7.1. The length of the panel is $0.5[m]$ and the breadth of the panel is taken as a unit width of $1[m]$. The script used to perform the numerical integration can be seen in appendix H under section H.1.

Table 7.1: Generalised parameters used in SDOF of 2D test rig

$\bar{k}[kg]$	$\bar{m}_{total}[N/m]$	$T[s]$
60.5	7341879.82	0.026

The maximum deflection for the deformable plate was estimated to equal $9.7 [mm]$ in LS-Dyna, slightly lower than $11.5 [mm]$ which was found using time integration with the same pressure pulse. For the estimates in LS-Dyna, the added mass force causes the deflection amplitude to decrease to $5 [mm]$ after the initial maximum deflection. A comparison of the deflection estimated by numerical integration and LS-Dyna may be seen in figure 7.1. This is a difference of approximately 15% where the numerical solution is more conservative than the results extracted from LS-Dyna. This complies with the theory in (DNV, 2014b) where hydroelastic calculations are indicated to be smaller.

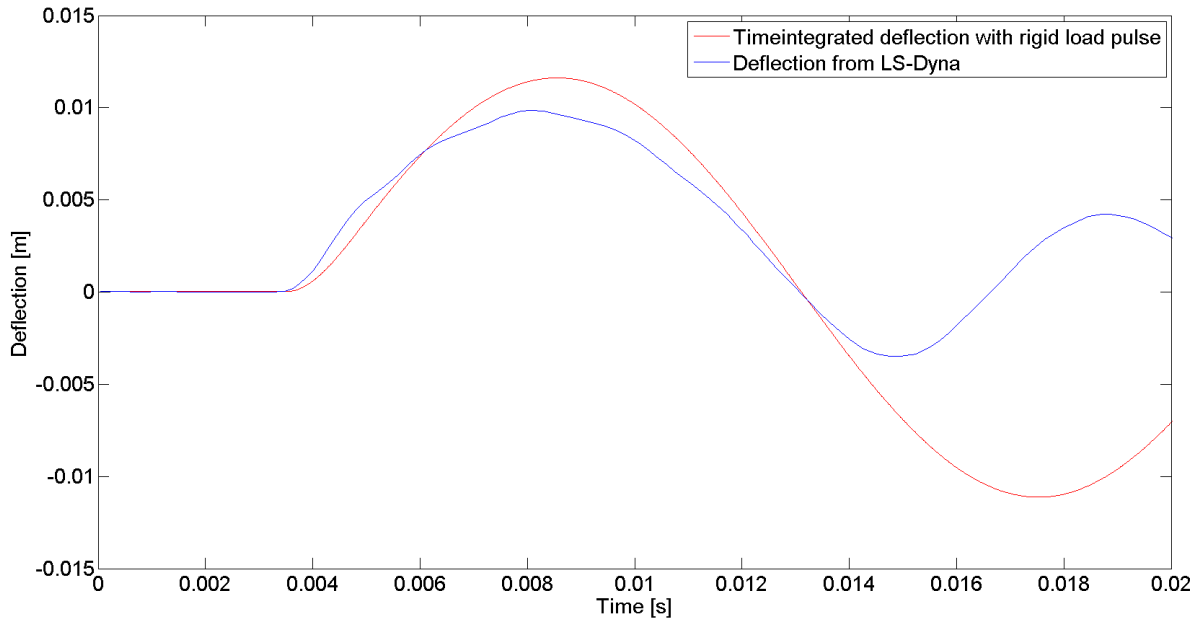


Figure 7.1: Comparison of maximum deflection estimated from numerical integration and LS-Dyna

7.2 3D Simplified Response

7.2.1 Beam Analogy for Stiffened Panel

The effective flange width of the plate was estimated according to the graph in figure 7.2 from (Veritas, 2011a). A graph is given for a number of evenly distributed point loads. As the loads are assumed to be evenly distributed pressures, the graph for more than 5 point loads are used in the response calculations. $l_0/s = 6$ yields an effective width of the plate flange approximately equal to the stiffener spacing of $0.5[m]$.

The area of the stiffener is equal to $22.46[cm^2]$ and the plate thickness is equal to $8[mm]$. Thus the total area of the section being analysed is equal to the sum of the stiffener area and the area of the effective plate flange and equal to $26.46[cm^2]$. The mass of the effective area of the cross section, assuming a steel density of $7850[kg/m^3]$, is equal to $147[kg]$.

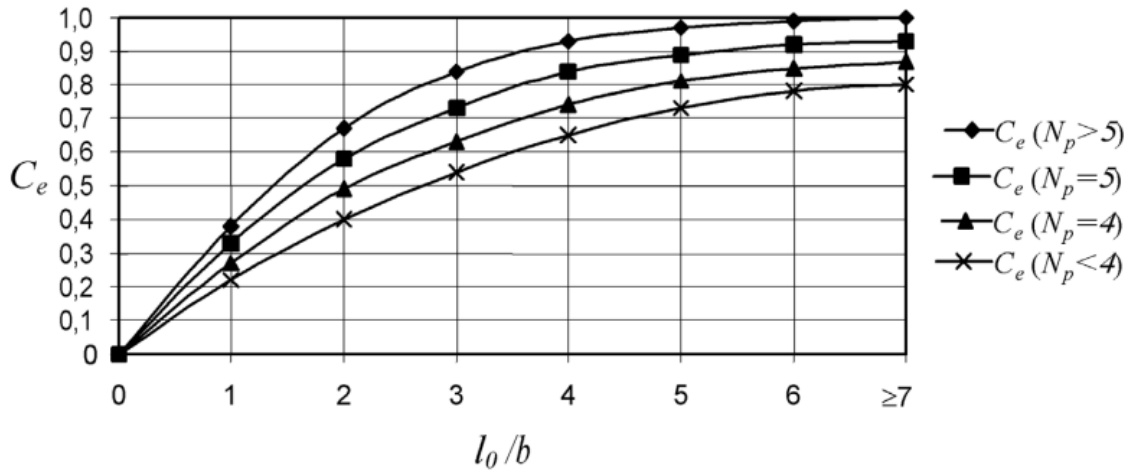


Figure 7.2: Coefficient for establishing effective flange width (Veritas, 2011a)

The SDOF model for generalised mass is developed by the coefficients found in (DNV, 2014a) as seen in equation 7.1.

$$\frac{K_m}{K_l}(M + M_a)\ddot{w} + k_1 w = F(t) \quad (7.1)$$

A trilinear model is applied where the properties are elastic to the elastic limit, linear in the elasto-plastic region and linear in the plastic region. In the elasto-plastic region phase, the mass and load properties are taken as the average given in the elastic and plastic region. The SDOF analysis was carried out using pressure curves from LS-Dyna as input pressures and the results were obtained from timeintegration by the method of mean acceleration. Geometric and material nonlinearities are considered for large deformations. If the deformation w exceeds the elastic limit, plastic resistance is formed in the stiffener. It is further assumed that yield hinges may form in the connections between the stiffeners and girders.

7.2.2 Added Mass Calculation

The added mass calculation based on the formulation in (Meyerhoff, 1970) used for calculating added mass of the 3[m] by 3[m] FEM model in section 5.2.2 is applied. There, the added mass was found to equal 8070[kg]. For the SDOF analysis, a width of 0.5[m] is considered, i.e. the plate is 6 times wider than the section considered. Thus, the added mass is divided by 6, yielding an added mass of 1345[kg] and an effective added mass factor

of approximately 10.

7.2.3 Parameters for SDOF Analysis by RP Stiffness Model

The coefficients are given for a clamped and simply supported beam in appendix G. The SDOF model assumes clamped boundary conditions with the coefficient factors used collected from figure G.2.

The plastic properties for the chosen stiffened plate are given in table 7.2. The stiffness from the boundary was neglected in establishing k_1 used to estimate c . By applying the resistance curve for $c = inf$, the plastic stiffness is calculated from the slope of the stiffness curve. The stiffness curve for the plastic stiffness may be viewed in figure 7.3.

Table 7.2: Structural parameters for stiffened plate response for clamped beam

$I[mm^4]$	$W_p[m^3]$	$w_c[m]$	$R_0[MN/m]$	$k[MN/m]$	$w_{el}[mm]$	$k_1[MN/m]$	c	$c1$
2.71E07	0.00024	0.1272	0.45	80.91	5.60	874	17	2

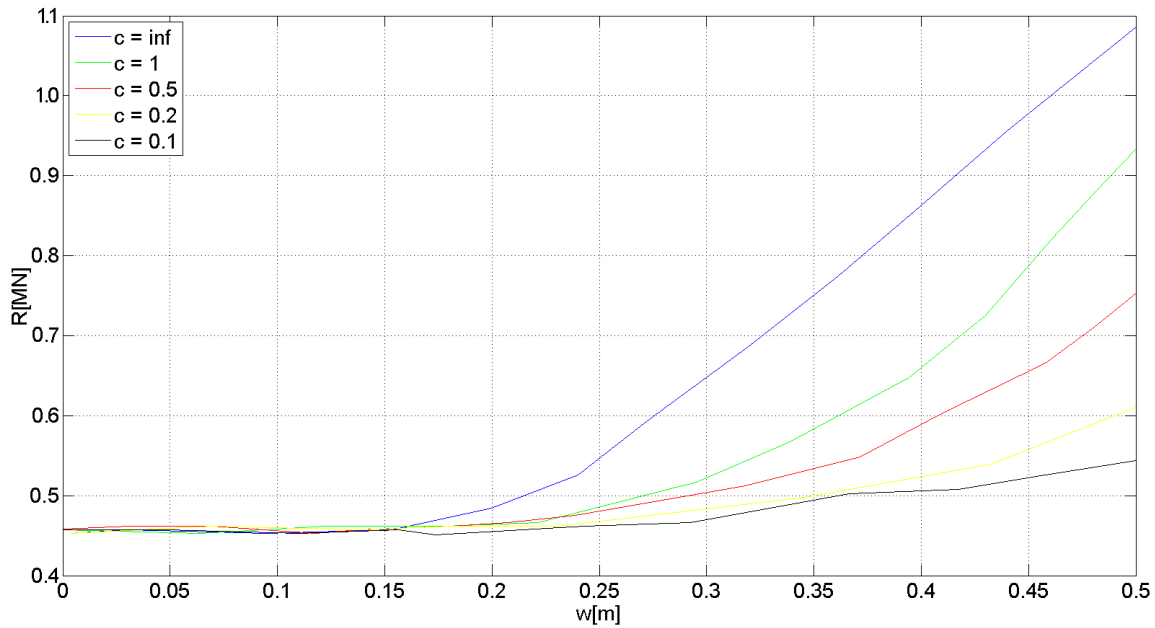


Figure 7.3: Plastic resistance for beam model of the stiffened clamped plate

The parameters used in the trilinear model are tabulated in table 7.3. The masses are the resulting masses when accounting for the load factor, K_l , and mass factor, K_m . The natural elastic period of the structure under uniform loading is equal to 0.0237[s], significantly lower than the eigen period found in the drop test of the elastic plate equalling 0.05[s].

Table 7.3: Parameters for elastic and plastic part of the SDOF analysis for clamped beam

	K_l	K_m	$\overline{M}[kg]$	$\overline{M}_a[kg]$	$k[MN/m]$
Elastic	0.53	0.41	114	1040	80.91
Elasto-plastic	0.515	0.37	105	964	0.21
Plastic	0.5	0.33	97	888	2.2

7.2.4 Linear Stiffness from FEA

The structure's stiffness is linear up until the elastic limit is reached. The elastic limit w_{el} of the structure is seen to approximately equal $5.7[mm]$, which is slightly larger than the elastic limit calculated for a clamped beam based on the standards from (Standard, 2004). The resistance curve is approximately linear after reaching a deformation of $50[mm]$. It is to note that since the load has been applied slowly, strain rate hardening effects are neglected in the stiffness curve. The maximum deformation versus applied pressure can be seen in figure 7.4.

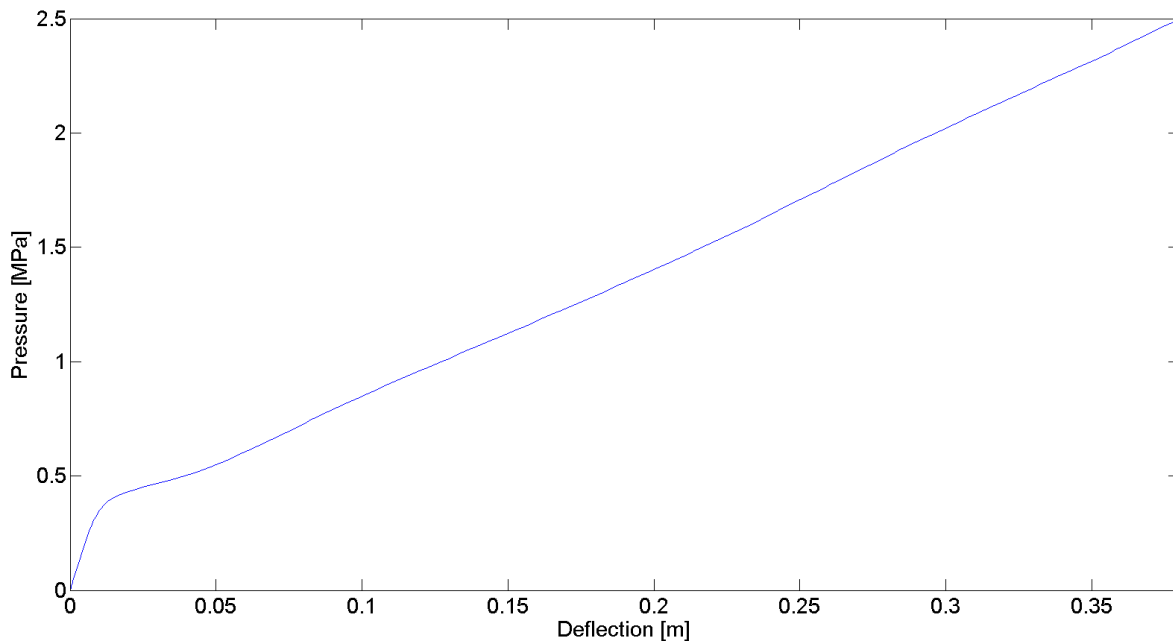


Figure 7.4: Pressure deflection curve obtained from LS-Dyna

By differentiating the load response curve with respects to the deflection, a curve for the stiffness was developed. To easily compare the results with the SDOF model, the pressure was multiplied with the effective area of the beam in the SDOF model, equalling $1.5[m^2]$. This yielded an initial elastic stiffness of approximately $60[MN/m]$ and a plastic stiffness of

9.7[MN/m]. The resulting stiffness versus deflection may be seen in appendix H in figure H.1. R_0 is found by multiplying the elastic stiffness with the elastic limit and is found to equal 0.343[MN]. i.e. The limit lies between the clamped and rigid beam models.

The load and mass parameters of the stiffness model from FEA are assumed to be the mean of the clamped and pinned case. The parameters used in the analysis may be seen in table 7.4. In the elasto-plastic region, the function 7.2 is used as the stiffness. By this model, an elastic period of 0.0276[s] is obtained. This is slightly larger than the eigen period for the stiffness model based on the RP. This is expected as the clamped boundaries assumed in the RP-model decreases the elastic eigen period of the structure.

Table 7.4: Mass and stiffness parameters used in SDOF with stiffness model from FEA

	K_l	K_m	$\bar{M}[kg]$	$\bar{M}_a[kg]$	$k[MN/m]$
Elastic	0.59	0.46	114.35	1045.63	60
Elasto-plastic	0.54	0.39	105.72	966.66	Equation 7.2
Plastic	0.50	0.33	97.08	887.70	9.7

$$k = -7 \cdot 10^9 w^5 + 1 \cdot 10^9 w^4 - 6 \cdot 10^7 w^3 + 2 \cdot 10^6 w^2 - 3 \cdot 10^4 w + 2 \cdot 10^2 \quad (7.2)$$

7.2.5 Numerical Integration of Response

The response is numerically integrated using the method for constant acceleration where the applied Matlab function can be seen in section H.1 in appendix H.

Since the response is large and nonlinear, the response is linearised using the approach given in (DNV, 2014a) and the principle can be seen in figure 7.5. The selected mass is based upon the expected result. From the finite element analysis, the response is expected to be elasto-plastic. Hence, the response is given for elasto-plastic mass and load coefficients. The linearised stiffness is found by guessing the initial deflection and iteration to find the correct deformation.

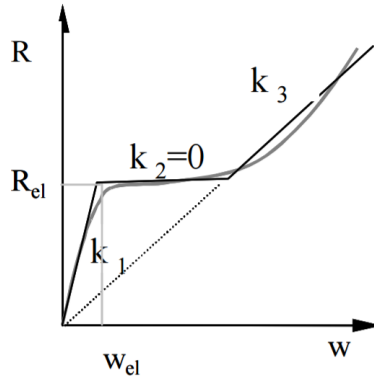


Figure 7.5: Linearisation of response as recommended in (DNV, 2014a)

7.2.6 RP Stiffness Model with "Rigid Drop Pulse"

The plate with the RP stiffness model subjected to the rigid drop pulse had a maximum deflection equal to 420[mm], a larger response than found for elasto-plastic plate without strain hardening in the finite element analyses. The deflection w.r.t time may be seen in figure 7.6.

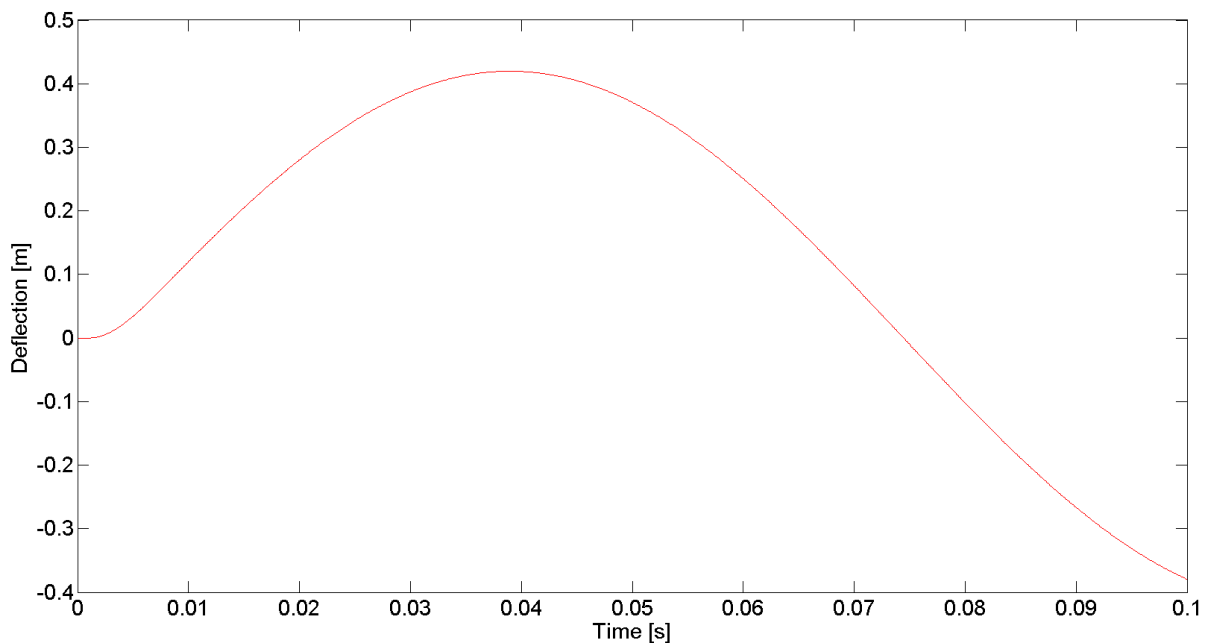


Figure 7.6: Deflection of the stiffened clamped plate subjected to the rigid design load pulse

The plots of the velocity and acceleration may be seen in appendix H in figure H.2 and figure H.3 respectively. The response is summarised in table 7.5. \bar{k} represents the linearised stiffness. The relative duration $\frac{t_d}{T}$ uses the wet elastic period as this is an elastic property

which is to be used for plotting the results in Biggs charts.

Table 7.5: Summary of the response for the plate with the RP stiffness model subjected to a rigid load pulse

$F_{max}[MN]$	$\frac{R_{el}}{F_{max}} []$	$w_{max}[mm]$	$\frac{w_{max}}{w_{el}} []$	$\frac{t_d}{T}$	$\bar{k}[MN/m]$
5.85	0.08	420.00	74.96	0.34	2.10

7.2.7 FEM Stiffness Model with "Rigid Drop Pulse"

The maximum deformation obtained for loading the plate with the stiffness obtained from LS-Dyna with the "rigid drop pulse" is equal to 170[mm]. This is less than the deformation obtained from the analysis in LS-Dyna. The deformation may be seen in figure 7.7.

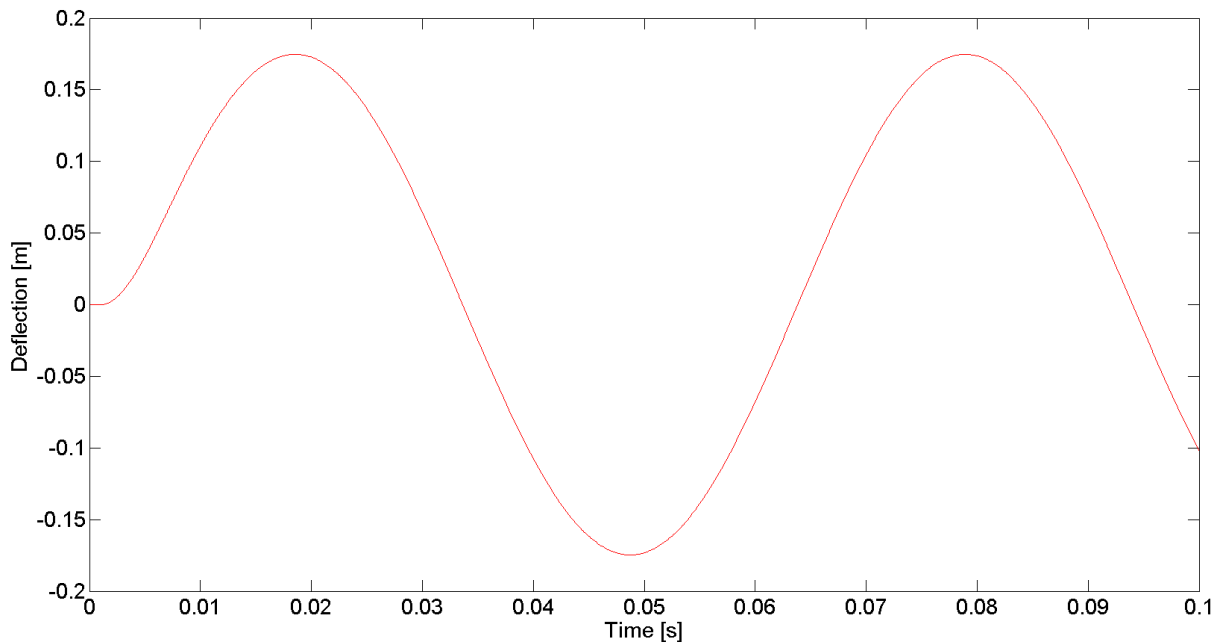


Figure 7.7: Deflection of the plate subjected to the "rigid design load pulse" with stiffness obtained from LS-Dyna

The plots of the velocity and acceleration are given in appendix H in figure H.4 and figure H.5. A summary of the response may be seen in table 7.6.

Table 7.6: Summary of the response for the plate with the LS-Dyna stiffness model subjected to a rigid load pulse

$F_{max}[MN]$	$\frac{R_{el}}{F_{max}} []$	$w_{max}[mm]$	$\frac{w_{max}}{w_{el}} []$	$\frac{t_d}{T}$	$\bar{k}[MN/m]$
5.85	0.06	170.00	29.73	0.29	11.76

7.2.8 RP Stiffness Model with OTG Load

The maximum deflection is found to equal 770[mm], much larger than what was obtained from the finite element analysis.

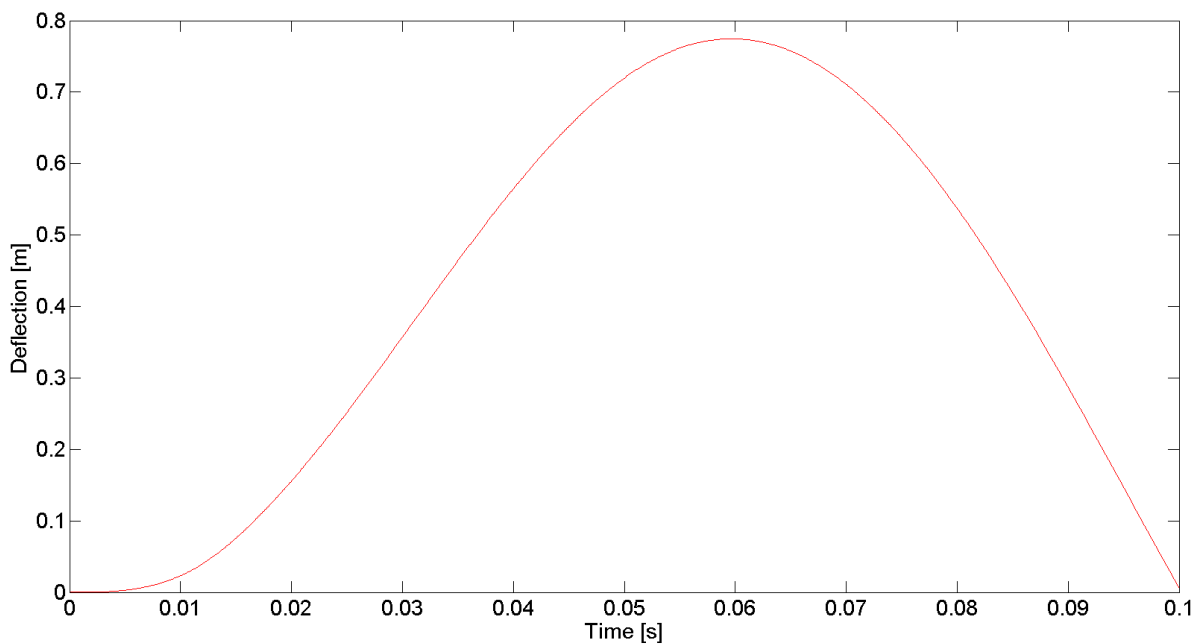


Figure 7.8: Deflection of the stiffened clamped plate subjected to the load pulse from the OTG

The velocity and acceleration for the structure may be seen in appendix H in figure H.6 and figure H.7. The results are summarised in table 7.7.

Table 7.7: Summary of the response for the plate with the RP stiffness model subjected to the OTG load

$F_{max}[MN]$	$\frac{R_{el}}{F_{max}} []$	$w_{max}[mm]$	$\frac{w_{max}}{w_{el}} []$	$\frac{t_d}{T}$	$\bar{k}[MN/m]$
1.80	0.25	770.00	137.43	8.44	2.18

7.2.9 FEM Stiffness Model with OTG Load

The maximum deformation for the model with the FEM stiffness model loaded with OTG load was equal to 200[mm]. The plot of the deflection versus time may be seen in figure 7.9.

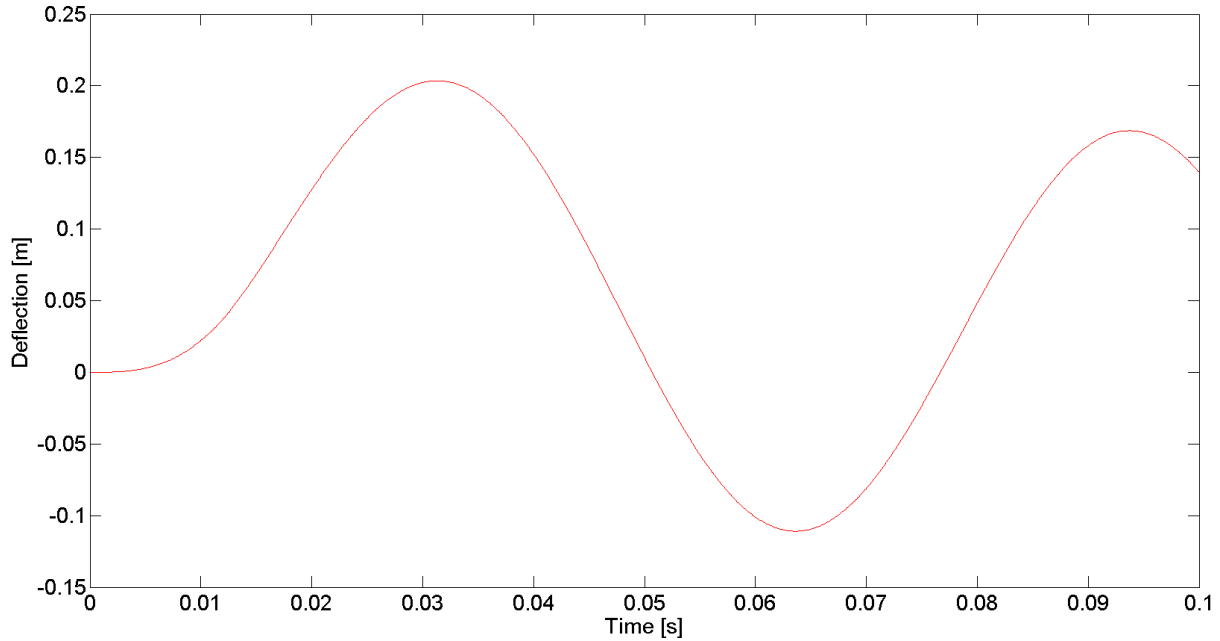


Figure 7.9: Deflection of the plate subjected to the load pulse from the OTG with stiffness extracted from LS-Dyna

Resulting velocity and acceleration from the response is given in appendix H in figure H.8 and figure H.9. The results are summarised in table 7.8.

Table 7.8: Summarised response for plate subjected to the load pulse from the OTG with stiffness extracted from LS-Dyna

$F_{max}[MN]$	$\frac{R_{el}}{F_{max}} []$	$w_{max}[mm]$	$\frac{w_{max}}{w_{el}} []$	$\frac{t_d}{T}$	$\bar{k}[MN/m]$
1.80	0.19	200.00	34.98	7.25	11.38

7.2.10 Summary SDOF Response

As stated in (DNV, 2014a), the stiffness model is conservative and for large nonlinear deformations, nonlinear FEM is recommended. Hence, the deformations obtained using the stiffness model was larger than those obtained using the model from LS-Dyna. As one would expect, the results with stiffness model obtained using LS-Dyna were close to the

results obtained with the same load in the software. The resulting deformations were smaller than those obtained by the RP-stiffness model, despite the RP-stiffness model having a larger elastic stiffness.

The results for the "rigid load pulses" are plotted in the Biggs chart in figure 7.10. One can see that the result is closer to the indicated line for the RP stiffness model than for the FEM stiffness model. This is partly due to the lower initial stiffness yet larger mean stiffness when accounting for stiffness in the nonlinear region.

Other possible reasons for the discrepancy for the line indicated by the relative loading could be due to the shape of the load pulse. The load pulse should be perfectly triangular with 0 rise time. However, the load pulse lies slightly below this curve and could thus cause the estimated responses to be larger than the actual responses are.

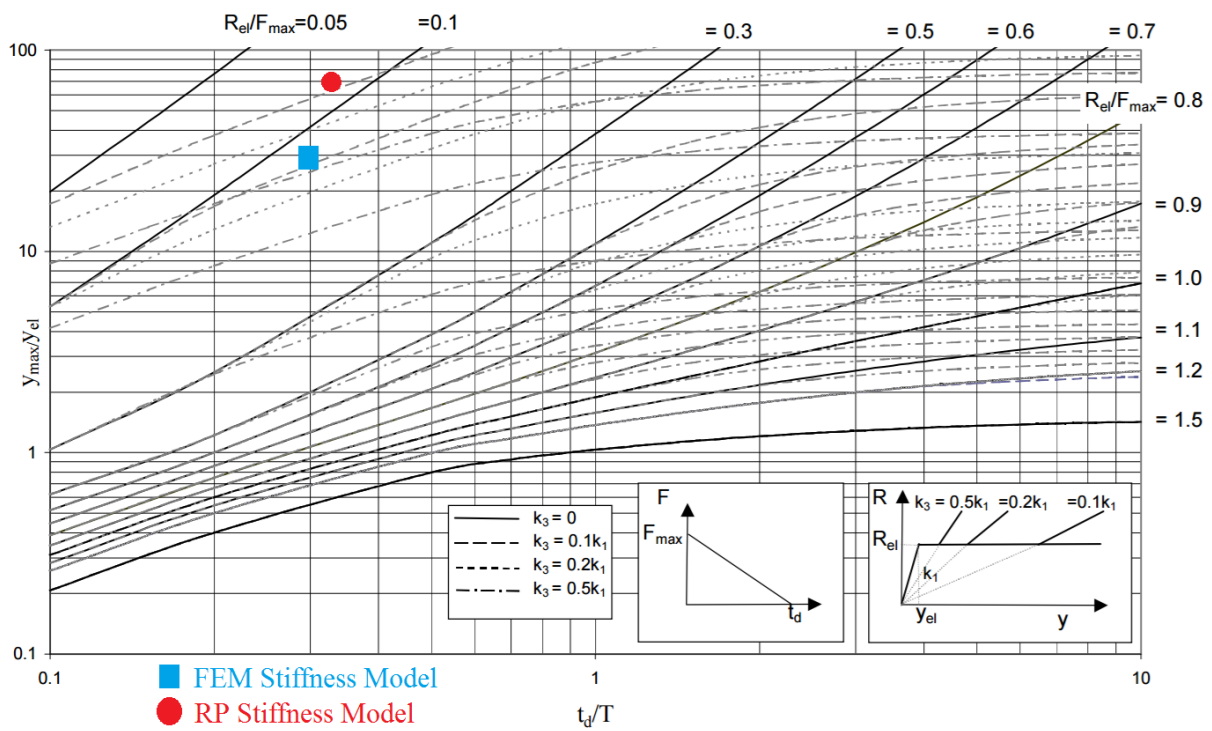


Figure 7.10: Deflection calculated for the stiffened plate subjected to the rigid design load pulse

The responses for the load given from the OTG are plotted in figure 7.11. Larger responses and larger discrepancies between the responses indicated by the relative loading are observed than for the case with the "rigid load pulse".

Also here, the indicated loading pulse is slightly conservative. The loading given by the OTG

does not lie perfectly beneath the triangular load impulse as indicated in the figure. The rise time is longer in the diagram with the rise time of the loading pulse equal to 6% of the loading duration as opposed to the 15% relative rise time the diagram is based upon .

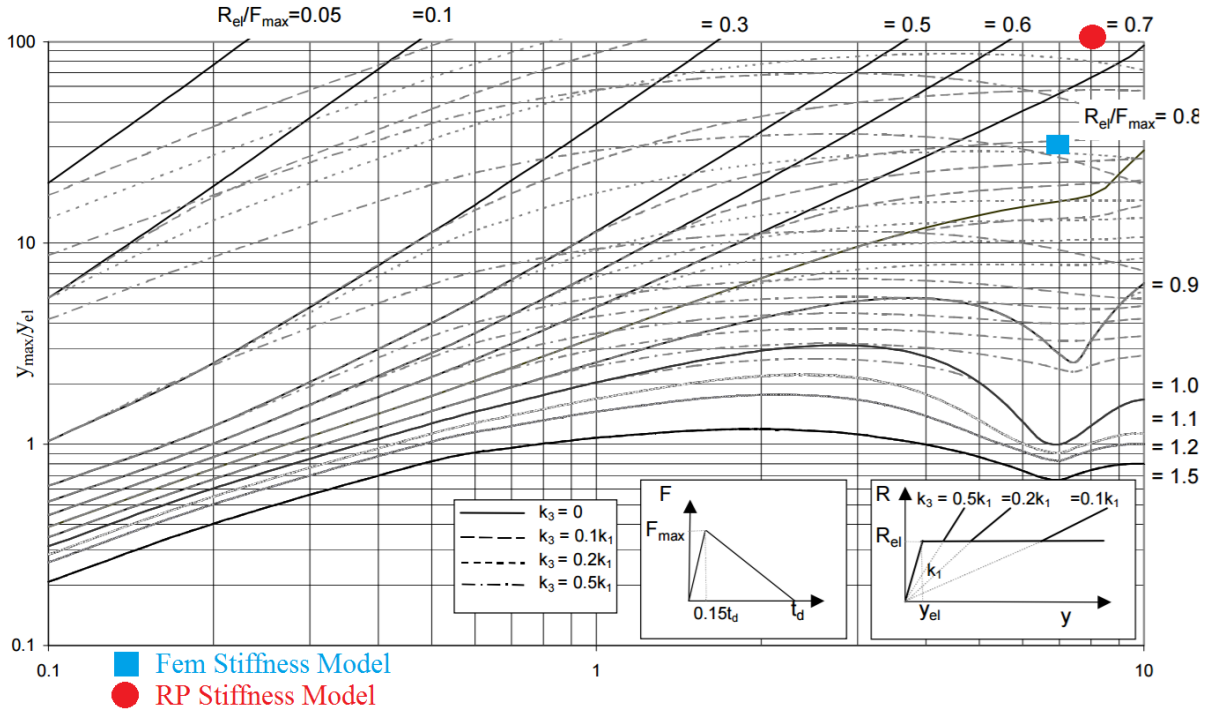


Figure 7.11: Deflection calculated for the stiffened plate subjected to the load given by the OTG

7.2.11 Energy Contents in Waves Relative to Response

In table 3.9 in section 3.3.3, the energy per 0.5[m] panel width is found to equal 485[kJ]. The relative energy content is calculated from the maximum deflection from the spring energy formula, seen in equation 7.3 with results seen in table 7.9.

$$E = \frac{1}{2}kw_{max}^2 \tag{7.3}$$

For OTG loading, the energy transferred to the plate for the stiffness model based on the RP exceeds the amount of energy estimated in the wave. Hence, the response seems unrealistically large. The rest of the analysis do not exceed the energy content in the wave.

Table 7.9: Energy in plate relative to wave energy calculated at maximum deflection for pinned and clamped plate

Stiffness model	"Rigid pulse"		OTG load	
	RP	FEM	RP	FEM
$\bar{k}[MN/m]$	2.10	11.76	2.18	11.38
$w_{max}[mm]$	420.00	170.00	0.77	200.00
$E[kJ]$	184.8	170	646.8	227.5
$\frac{E}{E_{wave}}$	0.38	0.35	1.33	0.47

The wave energy content is based upon the assumption that the wave is about to break. The energy in the structural response indicate that the initial estimation of wave energy content is unconservative. As the loading from the RP-model is based on the same geometric considerations, this indicates that the total load impulse is too small.

Chapter 8

Discussion

8.1 Establishing the Most Critical Sea State

The most critical sea state might not be solely defined by the largest negative air gap. The largest negative air gaps seldom occur in beam or head sea as the combined motions between different degrees of freedom lead to larger negative air gaps. This may cause waves to mainly hit at an angle greater than 0° . It is to note that (Huera-Huarte et al., 2011) indicates that the pressure pulse and thereby the response is related to the angle of impact with loads increasing drastically as the angle of impact approaches 0° .

8.2 Different Loading Models

Different loading models are discussed in the recommended practice and the offshore technical guidelines, with different factors of importance. In the recommended practises, the loading duration is longer, but the magnitude of the load is not as large as is the case for the offshore technical guidelines. The loading found from the OTG is also a better fit with the loading results found from experimental tests. The rigid drop tests carried out in the thesis have yielded even larger pressure peaks at even lower durations. It is to note that despite no plate deformation, the rigid drop tests are not completely rigid, as there is a stiffness at the boundaries. This would also be the case for experimental rigid drop tests as well. difficult to conduct in practical experiments.

For the three dimensional drop tests with deformable panels, pressure peaks of the same magnitude as found in the OTG were obtained. Loading coefficients found in drop tests in

(Huera-Huarte et al., 2011) gave a mean pressure equal to that found in the simulated drop test of $1.95[MPa]$ at the same impact velocity.

The resulting loads and deformations from the analysis assuming a non-breaking wave and methods given in (DNV, 2014b) were small compared to the rest of tested loading models. This indicates that ULS wave loads are mostly caused by breaking waves with a small relative angle of impact.

8.3 Hydroelasticity

By comparing the results from 3D drop tests of deformable panels with non-deformable panels, it is seen that the initial pressure impulse is larger for rigid panels than for deformable panels. This indicates that the response of the deformable panel has a noticeable effect on the pressure.

For the deformable panel, two phases of the pressures are observed; an initial pressure impulse and an added mass pressure. It is seen that the second pressure phase's duration decreases for high impact velocities. This could predominantly be caused by membrane forces increasing the stiffness and thus decreasing the natural period. It may also be caused by a decreased added mass for high impact velocities and deformation, or by a combination of the two. In addition, the peak of the second pressure surge doesn't have the same relationship as between velocity and pressure as the first pressure surge.

Even though the drop tests of rigid panel are theoretical, the pulses yield responses in the same order of magnitude for the 3D panels as well as the plate on the steel column. For the 2D model, the responses were 5% larger, indicating that the significance of hydroelasticity might vary based structural stiffness or other factors.

8.4 Applying Mean Pressure

As indicated in figure 4.8, the pressure varies both in the temporal and spacial domain. It is thereby difficult to find an appropriate shape of the spacial pressure to describe the pressure during the entire loading period. It has here been proposed to use the average pressure. This is a good fit at impact, as the pressure is found to be almost uniform at the time of impact. However, during deflection, the pressures at the end and middle of the plate are approximately 180° out of phase. In these periods, other pressure shapes could yield

more appropriate results. Overall, the mean pressure approximation could be justified, but for longer loading periods, a varying load shape could be more appropriate.

By loading the plate in the section between 10% and 90% of the plate's length, larger deformations were obtained as expected given the larger momentum applied onto the panel.

8.5 Simulating Wave Impacts in Drop Tests

In the literature, the peak pressures and loading due to wave impacts on offshore structures are proportional to the velocity squared. However, the findings from LS-Dyna indicates that for water impacts with an angle of 0° , the pressure peak is linearly dependent upon the the impact velocity. This might in part be due to the fact that the ALE approach in LS-Dyna doesn't include the drag component, where the loading is proportional to the velocity squared. In (Faltinsen, 2000), the impact velocity is used as an initial condition for calculating the deformation of the panel, and thus, the deformation by the approach is also linearly dependent, indicating that a linear relationship for the initial pressure pulse is reasonable when reviewing responses.

In terms of equation 2.28, this might indicate that for low impact angles, the product of the change in added mass and particle velocity might be the predominant factor in terms of establishing the total load. This may partially explain the linear relationship between the pressure and impact velocity.

When looking at the load pressure related to particle velocity in (DNV, 2014b), the factor C is small, in the range of 2 – 3. Thus, the loading given by $\frac{1}{2}\rho V^2 C$ adds a relatively small contribution to the overall pressure. This effect may thus be negligible when viewing the total pressure for low velocities. The differences between the load in the OTG and the load established from drop tests are the magnitude of the load as well as the duration of the load. The pressure peaks extracted from "rigid drop tests" are larger than those found in the OTG, but the duration of the load is far shorter. The OTG indicates that larger pressure peaks lead to shorter sustained load durations. Hence reducing the overall impact of large pressure peaks. Large pressure peaks are also indicated in (Huera-Huarte et al., 2011) where the pressure is indicated to approach infinity for small angles of impact.

In (Huera-Huarte et al., 2011), the load is parametrized in a manner which is more

conservative than the actual load development where the peak pressure is quadratically reduced between two pressure surges. A similar technique might be used with the deformable panel drop tests to obtain a more conservative result. A similar effect could possibly be obtained by adding components such as drag that are not included in the ALE procedure in LS-Dyna. The peak pressures obtained from deformable drop tests are in the same range as found from the OTG, and peak pressures calculated from the load factor found in (Huera-Huarte et al., 2011). This adds credibility to the proposed method. Even so, there are many factors and discrepancies that must be sorted out to use the model in order to accurately represent the loads of an incoming wave. The biggest upside to the coupled analysis looks to be the initial pressure and added mass pressure that is observed for the deformable plate upon water entry. As the ventilation effect is captured as well, the plate's response can also be accurately studied after the wave impact.

Chapter 9

Conclusion and Recommendations for Further Work

9.1 Conclusion

9.1.1 Influence of Negative Air Gap

Even in the survival condition, semi-submersibles may experience large negative air gaps. In all the tested methods for establishing the load, larger negative air gaps indicate larger loads. For the drop tests, this is mostly due to the increased particle velocities associated with larger waves. Larger negative air gaps yielded smaller relative upwelling values which lead to increased peak pressures by the loading model from the OTG.

9.1.2 Drop Tests

In the verification study, it was found that the ALE approach in LS-Dyna yielded results which agreed well with the results found in the drop test in (Faltinsen, 2005) indicating that the approach may be used to simulate drop tests with realistic results. It was assumed that as the wave is breaking, the impact angle would be close to 0° . However, for these impact angles, the pressure-time curve displayed different properties compared to the loading conditions from (GL, 2016b) with larger load peaks and shorter durations. For the three dimensional drop tests, the pressure peak was lower and in close to that found from the OTG. When viewing the added mass pressure, the duration of the pressure was closer as well.

The results from the verification study and drop tests based on the drop tests described in (Faltinsen, 2005) indicate that added mass forces are included in the analysis for deformable panels. As there are many uncertainties involved in accurately estimating added mass, this is a major benefit of conducting drop tests of stiffened panels, both in simulations and experimentally.

The initial peak pressure for the drop tests of the deformable plates are of limited interest as the contribution to the overall impulse is small due to the short duration. The pressure due to deformation is of more significance in terms of establishing the added mass. It is also to note that the overall structural response found from deformable panel drop tests are similar to those obtained using the OTG loading condition, both for the 3D panel and steel column. This indicates that the initiated velocities in the plate might be of higher importance than the pressure distribution found in these simulated drop tests.

9.1.3 Hydroelasticity

From the criterion given in (DNV, 2014a), it is clear that hydroelastic effects should be considered for the small impact angles evaluated in the thesis. The structural deformations obtained for a mean "rigid load pulse" was close to the deformations obtained for the coupled, hydroelastic calculations. When accounting for larger pressures near the panel centre, larger deformations were observed. It is to note that there is some uncertainty involved in the added mass modelling for the panels as well as the spatial pressure distribution.

Even though the difference in resulting deformations for the hydroelastic approach and non-hydroelastic response are small, the hydroelastic approach has some key benefits. The uncertainties involved in added mass modelling is reduced. In addition, the uncertainty regarding spatial pressure distribution is reduced. When simulating water entry problems, the hydroelastic analysis is also more simple than first simulating a drop test of a rigid panel to obtain the pressure pulse before applying that pressure to the structure. Therefore, the potential for increased accuracy is not at the expense of computational time by this approach.

9.1.4 Simulating Wave Impact by Water Entry

The pressure curves obtained by simulating drop tests do not share the peak nor the duration of the pressure curves obtained in wave impacts. This is the case both for pressure curves from deformable and non-deformable panels. Even so, the structural responses at drop velocities equivalent to the particle velocities in waves are in the same order of magnitude as when loaded by pressures equivalent to those from wave impacts. Further work has to be done in order to say anything conclusive, but based on the structural responses, the loading model shows promise with the added benefit of hydroelastic considerations included in the model.

9.1.5 Sources of Error

Boundary effects in LS-Dyna may yield some sources of error. As stated, there are no analytical solutions to slamming problems at an angle of impact of 0° . Hence, singularity effects due to the angle of impact might be significant and could lead to errors in the results. It is to note that in the experimental drop test described in (Faltinsen, 2005), the measured peak pressures varied for drop tests with the same input parameters and that narrow peak pressures are of limited interest as the response is approximately the same given the same drop angle and impact velocity.

There are also some difficulties in establishing the correct particle velocity. The same uncertainty in terms of establishing the particle velocity is also seen in the plate response. Also to note is that the rigid drop tests are not completely rigid. As for practical drop tests, the bottom plate is connected to the test rig via boundary components that are non-rigid. Some elastic motion is therefore observed for the plate, hence applying the obtained pressure as pressures without any observed deformation is not completely accurate.

9.2 Recommendations for Further Work

The approach has been to use linear wave and response theory with asymmetry factors and safety factors to predict the most critical sea state and relative upwelling. This may be non-conservative and lead to poor load and response calculations. It was initially proposed to investigate the effect of nonlinear floater pitch motions on the air gap calculations, both in the frequency domain and in the time domain. To get more accurate results regarding the

negative air gap and relative upwelling, these investigations should be carried out, both using potential theory and CFD.

The angle of impact appears to have an influence on both the duration and magnitude of the loads. More research on both the loads and response for angular drop tests at low impact angles should be carried out. Especially in terms of establishing a model between 0° and 5° as the pressures in the region appears to be characterised by a large amount of uncertainty and variance in the results.

More advanced stiffened plate response calculations for a plate under dynamic loading should be carried out. It was proposed to apply the resistance model for a stiffened plate developed by Yu & Amdahl, but at the time of writing the thesis, the work was not yet published and could not be applied. Additionally, response calculations considering other failure modes involving failure of several components should be carried out.

The ALE approach for establishing the load and response of stiffened panels show potential as hydroelastic effects are captured. Since there are some effects that are not captured in drop tests, analyses where these effects are accounted for should be carried out. This could be accomplished by adding pressure load curves onto the structure during the simulated drop tests to account for drag. The same effect would also be captured if the same drop tests was experimentally conducted in full scale.

In the outline of the thesis, CFD was proposed in order to establish the loading as well. Experimental drop tests and verification studies of the results using CFD and FEM coupling could be carried out.

As there are many uncertainties involved in establishing the loading condition based upon primarily angle of impact and water particle velocity, establishing the loads with more statistical data related to sea states could be of interest. 23 different sea states were tested and it could be of interest to investigate how loading curves related to relative upwelling as described in (GL, 2016b) would vary based upon the sea state in question.

Moreover, experiments with wave impacts on semi-submersibles where not only the pressures are measured, but also the angle of impact and water velocity is measured should be carried out. Thus, one could more accurately compare drop tests with values from incoming waves given similar velocities and angle of impact.

Nonlinear effects are of high importance above the mean water line, and especially in steep waves. Nonlinear wave theory should be applied to get a better representation of the

velocity in the wave. Because the SOK model yielded larger velocities than Wheeler stretching, it was applied as the most conservative velocity estimates. Different methods for establishing water particle velocities could be applied in order to get a more accurate load. CFD calculations might also be a good method for establishing said particle velocities for nonlinear theory.

References

- Review of wave in deck load assesment procedure author=Billington Osborne-Moss Engineer Ltd. (BOMEL), year=1998, journal=Report to Health & Safety Executive, Offshore Technology, Report OTO 97 073, London UK.
- Aksenov, A., Korenev, D., Shishaeva, A., Vucinic, D., and Mravak, Z. (2008). Drop-test fsi simulation with abaqus and flowvision based on the direct 2-way coupling approach. In *Abaqus Users' Conference, Newport, Rhode Island*, pages 611–624.
- Aquelet, N., Souli, M., and Olovsson, L. (2006). Euler–lagrange coupling with damping effects: Application to slamming problems. *Computer methods in applied mechanics and engineering*, 195(1):110–132.
- Bea, R., Iversen, R., and Xu, T. (2001). Wave-in-deck forces on offshore platforms. *Journal of Offshore Mechanics and Arctic Engineering*, 123(1):10–21.
- Brodtkorb, B. (2008). Prediction of wave-in-deck forces on fixed jacket-type structures based on cfd calculations. In *ASME 2008 27th International Conference on Offshore Mechanics and Arctic Engineering*, pages 713–721. American Society of Mechanical Engineers.
- DNV (2014a). Dnv-rp-c204: Design against accidental loads.
- DNV (2014b). Dnv-rp-c205: Environmental conditions and environmental loads.
- Donea, J., Giuliani, S., and Halleux, J.-P. (1982). An arbitrary lagrangian-eulerian finite element method for transient dynamic fluid-structure interactions. *Computer methods in applied mechanics and engineering*, 33(1-3):689–723.
- Faltinsen, O. (1993). *Sea loads on ships and offshore structures*, volume 1. Cambridge university press.

- Faltinsen, O. M. (2000). Hydroelastic slamming. *Journal of Marine Science and Technology*, 5(2):49–65.
- Faltinsen, O. M. (2005). *Hydrodynamics of high-speed marine vehicles*. Cambridge university press.
- GL, D. (2016a). Dnvgl-otg-13 prediction of airgap for column stabilized units.
- GL, D. (2016b). Dnvgl-otg-14 horizontal wave impact load for column stabilised units draft.
- Group, L.-D. A. W. et al. (2012). Modeling guidelines document.
- Huera-Huarte, F., Jeon, D., and Gharib, M. (2011). Experimental investigation of water slamming loads on panels. *Ocean Engineering*, 38(11):1347–1355.
- John, B. (1998). Numerical modelling of shock wave and pressure pulse generation by underwater explosions. NASA, (19990007753).
- Kaplan, P., Murray, J., and Yu, W. (1995). Theoretical analysis of wave impact forces on platform deck structures. Technical report, American Society of Mechanical Engineers, New York, NY (United States).
- Kazemi, S. and Incecik, A. (2007). Theoretical and experimental analysis of air gap response and wave-on-deck impact of floating offshore structures. In *ASME 2007 26th International Conference on Offshore Mechanics and Arctic Engineering*, pages 297–304. American Society of Mechanical Engineers.
- Kim, J.-H. and Shin, H.-C. (2008). Application of the ale technique for underwater explosion analysis of a submarine liquefied oxygen tank. *Ocean Engineering*, 35(8):812–822.
- Kjeldsen, S., Myrhaug, D., et al. (1979). Breaking waves in deep water and resulting wave forces. In *Offshore Technology Conference*. Offshore Technology Conference.
- Kjeldsen, S. P. and Myrhaug, D. (1978). *Kinematics and dynamics of breaking waves*. Vassdrags-og havnelaboratoriet ved Norges tekniske høgskole.
- Larsen, C. M. (2014). Tmr4180 marin dynamikk. *CM Larsen. Akademika*.
- Larsen, C. M. (2015). *Marine Dynamics: TMR4182 Marine Dynamics*, volume 1. Department of Marine Technology, Faculty of Engineering Science and Technology, NTNU.

- Lee, S.-G., Lee, I.-H., Baek, Y.-H., et al. (2010). Wet drop impact response analysis of cargo containment system in membrane-type lng carrier using fsi technique of ls-dyna. In *The Twentieth International Offshore and Polar Engineering Conference*. International Society of Offshore and Polar Engineers.
- Liu, M., Liu, G., and Lam, K. (2002). Investigations into water mitigation using a meshless particle method. *Shock waves*, 12(3):181–195.
- LSTC (2015). Ls-dyna keyword user's manual version volume ii. *Livermore Software Technology Corporation, Livermore, CA*.
- Manual, L.-D. K. U. and Volume, I. (2015). Material models. *Volume, 2*.
- Meyerhoff, W. (1970). Added masses of thin rectangular plates calculated from potential theory. *J Ship Res*, 14:100–111.
- Standard, N. (2004). N-004,“. *Design of steel structures*.
- Stenius, I., Rosén, A., and Kutteneuler, J. (2011). Hydroelastic interaction in panel-water impacts of high-speed craft. *Ocean Engineering*, 38(2):371–381.
- Tutt, B., Richard, C., Roland, S., and Noetscher, G. (2010). Development of parachute simulation techniques in ls-dyna. In *11th International LS-DYNA Users Conference*, pages 25–36. Livermore Software Technology Corporation.
- Tveitnes, T., Fairlie-Clarke, A., and Varyani, K. (2008). An experimental investigation into the constant velocity water entry of wedge-shaped sections. *Ocean Engineering*, 35(14):1463–1478.
- Veritas, D. N. (2008). Sesam user manual wadam.
- Veritas, D. N. (2011a). Dnv-os-c101 design of offshore steel structures, general (lrfd method). *April, Høvik*.
- Veritas, D. N. (2011b). Modelling and analysis of marine operations. *Det Norske Veritas, tech. rep. DNV-RP-H103*.
- Veritas, D. N. (2013). Determination of structural capacity by non-linear fe analysis methods. Technical report, DNV-RP-C208, DET NORSKE VERITAS (DNV), Oslo.

Von Karman, T. (1929). The impact on seaplane floats during landing.

Wheeler, J. et al. (1969). Methods for calculating forces produced by irregular waves. In *Offshore Technology Conference*. Offshore Technology Conference.

Yang, X., Zhang, Z., Yang, J., and Sun, Y. (2016). Fluid–structure interaction analysis of the drop impact test for helicopter fuel tank. *SpringerPlus*, 5(1):1573.

Appendix A

RAOs

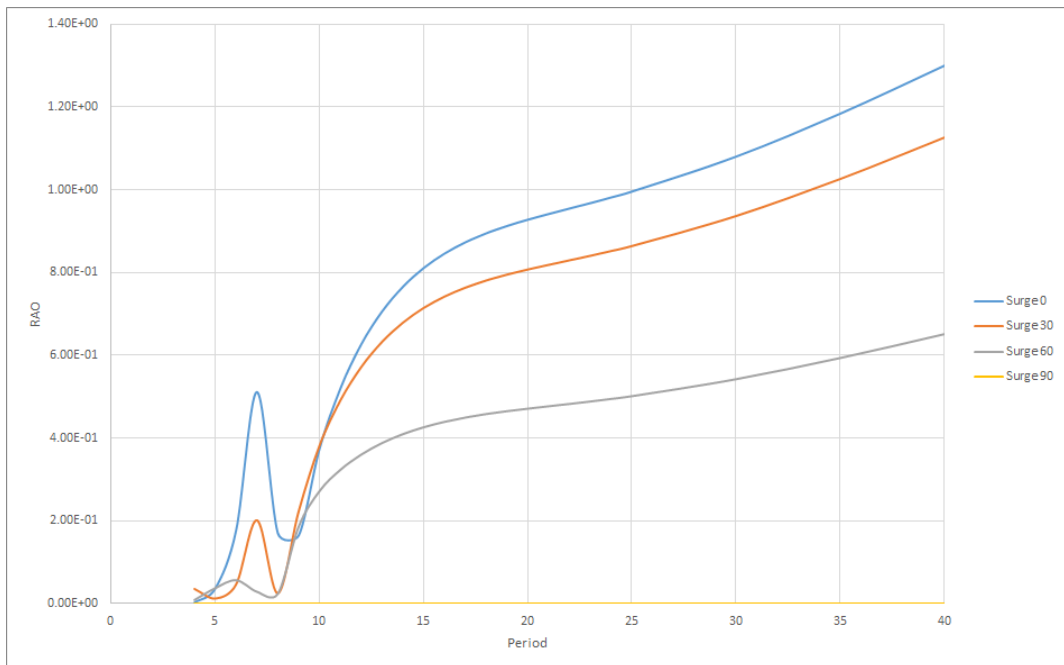


Figure A.1: Surge RAO from Wadam air gap analysis

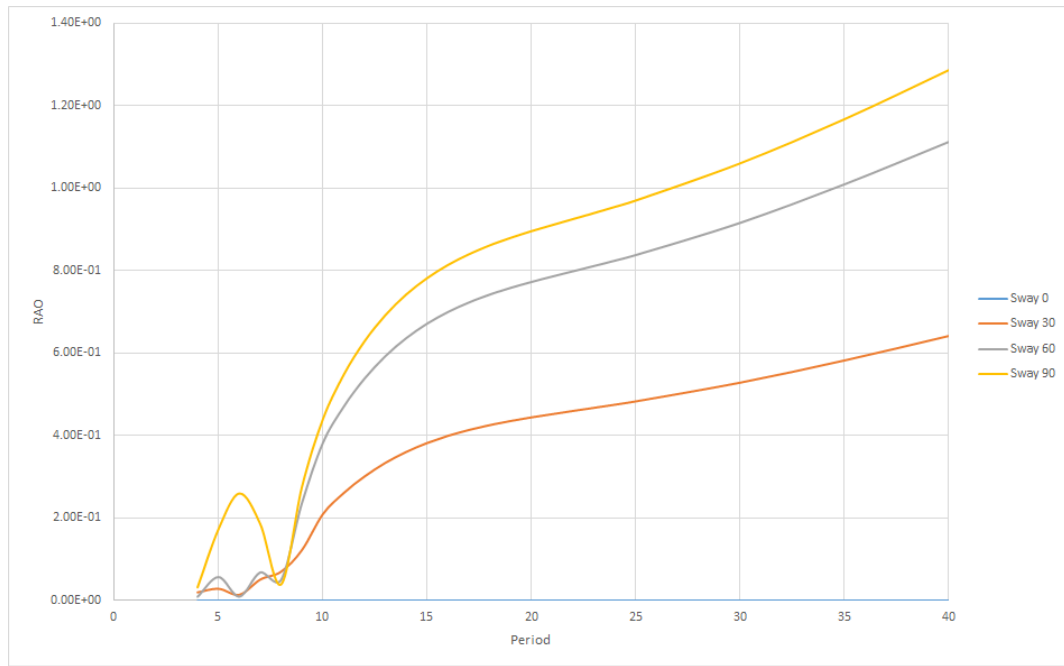


Figure A.2: Sway RAO from Wadam air gap analysis

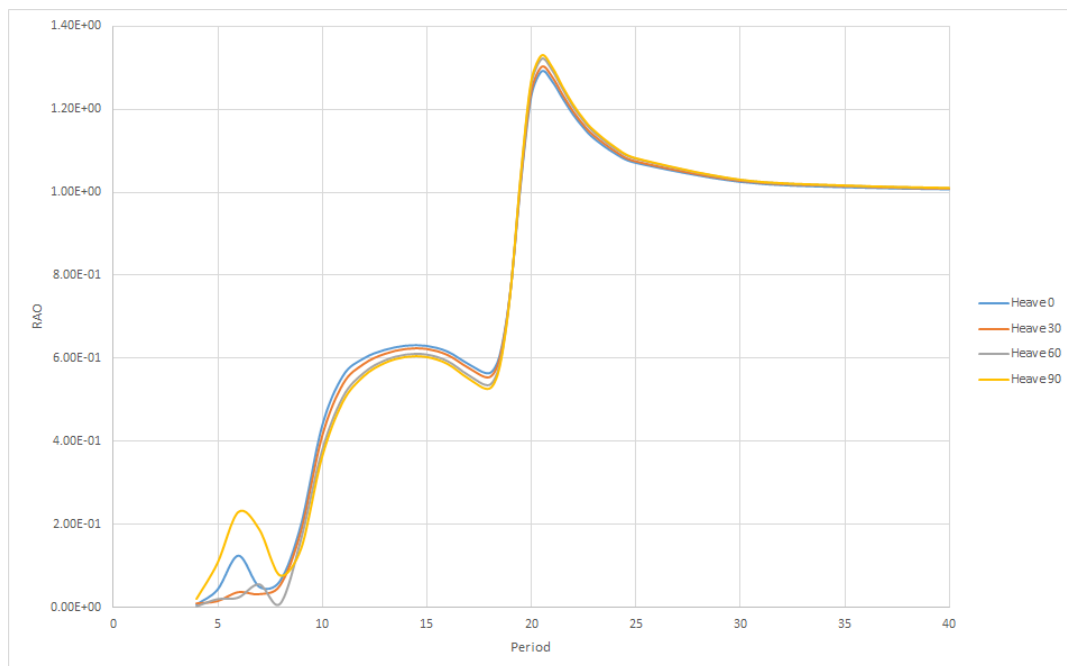


Figure A.3: Heave RAO from Wadam air gap analysis

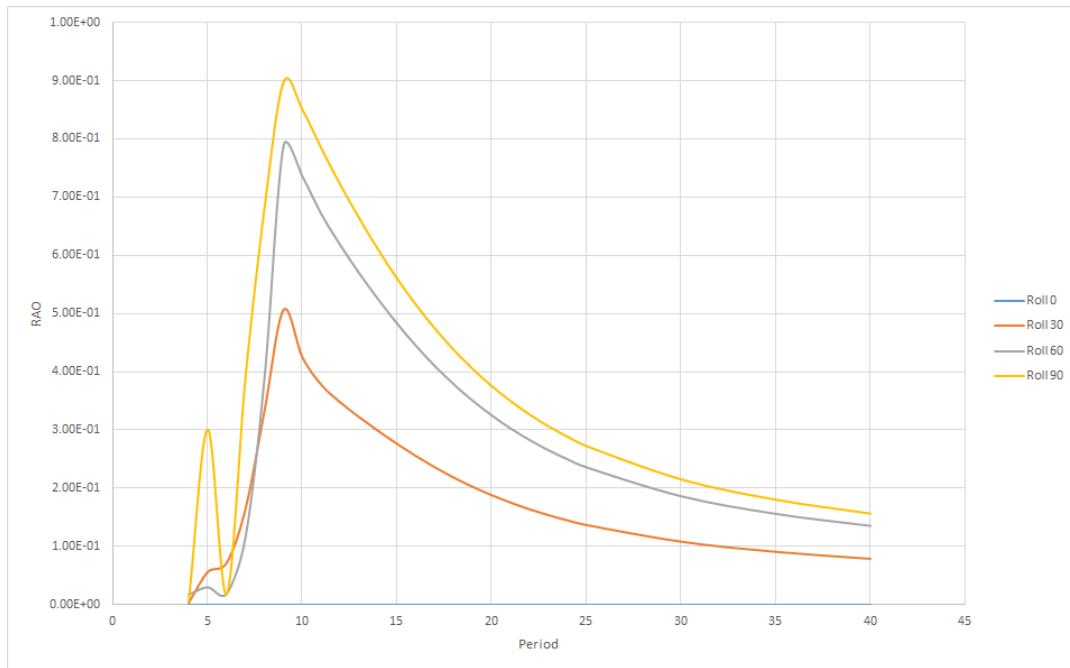


Figure A.4: Roll RAO from Wadam air gap analysis. The amplitude is in degrees

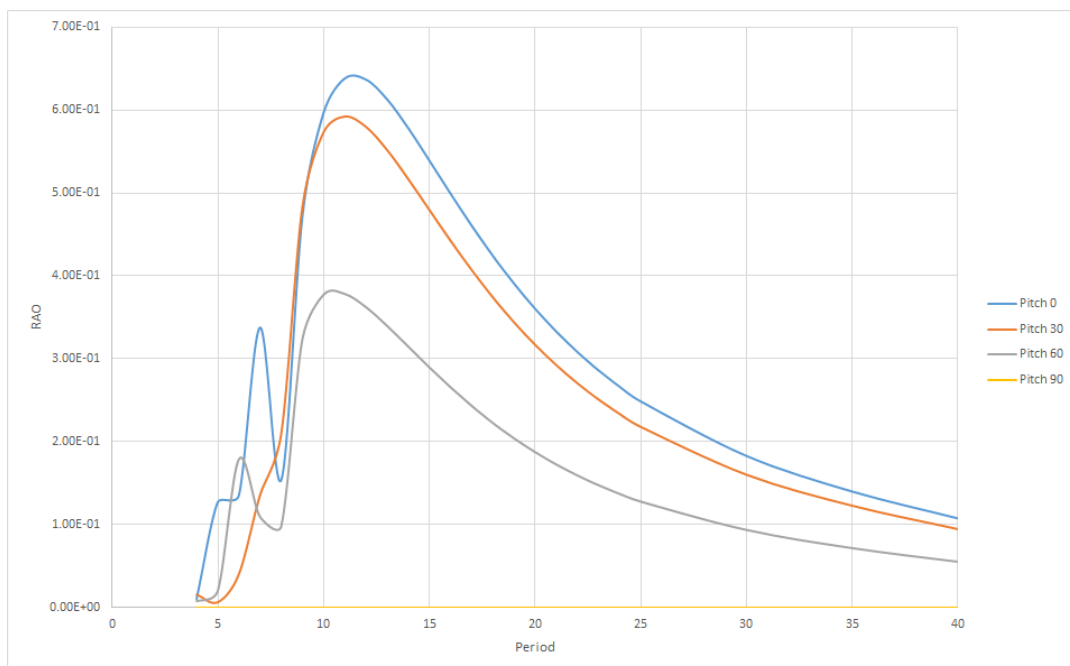


Figure A.5: Pitch RAO from Wadam air gap analysis. The amplitude is in degrees

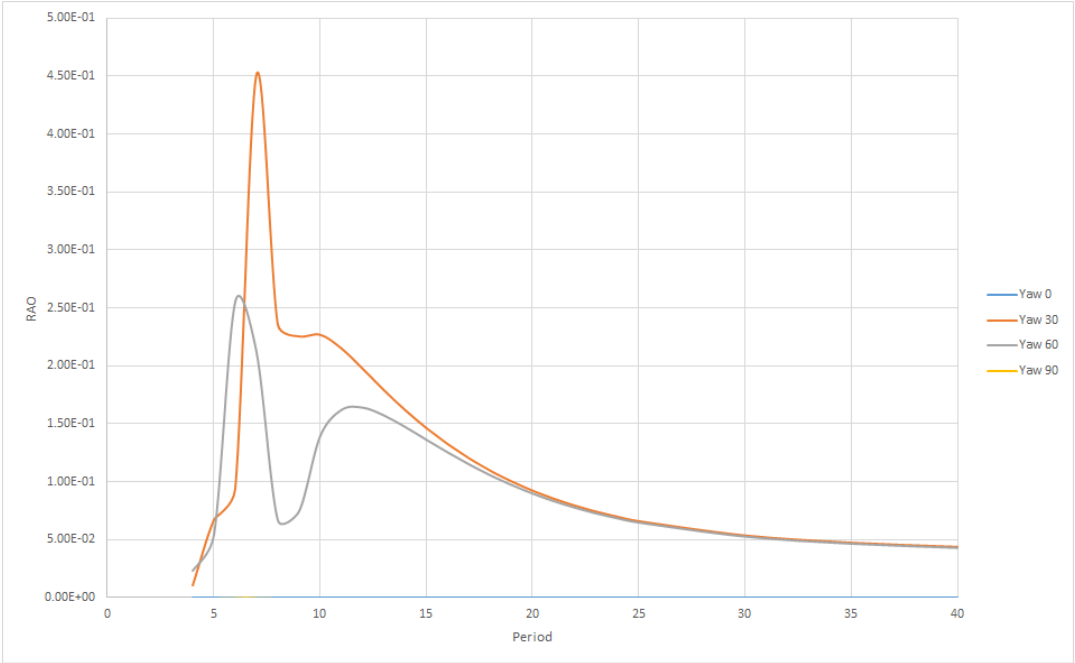


Figure A.6: Yaw RAO from Wadam air gap analysis. The amplitude is in degrees

Appendix B

Spectra

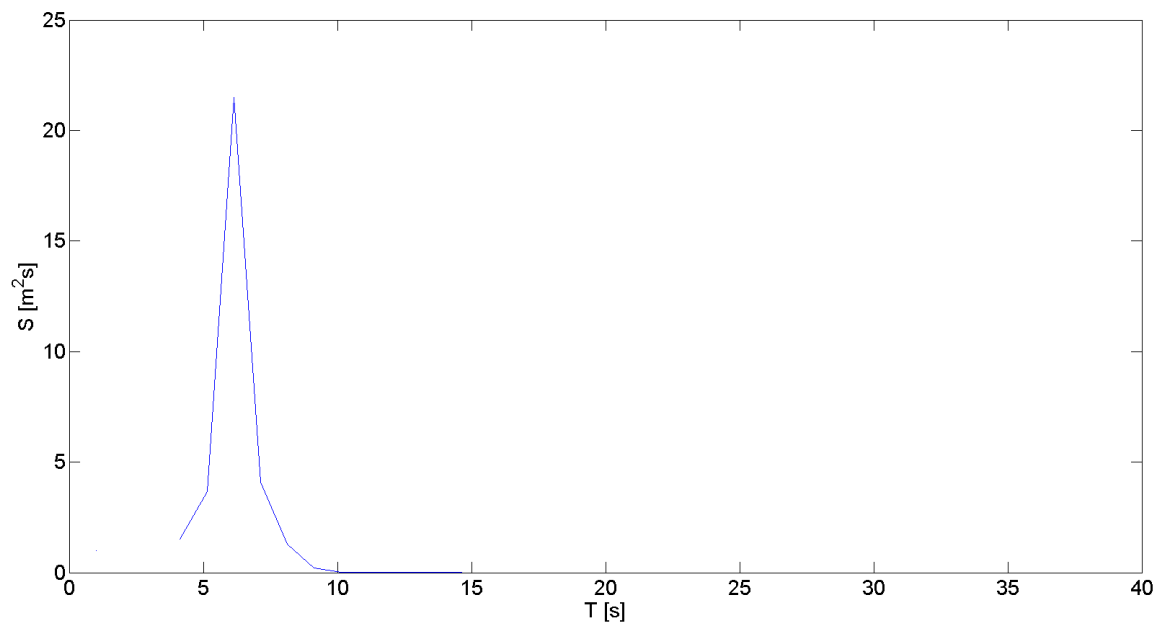


Figure B.1: Jonswap spectrum for run ID 6

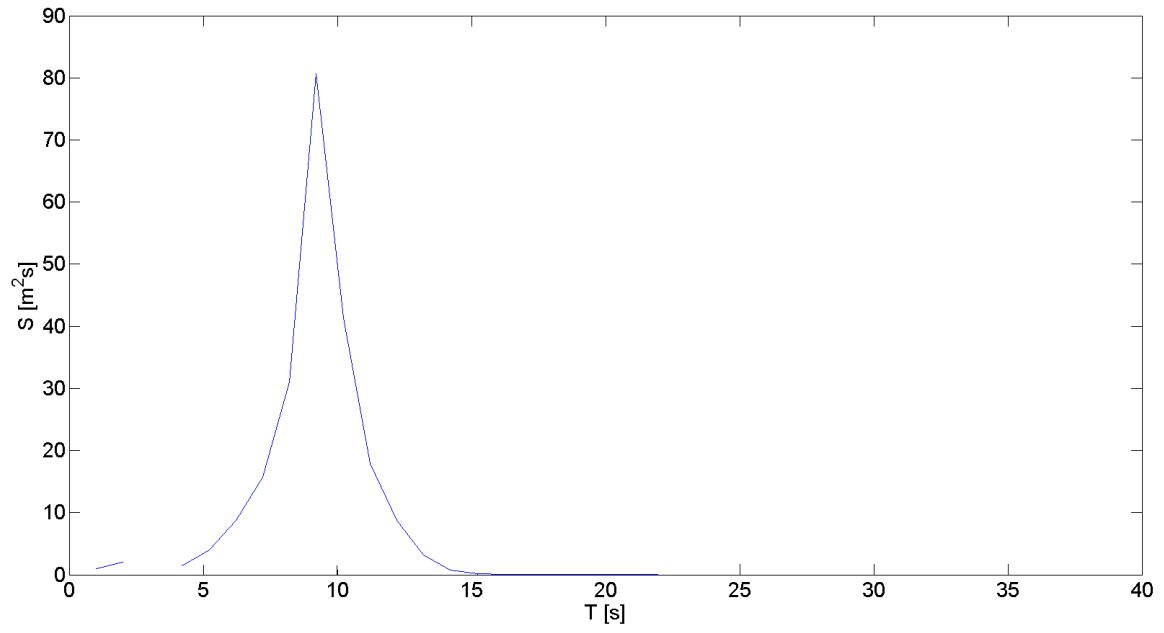


Figure B.2: Jonswap spectrum for run ID 15

Appendix C

Air Gap Results

Table C.1: Sea states leading to the largest negative air gaps for each sampling point

Point	$a_{min}[m]$	$H_S[m]$	$T_Z[s]$	$Direction[^\circ]$	$upwelling_{relative}[]$
AG1	-4.79	17.3	12.9	30	0.82
AG2	-4.82	17.3	12.9	30	0.81
AG3	-4.18	17.3	12.9	30	0.84
AG4	-3.54	17.3	12.9	30	0.88
AG5	-3.15	17.3	12.9	30	0.90
AG6	-3.00	17.3	12.9	30	0.91
AG7	-3.07	17.2	13.5	30	0.90
AG8	-3.59	17.3	12.9	30	0.87
AG9	-4.54	17.3	12.9	30	0.83
AG10	-5.54	17.3	12.9	30	0.78
AG11	-5.75	17.3	12.9	30	0.77
AG12	-5.07	17.3	12.9	45	0.80
AG13	-5.17	17.3	12.9	45	0.80
AG14	-3.65	17.3	12.9	150	0.87
AG15	-3.98	17.3	12.9	165	0.85
AG16	-3.92	17.3	12.9	15	0.86
AG17	-3.60	17.3	12.9	30	0.87
AG18	-5.21	17.3	12.9	135	0.80
AG19	-5.10	17.3	12.9	135	0.80

Appendix D

OTG Pressure Curves

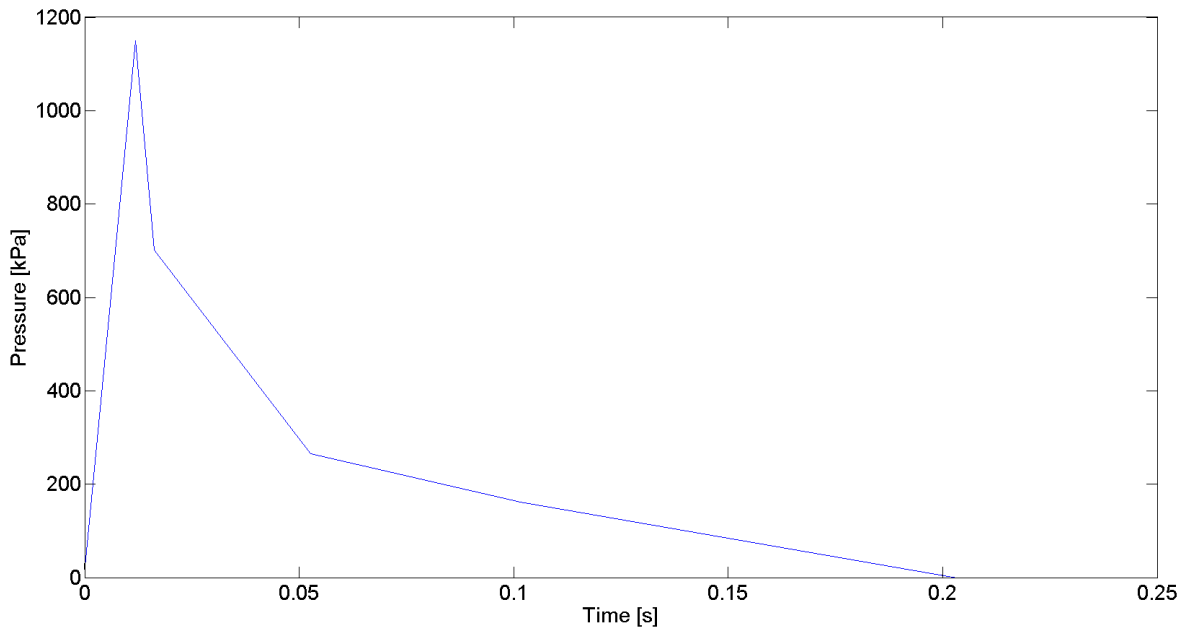


Figure D.1: Pressure development based on OTG for sea state 6

Appendix E

Air Gap Calculation Script

```
#####
% The file calculates the air-gap in certain point below the box bottom at 28 m
% Project: Erik Skjeggedal Master Thesis
%
%
#####
%-----
% Create Jonswap wave spectrum
%-----
%
FILE READ SIF-FORMATTED ' ' G1
%
SET TITLE
'TestStemi'
'Survival draught: 15.00m'
'JONSWAP asymmetry factor1.3'
',-'
%
%
DEFINE PRESENTATION-OPTION SIMULTANEOUS-BODIES SINGLE
DEFINE PRESENTATION-OPTION ABCISSA-AXIS PERIOD
DEFINE PRESENTATION-OPTION RESPONSE-VARIABLE ORDINATE-VALUES AMPLITUDE
DEFINE PRESENTATION-OPTION RESPONSE-VARIABLE ORDINATE-UNITS DEGREES
DEFINE PRESENTATION-OPTION RESPONSE-VARIABLE SECOND-ORDER-GRAPH FIRST-DIRECTION
DEFINE PRESENTATION-OPTION RESPONSE-VARIABLE CONTOUR-LEVELS -1.0 1.0 0.2
%
%
% Survival 300 meter water depth
%
%
CREATE WAVE-SPECTRUM
LOOP
%


|        |     |         |        |       | Hs[m] | Tz[s] | gamma | sigmaa | sigmab |
|--------|-----|---------|--------|-------|-------|-------|-------|--------|--------|
| JONS1  | ' ' | JONSWAP | SINGLE | HS-TZ | 5.62  | 6.00  | 5.00  | 0.07   | 0.09   |
| JONS2  | ' ' | JONSWAP | SINGLE | HS-TZ | 6.34  | 6.50  | 5.00  | 0.07   | 0.09   |
| JONS3  | ' ' | JONSWAP | SINGLE | HS-TZ | 7.14  | 7.00  | 5.00  | 0.07   | 0.09   |
| JONS4  | ' ' | JONSWAP | SINGLE | HS-TZ | 7.96  | 7.50  | 5.00  | 0.07   | 0.09   |
| JONS5  | ' ' | JONSWAP | SINGLE | HS-TZ | 8.78  | 8.00  | 5.00  | 0.07   | 0.09   |
| JONS6  | ' ' | JONSWAP | SINGLE | HS-TZ | 9.6   | 8.50  | 5.00  | 0.07   | 0.09   |
| JONS7  | ' ' | JONSWAP | SINGLE | HS-TZ | 10.42 | 9.00  | 5.00  | 0.07   | 0.09   |
| JONS8  | ' ' | JONSWAP | SINGLE | HS-TZ | 11.22 | 9.50  | 5.00  | 0.07   | 0.09   |
| JONS9  | ' ' | JONSWAP | SINGLE | HS-TZ | 12    | 10.00 | 5.00  | 0.07   | 0.09   |
| JONS10 | ' ' | JONSWAP | SINGLE | HS-TZ | 12.76 | 10.50 | 4.59  | 0.07   | 0.09   |
| JONS11 | ' ' | JONSWAP | SINGLE | HS-TZ | 13.48 | 11.00 | 4.04  | 0.07   | 0.09   |
| JONS12 | ' ' | JONSWAP | SINGLE | HS-TZ | 14.16 | 11.50 | 3.51  | 0.07   | 0.09   |


```



```

JONS13      ' '      JONSWAP    SINGLE    HS-TZ    14.98 12.00    3.15    0.07    0.09
JONS14      ' '      JONSWAP    SINGLE    HS-TZ    16.25 12.50    3.14    0.07    0.09
JONS15      ' '      JONSWAP    SINGLE    HS-TZ    17.3  12.90    3.15    0.07    0.09
JONS16      ' '      JONSWAP    SINGLE    HS-TZ    17.2  13.50    2.18    0.07    0.09
JONS17      ' '      JONSWAP    SINGLE    HS-TZ    17.1  14.00    1.60    0.07    0.09
JONS18      ' '      JONSWAP    SINGLE    HS-TZ    16.6  15.00    1.00    0.07    0.09
JONS19      ' '      JONSWAP    SINGLE    HS-TZ    14.7  16.00    1.00    0.07    0.09
JONS20      ' '      JONSWAP    SINGLE    HS-TZ    14.4  17.00    1.00    0.07    0.09
JONS21      ' '      JONSWAP    SINGLE    HS-TZ    12.4  18.00    1.00    0.07    0.09
JONS22      ' '      JONSWAP    SINGLE    HS-TZ    8.2   19.00    1.00    0.07    0.09
JONS23      ' '      JONSWAP    SINGLE    HS-TZ    8.2   20.00    1.00    0.07    0.09
END
%
% -----
% Create wave spreading function
% -----
%
% Print to file
%
%
% SWL to deck bottom 28m - 15m = 13m
%
SET PRINT DESTINATION CSV-FILE
%
%=====
%CREATE POINTS FOR AIR GAP
%=====
%
CREATE SPECIFIC-POINT AP1  'Point for air gap'    -48    25    13
CREATE SPECIFIC-POINT AP2  'Point for air gap'    -48    20    13
CREATE SPECIFIC-POINT AP3  'Point for air gap'    -48    15    13
CREATE SPECIFIC-POINT AP4  'Point for air gap'    -48    10    13
CREATE SPECIFIC-POINT AP5  'Point for air gap'    -48     5    13
CREATE SPECIFIC-POINT AP6  'Point for air gap'    -48     0    13
CREATE SPECIFIC-POINT AP7  'Point for air gap'    -48    -5    13
CREATE SPECIFIC-POINT AP8  'Point for air gap'    -48   -10    13
CREATE SPECIFIC-POINT AP9  'Point for air gap'    -48   -15    13
CREATE SPECIFIC-POINT AP10 'Point for air gap'    -48   -20    13
CREATE SPECIFIC-POINT AP11 'Point for air gap'    -48   -25    13
CREATE SPECIFIC-POINT AP12 'Point for air gap'    -44   -33    13
CREATE SPECIFIC-POINT AP13 'Point for air gap'    -40   -33    13
CREATE SPECIFIC-POINT AP14 'Point for air gap'    -20   -33    13
CREATE SPECIFIC-POINT AP15 'Point for air gap'    -10   -33    13
CREATE SPECIFIC-POINT AP16 'Point for air gap'     10   -33    13
CREATE SPECIFIC-POINT AP17 'Point for air gap'     20   -33    13
CREATE SPECIFIC-POINT AP18 'Point for air gap'     40   -33    13
CREATE SPECIFIC-POINT AP19 'Point for air gap'     44   -33    13
%
%=====
% CREATE POINTS FOR ACCELERATION
%=====
%
%=====
%AIR GAP VERTICAL MOTION
%=====
CREATE RESPONSE-VARIABLE MOT1 'Vertical motion at AP1' COMBINED-MOTION AP1 ( ONLY HEAVE PITCH ROLL SURGE SWAY YAW ) DISPLACEMENT ABSOLUTE Z
CREATE RESPONSE-VARIABLE MOT2 'Vertical motion at AP2' COMBINED-MOTION AP2 ( ONLY HEAVE PITCH ROLL SURGE SWAY YAW ) DISPLACEMENT ABSOLUTE Z
CREATE RESPONSE-VARIABLE MOT3 'Vertical motion at AP3' COMBINED-MOTION AP3 ( ONLY HEAVE PITCH ROLL SURGE SWAY YAW ) DISPLACEMENT ABSOLUTE Z
CREATE RESPONSE-VARIABLE MOT4 'Vertical motion at AP4' COMBINED-MOTION AP4 ( ONLY HEAVE PITCH ROLL SURGE SWAY YAW ) DISPLACEMENT ABSOLUTE Z
CREATE RESPONSE-VARIABLE MOT5 'Vertical motion at AP5' COMBINED-MOTION AP5 ( ONLY HEAVE PITCH ROLL SURGE SWAY YAW ) DISPLACEMENT ABSOLUTE Z
CREATE RESPONSE-VARIABLE MOT6 'Vertical motion at AP6' COMBINED-MOTION AP6 ( ONLY HEAVE PITCH ROLL SURGE SWAY YAW ) DISPLACEMENT ABSOLUTE Z
CREATE RESPONSE-VARIABLE MOT7 'Vertical motion at AP7' COMBINED-MOTION AP7 ( ONLY HEAVE PITCH ROLL SURGE SWAY YAW ) DISPLACEMENT ABSOLUTE Z
CREATE RESPONSE-VARIABLE MOT8 'Vertical motion at AP8' COMBINED-MOTION AP8 ( ONLY HEAVE PITCH ROLL SURGE SWAY YAW ) DISPLACEMENT ABSOLUTE Z
CREATE RESPONSE-VARIABLE MOT9 'Vertical motion at AP9' COMBINED-MOTION AP9 ( ONLY HEAVE PITCH ROLL SURGE SWAY YAW ) DISPLACEMENT ABSOLUTE Z
CREATE RESPONSE-VARIABLE MOT10 'Vertical motion at AP10' COMBINED-MOTION AP10 ( ONLY HEAVE PITCH ROLL SURGE SWAY YAW ) DISPLACEMENT ABSOLUTE Z
CREATE RESPONSE-VARIABLE MOT11 'Vertical motion at AP11' COMBINED-MOTION AP11 ( ONLY HEAVE PITCH ROLL SURGE SWAY YAW ) DISPLACEMENT ABSOLUTE Z

```

```

CREATE RESPONSE-VARIABLE MOT12 'Vertical motion at AP12' COMBINED-MOTION AP12 ( ONLY HEAVE PITCH ROLL SURGE SWAY YAW ) DISPLACEMENT ABSOLUTE Z
CREATE RESPONSE-VARIABLE MOT13 'Vertical motion at AP13' COMBINED-MOTION AP13 ( ONLY HEAVE PITCH ROLL SURGE SWAY YAW ) DISPLACEMENT ABSOLUTE Z
CREATE RESPONSE-VARIABLE MOT14 'Vertical motion at AP14' COMBINED-MOTION AP14 ( ONLY HEAVE PITCH ROLL SURGE SWAY YAW ) DISPLACEMENT ABSOLUTE Z
CREATE RESPONSE-VARIABLE MOT15 'Vertical motion at AP15' COMBINED-MOTION AP15 ( ONLY HEAVE PITCH ROLL SURGE SWAY YAW ) DISPLACEMENT ABSOLUTE Z
CREATE RESPONSE-VARIABLE MOT16 'Vertical motion at AP16' COMBINED-MOTION AP16 ( ONLY HEAVE PITCH ROLL SURGE SWAY YAW ) DISPLACEMENT ABSOLUTE Z
CREATE RESPONSE-VARIABLE MOT17 'Vertical motion at AP17' COMBINED-MOTION AP17 ( ONLY HEAVE PITCH ROLL SURGE SWAY YAW ) DISPLACEMENT ABSOLUTE Z
CREATE RESPONSE-VARIABLE MOT18 'Vertical motion at AP18' COMBINED-MOTION AP18 ( ONLY HEAVE PITCH ROLL SURGE SWAY YAW ) DISPLACEMENT ABSOLUTE Z
CREATE RESPONSE-VARIABLE MOT19 'Vertical motion at AP19' COMBINED-MOTION AP19 ( ONLY HEAVE PITCH ROLL SURGE SWAY YAW ) DISPLACEMENT ABSOLUTE Z
%
% N.B. Not necessary to create Is relative motion to undisturbed %wave
%
%
CREATE RESPONSE-VARIABLE AGT1 'Air gap based on total wave' GENERAL-COMBINATION ( ONLY MOT1 1.0 ELEV1 -1.3 )
CREATE RESPONSE-VARIABLE AGT2 'Air gap based on total wave' GENERAL-COMBINATION ( ONLY MOT2 1.0 ELEV2 -1.3 )
CREATE RESPONSE-VARIABLE AGT3 'Air gap based on total wave' GENERAL-COMBINATION ( ONLY MOT3 1.0 ELEV3 -1.3 )
CREATE RESPONSE-VARIABLE AGT4 'Air gap based on total wave' GENERAL-COMBINATION ( ONLY MOT4 1.0 ELEV4 -1.3 )
CREATE RESPONSE-VARIABLE AGT5 'Air gap based on total wave' GENERAL-COMBINATION ( ONLY MOT5 1.0 ELEV5 -1.3 )
CREATE RESPONSE-VARIABLE AGT6 'Air gap based on total wave' GENERAL-COMBINATION ( ONLY MOT6 1.0 ELEV6 -1.3 )
CREATE RESPONSE-VARIABLE AGT7 'Air gap based on total wave' GENERAL-COMBINATION ( ONLY MOT7 1.0 ELEV7 -1.3 )
CREATE RESPONSE-VARIABLE AGT8 'Air gap based on total wave' GENERAL-COMBINATION ( ONLY MOT8 1.0 ELEV8 -1.3 )
CREATE RESPONSE-VARIABLE AGT9 'Air gap based on total wave' GENERAL-COMBINATION ( ONLY MOT9 1.0 ELEV9 -1.3 )
CREATE RESPONSE-VARIABLE AGT10 'Air gap based on total wave' GENERAL-COMBINATION ( ONLY MOT10 1.0 ELEV10 -1.3 )
CREATE RESPONSE-VARIABLE AGT11 'Air gap based on total wave' GENERAL-COMBINATION ( ONLY MOT11 1.0 ELEV11 -1.3 )
CREATE RESPONSE-VARIABLE AGT12 'Air gap based on total wave' GENERAL-COMBINATION ( ONLY MOT12 1.0 ELEV12 -1.3 )
CREATE RESPONSE-VARIABLE AGT13 'Air gap based on total wave' GENERAL-COMBINATION ( ONLY MOT13 1.0 ELEV13 -1.3 )
CREATE RESPONSE-VARIABLE AGT14 'Air gap based on total wave' GENERAL-COMBINATION ( ONLY MOT14 1.0 ELEV14 -1.3 )
CREATE RESPONSE-VARIABLE AGT15 'Air gap based on total wave' GENERAL-COMBINATION ( ONLY MOT15 1.0 ELEV15 -1.3 )
CREATE RESPONSE-VARIABLE AGT16 'Air gap based on total wave' GENERAL-COMBINATION ( ONLY MOT16 1.0 ELEV16 -1.3 )
CREATE RESPONSE-VARIABLE AGT17 'Air gap based on total wave' GENERAL-COMBINATION ( ONLY MOT17 1.0 ELEV17 -1.3 )
CREATE RESPONSE-VARIABLE AGT18 'Air gap based on total wave' GENERAL-COMBINATION ( ONLY MOT18 1.0 ELEV18 -1.3 )
CREATE RESPONSE-VARIABLE AGT19 'Air gap based on total wave' GENERAL-COMBINATION ( ONLY MOT19 1.0 ELEV19 -1.3 )

%
%
%
SET DISPLAY DEVICE WINDOWS
SET DISPLAY DESTINATION FILE
SET DISPLAY WORKSTATION-WINDOW 60 120 40 100
%SET PRINT PAGE-ORIENTATION LANDSCAPE
SET PLOT COLOUR ON
SET PLOT FORMAT CGM-BINARY
SET PLOT PAGE-SIZE A4
%
SET PRINT DESTINATION CSV-FILE
SET PRINT PAGE-HEIGHT 10000
SET PRINT PAGE-ORIENTATION PORTRAIT
SET PRINT SCREEN-HEIGHT 24
%
CREATE RESPONSE-SPECTRUM
(ONLY AGT1 MOT1)
(ONLY 0.0 15.0 30.0 45.0 60.0 75.0 90.0 105.0 120. 135. 150. 165. 180. )
( ONLY JONS1 JONS2 JONS3 JONS4 JONS5 JONS6 JONS7 JONS8 JONS9 JONS10 JONS11 JONS12 JONS13 JONS14 JONS15 JONS16 JONS17 JONS18 JONS19 JONS20 JONS21
JONS22 JONS23) NONE
%
SET PRINT FILE ' ' ABSOLUTE_MOTIONS_POINT1_OVERVIEW_Testsemi
PRINT OVERVIEW RESPONSE-SPECTRUM
%
SET PRINT FILE ' ' ABSOLUTE_MOTIONS_POINT1_STATISTICS_ULS_Testsemi
PRINT SHORT-TERM-STATISTICS RAYLEIGH SEA-STATE-DURATION ( ONLY 10800 ) *
DELETE RESPONSE-SPECTRUM *
XXXXXXXXXXXXXXXXXXXXXXXXXXXXXXXXXXXXXXXXXXXXXXXXXXXXXXXXXXXXXXXXXXXXXXXXXXXX
CREATE RESPONSE-SPECTRUM
(ONLY AGT2 MOT2)
(ONLY 0.0 15.0 30.0 45.0 60.0 75.0 90.0 105.0 120. 135. 150. 165. 180. )
( ONLY JONS1 JONS2 JONS3 JONS4 JONS5 JONS6 JONS7 JONS8 JONS9 JONS10 JONS11 JONS12 JONS13 JONS14 JONS15 JONS16 JONS17 JONS18 JONS19 JONS20 JONS21
JONS22 JONS23) NONE

```

```
%
SET PRINT FILE ' ' ABSOLUTE_MOTIONS_POINT2_OVERVIEW_Testsemi
PRINT OVERVIEW RESPONSE-SPECTRUM
%
SET PRINT FILE ' ' ABSOLUTE_MOTIONS_POINT2_STATISTICS_ULS_Testsemi
PRINT SHORT-TERM-STATISTICS RAYLEIGH SEA-STATE-DURATION ( ONLY 10800 ) *
DELETE RESPONSE-SPECTRUM *
%%%%%%%%%%%%%%%%%%%%%%%%%%%%%%%%%%%%%%%%%%%%%%%%%%%%%%%%%%%%%%%%%%%%%%%%
CREATE RESPONSE-SPECTRUM
(ONLY AGT3 MOT3)
(ONLY 0.0 15.0 30.0 45.0 60.0 75.0 90.0 105.0 120. 135. 150. 165. 180. )
( ONLY JONS1 JONS2 JONS3 JONS4 JONS5 JONS6 JONS7 JONS8 JONS9 JONS10 JONS11 JONS12 JONS13 JONS14 JONS15 JONS16 JONS17 JONS18 JONS19 JONS20 JONS21
JONS22 JONS23) NONE
%
SET PRINT FILE ' ' ABSOLUTE_MOTIONS_POINT3_OVERVIEW_Testsemi
PRINT OVERVIEW RESPONSE-SPECTRUM
%
SET PRINT FILE ' ' ABSOLUTE_MOTIONS_POINT3_STATISTICS_ULS_Testsemi
PRINT SHORT-TERM-STATISTICS RAYLEIGH SEA-STATE-DURATION ( ONLY 10800 ) *
DELETE RESPONSE-SPECTRUM *
%%%%%%%%%%%%%%%%%%%%%%%%%%%%%%%%%%%%%%%%%%%%%%%%%%%%%%%%%%%%%%%%%%%%%%%%
CREATE RESPONSE-SPECTRUM
(ONLY AGT4 MOT4)
(ONLY 0.0 15.0 30.0 45.0 60.0 75.0 90.0 105.0 120. 135. 150. 165. 180. )
( ONLY JONS1 JONS2 JONS3 JONS4 JONS5 JONS6 JONS7 JONS8 JONS9 JONS10 JONS11 JONS12 JONS13 JONS14 JONS15 JONS16 JONS17 JONS18 JONS19 JONS20 JONS21
JONS22 JONS23) NONE
%
SET PRINT FILE ' ' ABSOLUTE_MOTIONS_POINT4_OVERVIEW_Testsemi
PRINT OVERVIEW RESPONSE-SPECTRUM
%
SET PRINT FILE ' ' ABSOLUTE_MOTIONS_POINT4_STATISTICS_ULS_Testsemi
PRINT SHORT-TERM-STATISTICS RAYLEIGH SEA-STATE-DURATION ( ONLY 10800 ) *
DELETE RESPONSE-SPECTRUM *
%%%%%%%%%%%%%%%%%%%%%%%%%%%%%%%%%%%%%%%%%%%%%%%%%%%%%%%%%%%%%%%%%%%%%%%%
CREATE RESPONSE-SPECTRUM
(ONLY AGT5 MOT5)
(ONLY 0.0 15.0 30.0 45.0 60.0 75.0 90.0 105.0 120. 135. 150. 165. 180. )
( ONLY JONS1 JONS2 JONS3 JONS4 JONS5 JONS6 JONS7 JONS8 JONS9 JONS10 JONS11 JONS12 JONS13 JONS14 JONS15 JONS16 JONS17 JONS18 JONS19 JONS20 JONS21
JONS22 JONS23) NONE
%
SET PRINT FILE ' ' ABSOLUTE_MOTIONS_POINT5_OVERVIEW_Testsemi
PRINT OVERVIEW RESPONSE-SPECTRUM
%
SET PRINT FILE ' ' ABSOLUTE_MOTIONS_POINT5_STATISTICS_ULS_Testsemi
PRINT SHORT-TERM-STATISTICS RAYLEIGH SEA-STATE-DURATION ( ONLY 10800 ) *
DELETE RESPONSE-SPECTRUM *
%%%%%%%%%%%%%%%%%%%%%%%%%%%%%%%%%%%%%%%%%%%%%%%%%%%%%%%%%%%%%%%%%%%%%%%%
CREATE RESPONSE-SPECTRUM
(ONLY AGT6 MOT6)
(ONLY 0.0 15.0 30.0 45.0 60.0 75.0 90.0 105.0 120. 135. 150. 165. 180. )
( ONLY JONS1 JONS2 JONS3 JONS4 JONS5 JONS6 JONS7 JONS8 JONS9 JONS10 JONS11 JONS12 JONS13 JONS14 JONS15 JONS16 JONS17 JONS18 JONS19 JONS20 JONS21
JONS22 JONS23) NONE
%
SET PRINT FILE ' ' ABSOLUTE_MOTIONS_POINT6_OVERVIEW_Testsemi
PRINT OVERVIEW RESPONSE-SPECTRUM
%
SET PRINT FILE ' ' ABSOLUTE_MOTIONS_POINT6_STATISTICS_ULS_Testsemi
PRINT SHORT-TERM-STATISTICS RAYLEIGH SEA-STATE-DURATION ( ONLY 10800 ) *
DELETE RESPONSE-SPECTRUM *
%%%%%%%%%%%%%%%%%%%%%%%%%%%%%%%%%%%%%%%%%%%%%%%%%%%%%%%%%%%%%%%%%%%%%%%%
CREATE RESPONSE-SPECTRUM
(ONLY AGT7 MOT7)
(ONLY 0.0 15.0 30.0 45.0 60.0 75.0 90.0 105.0 120. 135. 150. 165. 180. )
( ONLY JONS1 JONS2 JONS3 JONS4 JONS5 JONS6 JONS7 JONS8 JONS9 JONS10 JONS11 JONS12 JONS13 JONS14 JONS15 JONS16 JONS17 JONS18 JONS19 JONS20 JONS21
JONS22 JONS23) NONE
%
```

```

SET PRINT FILE ' ' ABSOLUTE_MOTIONS_POINT7_OVERVIEW_Testsemi
PRINT OVERVIEW RESPONSE-SPECTRUM
%
SET PRINT FILE ' ' ABSOLUTE_MOTIONS_POINT7_STATISTICS_ULS_Testsemi
PRINT SHORT-TERM-STATISTICS RAYLEIGH SEA-STATE-DURATION ( ONLY 10800 ) *
DELETE RESPONSE-SPECTRUM *
XXXXXXXXXXXXXXXXXXXXXXXXXXXXXXXXXXXXXXXXXXXXXXXXXXXXXXXXXXXXXXXXXXXX
CREATE RESPONSE-SPECTRUM
(ONLY AGT8 MOT8)
(ONLY 0.0 15.0 30.0 45.0 60.0 75.0 90.0 105.0 120. 135. 150. 165. 180. )
( ONLY JONS1 JONS2 JONS3 JONS4 JONS5 JONS6 JONS7 JONS8 JONS9 JONS10 JONS11 JONS12 JONS13 JONS14 JONS15 JONS16 JONS17 JONS18 JONS19 JONS20 JONS21
JONS22 JONS23) NONE
%
SET PRINT FILE ' ' ABSOLUTE_MOTIONS_POINT8_OVERVIEW_Testsemi
PRINT OVERVIEW RESPONSE-SPECTRUM
%
SET PRINT FILE ' ' ABSOLUTE_MOTIONS_POINT8_STATISTICS_ULS_Testsemi
PRINT SHORT-TERM-STATISTICS RAYLEIGH SEA-STATE-DURATION ( ONLY 10800 ) *
DELETE RESPONSE-SPECTRUM *
XXXXXXXXXXXXXXXXXXXXXXXXXXXXXXXXXXXXXXXXXXXXXXXXXXXXXXXXXXXXXXXXXXXX
CREATE RESPONSE-SPECTRUM
(ONLY AGT9 MOT9)
(ONLY 0.0 15.0 30.0 45.0 60.0 75.0 90.0 105.0 120. 135. 150. 165. 180. )
( ONLY JONS1 JONS2 JONS3 JONS4 JONS5 JONS6 JONS7 JONS8 JONS9 JONS10 JONS11 JONS12 JONS13 JONS14 JONS15 JONS16 JONS17 JONS18 JONS19 JONS20 JONS21
JONS22 JONS23) NONE
%
SET PRINT FILE ' ' ABSOLUTE_MOTIONS_POINT9_OVERVIEW_Testsemi
PRINT OVERVIEW RESPONSE-SPECTRUM
%
SET PRINT FILE ' ' ABSOLUTE_MOTIONS_POINT9_STATISTICS_ULS_Testsemi
PRINT SHORT-TERM-STATISTICS RAYLEIGH SEA-STATE-DURATION ( ONLY 10800 ) *
DELETE RESPONSE-SPECTRUM *
XXXXXXXXXXXXXXXXXXXXXXXXXXXXXXXXXXXXXXXXXXXXXXXXXXXXXXXXXXXXXXXXXXXX
CREATE RESPONSE-SPECTRUM
(ONLY AGT10 MOT10)
(ONLY 0.0 15.0 30.0 45.0 60.0 75.0 90.0 105.0 120. 135. 150. 165. 180. )
( ONLY JONS1 JONS2 JONS3 JONS4 JONS5 JONS6 JONS7 JONS8 JONS9 JONS10 JONS11 JONS12 JONS13 JONS14 JONS15 JONS16 JONS17 JONS18 JONS19 JONS20 JONS21
JONS22 JONS23) NONE
%
SET PRINT FILE ' ' ABSOLUTE_MOTIONS_POINT10_OVERVIEW_Testsemi
PRINT OVERVIEW RESPONSE-SPECTRUM
%
SET PRINT FILE ' ' ABSOLUTE_MOTIONS_POINT10_STATISTICS_ULS_Testsemi
PRINT SHORT-TERM-STATISTICS RAYLEIGH SEA-STATE-DURATION ( ONLY 10800 ) *
DELETE RESPONSE-SPECTRUM *
XXXXXXXXXXXXXXXXXXXXXXXXXXXXXXXXXXXXXXXXXXXXXXXXXXXXXXXXXXXXXXXXXXXX
CREATE RESPONSE-SPECTRUM
(ONLY AGT11 MOT11)
(ONLY 0.0 15.0 30.0 45.0 60.0 75.0 90.0 105.0 120. 135. 150. 165. 180. )
( ONLY JONS1 JONS2 JONS3 JONS4 JONS5 JONS6 JONS7 JONS8 JONS9 JONS10 JONS11 JONS12 JONS13 JONS14 JONS15 JONS16 JONS17 JONS18 JONS19 JONS20 JONS21
JONS22 JONS23) NONE
%
SET PRINT FILE ' ' ABSOLUTE_MOTIONS_POINT11_OVERVIEW_Testsemi
PRINT OVERVIEW RESPONSE-SPECTRUM
%
SET PRINT FILE ' ' ABSOLUTE_MOTIONS_POINT11_STATISTICS_ULS_Testsemi
PRINT SHORT-TERM-STATISTICS RAYLEIGH SEA-STATE-DURATION ( ONLY 10800 ) *
DELETE RESPONSE-SPECTRUM *
XXXXXXXXXXXXXXXXXXXXXXXXXXXXXXXXXXXXXXXXXXXXXXXXXXXXXXXXXXXXXXXXXXXX
CREATE RESPONSE-SPECTRUM
(ONLY AGT12 MOT12)
(ONLY 0.0 15.0 30.0 45.0 60.0 75.0 90.0 105.0 120. 135. 150. 165. 180. )
( ONLY JONS1 JONS2 JONS3 JONS4 JONS5 JONS6 JONS7 JONS8 JONS9 JONS10 JONS11 JONS12 JONS13 JONS14 JONS15 JONS16 JONS17 JONS18 JONS19 JONS20 JONS21
JONS22 JONS23) NONE
%
SET PRINT FILE ' ' ABSOLUTE_MOTIONS_POINT12_OVERVIEW_Testsemi

```

```
PRINT OVERVIEW RESPONSE-SPECTRUM
%
SET PRINT FILE ' ' ABSOLUTE_MOTIONS_POINT12_STATISTICS_ULS_Testsemi
PRINT SHORT-TERM-STATISTICS RAYLEIGH SEA-STATE-DURATION ( ONLY 10800 ) *
DELETE RESPONSE-SPECTRUM *
XXXXXXXXXXXXXXXXXXXXXXXXXXXXXXXXXXXXXXXXXXXXXXXXXXXXXXXXXXXXXXXXXXXX
CREATE RESPONSE-SPECTRUM
(ONLY AGT13 MOT13)
(ONLY 0.0 15.0 30.0 45.0 60.0 75.0 90.0 105.0 120. 135. 150. 165. 180. )
( ONLY JONS1 JONS2 JONS3 JONS4 JONS5 JONS6 JONS7 JONS8 JONS9 JONS10 JONS11 JONS12 JONS13 JONS14 JONS15 JONS16 JONS17 JONS18 JONS19 JONS20 JONS21
JONS22 JONS23) NONE
%
SET PRINT FILE ' ' ABSOLUTE_MOTIONS_POINT13_OVERVIEW_Testsemi
PRINT OVERVIEW RESPONSE-SPECTRUM
%
SET PRINT FILE ' ' ABSOLUTE_MOTIONS_POINT13_STATISTICS_ULS_Testsemi
PRINT SHORT-TERM-STATISTICS RAYLEIGH SEA-STATE-DURATION ( ONLY 10800 ) *
DELETE RESPONSE-SPECTRUM *
XXXXXXXXXXXXXXXXXXXXXXXXXXXXXXXXXXXXXXXXXXXXXXXXXXXXXXXXXXXXXXXXXXXX
CREATE RESPONSE-SPECTRUM
(ONLY AGT14 MOT14)
(ONLY 0.0 15.0 30.0 45.0 60.0 75.0 90.0 105.0 120. 135. 150. 165. 180. )
( ONLY JONS1 JONS2 JONS3 JONS4 JONS5 JONS6 JONS7 JONS8 JONS9 JONS10 JONS11 JONS12 JONS13 JONS14 JONS15 JONS16 JONS17 JONS18 JONS19 JONS20 JONS21
JONS22 JONS23) NONE
%
SET PRINT FILE ' ' ABSOLUTE_MOTIONS_POINT14_OVERVIEW_Testsemi
PRINT OVERVIEW RESPONSE-SPECTRUM
%
SET PRINT FILE ' ' ABSOLUTE_MOTIONS_POINT14_STATISTICS_ULS_Testsemi
PRINT SHORT-TERM-STATISTICS RAYLEIGH SEA-STATE-DURATION ( ONLY 10800 ) *
DELETE RESPONSE-SPECTRUM *
XXXXXXXXXXXXXXXXXXXXXXXXXXXXXXXXXXXXXXXXXXXXXXXXXXXXXXXXXXXXXXXXXXXX
CREATE RESPONSE-SPECTRUM
(ONLY AGT15 MOT15)
(ONLY 0.0 15.0 30.0 45.0 60.0 75.0 90.0 105.0 120. 135. 150. 165. 180. )
( ONLY JONS1 JONS2 JONS3 JONS4 JONS5 JONS6 JONS7 JONS8 JONS9 JONS10 JONS11 JONS12 JONS13 JONS14 JONS15 JONS16 JONS17 JONS18 JONS19 JONS20 JONS21
JONS22 JONS23) NONE
%
SET PRINT FILE ' ' ABSOLUTE_MOTIONS_POINT15_OVERVIEW_Testsemi
PRINT OVERVIEW RESPONSE-SPECTRUM
%
SET PRINT FILE ' ' ABSOLUTE_MOTIONS_POINT15_STATISTICS_ULS_Testsemi
PRINT SHORT-TERM-STATISTICS RAYLEIGH SEA-STATE-DURATION ( ONLY 10800 ) *
DELETE RESPONSE-SPECTRUM *
XXXXXXXXXXXXXXXXXXXXXXXXXXXXXXXXXXXXXXXXXXXXXXXXXXXXXXXXXXXXXXXXXXXX
CREATE RESPONSE-SPECTRUM
(ONLY AGT16 MOT16)
(ONLY 0.0 15.0 30.0 45.0 60.0 75.0 90.0 105.0 120. 135. 150. 165. 180. )
( ONLY JONS1 JONS2 JONS3 JONS4 JONS5 JONS6 JONS7 JONS8 JONS9 JONS10 JONS11 JONS12 JONS13 JONS14 JONS15 JONS16 JONS17 JONS18 JONS19 JONS20 JONS21
JONS22 JONS23) NONE
%
SET PRINT FILE ' ' ABSOLUTE_MOTIONS_POINT16_OVERVIEW_Testsemi
PRINT OVERVIEW RESPONSE-SPECTRUM
%
SET PRINT FILE ' ' ABSOLUTE_MOTIONS_POINT16_STATISTICS_ULS_Testsemi
PRINT SHORT-TERM-STATISTICS RAYLEIGH SEA-STATE-DURATION ( ONLY 10800 ) *
DELETE RESPONSE-SPECTRUM *
XXXXXXXXXXXXXXXXXXXXXXXXXXXXXXXXXXXXXXXXXXXXXXXXXXXXXXXXXXXXXXXXXXXX
CREATE RESPONSE-SPECTRUM
(ONLY AGT17 MOT17)
(ONLY 0.0 15.0 30.0 45.0 60.0 75.0 90.0 105.0 120. 135. 150. 165. 180. )
( ONLY JONS1 JONS2 JONS3 JONS4 JONS5 JONS6 JONS7 JONS8 JONS9 JONS10 JONS11 JONS12 JONS13 JONS14 JONS15 JONS16 JONS17 JONS18 JONS19 JONS20 JONS21
JONS22 JONS23) NONE
%
SET PRINT FILE ' ' ABSOLUTE_MOTIONS_POINT17_OVERVIEW_Testsemi
PRINT OVERVIEW RESPONSE-SPECTRUM
```


Appendix F

LS-Dyna Results

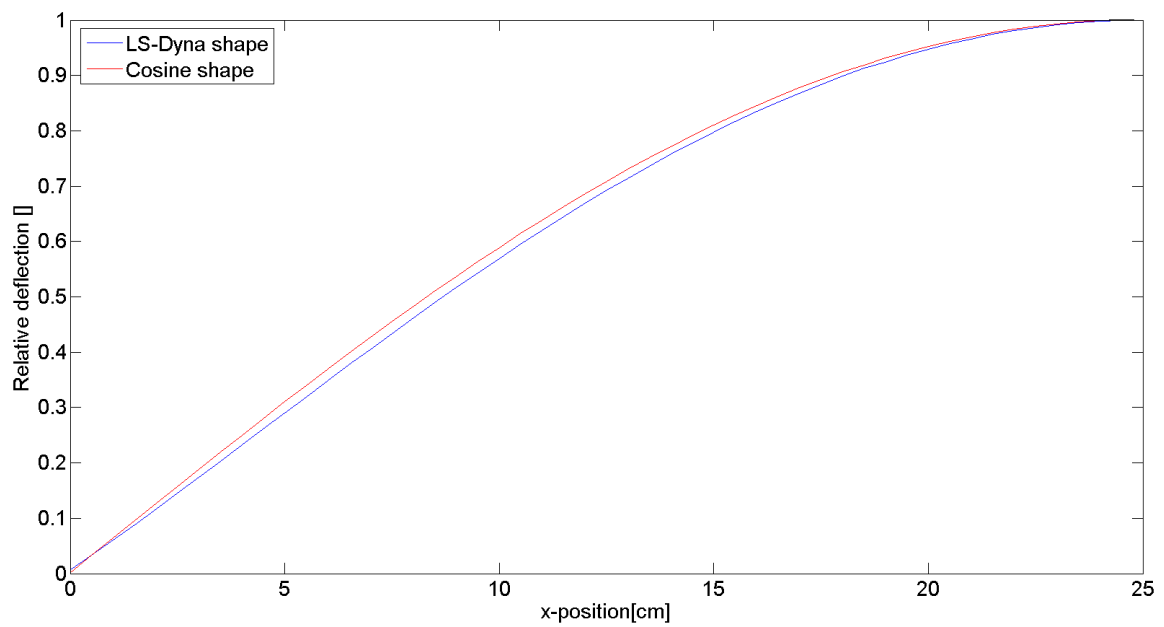


Figure F.1: The 2D defection shape in LS-Dyna compared to the chosen cosine deflection shape

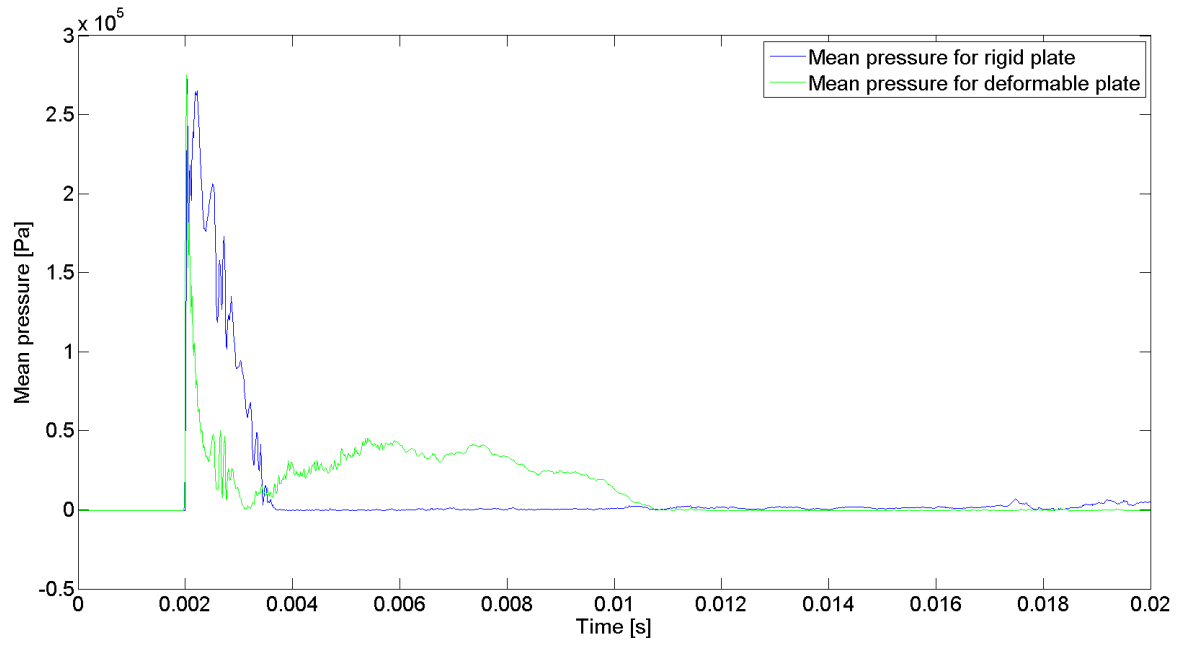


Figure F.2: Mean pressure development for a drop velocity of 0.75 m/s for 2D plate

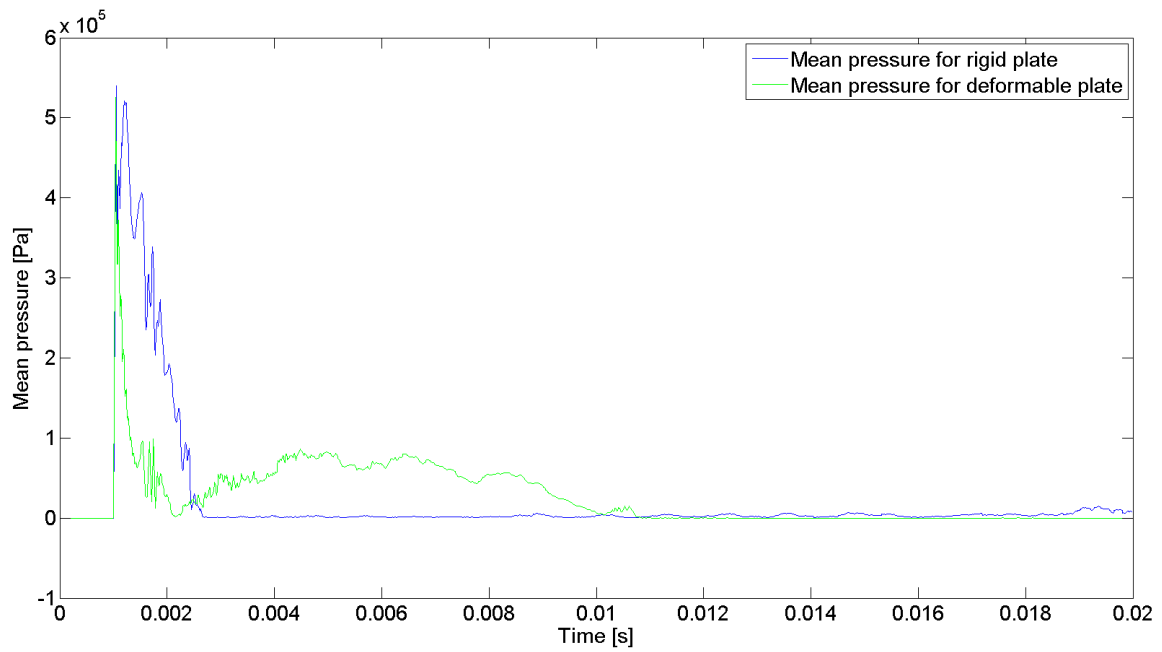


Figure F.3: Mean pressure development for a drop velocity of 1.5 m/s for 2D plate

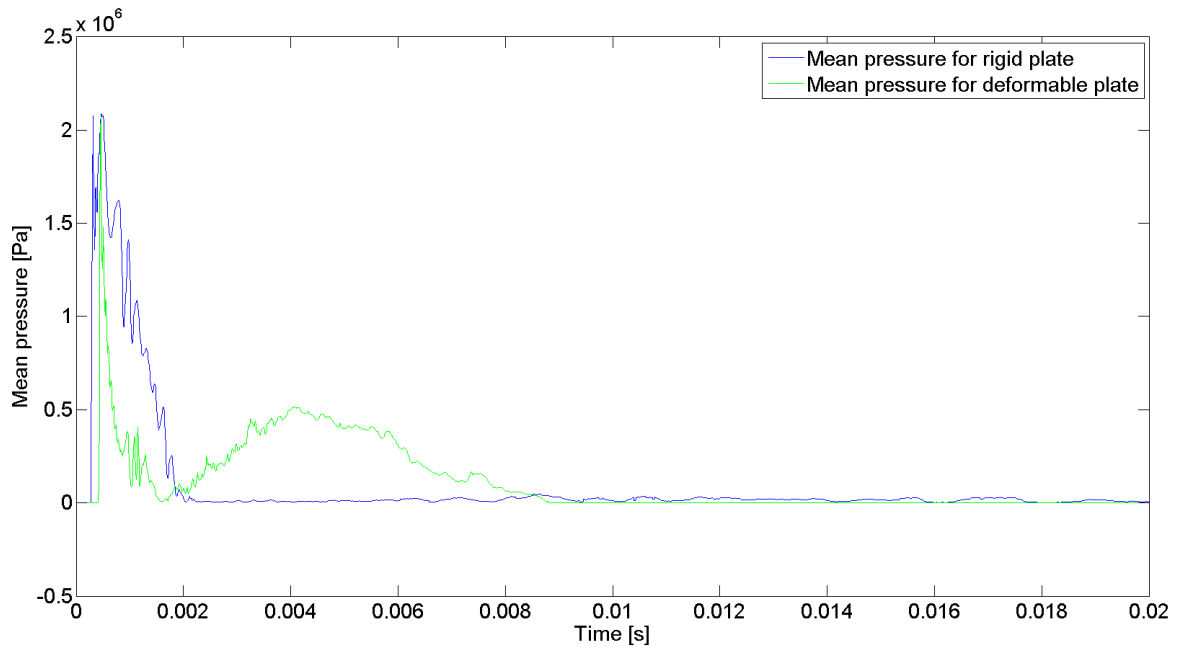


Figure F4: Mean pressure development for a drop velocity of 6 m/s for 2D plate

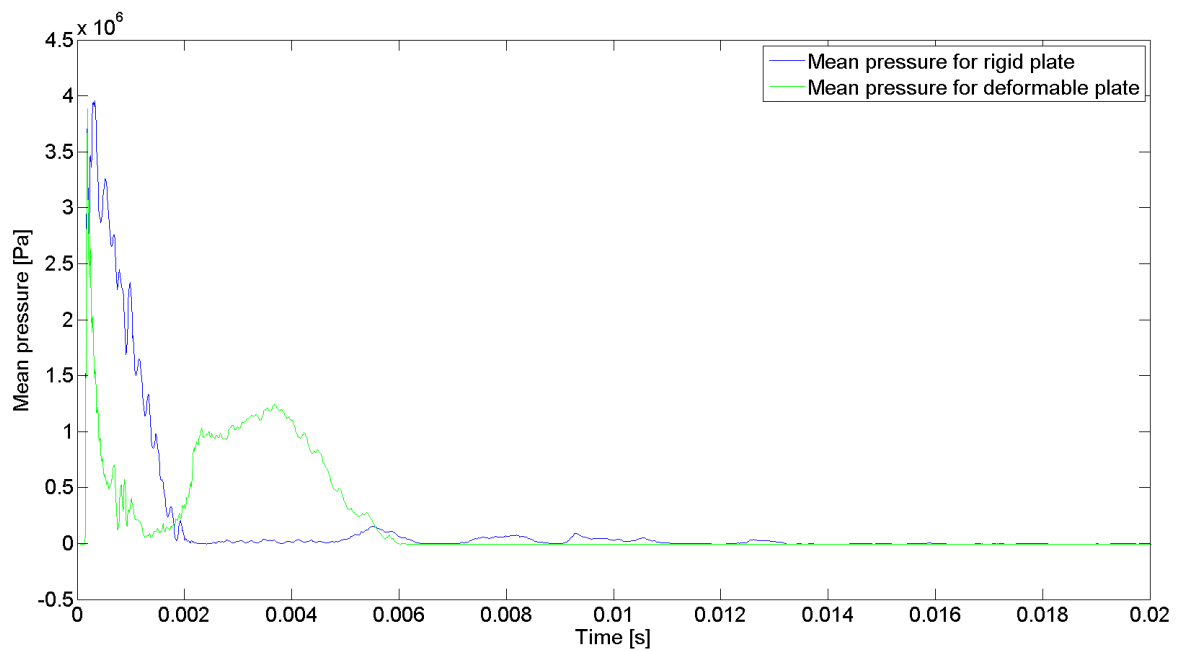


Figure F5: Mean pressure development for a drop velocity of 11.19 m/s into sea water for 2D plate

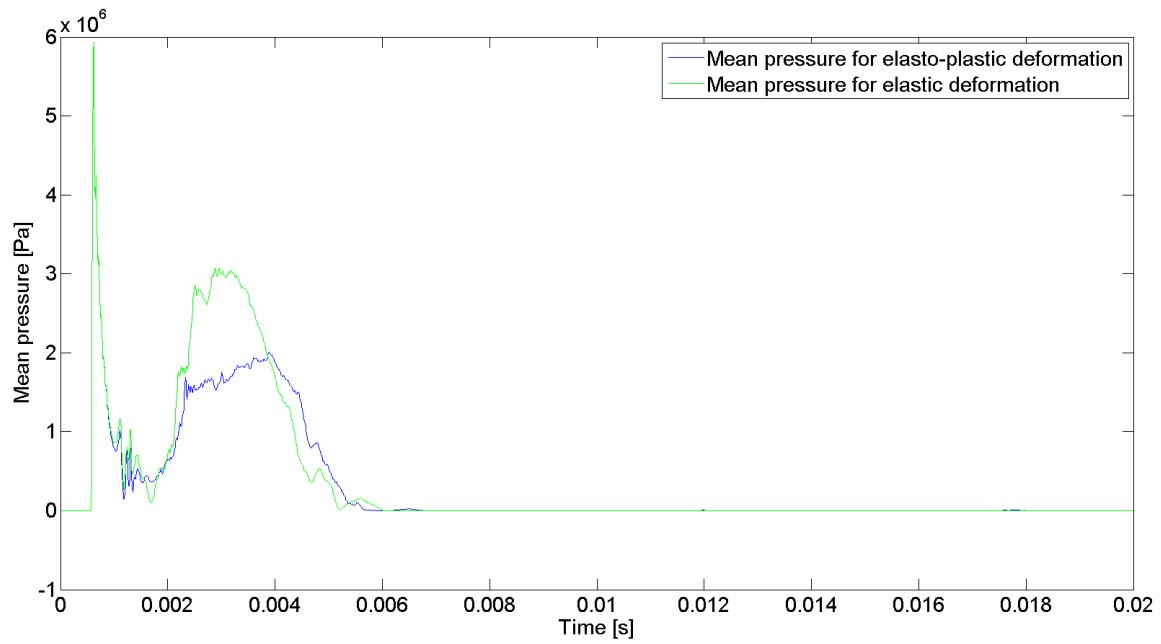


Figure F6: Mean pressure development for a drop velocity of 18[m/s] for 2D plate

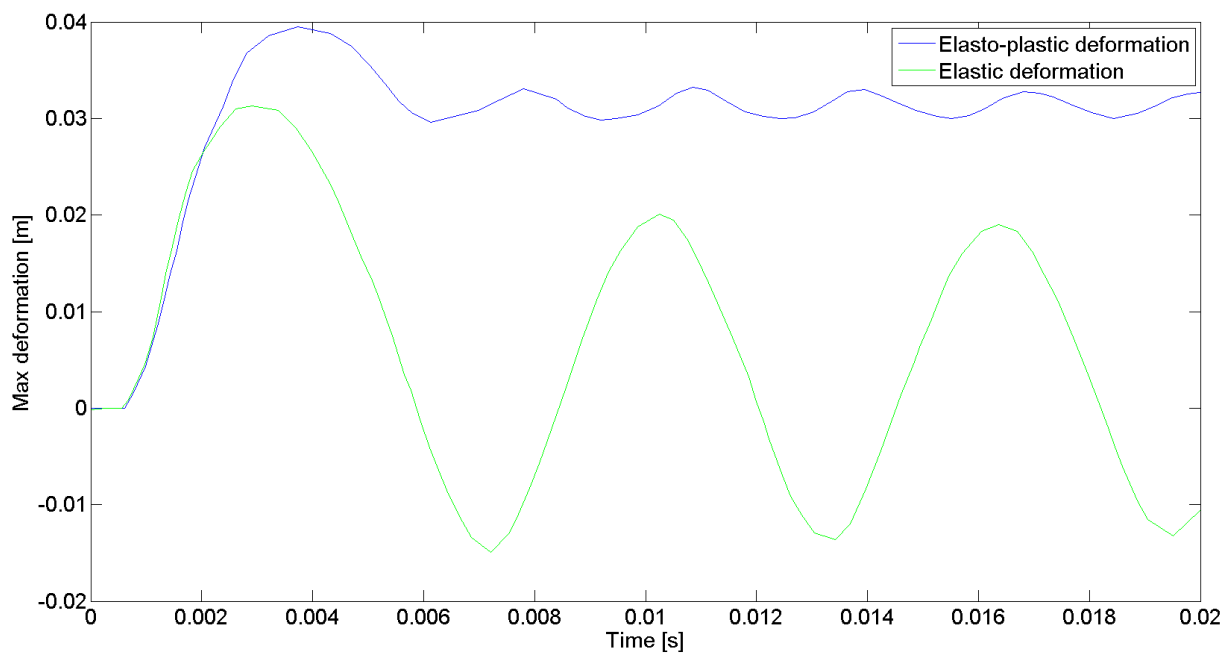


Figure F7: Elastic and elasto plastic deflection at a drop velocity of 18[m/s] for 2D plate

Appendix G

Transformation Factors for Beams

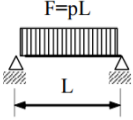
Load case	Resistance domain	Load Factor K_l	Mass factor K_m		Load-mass factor K_{lm}		Maximum resistance R_{el}	Linear stiffness k_l	Dynamic reaction V
			Concentrated mass	Uniform mass	Concentrated mass	Uniform mass			
	Elastic	0.64		0.50		0.78	$\frac{8M_p}{L}$	$\frac{384EI}{5L^3}$	$0.39R + 0.11F$
	Plastic bending	0.50		0.33		0.66	$\frac{8M_p}{L}$	0	$0.38R_{el} + 0.12F$
	Plastic membrane	0.50		0.33		0.66		$\frac{4N_p}{L}$	$\frac{2N_p y_{max}}{L}$

Figure G.1: Transformation factor for simply supported beam in SDOF

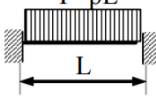
Load case	Resistance domain	Load Factor K_l	Mass factor K_m		Load-mass factor K_{lm}		Maximum resistance R_{el}	Linear stiffness k_l	Equivalent linear stiffness k_e	Dynamic reaction V
			Concentrated mass	Uniform mass	Concentrated mass	Uniform mass				
	Elastic	0.53		0.41		0.77	$\frac{12M_{ps}}{L}$	$\frac{384EI}{L^3}$	$\left(\frac{307EI}{L^3}\right) \cdot m_1$	$0.36R + 0.14F$
	Elasto-plastic bending	0.64		0.50		0.78	$\frac{8(M_{ps} + M_{pm})}{L}$	$\frac{384EI}{5L^3}$		$0.39R_{el} + 0.11F$
	Plastic bending	0.50		0.33		0.66	$\frac{8(M_{ps} + M_{pm})}{L}$	0	$0.38R_{el} + 0.12F$	
	Plastic membrane	0.50		0.33		0.66		$\frac{4N_p}{L}$	$\frac{2N_p y_{max}}{L}$	

Figure G.2: Transformation factor for clamped beam in SDOF

Appendix H

SDOF Analysis

H.1 Timeintegration Function from MatLab

```
function [w,v,a, omega] = timepulseint(p,t) % p is to be given in terms of mean pressure
%% Defign input parameters here:
L = ; %Length of panel
s = ; %Breadth of panel
Ma = %Insert generalised added mass
M = ; %Insert generalised mass
k = ;%Insert generalised stiffness, 0 for nonlinear analysis
Rmax = ; %Expected maximum resistance for nonlinear analysis
wmax = ; %Expected maximumdeformation for nonlinear analysis
c = 0; %Damping
tlim = 0.1;% Limit for axis
%% Section for dynamic calculation
if k == 0
k = Rmax/wmax;
end
m = (Ma+M);
omega = sqrt(k./m);
h = zeros(1,length(t));
for i = 2:length(h)
h(i) = t(i)-t(i-1);
end
qbar = p*L*s; %Pressure times area
a = zeros(1,length(t));
v = zeros(1,length(t));
w = zeros(1,length(t));
for i = 2:length(t)
w(i) = (qbar(i)+m*a(i-1)+(4*m/h(i)+c)*v(i-1)+(4*m/h(i)^2+2*c/h(i))*w(i-1))/(4*m/h(i)^2+2*c/h(i)+k);
a(i) = 4*(w(i)-w(i-1)-v(i-1)*h(i))/h(i)^2-a(i-1);
v(i) = v(i-1)+0.5*(a(i)+a(i-1))*h(i);
end
figure('Name','Displacements')
hold on
box on
xlim([0 tlim])
set(gca,'fontsize',18)
xlabel('Time [s]')
ylabel('Deflection [m]')
plot(t,w,'r');
figure('Name','Velocity')
hold on
box on
xlim([0 tlim])
set(gca,'fontsize',18)
```

```
xlabel('Time [s]')
ylabel('Velocity [m/s]')
plot(t,v,'r');
figure('Name','Acceleration')
hold on
box on
xlim([0 tlim])
set(gca,'fontsize',18)
xlabel('Time [s]')
ylabel('Acceleration [m/s^2]')
plot(t,a,'r');
end
```

H.2 SDOF Plots

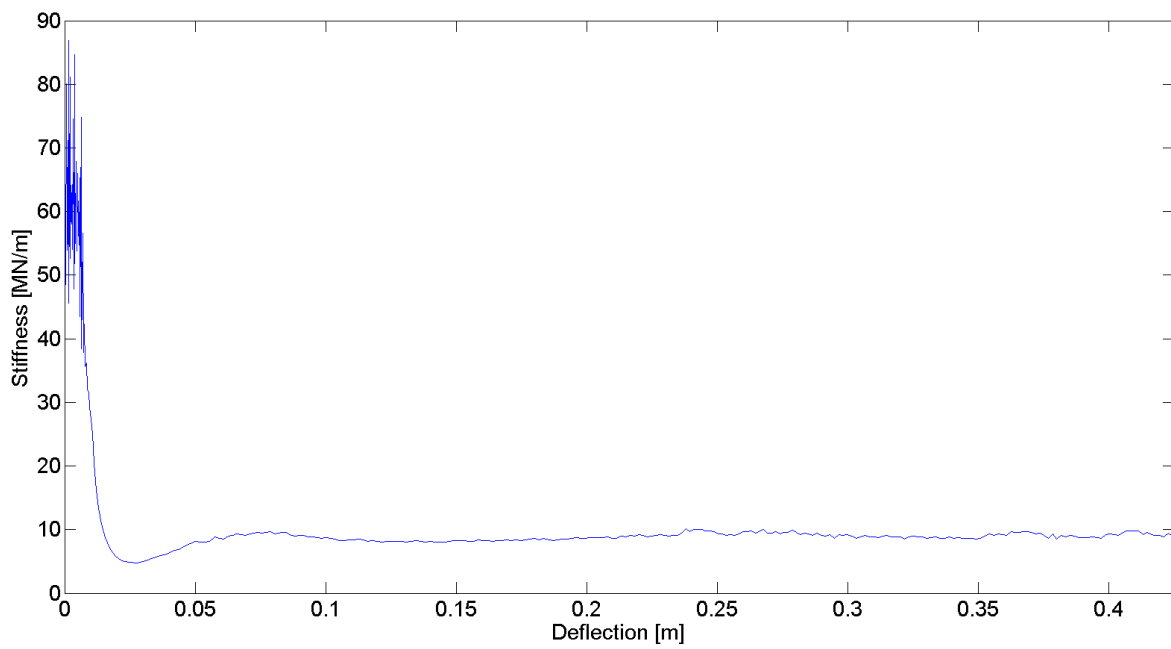


Figure H.1: Beam stiffness k found from LS-Dyna w.r.t. maximum deflection

H.2.1 Rigid Load Pressure

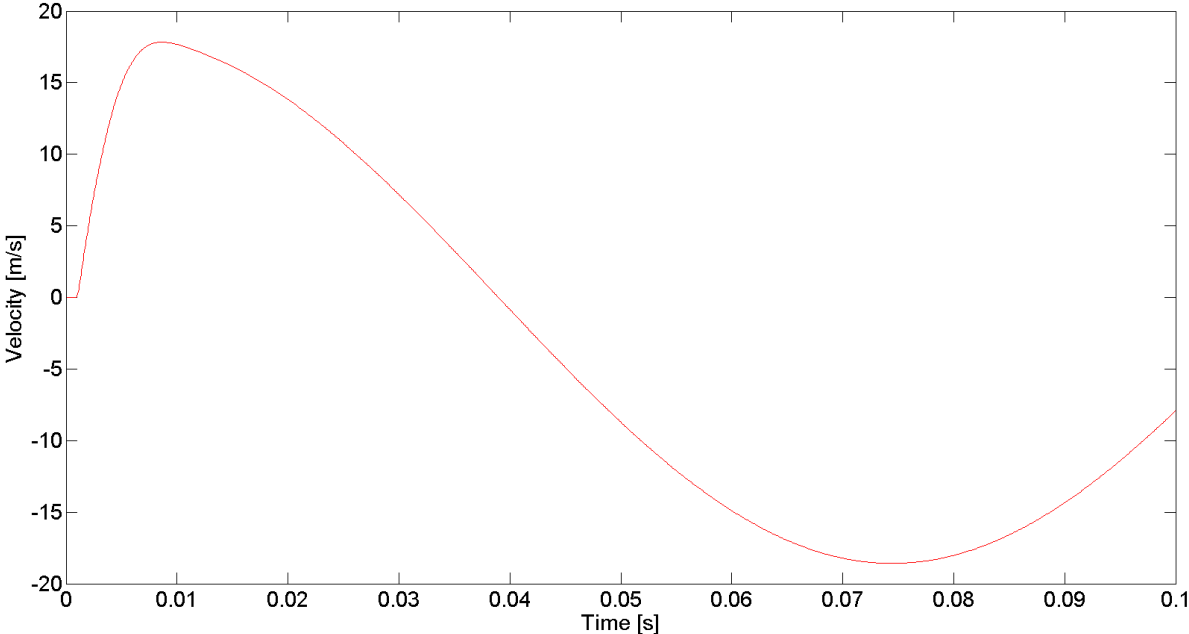


Figure H.2: Velocity of the stiffened clamped plate subjected to the rigid design load pulse

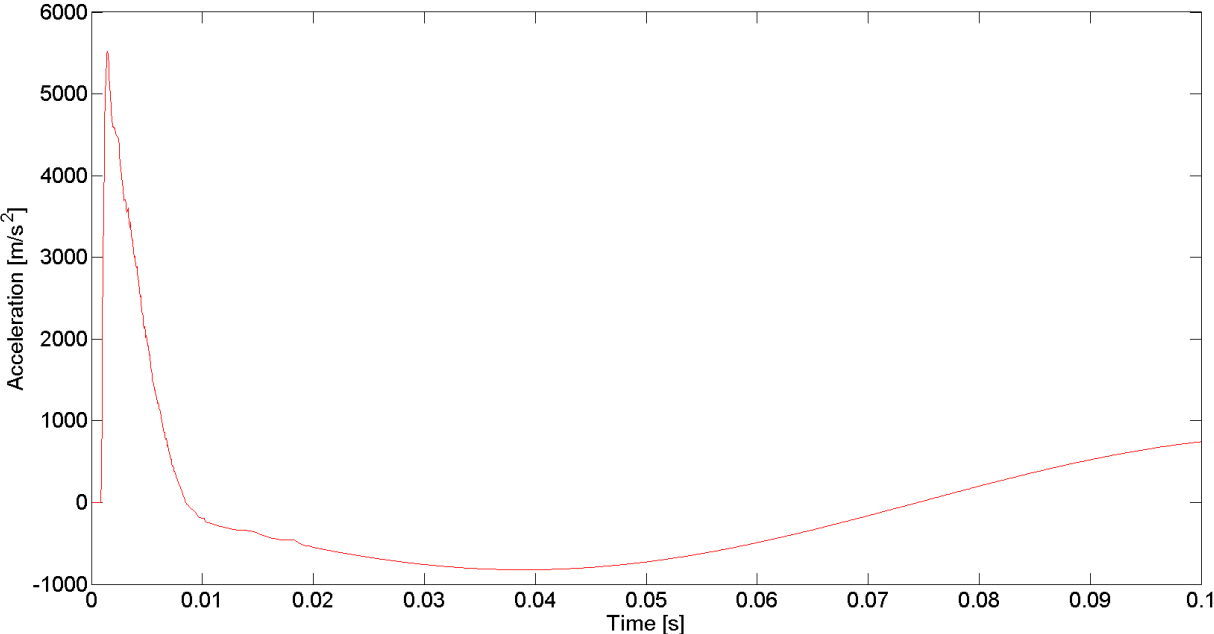


Figure H.3: Acceleration of the stiffened clamped plate subjected to the rigid design load pulse

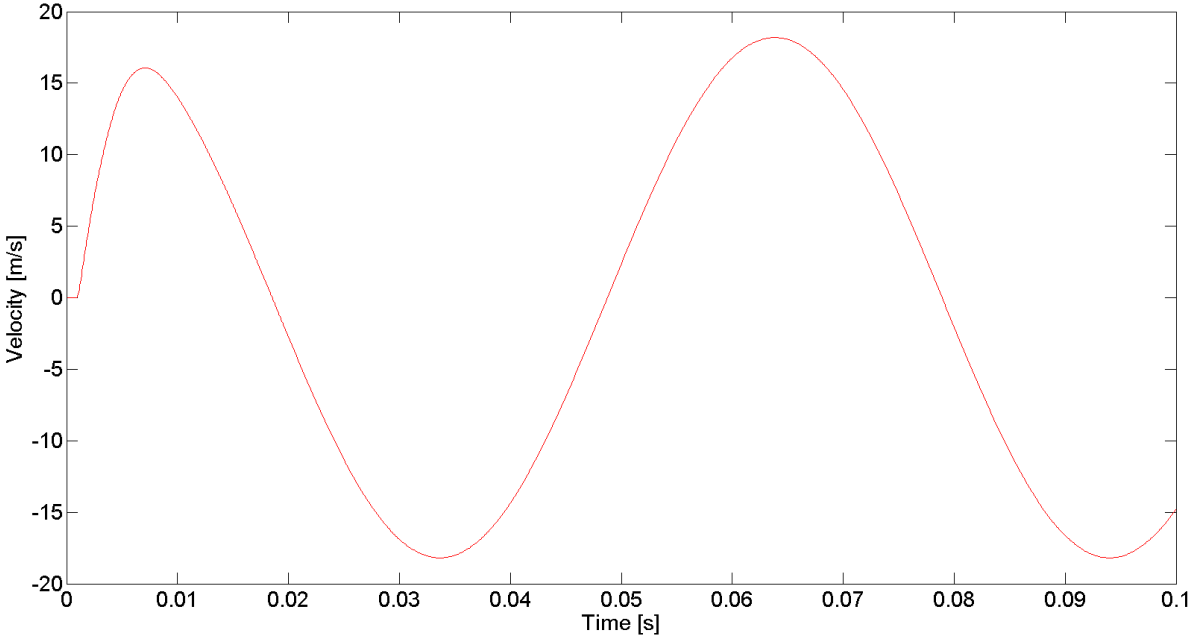


Figure H.4: Velocity of the stiffened plate with the stiffness function obtained from LS-Dyna subjected to the rigid design load pressure

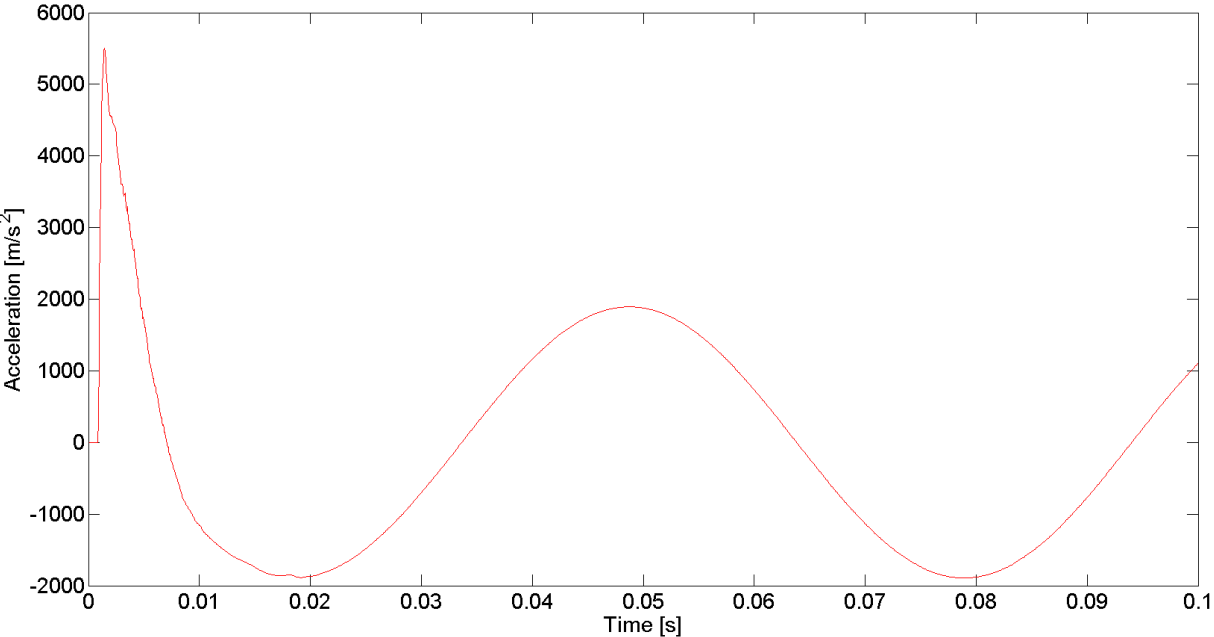


Figure H.5: Acceleration of the stiffened plate with the stiffness function obtained from LS-Dyna subjected to the rigid design load pressure

H.2.2 Load From OTG

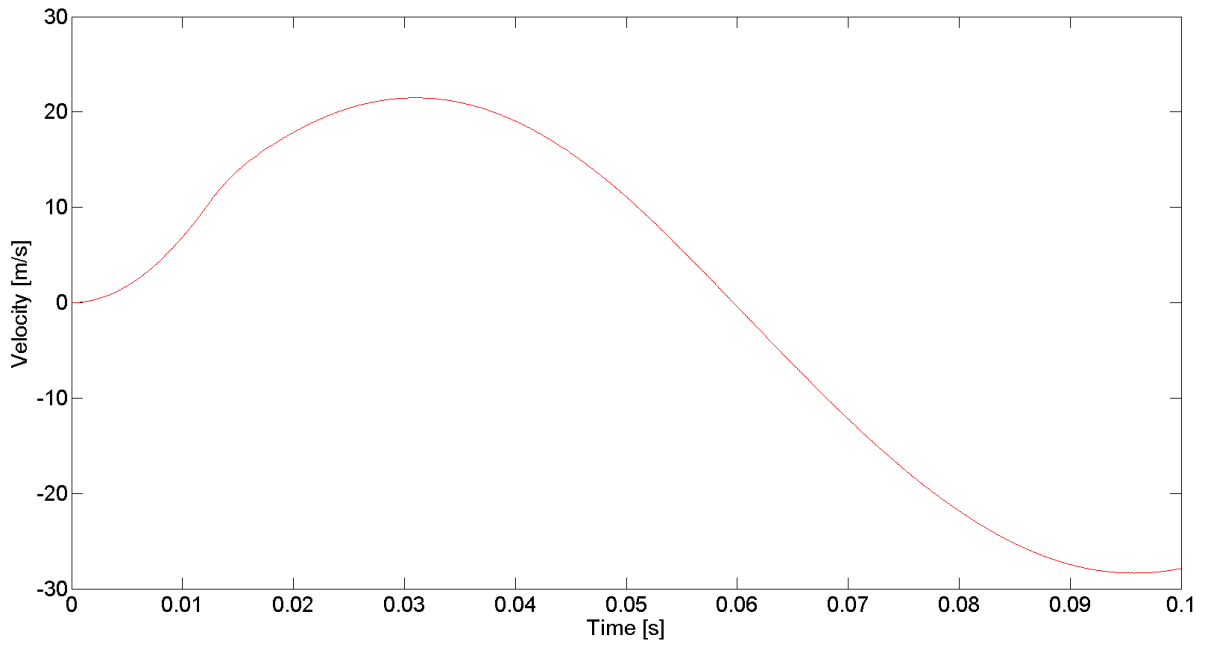


Figure H.6: Velocity of the stiffened clamped plate subjected to pressure from the OTG

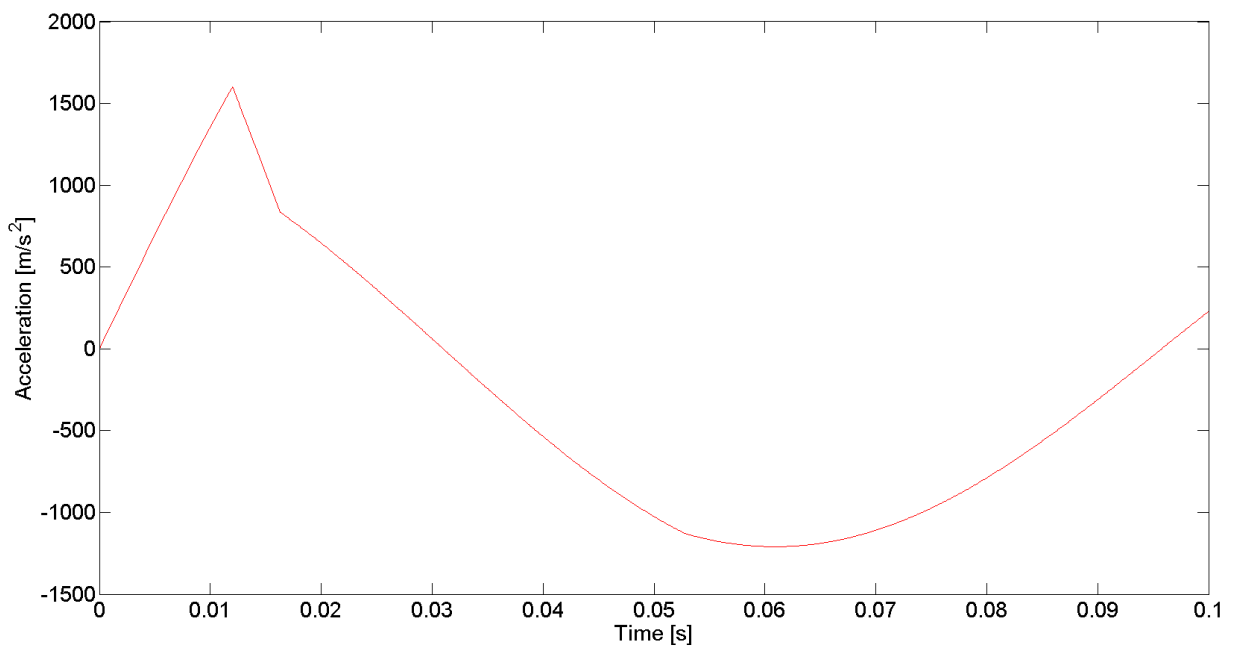


Figure H.7: Acceleration of the stiffened clamped plate subjected to pressure from the OTG

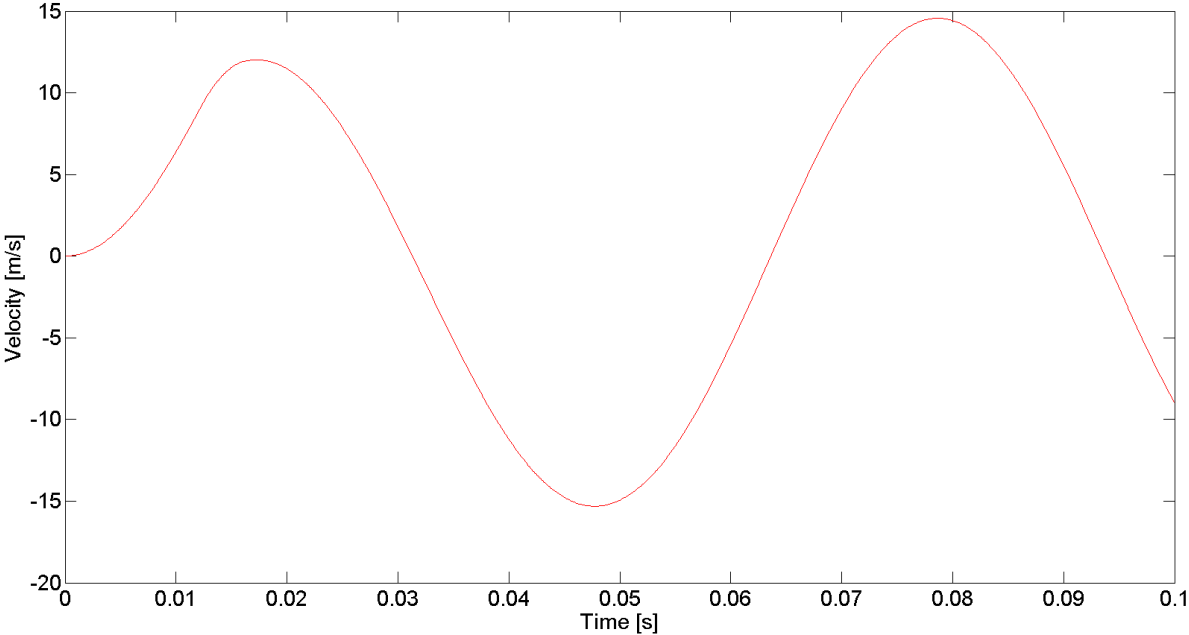


Figure H.8: Velocity of the stiffened plate with the stiffness function obtained from LS-Dyna subjected to the pressure from the OTG

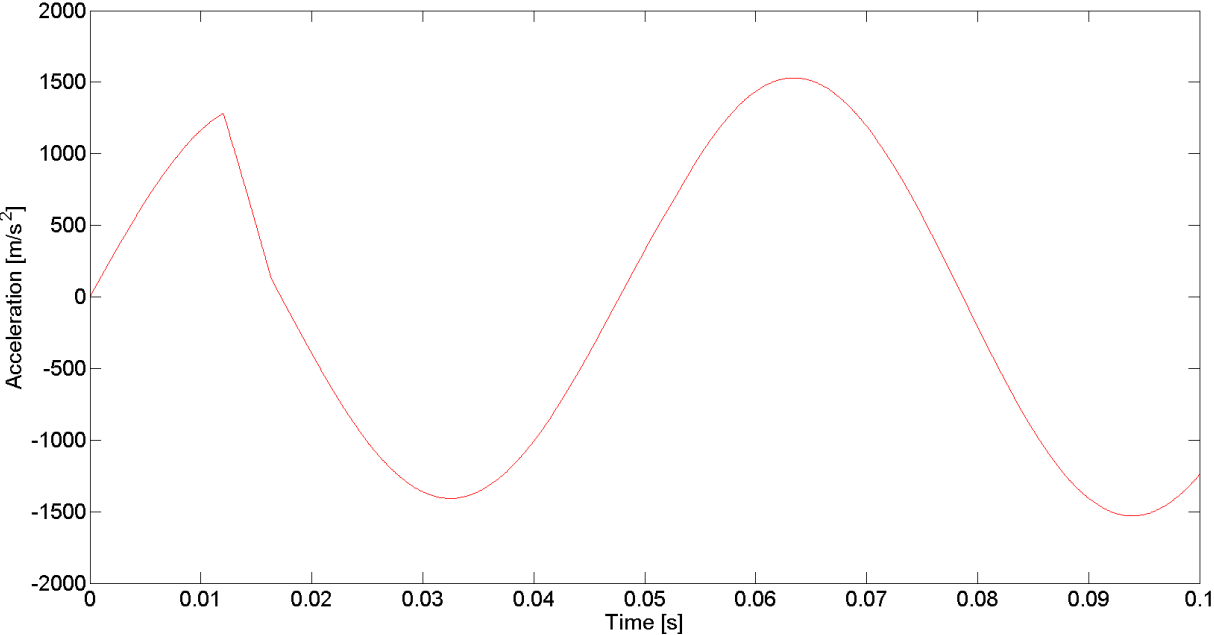


Figure H.9: Acceleration of the stiffened plate with the stiffness function obtained from LS-Dyna subjected to the pressure from the OTG